

PREPARATION AND DIELECTRIC PROPERTIES OF
PIEZOELECTRIC/POLYMER NANOCOMPOSITE MATERIALS

CHANISA NAWANIL

A THESIS SUBMITTED IN PARTIAL FULFILLMENT
OF THE REQUIREMENT FOR THE DEGREE OF
DOCTOR OF PHILOSOPHY IN NANOSCIENCE AND NANOTECHNOLOGY
COLLEGE OF NANOTECHNOLOGY
KING MONGKUT'S INSTITUTE OF TECHNOLOGY LADKRABANG

2015

KMITL-2015-NT-D-001-010

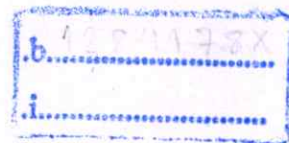
สำนักหอสมุดกลาง พระจอมเกล้าลาดกระบัง

PREPARATION AND DIELECTRIC PROPERTIES OF
PIEZOELECTRIC/POLYMER NANOCOMPOSITE MATERIALS



CHANISA NAWANIL

เลขหมู่.....
เลขทะเบียน.....**078171**.....
วัน,เดือน,ปี**1.6.2560**.....



A THESIS SUBMITTED IN PARTIAL FULFILLMENT
OF THE REQUIREMENT FOR THE DEGREE OF
DOCTOR OF PHILOSOPHY IN NANOSCIENCE AND NANOTECHNOLOGY
COLLEGE OF NANOTECHNOLOGY

KING MONGKUT'S INSTITUTE OF TECHNOLOGY LADKRABANG

2015

KMITL-2015-NT-D-001-010

การเตรียมและสมบัติไดอิเล็กทริกของวัสดุเพียโซอิเล็กทริก/พอลิเมอร์
นาโนคอมโพสิต

PREPARATION AND DIELECTRIC PROPERTIES OF
PIEZOELECTRIC/POLYMER NANOCOMPOSITE MATERIALS

ชนิศา นวนิล
CHANISA NAWANIL

วิทยานิพนธ์นี้เป็นส่วนหนึ่งของการศึกษาตามหลักสูตรปริญญาปรัชญาดุษฎีบัณฑิต

สาขาวิชานาโนวิทยาและนาโนเทคโนโลยี

วิทยาลัยนาโนเทคโนโลยีพระจอมเกล้าลาดกระบัง

สถาบันเทคโนโลยีพระจอมเกล้าเจ้าคุณทหารลาดกระบัง

พ.ศ. 2558

KMITL-2015-NT-D-001-010

COPYRIGHT 2015

COLLEGE OF NANOTECHNOLOGY

KING MONGKUT'S INSTITUTE OF TECHNOLOGY LADKRABANG

หัวข้อวิทยานิพนธ์	การเตรียมและสมบัติไดอิเล็กทริกของวัสดุเพียโซอิเล็กทริก/พอลิเมอร์นาโนคอมโพสิต
นักศึกษา	ชนิศา นวนิล
รหัสประจำตัว	53670201
ปริญญา	ปรัชญาดุษฎีบัณฑิต
สาขาวิชา	นาโนวิทยาและนาโนเทคโนโลยี
พ.ศ.	2558
อาจารย์ที่ปรึกษาวิทยานิพนธ์	รศ.ดร.นราธิป วิทยากร
อาจารย์ที่ปรึกษาวิทยานิพนธ์ร่วม	รศ.ดร.จุฑารัตน์ ปรัชญาวารการ

บทคัดย่อ

งานวิจัยนี้มีวัตถุประสงค์เพื่อศึกษาการเตรียมและสมบัติไดอิเล็กทริกของวัสดุเพียโซอิเล็กทริก/พอลิเมอร์นาโนคอมโพสิต โดยใช้เส้นใยนาโนเลดเซอร์โคเนตเป็นเฟสกระจายตัวและพอลิไวนิลลิดีนไคฟลูออไรด์เป็นเมทริกซ์เฟส โดยทำการศึกษาเส้นใยนาโนเพียโซเซรามิกด้วยการสังเคราะห์เส้นใยจากสองกระบวนการร่วมกันคือกระบวนการอิเล็กโตรสปินนิงและโซลเจล และทำการเปลี่ยนแปลงความเข้มข้น อัตราส่วนโดยปริมาตรของสารละลายตั้งต้นต่อพอลิเมอร์ อัตราการไหล อุณหภูมิเคลไซน์ และชนิดของพอลิเมอร์ นอกจากนี้ยังได้ทำการศึกษาผลของการทำโซลโวเทอร์มอลที่มีต่อการเปลี่ยนแปลงของเส้นใยนาโนเลดเซอร์โคเนต อีกทั้งงานวิจัยนี้ยังได้ทำการศึกษากการเตรียมและสมบัติไดอิเล็กทริกของเพียโซอิเล็กทริก/พอลิเมอร์นาโนคอมโพสิตที่ทำการปรับปรุงด้วยท่อนาโนคาร์บอนอีกด้วย

งานวิจัยนี้ได้ทำการสังเคราะห์เส้นใยเลดเซอร์โคเนตด้วยเทคนิคอิเล็กโตรสปินนิงโดยใช้สารละลายที่ประกอบด้วยพอลิเอทิลีนออกไซด์ 5% โดยน้ำหนักในเอทานอลและสารละลายโซลเจลของเลดเซอร์โคเนต และทำการเปลี่ยนแปลงตัวแปรที่เกี่ยวข้อง ได้แก่ อัตราส่วนระหว่างเลดเซอร์โคเนตกับพอลิเอทิลีนออกไซด์ ความเข้มข้นของสารละลายตั้งต้น อัตราการไหล และอุณหภูมิเผาแคลไซน์ พบว่าได้เส้นใยเลดเซอร์โคเนตที่มีโครงสร้างแบบเพอโรฟสไกต์ที่สมบูรณ์ภายหลังการเผาแคลไซน์เส้นใยคอมโพสิตของเลดเซอร์โคเนตกับพอลิเอทิลีนออกไซด์ที่ 650°C เป็นเวลา 4 ชั่วโมง โดยใช้อัตราส่วนโดยปริมาตรของเลดเซอร์โคเนตกับพอลิเอทิลีนออกไซด์เป็น 10:3 และความเข้มข้นของเลดเซอร์โคเนต 1 โมลาร์ เส้นใยที่ได้มีขนาดเส้นผ่านศูนย์กลางเฉลี่ย 300 ± 64 นาโนเมตร อีกทั้งเส้นใยเลดเซอร์โคเนตที่ได้อังแสดงอุณหภูมิคูรีที่เพิ่มขึ้นถึง 130°C เมื่อเปรียบเทียบกับอนุภาคเลดเซอร์โคเนตทั่วไป

อีกทั้งงานวิจัยนี้ยังได้ทำการศึกษากการสังเคราะห์เส้นใยนาโนของเลดเซอร์โคเนตกับพอลิเอทิลีนออกไซด์และแป่งข้าวเหนียวด้วยวิธีอิเล็กโตรสปินนิง โดยทำการศึกษาผลของตัวแปรต่างๆ ได้แก่ อัตราส่วนระหว่างพอลิเอทิลีนออกไซด์กับแป่งข้าวเหนียว และอุณหภูมิเคลไซน์ จากภาพถ่ายอิเล็กตรอนแบบส่องกราดพบว่าเส้นใยที่ได้มีพื้นผิวเรียบและสม่ำเสมอที่อัตราส่วนของเลดเซอร์โคเนต

กับพอลิเอทิลีนออกไซด์และแป้งข้าวเหนียวเป็น 10:2:1 ภายหลังจากเผาแคลไซน์ที่ 650°C เป็นเวลา 4 ชั่วโมง เส้นใยนาโนเลดเซอร์โคเนตมีโครงสร้างเพอรอฟสไกต์ที่สมบูรณ์ เส้นใยที่ได้มีความสม่ำเสมอ และมีพื้นผิวเรียบโดยไม่พบขอบเกรนเกิดขึ้น อย่างไรก็ตามเมื่อเพิ่มอุณหภูมิเผาแคลไซน์เป็น 750°C และ 850°C เส้นใยแสดงโครงสร้างคล้ายสายสร้อยที่มีขอบเกรนและจัดเรียงตัวกันแบบเกรนต่อเกรน

นอกจากนี้ยังได้ทำการศึกษาผลของการรักษาทางเคมีที่มีต่อการเปลี่ยนแปลงเฟสของเส้นใยนาโนเลดเซอร์โคเนตด้วยวิธีโซลโวเทอร์มอลในสารละลายไดเมทิลฟอร์มาไมด์ โดยศึกษาผลของอุณหภูมิและเวลาในการทำปฏิกิริยา จากผลการทดสอบด้วยเทคนิคดีฟเฟอแรนเชียลสแกนนิ่งแคลลอริเมทรี สามารถยืนยันได้ว่าการรักษาทางเคมีด้วยไดเมทิลฟอร์มาไมด์ มีผลต่อการเปลี่ยนแปลงเฟสของเส้นใยนาโนเลดเซอร์โคเนต และพบว่าขนาดของเส้นใยและโครงสร้างทางจุลภาคมีการเปลี่ยนแปลงภายหลังการรักษาทางเคมีอีกด้วย

จากนั้นได้ทำการเตรียม 3-3 นาโนคอมโพสิตของเลดเซอร์โคเนตกับพอลิไวนิลิดีนไดฟลูออไรด์ โดยการเติมสารละลายพอลิไวนิลิดีนไดฟลูออไรด์ลงในแผ่นเส้นใยนาโนเลดเซอร์โคเนตและให้ความร้อนที่อุณหภูมิ 80°C โดยพบว่าค่าคงที่ไดอิเล็กทริกของนาโนคอมโพสิตเลดเซอร์โคเนตกับพอลิไวนิลิดีนไดฟลูออไรด์ค่อนข้างเสถียรและมีค่าอยู่ในช่วง 18 ถึง 21 ในช่วงความถี่ที่วัดจาก 100 เฮิร์ตซ์ ถึง 2 เมกะเฮิร์ตซ์ ซึ่งมีค่าสูงกว่าค่าคงที่ไดอิเล็กทริกของพอลิไวนิลิดีนไดฟลูออไรด์ นอกจากนี้พบว่านาโนคอมโพสิตที่ได้มีค่าการสูญเสียไดอิเล็กทริกต่ำกว่า 0.09 ที่ความถี่ต่ำ

อีกทั้งงานวิจัยนี้ยังได้ทำการศึกษาการเตรียมนาโนคอมโพสิตที่ประกอบด้วยสามเฟสของเลดเซอร์โคเนตกับพอลิไวนิลิดีนไดฟลูออไรด์และท่อนาโนคาร์บอนด้วยเทคนิคการหล่อด้วยสารละลาย โดยพบว่าค่าคงที่ไดอิเล็กทริกของนาโนคอมโพสิตของเลดเซอร์โคเนตกับพอลิไวนิลิดีนไดฟลูออไรด์และท่อนาโนคาร์บอนอยู่ในช่วง 18 ถึง 61 ในช่วงความถี่ที่วัดจาก 100 เฮิร์ตซ์ ถึง 2 เมกะเฮิร์ตซ์ ซึ่งมีค่าสูงกว่าค่าคงที่ไดอิเล็กทริกของนาโนคอมโพสิตของเลดเซอร์โคเนตกับพอลิไวนิลิดีนไดฟลูออไรด์ จากสมบัติไดอิเล็กทริกที่ได้แสดงให้เห็นว่าการเติมท่อนาโนคาร์บอนสามารถปรับปรุงสมบัติไดอิเล็กทริกของคอมโพสิตได้

คำสำคัญ: เพียโซอิเล็กทริก, นาโนคอมโพสิต, อิเล็กโตรสปินนิง, โซลเจล

Thesis Title	Preparation and Dielectric Properties of Piezoelectric/Polymer Nanocomposite Materials
Student	Chanisa Nawaniil
Student ID	53670201
Degree	Doctor of Philosophy
Program	Nanoscience and Nanotechnology
Year	2015
Thesis Advisor	Assoc.Prof.Dr.Naratip Vittayakorn
Thesis Coadvisor	Assoc.Prof.Dr.Jutarat Prachayawarakorn

ABSTRACT

The aim of this study is to investigate the preparation and dielectric properties of piezoelectric/polymer nanocomposite materials by using lead zirconate (PZ) nanofiber as disperse phase and polyvinylidenedifluoride (PVDF) as matrix phase. A systematic investigation was conducted of piezoceramic nanofiber using two synthesis routes, namely the sol-gel and electrospinning process by varying the concentration, volume ratio of precursor solution to polymer, feeding rate, calcination temperature and polymer type. Moreover, the effect of solvothermal treatment on phase transformation in PZ nanofibers was studied. In addition, this research reports the preparation and dielectric properties of piezoelectric/polymer nanocomposite, with modification of the carbon nanotube (CNT).

Lead zirconate fibers were synthesized by the electrospinning method using a solution that contained 5 wt% poly(ethylene oxide) (PEO) in ethanol and a sol-gel solution of PZ. Some parameters varied, for example, the ratio between PZ and PEO, concentrations of the precursor solution, feeding rate, and calcination temperature. PZ fibers were obtained successfully with a well developed perovskite structure after as-spun PZ/PEO composite fibers were calcined using the PZ/PEO volume ratio of 10:3 at a PZ concentration of 1.0 M at 650°C for 4 h. Stable nanofibers were produced with an average diameter of 300±64 nm. Additionally, the PZ fibers showed a Curie temperature that rose by nearly 13°C, when comparing with a normal PZ particle.

Moreover, this study synthesized blended lead zirconate/poly(ethylene oxide)/Glutinous rice starch (GRS) nanofibers by the electrospinning method. A

number of parameters such as the ratio between PEO and GRS and calcination temperature have been studied. SEM results showed that smooth and continuous fibers were obtained at the volume ratio of 10:2:1, PZ/PEO/GRS. After calcination of the as-spun PZ/PEO/GRS composite nanofibers at 650°C for 4 h, PZ nanofibers with perovskite structure were obtained successfully. The fibers had a uniform and smooth surface without grain boundaries. However, when the calcinations temperature increased to 750°C and 850°C, the fiber represented a necklace-like structure with grain boundaries arranged by grain to grain unit cell clusters.

Additionally, PZ nanofibers were treated by the solvothermal method in the presence of dimethyl formamide (DMF) solution in order to investigate the effect of chemical treatment on phase transition of PZ nanofibers. The influences of temperature and reaction time are described. The results of DSC confirmed that chemical treatment with DMF could effect the AFE-PE phase transition of PZ nanofibers efficiently. Significant changes of fiber size and morphology after chemical treatment are shown by SEM images.

Then, 3-3 lead zirconate/polyvinylidenedifluoride (PVDF) nanocomposites was prepared by infusion of PVDF solution into the PZ nanofiber mat followed by heating of the composite at 80°C. The dielectric constant of the PZ/PVDF nanocomposite are relatively stable in the range of 18–21 within the measurement frequencies from 100 Hz to 2 MHz. This value is higher than the dielectric constant of the PVDF. Moreover, the dielectric loss of the composite is below 0.09 at low frequencies.

Furthermore, a three-phase PZ/CNT/PVDF nanocomposite comprising lead zirconate nanofibers, polyvinylidene fluoride and a small volume fraction of carbon nanotubes was prepared by the solvent casting technique. The dielectric constant of the PZ/CNT/PVDF nanocomposite was found to be in the range of 18–61 within the measurement frequencies from 100 Hz to 2MHz. This value is higher than the dielectric constant of the PZ/PVDF nanocomposite. The measured dielectric properties demonstrate that the addition of CNT can improve the dielectric property appearance of the composite.

Keywords: Piezoelectric, Nanocomposite, Electrospinning, Sol-gel

ACKNOWLEDGEMENT

This work was supported by the Royal Golden Jubilee Ph.D. Program (RGJ) under The Thailand Research Fund (TRF).

I would like to express my sincere thanks to my thesis advisor, Assoc.Prof.Dr.Naratip Vittayakorn, for his teaching, advice, and invaluable help throughout the course of this research. He is expertise, understanding, and generous guidance. It was a pleasure working with him.

I am grateful to my co-advisor, Assoc.Prof.Dr.Jutarat Prachayawarakorn, for giving kind advice regarding the topic of my research and for finding time for me in her busy schedule.

I would also like to thank Dr.Andrey Berenov for his teaching and advice throughout the period of my research at Imperial College London, UK.

I would like to express my gratitude to all my teachers for giving me the knowledge and being a source of motivation.

I am grateful to my family and my friends for all their support. They always pick me up when I fall and surround me with a circle of love.

I am thankful to Mr.Parinya Panprom for his love and encouragement, and for being beside me.

Finally, I most gratefully acknowledgement to my father and my mother, Mr.Amnat Nawani and Mrs.Chalapinya Nawani, respectively, who put their faith in me and urged me to do better. I am most grateful for their teaching and advice for the methodologies in life. I would not have achieved this far and this thesis would have not been completed without all the support that I have always received from them.

Chanisa Nawani

TABLE OF CONTENTS

	Page No.
THAI Abstract	i
ENGLISH Abstract	iii
Acknowledgement	v
Table of Contents	vi
List of Figures	x
CHAPTER 1 INTRODUCTION	1
1.1 Statement and Significance of Problems	1
1.2 Goal and Objective	2
1.3 Scope of the Study	3
1.4 Process of the Study	3
REFERENCE	5
CHAPTER 2 LITERATURE REVIEW	6
2.1 Basis for Ferroelectric	6
2.2 Perovskite Structure	7
2.3 Piezoelectric Materials	8
2.3.1 Piezoelectric Effect	9
2.4 Important Ferroelectric Materials	12
2.4.1 Barium Titanate	12
2.4.2 Lead Zirconate	15
2.4.3 Lead Zirconate-Lead Titanate	17
2.5 Powder Preparation	19
2.5.1 Mixed-Oxide Method	19
2.5.1.1 Mixing and Milling	19
2.5.1.2 Solid State Reaction	20
2.5.2 Hydrothermal and Solvothermal Processes	22
2.5.3 Sol-Gel Processing	24
2.6 Nanofiber Preparation	26
2.6.1 Electrospinning Technique	27

TABLE OF CONTENTS

	Page No.
2.6.2 Experimental Setup for E-Spinning	30
2.6.3 Characteristics of Electrospun Fibers	32
2.7 Polymer-Ceramic Composite Materials	32
2.7.1 Design of Composites-Connectivity Models	33
2.7.2 Fabrication of Polymer-Ceramic Composites	34
2.7.3 Properties of Piezoelectric-Polymer Composites	35
2.7.4 Dielectric Properties of Polymer-Ceramic Composites	37
2.8 Polymer Matrix	38
2.8.1 Poly(vinylidenedifluoride) (PVDF)	39
2.9 Carbon Nanotubes based Composites	40
2.9.1 Carbon Nanotubes	40
2.9.2 Dispersion of Carbon Nanotubes	41
2.9.3 Properties, Manufacturing, and Application	43
2.10 Literature Review	44
REFERENCE	65
CHAPTER 3 RESEARCH METHODOLOGY	69
3.1 Sample Preparation	69
3.1.1 Preparation of Nanofibers	69
3.1.2 Fabrication of Nanocomposite Materials	70
3.2 Characterization Techniques	70
3.2.1 Structural Characterization	70
3.2.1.1 X-Ray Diffraction (XRD)	70
3.2.1.2 Fourier Transform Infrared Spectroscopy (FT-IR)	72
3.2.1.3 Raman Spectroscopy	73
3.2.2 Morphology	74
3.2.2.1 Scanning Electron Microscopy (SEM)	74
3.2.2.2 Transmission Electron Microscopy (TEM)	75

TABLE OF CONTENTS

	Page No.
3.3 Thermal Analysis	76
3.3.1 Differential Thermal Analysis (DTA)	76
3.3.2 Thermogravimetry (TG)	78
3.3.3 Differential Scanning Calorimetry (DSC)	80
3.4 Dielectric Measurement	81
3.4.1 Dielectric Constant	81
3.4.2 Dielectric Loss	82
REFERENCE	84
CHAPTER 4 SYNTHESIS AND PHASE EVOLUTION OF ELECTROSPUN ANTIFERROELECTRIC LEAD ZIRCONATE (PbZrO₃) NANOFIBERS	86
4.1 Introduction	86
4.2 Experimental Procedure	88
4.3 Results and Discussion	91
4.3.1 Effect of PZ/PEO Volume Ratios	91
4.3.2 Effect of PZ concentrations	93
4.3.3 Effect of calcination temperature	99
4.3.4 Thermal properties	102
4.4 Summary	103
REFERENCE	104
CHAPTER 5 THE EFFECT OF THAI GLUTINOUS RICE STARCH ON THE SYNTHESIS OF LEAD ZIRCONATE (PbZrO₃) NANOFIBERS VIA THE ELECTROSPINNING METHOD	107
5.1 Introduction	107
5.2 Experimental Procedure	109
5.3 Results and Discussion	110
5.4 Summary	118
REFERENCE	119

TABLE OF CONTENTS

	Page No.
CHAPTER 6 EFFECT OF CHEMICAL TREATMENT ON PHASE TRANSITION OF LEAD ZIRCONATE NANOFIBERS	121
6.1 Introduction	121
6.2 Experimental Procedure	123
6.3 Results and Discussion	123
6.4 Summary	130
REFERENCE	131
CHAPTER 7 PREPARATION AND DIELECTRIC PROPERTIES OF 3-3 LEAD ZIRCONATE/ POLYVINYLIDENE FLUORIDE NANOCOMPOSITE	133
7.1 Introduction	133
7.2 Experimental Procedure	135
7.3 Results and Discussion	135
7.4 Summary	140
REFERENCE	141
CHAPTER 8 CHARACTERIZATION AND DIELECTRIC PROPERTIES OF NANOCOMPOSITE MADE OF LEAD ZIRCONATE NANOFIBERS AND POLYVINYLIDENE FLUORIDE IMPROVED WITH CARBON NANOTUBES	143
8.1 Introduction	143
8.2 Experimental Procedure	145
8.3 Results and Discussion	145
8.5 Summary	151
REFERENCE	152
CHAPTER 9 CONCLUSIONS AND SUGGESTIONS	154
APPENDIX	
CURRICULUM VITAE	

LIST OF FIGURES

Figure No.	Page No.
2.1 The crystallographic classification of the point groups	7
2.2 Cubic perovskite-type structure	8
2.3 Piezoelectric effects on ferroelectric ceramics	9
2.4 The temperature dependence of the relative permittivity of BaTiO ₃	13
2.5 The hysteresis loop of BaTiO ₃ samples at room temperature	14
2.6 The change in shape of the barium titanate ferroelectric hysteresis loop by temperature	14
2.7 Perovskite structure of lead zirconate	16
2.8 Typical AFE hysteresis loop	16
2.9 The phase diagram of the PZT system	18
2.10 Dependence of several <i>d</i> constants on the composition near the morphotropic phase boundary	18
2.11 Low energy mechanical milling variable that controls particle grinding and efficiency	20
2.12 Various types of high energy ball mills	20
2.13 Schematic of the solid-state reaction in single crystals	21
2.14 Schematic of the solid-state reaction in mixed powders	22
2.15 Experimental scheme for hydrothermal and solvothermal processes and their possible products	23
2.16 Schematic diagram of the structure of a particulate gel formed from a suspension of fine particles and a polymeric gel from a solution	25
2.17 Basic flow charts for sol-gel	25
2.18 Various electrospun architecture	29
2.19 A schematic diagram of the experimental setup and picture of a typical laboratory setup	31
2.20 Connectivity Models	34
2.21 Schematic diagram of different piezoelectric ceramic/polymer composites	36
2.22 The d_{33} figures of merit of these composites	37
2.23 Structure of polyvinylidenedifluoride (PVDF)	40

LIST OF FIGURES

Figure No.	Page No.
2.24 A photograph of the piezoelectric fiber composite	45
2.25 Displacement behavior of the 1–3 composite with polymer and PZT fibers	45
2.26 The dependence of nanofiber diameter on various processing parameters	46
2.27 Plots demonstrating the ability to control the diameter of electrospun nanofibers by simply adjusting the composition of spinning solutions	47
2.28 Local piezoelectric response as a function of the electric field applied for a single BNT nanofiber	48
2.29 The frequency-dependent dielectric constant and dissipation factor of a PbZrO_3 film	49
2.30 X-ray diffraction pattern of PZ gel powder	49
2.31 Scanning electron microscope images of PZT nanofibres	50
2.32 Magnetic hysteresis loops for the CFO-PZT composite nanofibers	51
2.33 SEM images of composite CFO-PZT nanofibers	52
2.34 Magnetic hysteresis loops for NiFe_2O_4 nanoparticles and nanofibers	52
2.35 (a) SEM image of as-synthesized barium titanium and PVP composite nanofibers (b) SEM image of BaTiO_3 nanofibers annealed at 750°C	53
2.36 SEM images of BaTiO_3 nanofibers under different conditions	54
2.37 Response and recovery properties	55
2.38 Long-term stable property	55
2.39 Mechanical properties of (a) dynamic Young's modulus versus weight percentage of the TiO_2 nanofillers	56
2.40 Schematic view of the PZT NAFC/AE sensor	57
2.41 Output signal from the sensor cell of acoustic surface energy	58
2.42 Hysteresis loop of PZT NFACs	58
2.43 Schematic view of the PZT nanofiber generator	59
2.44 Power delivered to the load resistors versus load resistance	59
2.45 Measurements of voltage output from a PZT nanofiber generator	60
2.46 Piezoelectric PVDF nanogenerator	61

LIST OF FIGURES

Figure No.	Page No.
2.47 Energy conversion efficiency of a piezoelectric PVDF nanogenerator	62
2.48 Transmission electron microscope images of the freeze-fractured (NBT-MWNT)/PVDF composites and schematic illustration of the microstructure of (NBT-MWNT)/PVDF composites	63
2.49 The measured voltage output and current signals of the NCG device	64
2.50 A captured photograph showing an LED lit by electric energy generated from a NCG device	64
3.1 Electrospinning setup	69
3.2 Scatter and diffraction from an ordered arrangement of atoms	71
3.3 Basic components of an FTIR spectrometer	72
3.4 Schematic diagram of Raman spectrometer	73
3.5 Schematic diagram of SEM	74
3.6 Transmission electron microscope with all of its components	76
3.7 Block diagram of DTA	77
3.8 Measurement principles of DTA	78
3.9 Schematic single-stage TG curve	79
3.10 The structure of TG instrument	79
3.11 Block diagram of Heat Flux DSC	80
3.12 An idealized DSC curve showing the shapes associated with particular phase transitions	81
3.13 Phase diagram of current and voltage in a capacitor energized by an alternating voltage	83
4.1 Process for the preparation of PZ fibers	90
4.2 SEM micrographs of the as-spun PZ/PEO nanofibers with a PZ concentration of 0.7 M at the PZ/PEO volume ratio of (a) 10:1, (b) 10:2 and (c) 10:3	92
4.3 SEM micrograph of the as-spun PZ/PEO volume ratio of 10:3 at PZ concentrations of (a) 0.3, (b) 0.5, (c) 0.7 (d) 0.9 and (e) 1.0 M	93

LIST OF FIGURES

Figure No.	Page No.
4.4 TG-DTA curves of thermal decomposition of the as-spun PZ/PEO composite nanofiber	95
4.5 XRD patterns of electrospun PZ/PEO composite nanofibers calcined in air for 4 h at different temperatures	96
4.6 FT-IR spectra of electrospun PZ/PEO composite nanofibers calcined in air for 4h	97
4.7 (a)–(c) SEM micrographs and (d)–(f) TEM micrographs of the PZ fibers calcined at 650°C with the PZ/PEO volume ratio of 10:3 at PZ concentrations of 0.7, 0.9 and 1.0 M	99
4.8 SEM micrograph of the fibers using: (a)–(d) feeding rate of 2 ml/h and (e)–(h) feeding rate of 0.5 ml/h of the as-spun fibers with the volume ratio of 10:3 at PZ concentrations of 1.0 M, and PZ fibers calcined in air for 4 h at 650°C, 750°C and 850°C	101
4.9 Typical DSC curves for PZ fibers and PZ particles	102
5.1 SEM photographs of the as-spun PZ/PEO/GRS volume ratios of 10:2:1 (a) compared with the as-spun PZ/PEO volume ratios of 10:2 (b), with a PZ concentration of 1.0 M	111
5.2 SEM micrographs of the as-spun PZ/PEO/GRS nanofibers with a PZ concentration of 1.0 M at the PZ/PEO/GRS volume ratios of (a) 10:2:1, (b) 10:1.5:1.5, (c) 10:1:2 and (d) 10:0:3	111
5.3 TG-DTA curves of thermal decomposition of the as-spun PZ/PEO/GRS composite nanofiber	112
5.4 XRD patterns of electrospun PZ/PEO/GRS composite nanofibers, with a PZ concentration of 1.0 M at the PZ/PEO volume ratio of 10:2:1, calcined in air for 4 h at different temperatures	114
5.5 FTIR spectra of electrospun PZ/PEO/GRS composite nanofiber, with a PZ concentration of 1.0 M at the PZ/PEO volume ratio of 10:2:1, calcined in air for 4 h at different temperatures	115

LIST OF FIGURES

Figure No.	Page No.
5.6 SEM micrograph of (a) the as-spun and PZ fibers calcined in air for 4 h at (b) 650°C, (c) 750°C and (d) 850°C	117
5.7 Schematic diagram of (a) PZ fibers calcined at 650°C and (b) PZ fibers calcined at 750°C	117
6.1 SEM micrographs of the PZ fibers (a) before and after chemical treatment for (b) 6 h at 170°C (c) 24 h at 170°C (d) 6 h at 200°C and (e) 24 h at 200°C	125
6.2 XRD patterns of the PZ particles compared with those of the PZ nanofibers before and after chemical treatment	126
6.3 FT-IR spectra of the PZ particles compared with those of the PZ nanofibers before and after chemical treatment	127
6.4 DSC results for the PZ particles compared with those for PZ nanofibers before and after chemical treatment	128
7.1 SEM micrograph of the composite structure of 3-3 PZ/PVDF nanocomposite	136
7.2 XRD patterns of 3-3 PZ/PVDF nanocomposite compared with PZ fibers and PVDF powder	137
7.3 FT-IR spectra of 3-3 PZ/PVDF nanocomposite	138
7.4 Dielectric properties of 3-3 PZ/PVDF nanocomposite within the measurement frequencies from 100 Hz to 2 MHz	139
8.1 SEM micrograph of the PZ fibers	146
8.2 SEM micrographs of the (a) secondary electron and (b) backscattering electrons images of the PZ/CNT/PVDF nanocomposite	146
8.3 XRD patterns of PZ/CNT/PVDF nanocomposite compared with those of PZ Fibers	147
8.4 FT-IR spectra of PZ/CNT/PVDF nanocomposite compared with those of PZ Fibers	148
8.5 Dielectric constant and dielectric loss of PZ/CNT/PVDF nanocomposite compared with that of PZ/PVDF nanocomposite as a function of log frequencies	149
8.6 Schematics of the cross-sectional structure of PZ/PVDF nanocomposite (a) without CNT and (b) with CNT	151

CHAPTER 1

INTRODUCTION

1.1 Statement and Significance of Problems

Ferroelectric materials have become an interesting recently in the physics research of condensed matter, due to their very high dielectric constant and piezoelectric coefficient, which are useful for high dielectric ceramic capacitors and electromechanical transducers. Piezoelectric effect is one of the most important factors in the behaviors of ferroelectric materials. It has the ability to transform electrical energy into mechanical strain energy, and vice versa [1]. In recent years, fine scale piezoelectric fibers have received extensive attention, due to their potential as applications for building blocks in various nanotechnologies, which include mechanics, photonics, electronics, and sensing [2]. The high surface to volume ratio is an attractive characteristic that can be achieved from nanofibers, and more attention has been paid to this area. With the miniaturization of electronic devices, nanofibers of piezoelectric material are currently attracting a great deal of interest in the design of smart materials, due to their novel properties that are significantly different from their bulk, such as physical and chemical properties [3]. The electrospinning process has created more interest in recent times, as it involves the direct process of crystallite nanofibers by using electrostatic force.

Lead zirconate (PbZrO_3 ; PZ) is a well known antiferroelectric (AFE) material that can be processed into various forms such as bulk ceramics, thin films, and fibers. The hysteresis characteristics of AFE PbZrO_3 regions are well suited for either power-storage or actuator applications [4]. Furthermore, the extremely large charge released from the ferroelectric (FE) to AFE state may be useful as alternate capacitor materials in DRAMs [5].

It is known that piezoelectric ceramics have high piezoelectric strain and a high electromechanical coupling coefficient [6], but their relatively high density, high acoustic impedance and mechanical stiffness limit their applications [7]. On the other hand, piezoelectric polymers have acoustic impedance that is well matched to water and biological issues, but their piezoelectric strain coefficient and electromechanical

coupling coefficient, are lower than those of piezoelectric ceramics [8]. Thus, one might optimize conflicting requirements in many applications by combining the most useful properties of two or more phases that do not ordinarily appear together in nature. Therefore, different kinds of composites such as porous ceramics and ceramic-polymer composites are developed typically. Piezoelectric ceramic-polymer composites have been studied intensively within the last few decades because of their considerable potential for applications such as pyroelectric sensors, ultrasonic transducers, and hydrophones [9]. In addition, they are exceptionally sensitive; for example, sensors based on polyvinylidene difluoride (PVDF) film have been applied even in erosive media to detect pressure; in biological environments to aid minimally invasive surgery; in testing and characterizing fabrics; and in monitoring human health [10].

1.2 Goal and Objective

1.2.1 To study the preparation of piezoceramic nanofibers of lead zirconate using the electrospinning method via the sol-gel process.

1.2.2 To study the optimization of the electrospinning process during synthesis by varying the reaction parameters such as concentration, volume ratio of precursor to polymer solution and feeding rate.

1.2.3 To study and evaluate the calcination parameters during the optimization process.

1.2.4 To study characterization of the materials synthesized using different techniques. Particle size and morphological studies were carried out using scanning electron microscope (SEM), and crystallite size and crystal structures were determined using X-ray diffraction (XRD). The functional groups were confirmed using Fourier transform-infrared spectroscopy (FT-IR) and Raman.

1.2.5 To reduce the cost in preparing ceramic nanofiber by using Glutinous rice starch as the polymer electrolyte.

1.2.6 To study the effect of solvothermal treatment on lead zirconate nanofiber.

1.2.7 To study characterization and dielectric properties of the piezoelectric/polymer nanocomposites of lead zirconate and polyvinylidenedifluoride.

1.2.8 To study the preparation and dielectric properties of piezoelectric/polymer nanocomposite, with modification of the carbon nanotube (CNT).

1.3 Scope of the Study

1.3.1 Study the preparation of piezoceramic nanofibers of lead using the electrospinning method.

1.3.2 Study the synthesis parameters; concentration, volume ratio of precursor to polymer solution and feeding rate to obtain the optimized condition of the electrospinning process.

1.3.3 Study and evaluate the calcination parameters during the optimization process.

1.3.4 Study characterization of the materials synthesized using different techniques. The particle size and morphological studies were carried out using SEM, and crystallite size and crystal structures determined by XRD. The functional groups were confirmed using FT-IR and Raman.

1.3.5 Reduce the cost in preparing ceramic nanofiber by using Glutinous rice starch as the polymer electrolyte.

1.3.6 Study the effect of solvothermal treatment on lead zirconate nanofiber.

1.3.7 Study the characterization and dielectric properties of piezoelectric/polymer nanocomposite of lead zirconate and polyvinylidenedifluoride.

1.3.8 Study the preparation and dielectric properties of piezoelectric/polymer nanocomposite, with modification of CNT.

1.4 Process of the Study

This study, conducted a systematic investigation of piezoceramic nanofiber using two synthesis routes, namely the sol-gel and electrospinning process by varying the concentration, volume ratio of precursor solution to polymer, feeding rate and calcination temperature. Synthesis of the nanofiber antiferroelectric PZ system by

electrospinning, followed by calcinations at high temperature, was focused on to improve the desired properties. The ceramic nanofibers and conventional sol-gel precursors from the electrospinning method were mixed with various kinds of polymers in order to increase viscosity. However, most polymers are fairly expensive, whereas, glutinous rice starch (GRS) is of a kind commonly cultivated in Thailand, and has low cost, and high viscosity. Thus, this study also synthesized lead zirconate fibers by the electrospinning method using solution that contained commercial polymer combined with Thai GRS in order to increase viscosity and reduce cost of the precursor solution. Furthermore, this research also examined the effect of solvothermal treatment on phase transformation in lead zirconate nanofibers. The optimum condition of chemical treatment for the phase transition in lead zirconate fibers was determined at different temperatures and times using dimethyl formamide as an effective solvent. In addition, the characterization and dielectric properties of the piezoelectric/polymer nanocomposites of lead zirconate and polyvinylidenedifluoride were studied. Furthermore, the preparation and dielectric properties of piezoelectric/polymer nanocomposite were examined, with modification of the CNT.

REFERENCE

- [1] Haertling, G. H. 1999. "Ferroelectric Ceramics: History and Technology." **J. Am. Ceram. Soc.** 82[4] : 797-818.
- [2] Li, D., and Xia, Y. 2003. "Fabrication of Titania Nanofibers by Electrospinning." **Nano Lett.** 3[4] : 555-560.
- [3] Cai, Z., Li, J., Wang, Y. 2010. "Fabrication of Zinc Titanate Nanofibers by Electrospinning Technique." **J. Alloys Compd.** 489 : 167-169.
- [4] Tang, X.G., Ding, A.L., and Luo, W.G. 2001. "Surface Morphology and Chemical States of Highly Oriented PbZrO₃ Thin Films Prepared by a Sol-Gel Process." **Appl. Surf. Sci.** 174 : 148-154.
- [5] Kim, I., Bae, S., Kim, K., Kim, H., Lee, J. S., Jeong, J., and Yamakawa, K. 1998. "Characteristics of Antiferroelectric PbZrO₃ Thin Films." **J. Korean Phys. Soc.** 33[2] : 180-183.
- [6] Wu, M., Huang, H., and Chu, W., et al. 2010. "Tuning the Ferroelectric and Piezoelectric Properties of 0.91Pb(Zn_{1/3}Nb_{2/3})O₃-0.09PbTiO₃ Single Crystals and Lead Zirconate Titanate Ceramics by Doping Hydrogen." **J. Phys. Chem. C.** 114 : 9955-9960.
- [7] Joshi, N. J. 2012. "Studies of Nano-Sized High Dielectric Constant Materials." The Maharaja Sayajirao University of Baroda Vadodara, Gujarat India.
- [8] Xiaofang, L., Chuanxi, X., Huajun, S., Lijie, D., Rui, L., and Yang, L. 2005. "Characterization of PZT/PVC Composites Added with Carbon Black." **J. Wuhan University of Technology-Mater. Sci. Ed.** 20[4] : 60.
- [9] Petchsuk, A., Supmak, W., and Thanaboonsombut, A. 2009. "A Series of 0-3 Composites of Lead Zirconate Titanate and Ferroelectric Nylon77: Preparation and Electrical Properties." **J. Appl. Polym. Sci.** 114 : 1048.
- [10] Wang, Y.R., Zheng, J.M., Ren, G.Y., Zhang, P.H., and Xu, C. 2011. "A Flexible Piezoelectric Force Sensor Based on PVDF Fabrics." **Smart Mater. Struct.** 20 : 045009.

CHAPTER 2

LITERATURE REVIEW

2.1 Basis for Ferroelectric [1, 3]

All crystals can be classified into 32 point groups according to their crystallographic symmetry. These point groups are divided into two classes. One has a center of symmetry and the other does not. There are 21 noncentrosymmetric point groups, of which crystals belonging to 20 of them exhibit piezoelectricity. Although cubic class 432 lacks a center of symmetry, it does not permit piezoelectricity. Of the 20 noncentrosymmetric point groups, 10 polar crystal classes contain a unique axis, along which an electric dipole moment is oriented in the unstrained condition. The pyroelectric effect appears in any material that possesses a polar symmetry axis. The material in this category develops an electric charge on the surface owing to the change in dipole moment as temperature changes. Pyroelectric crystals of which spontaneous polarization is re orientable by applying an electric field of sufficient magnitude (not exceeding the breakdown limit of the crystal) are called ferroelectrics. In classifying a ferroelectric (FE), the two conditions necessary in a material are (1) existence of spontaneous polarization and (2) demonstrated reorienting of the polarization. Four types of ferroelectric ceramics also are given in Figure 2.1 as subcategories of the general group of ferroelectric materials, with typical examples representing the type based on its unitcell structure: (1) the tungsten-bronze group, (2) oxygen octahedral group, (3) pyrochlore group, and (4) bismuth layer-structure group. Of these, the second group (ABO_3 perovskite type) is by far the most important category, economically. The families of listed compositions: $BaTiO_3$, PZT, PLZT, PT, PMN, and $(Na,K)NbO_3$ represent the bulk of current ferroelectric ceramics manufactured worldwide.

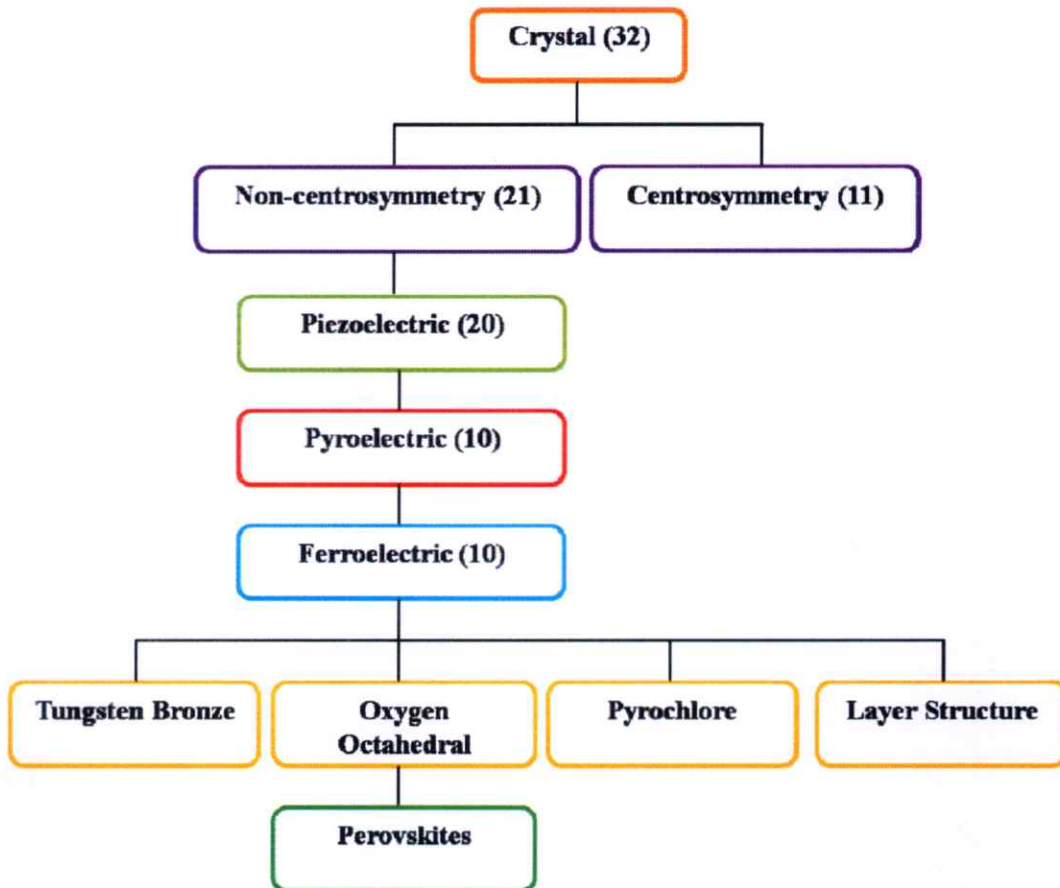


Figure 2.1 The crystallographic classification [adapted from Ref 3].

2.2 Perovskite Structure [2]

Many oxides with the ABO_3 chemical formula have adopted the perovskite structure and barium titanate is a member of this perovskite family. This structure takes its name from the mineral perovskite, $CaTiO_3$. The general crystal structure is a primitive cube, with the A-larger cation on the corners of the cube, the B-smaller cation in the middle, and the anion, commonly oxygen, located centrally on the six cube faces, where A is a monovalent, divalent or trivalent metal and B a pentavalent, tetravalent or trivalent element. Geometrical ion packing in the lattice is a very important factor in determining the type of structure. The perovskite structure can be considered not only as a three-dimensional framework of BO_6 octahedra (Figure 2.2a), but also a cubic close packed arrangement of A and O ions, with the B ions filling the interstitial positions (Figure 2.2b). The unit cell of the cubic perovskite type lattice is shown in Figure 2.2. The coordination number of cation A and B was

found to be 12 and 6, respectively. The perovskite family includes not only compounds with an ideal cubic perovskite lattice, but also all compounds with structures that derived from an ideal one by way of small lattice distortions or omission of some atoms. For example a large number of double fluorides, such as KMgF_3 , KZnF_3 and others, also belong to the perovskite family.

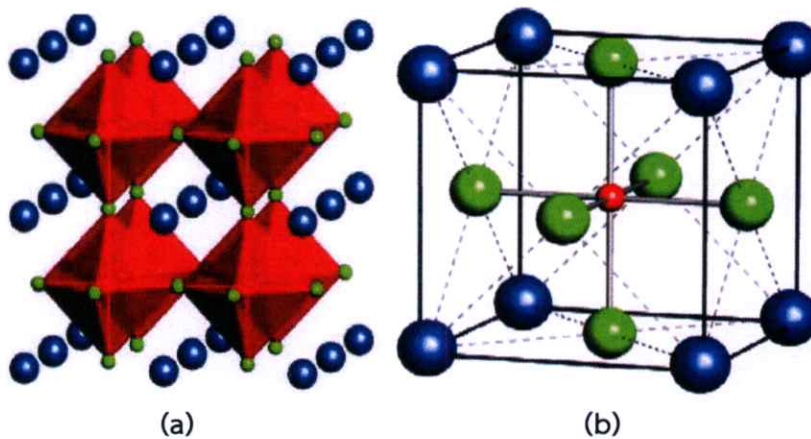


Figure 2.2 Cubic perovskite-type structure. [2]

2.3 Piezoelectric Materials [1, 3]

Piezoelectricity is a property possessed by a select group of materials, and was discovered in 1880 by Jacques and Pierre Curie during their systematic study of the pressure effect on the generation of electrical charge by crystals, such as quartz, zincblende, and tourmaline. The name “piezo” derives from the Greek meaning of “to press;” hence, piezoelectricity is the generation of electricity as a result of mechanical pressure. Piezoelectric materials couple electrical and mechanical parameters. Single crystal quartz was the earliest material used for its piezoelectric properties. Ferroelectric polycrystalline ceramics, such as barium titanate and lead zirconate titanate (PZT), exhibit piezoelectricity when poled electrically. As these ceramics possess significant and stable piezoelectric effects, including high electromechanical coupling, they can produce large strains or forces and are hence used extensively as transducers. Piezoelectric polymers, notably polyvinylidene difluoride (PVDF) and its copolymers with trifluoroethylene and piezoelectric composites that combine a piezoelectric ceramic and passive polymer, have been

developed and offer high potential. Recently, thin films of piezoelectric materials have been researched, due to their potential use in microdevices (sensors and microelectromechanical systems [MEMS]). Piezoelectricity is being used extensively in fabricating various devices such as transducers, sensors, actuators, surface acoustic wave (SAW) devices, and frequency controls.

2.3.1 Piezoelectric Effect [3]

The poling process is the critical element in the ability to utilize the piezoelectric effect in a ferroelectric ceramic. Without poling, the ceramic is inactive, even though each individual crystallite is piezoelectric in itself. With poling, however, the ceramic becomes extremely useful, provided it is not heated above its Curie temperature (T_C), when it would lose its polarization and all orientation of the polarization produced by the poling process. Two effects are operative in piezoelectric crystals in general and ferroelectric ceramics in particular. The direct effect (designated as a generator) is identified with the phenomenon, whereby electrical charge (polarization) is generated from mechanical stress, whereas the converse effect (designated as a motor) is associated with the mechanical movement generated by applying an electrical field. Both of these effects are illustrated in Figure 2.3.

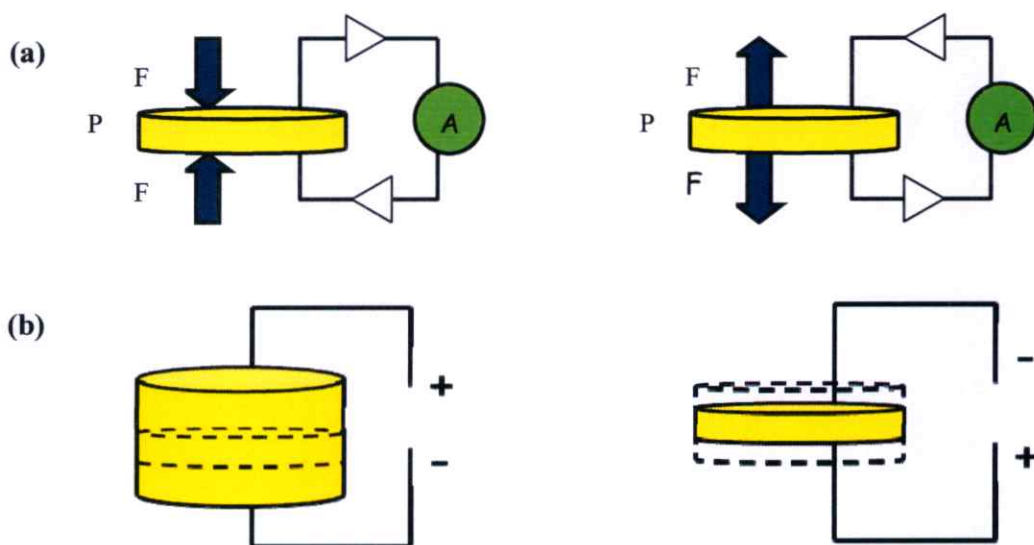


Figure 2.3 Piezoelectric effects on ferroelectric ceramics (a) direct effect (b) inverse effect [adapted from Ref 3].

The basic equations that describe these two effects regarding electric and elastic properties are:

$$D = dE + \varepsilon^T E \quad (\text{generator}) \quad (2.1)$$

$$S = s^E T + dE \quad (\text{motor}) \quad (2.2)$$

Where D is the dielectric displacement (considered as equal to polarization)

T is the stress

E is the electric field

S is the strain

d is a piezoelectric coefficient

s is the material compliance (inverse modulus of elasticity)

and ε is the dielectric constant (permittivity).

The superscripts indicate a quantity held constant: in the case of ε^T , the stress is held constant, which means that the piezoelectric element is unconstrained mechanically, and, in the case of s^E , the electric field is held constant, meaning the electrodes on the element are shorted together. Equations (2.1) and (2.2) actually describe in matrix form a set of equations that relate these properties along different orientations of the material. Due to the detailed nature of the many equations involved, the reader is referred to several sources on the subject. Suffice it to say that as this is a piezoelectric solid, equation (2.1) and (2.2) relate to given properties, such as electric displacement (polarization) and strain to both the mechanical and electrical states of the material. Furthermore, these properties are directional quantities, and hence, usually specified with subscripts to identify the conditions under which they are determined. For example, d_{31} indicates that this piezoelectric coefficient relates to the generation of polarization (direct effect) in the electrodes perpendicular to the 3 or vertical direction, and the stress applied mechanically in the 1 or lateral direction; and d_{33} indicates both the polarization generated and stress applied in the 3 direction. Typical relationships for this coefficient are:

$$D_3 = d_{33}T_3 \quad (\text{direct effect}) \quad (2.3)$$

$$S_3 = d_{33}E_3 \quad (\text{converse effect}) \quad (2.4)$$

where, the d coefficients are equal numerically in both equations. The d coefficients are expressed usually as $\times 10^{-12}$ C/N and $\times 10^{-12}$ m/V for the direct and converse

effect, respectively. High d coefficients are desirable for materials that are utilized in motional or vibrational devices, such as sonar and sounders. In addition to the d coefficients, open-circuit g coefficients also are used to evaluate piezoelectric ceramics for their ability to generate large amounts of voltage per unit of input stress. The g constant is related to the d constant via the relationship:

$$g = dK\epsilon_0 \quad (2.5)$$

where K is the relative dielectric constant and ϵ_0 the permittivity of free space (8.854×10^{-12} F/m). Thus, a high g constant is possible for a given d coefficient if the material has a low K . High g constant ceramics are usually ferroelectrically hard materials that do not switch their polarization readily, and possess lower K values. They are used in devices such as portable gas ignitors and patio lighters. The piezoelectric coupling factor (e.g., k_{33} , k_{31} , and k_p) is a convenient and direct measurement of the overall strength of the electromechanical effect, i.e., the ability of the ceramic transducer to convert one form of energy to another. It is defined as the square root of the ratio of energy output in electrical form to the total mechanical energy input (direct effect), or the square root of the ratio of the energy available in mechanical form to the total electrical energy input (converse effect). As the conversion of electrical to mechanical energy (or vice versa) is always incomplete, k is always less than unity. The higher k values commonly used as a figure-of-merit for piezoelectrics are most desirable and constantly sought after in new materials. For ceramics, k_p is a typical measurement used in comparing materials with values ranging from 0.35 for BaTiO_3 to as high as 0.72 for lead zirconate titanate (PZT). All of the properties mentioned here may be realized in a piezoelectric ceramic, which is, in reality, a poled ferroelectric ceramic material. During the process of poling, there is a small expansion of the material along the poling axis and a slight contraction in both directions perpendicular to it. The strength of the poling field, often in combination with elevated temperature, is an important factor in determining the extent of alignment and, hence, the resulting properties. Alignment is never complete; however, depending on the type of crystal structure involved, the thoroughness of poling can be quite high, ranging from 83% for the tetragonal phase to 86% for the rhombohedral phase, and 91% for the orthorhombic phase, when compared with single-domain, single-crystal values. As all ceramic bodies are

macroscopically isotropic in the “as-sintered” condition, and must be poled to render them useful as piezoelectric materials, they are all ferroelectric as well as piezoelectric.

2.4 Important Ferroelectric Materials

2.4.1 Barium Titanate [1, 4, 5]

Barium titanate was the first known ferroelectric ceramic and a good candidate for a variety of applications, due to its excellent dielectric, ferroelectric and piezoelectric properties. BaTiO_3 was the first material used for manufacturing dielectric ceramic capacitors, multilayer capacitors, etc. It was used for this application due to its high dielectric constant and low dielectric loss. The values of the dielectric constant depend on the synthesis route, which means purity, density, grain size, etc. The dielectric constant also is dependent on temperature, frequency and dopants. Figure 2.4 shows the temperature dependence of dielectric constants in BaTiO_3 that demonstrate the phase transitions in BaTiO_3 single crystals. Three anomalies can be observed. The discontinuity at the Curie point (130°C) is due to transition from a ferroelectric to paraelectric phase. The other two discontinuities are accompanied by transitions from one ferroelectric phase to another. The crystal structure is cubic above the Curie point and has no spontaneous dipole moments. The crystal becomes polar at the Curie point and the structure changes from a cubic to tetragonal phase. The dipole moment and spontaneous polarization are parallel to the tetragonal axis. At just below the Curie temperature, the cubic structure is distorted slightly to a ferroelectric tetragonal structure with a dipole moment in the direction of “c”. The vector of the spontaneous polarization points is in the [001] direction (tetragonal phase). When the temperature goes down to below 0°C , the tetragonal structure transforms into an orthorhombic ferroelectric phase, with the polar axis parallel to a diagonal face. It reorients in the [011] phase (orthorhombic phase). In addition, when the temperature is reduced further to -80°C , the tetragonal structure transforms into a rhombohedral structure, with the polar axis directed along a diagonal body. It reorients in the [111] phase (rhombohedral phase).

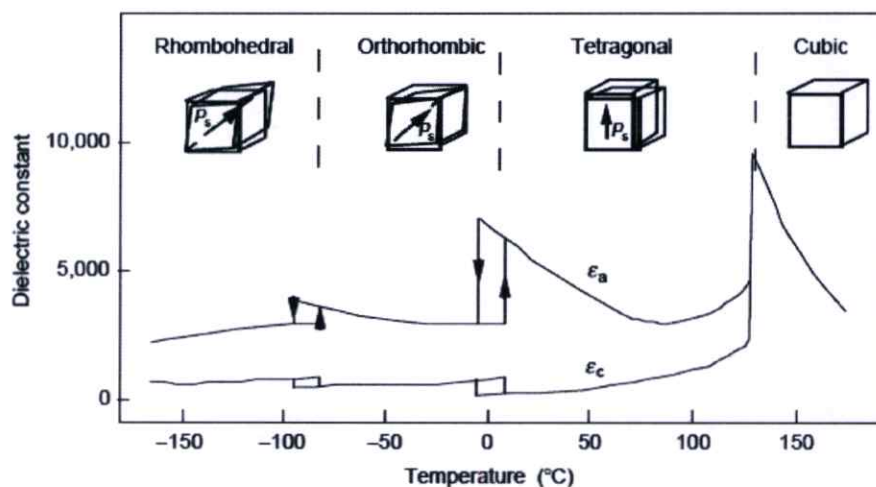


Figure 2.4 The temperature dependence of the relative permittivity of BaTiO₃. [5]

The temperature dependence of the dielectric constant and also other properties can be modified by forming a solid solution over a wide range of compositions. The perovskite structure has the capability of hosting ions of different sizes, so a large number of different dopants can be accommodated in the BaTiO₃ lattice. For many years, A- and B-site dopants have been used to modify the electrical properties of BaTiO₃. Acceptor dopants are usually monovalent, divalent and trivalent ions, which substitute Ba²⁺, and barium titanate becomes a p-type semiconductor, which substitutes Ti⁴⁺ ions with donor dopants, and trivalent, tetravalent and pentavalent ions, with the barium titanate becoming an n-type semiconductor. The addition of donor dopants at a relatively low concentration leads to room-temperature semiconducting ceramics, whereas higher dopant contents lead to insulating materials. For example, the substitution of Pb²⁺, Sr²⁺, Ca²⁺ and Cd²⁺ can be made for part of the Ba²⁺ ions, thus maintaining the ferroelectric characteristics. Similarly, the Ti⁴⁺ ion can be replaced partially with Sn⁴⁺, Hf⁴⁺, Zr⁴⁺, Ce⁴⁺ and Th⁴⁺.

Barium titanate is used most widely for its strong piezoelectric characteristics. Barium titanate prepolarized ceramics have the advantage of a high coupling coefficient while being mechanically and thermally stable. Some typical values of k_p , k_{33} , d_{33} , d_{31} and g_{33} for BaTiO₃ are 0.36, 0.5, 190, -78 and 11.4, respectively. Barium titanate can be manufactured in a variety of shapes and subsequently polarized in order to obtain optimum efficiency as piezoelectric

elements. Since the Curie temperature of barium titanate is relatively high, piezoelectric properties are maintained, and barium titanate can be used for these purposes at temperature as high as 70°C. Seveyrat et al. prepared BaTiO₃ by conventional solid state reaction and the oxalate co-precipitation route, and they measured electric field dependence of relative permittivity and piezoelectric coefficient d_{33} . They concluded that powder from a chemical process is made of finer grains, which leads to ceramics with very good properties. The piezoelectric d_{33} constant is more than 260 pC/N at around 25°C. This value is higher than those usually published for barium titanate ceramics: classically, values of room temperature ϵ_r (1kHz) and d_{33} are around 1,700 and 190 pC/N, respectively.

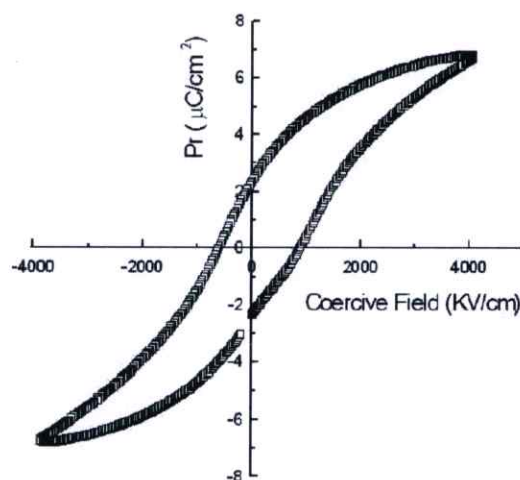


Figure 2.5 The hysteresis loop of BaTiO₃ samples at room temperature. [5]

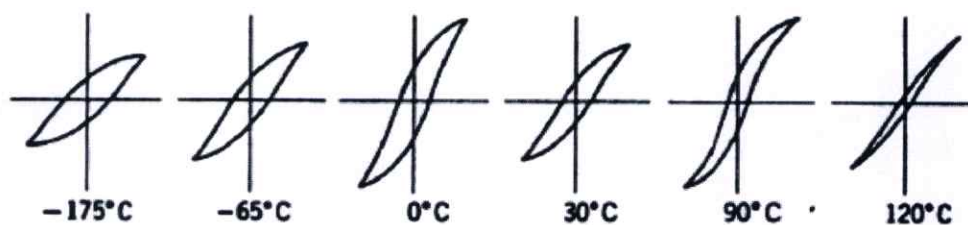


Figure 2.6 The change in shape of the barium titanate ferroelectric hysteresis loop by temperature. [5]

Stojanovic et al. obtained a very well formed loop, with a regular shape typical of ferroelectric materials. They prepared barium titanate by mechano-chemical synthesis. The remanent polarization and coercitive field was $2.0 \mu\text{C}/\text{cm}^2$ and $1,060 \text{ kV}/\text{cm}$, respectively. The hysteresis loop is presented in Figure 2.5.

The hysteresis loops become fatter at low temperature, while the coercitive field becomes greater, corresponding to the larger energy requirement for reorienting the domain walls; i.e., the domain configuration is frozen in. At higher temperatures, the coercive force decreases until no hysteresis remains at the Curie temperature, and there is only a single value for the dielectric constant. Hysteresis loops for barium titanate are illustrated in Figure 2.6.

The dielectric and piezoelectric properties of the ferroelectric ceramic, BaTiO_3 , can be affected by its own stoichiometry and microstructure, and by dopants entering the A- or B-site of solid solution. Modified BaTiO_3 ceramics that contain dopants such as Pb or Ca ions have been used as commercial piezoelectric materials.

2.4.2 Lead Zirconate (PbZrO_3) [3, 6]

Antiferroelectric (AFE) materials have ionic chains that are polarized spontaneously, with the adjacent chains of one kind of ions polarized in the opposite direction. Therefore, there is no net spontaneous polarization. Lead zirconate (PbZrO_3) was the first compound identified as an antiferroelectric. In its low-temperature phase ($T < T_C = 230^\circ\text{C}$), PbZrO_3 crystallizes in the orthorhombic structure, and its unit cell parameters are $a = 5.888 \text{ \AA}$, $b = 11.758 \text{ \AA}$, and $c = 8.222 \text{ \AA}$. The orthorhombic phase of PbZrO_3 is strongly antiferroelectric in the plane that is perpendicular to the c-axis.

Lead zirconate is a well known antiferroelectric material that can be processed into various forms such as bulk ceramics, thin films, and fibers. The hysteresis characteristics of antiferroelectric PbZrO_3 regions are well suited for either power-storage or actuator applications. Furthermore, the extremely large charge released from the FE to AFE state may be useful as alternate capacitor materials in DRAMs. Lead zirconate (PbZrO_3 or PZ) is an important precursor in preparing a number of technologically important solid solutions, particularly those of the $\text{PbZr}_{1-x}\text{Ti}_x\text{O}_3$ series. Recently, new studies revealed novel applications of lead

zirconate (PZ) as a phase-transformation-induced electromechanical actuator and pyroelectric sensor.

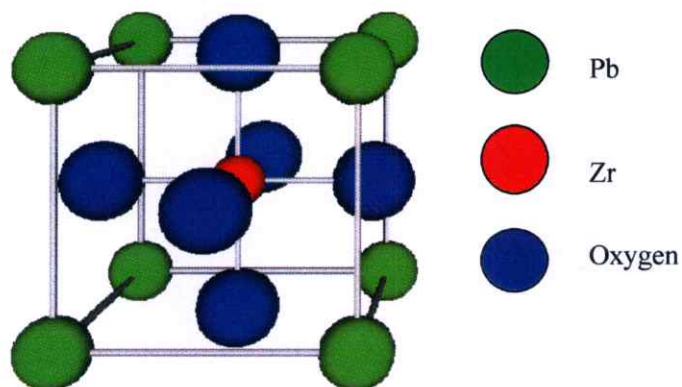


Figure 2.7 Perovskite structure of lead zirconate [adapted from Ref 3].

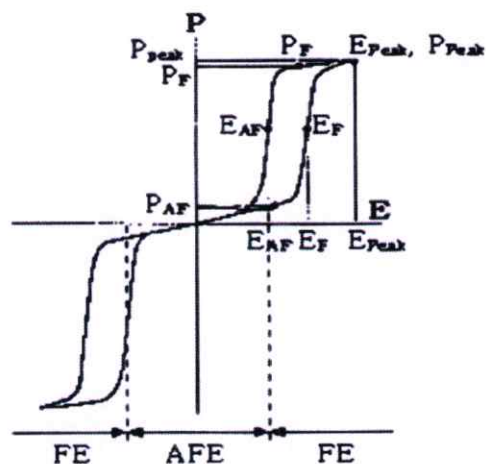


Figure 2.8 Typical AFE hysteresis loop. [6]

The double hysteresis loops that result from the field-forced AFE to FE phase transformation are useful for charge storage devices. A typical AFE hysteresis loop, which shows an induced or field-forced metastable ferroelectric, is present in electric fields higher than E_0 , and spontaneous polarization is zero for a zero electric field (Figure 2.8). The hysteresis regions are well suited for either power-storage or actuator applications. Conversely, the linear section of the polarization-electric field

curve (i.e., the low-field AFE region) can be used for capacitor applications. This has the advantage of bias-independent capacitance coupled with a reasonably good volumetric efficiency. In bulk ceramics, however, the AFE to FE transformation is difficult to observe at room temperature, as the electric field required to induce phase switching is often larger than the dielectric strength. Brodeur et al. observed multiple phase transitions in AFE bulk ceramics. However, there are several recent reports which show that PbZrO_3 thin films undergo room-temperature field-induced phase switching, due to appreciably induced strains

PbZrO_3 -based antiferroelectric materials have been studied extensively over the past several decades as applications for high-energy storage capacitors and high-strain actuators/transducers. With more recent development of microelectronic devices, antiferroelectric thin films have been explored for applications such as microactuators in microelectromechanical systems (MEMS) and decoupling capacitors in high-speed Dynamic Random Access Memory (DRAM) devices. An electric-field-forced phase transformation from an AFE phase to a ferroelectric (FE) phase occurs in PbZrO_3 owing to the small free-energy difference between the two phases. Fesenko et al. reported phase transformations, which occur in PbZrO_3 single crystals. It was observed that different hysteresis loops can be induced at various temperatures and electric fields.

2.4.3 Lead Zirconate–Lead Titanate [1]

Piezoelectric $\text{Pb}(\text{Ti},\text{Zr})\text{O}_3$ solid solution (PZT) ceramics are used widely because of their superior piezoelectric properties. The phase diagram of the PZT system [$\text{Pb}(\text{Zr}_x\text{Ti}_{1-x})\text{O}_3$] is shown in Figure 2.9. The crystalline symmetry of this solid solution is determined by the Zr content. PT also has a tetragonal ferroelectric phase in the perovskite structure. As the Zr content x increases, the tetragonal distortion decreases, and when x is > 0.52 , the structure changes from a $4mm$ tetragonal phase to another ferroelectric phase of rhombohedral $3m$ symmetry. Figure 2.10 shows the dependence of several d constants on the composition near the morphotropic phase boundary between the tetragonal and rhombohedral phases. The d constants have their highest values near the morphotropic phase boundary. This enhancement in the piezoelectric effect is attributed to the increased ease of reorientation of the polarization in an electric field. Doping the PZT material with donors or acceptors

changes the properties dramatically. Donor doping with ions such as Nb^{5+} or Ta^{5+} provides soft PZTs like PZT-5, due to the facility of domain motion caused by charge compensation of the Pb vacancy, which is generated during sintering. On the other hand, acceptor doping with Fe^{3+} or Sc^{3+} leads to hard PZTs such as PZT-8 because oxygen vacancies pin the domain wall motion.

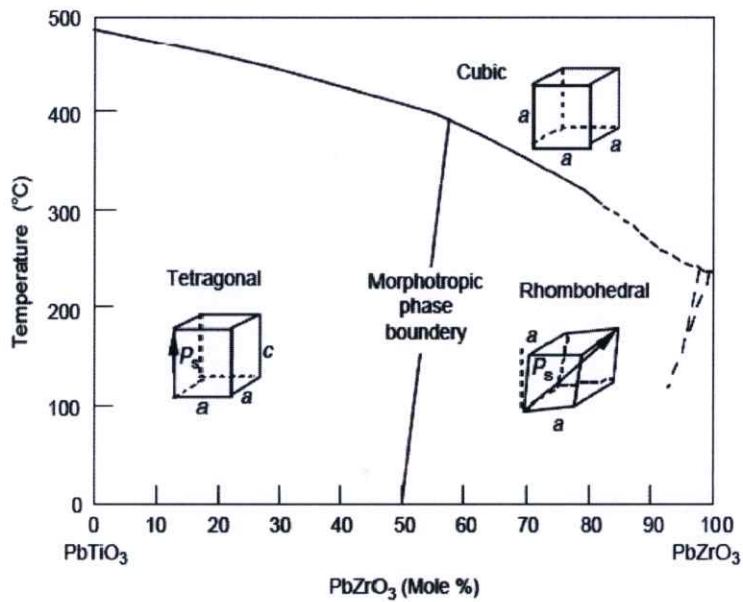


Figure 2.9 The phase diagram of the PZT system. [1]

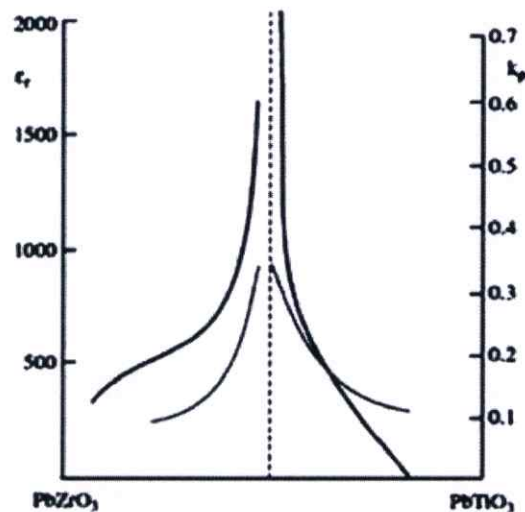


Figure 2.10 Dependence of several d constants on the composition near the morphotropic phase boundary. [1]

2.5 Powder Preparation

2.5.1 Mixed-Oxide Method [7]

The most direct method of making mixed-oxides is to obtain reaction from a mixture of metal oxides, hydroxides or salts in the solid state. Conventional processing to prepare multicomponent mixed-oxide ceramic powders involves three consecutive steps such as mixing, solid-state reaction and milling.

2.5.1.1 Mixing and Milling [7]

Mechanical milling as a solid state synthesis is performed usually using ball milling equipment; generally divided in to a “low energy” and “high energy” category, based on the value of mechanical energy induced in the powder mixture. The ball milling equipment used for mechanical grinding or mixing has low energy, such as the Horizontal mill (Tumbler). The speed of the low energy rod or ball mill is quite critical regarding efficiency of the process (Figure 2.11). It is necessary for the balls (or rods) to drop from the top of the mill onto the feedstock material being ground (Figure 2.11b). If the mill speed is too fast, the media will not fall at all due to centrifugal forces, or it will fall directly onto the media near the bottom of the mill (Figure 2.11c). At low speeds the media does not drop at all, whereas, at the optimum speed the media continuously "cascades" onto the feedstock material that is being crushed.

In mechanical milling processes, which are utilized for changing the chemical composition of precursors, high energy ball milling equipment is used in general. This phenomenon can be performed in various types of high energy ball mills, including attrition, planetary, and vibratory mills that are schematically shown in Figure 2.12. The rotating impeller in an attrition mill causes relative movement between balls and powders, while a rotating disc and vials in a planetary ball mill revolve in opposite directions at 700 rpm, and the vessel in the vibratory mill, also known as a shaker mill, is set at 1D or 3D vertical oscillatory motion. Spex 8000 is a commercial type of 3D vibratory mill. Of the above types of mills, the attrition mill has the highest capacity of powder charge. Accordingly, attrition milling is employed to synthesize thermal spray feedstock powders that are used for fabricating nanostructured coatings.

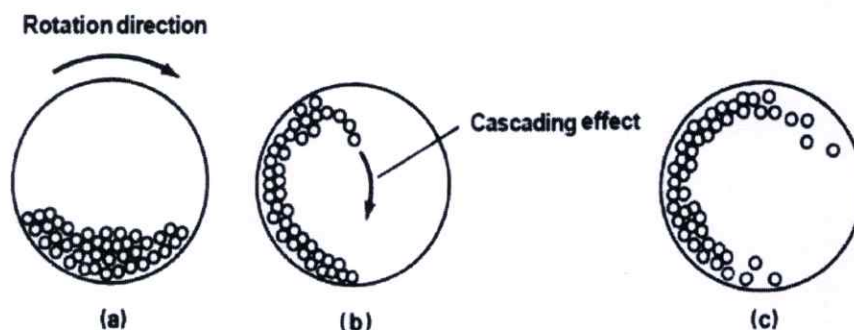


Figure 2.11 Low energy mechanical milling variable that controls particle grinding and efficiency: (a) low speed, (b) optimum speed, and (c) high speed. [7]

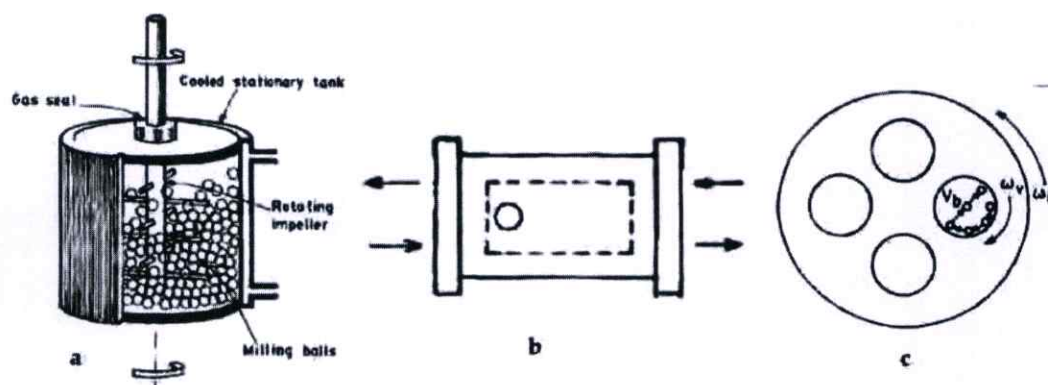


Figure 2.12 Various types of high energy ball mills: (a) attrition mill, (b) vibratory mill, and (c) planetary mill. [7]

2.5.1.2 Solid State Reaction [8, 9]

Electroceramic powders are fabricated usually by the thermal decomposition of inorganic and organic salts such as carbonates, nitrates, sulfates, acetates and oxalates or solid-solid reaction between constituent oxides. Both inorganic and organic salts thermally decompose to produce an oxide of constituent metal atoms. In this case the synthetic reaction is basically a solid-solid reaction between oxides. In such systems, the reaction between solid particles takes place in restricted regions. With a higher temperature and longer reaction time the reaction proceeds further inside the particles. However, this results in strong sintering of the powders, which cannot be broken down easily into fine particles. Then, optimum temperature and time of calcinations exist. In an optimum condition, the reaction is thought to be restricted usually near the contact regions, and particles are reduced

easily to fine powders. Also, several calcination-grinding operations are carried out to complete the reaction. In spite of this problem, the resultant powders from some operations contain more or less unreaction zones. In this method, the compositional inhomogeneity of powders depends on the particle size of the starting powder. [8]

The simplest system involves the reaction between two solid phases, A and B, to produce a solid solution, C. A and B are common elements for metallic systems, while crystalline compounds are common for ceramics. After initiating the reaction, A and B are separated by the solid reaction product, C (Figure 2.13). Further reaction involves transporting atoms, ions or molecules through the phase boundaries and reaction product by several possible mechanisms. Reactions between mixed powders are important technologically for powder synthesis. However, the study of reaction mechanisms is facilitated greatly by the use of single crystals because of their simplified geometry and boundary conditions. [9]

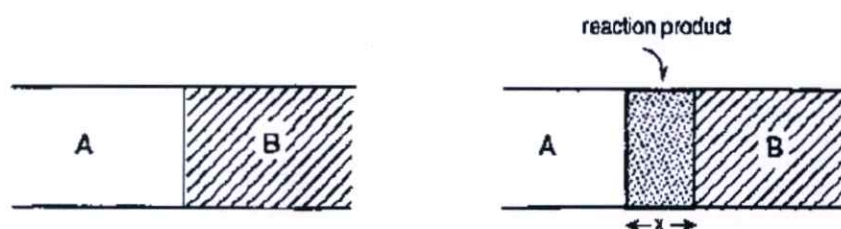


Figure 2.13 Schematic of the solid-state reaction in single crystals. [9]

Growth of the reaction product in powder systems for a solid-state diffusion mechanism occurs at the contact points, of which, the number is small for nearly equal-sized spheres. Nevertheless, for many systems, the Jander equation and Carter equation give good description of the kinetic reaction for at least the initial reaction stages. It appears that rapid surface diffusion provides a uniform supply of one reactant over another. Alternatively, if the vapor pressure of one reactant is high enough, a uniform supply of another one can be provided by condensation on the latter's surface. In this case, the powder reaction can be best described as gas-solid rather than solid-state. In practical systems, solid state reaction in powder systems depends on several parameters such as the chemical nature of the reactants and the product; the size, size distribution, and shape of the particles; the relative sizes of the reactant particles in the mixture; the uniformity of the mixing and the reaction

atmosphere; the temperature; and the time. The reaction rate decreases with an increase in particle size of the reactants because, on average, the diffusion distances increase. The reaction rate increases with temperature according to the Arrhenius relation. Commonly, the homogeneity of mixing is one of the most important parameters, as it influences the diffusion distance between the reactants and the relative number of contacts between the reactant particles, and thus enables production of homogeneous, single-phase powders. [9]

Powder preparation by solid-state reactions generally has an advantage in terms of production cost, but as outlined earlier, the powder quality also is an important consideration for advanced ceramics. The powders are normally agglomerated and a grinding step is almost always required to produce powders with better characteristics. Grinding in ball mills leads to impurities contaminating the powder. Incomplete reactions, especially in poorly mixed powders, may produce undesirable phases. Furthermore, the particle shape of ground powders is usually difficult to control. [8]

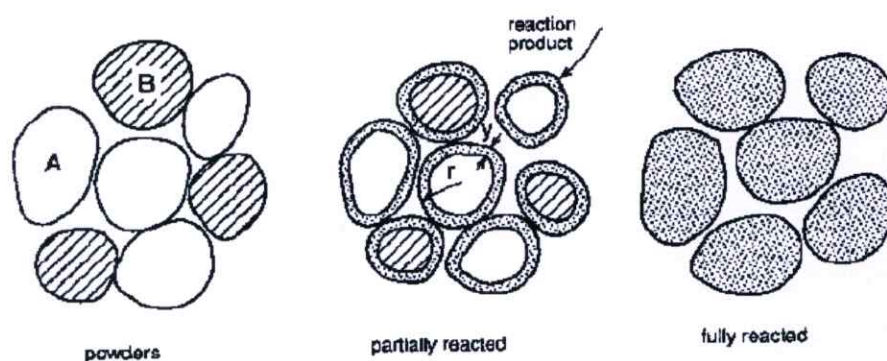


Figure 2.14 Schematic of the solid-state reaction in mixed powders. [9]

2.5.2 Hydrothermal and Solvothermal Processes [10]

There are several definitions of hydrothermal and solvothermal processes; however, hydrothermal and solvothermal reactions can be described as purely heterogeneous at temperatures above the boiling point of mineralizers in a closed system at 1 atm pressure. Water and organic solvents are used as main mineralizers in hydrothermal and solvothermal processes, respectively. These processes are of relatively low temperature and have many advantages such as fast kinetic reaction,

short processing times, phase purity, high crystallinity, high yield, homogeneous particle products, composite formation, narrow particle-size distributions, post-calcinations at only low temperature and cost effectiveness, and they are environmentally benign, and easily scalable. Furthermore, they facilitate different reactions, such as multicomponent reactions; heat treatment reactions that modify or change the composition; phase transformation reactions; ion exchange, crystal growth and dehydration reactions; decomposition reactions; extraction, precipitation and disproportionation reactions; and crystallization and solidification reactions.

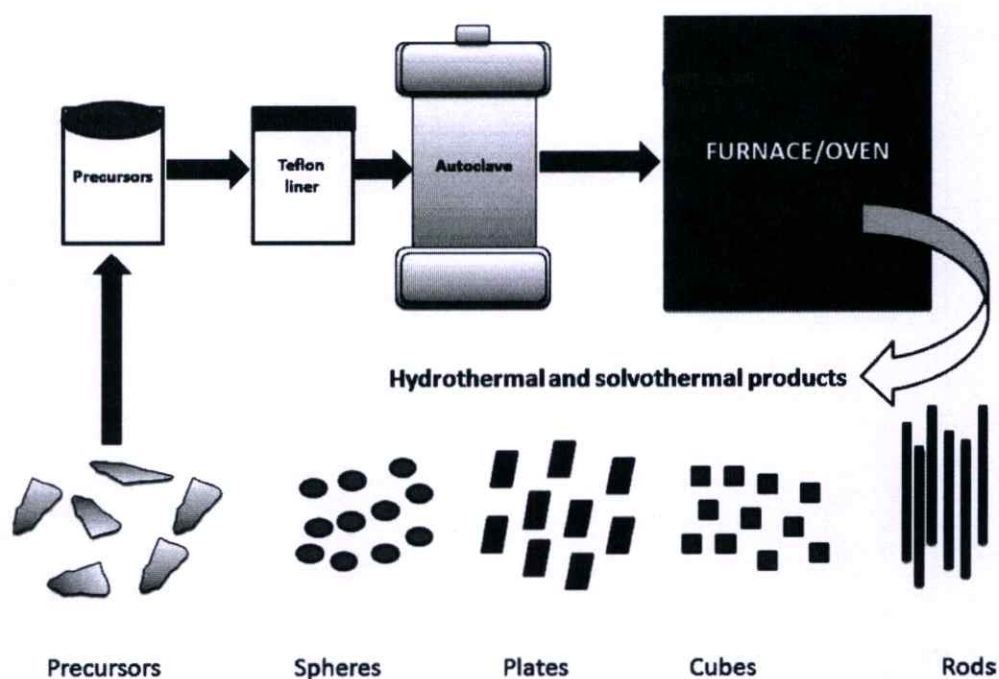


Figure 2.15 Experimental scheme for hydrothermal and solvothermal processes and their possible products. [10]

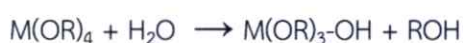
There are also a few disadvantages in hydrothermal and solvothermal processes, such as the need for expensive stainless-steel autoclaves and Teflon liners, possible safety issues during reaction processes, and the impossibility of studying in-situ reactions due to their closed (or “black box”) systems. Even though various synthetic methods are available, hydrothermal and solvothermal techniques are solution-based and capable of converting metal oxides into desirable nanostructures known for their unique electronic and electrochemical applications.

Nanomaterials, in particular, are beneficial for Li ion batteries by providing short diffusion lengths. The experimental scheme for hydrothermal and solvothermal processes and their possible products are illustrated in Figure 2.15. The precursor for hydrothermal and solvothermal reactions is usually in solution, slurry, or gel form, which is taken in Teflon liners and put into autoclaves, followed by heat treatment in a furnace or oven. Finally, the desired product of various shapes and sizes can be collected after several washings.

2.5.3 Sol–Gel Processing [11]

In the sol–gel process, a solution of metal compounds or suspension of very fine particles in liquid (referred to as sol) is converted into a highly viscous mass (the gel). Two different sol–gel processes can be distinguished, depending on whether a sol or solution is used (Figure 2.16). In starting with a sol, the gelled material consists of identifiable colloidal particles that have been joined together by surface forces to form a network (Figure 2.17a). A solution is typically metal-organic compounds (such as metal alkoxides), and in many cases the gelled material may comprise a network of polymer chains formed by hydrolysis and condensation reactions (Figure 2.17b). This “solution sol–gel process” is receiving considerable interest in research; however, the sol–gel process based on the gelling of suspensions sees more widespread industrial application. As indicated above, the starting material normally consists of a solution of metal alkoxides in an appropriate alcohol. Metal alkoxides have the general formula of $M(OR)_x$ and can be considered as either a derivative of an alcohol, ROH, where R is an alkyl group, in which the hydroxyl proton is replaced by a metal, M, or a metal hydroxide, $M(OH)_x$. Water is added to this solution in either a pure state or diluted with more alcohol. Under constant stirring at a heat slightly above room temperature (normally 50–90°C), and with a suitable concentration of reactants and pH of the solution, hydrolysis and condensation reactions may occur, leading to the formation of polymer chains. Taking the example of a tetravalent metal (e.g., M-Si), the reactions may be expressed as follows:

Hydrolysis



Condensation



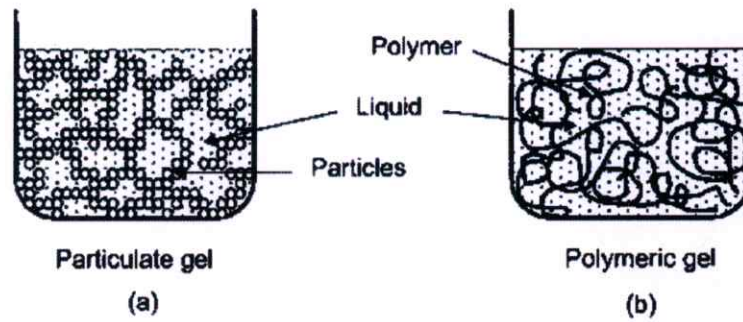


Figure 2.16 Schematic diagram of the structure of (a) a particulate gel formed from a suspension of fine particles and (b) a polymeric gel from a solution. [11]

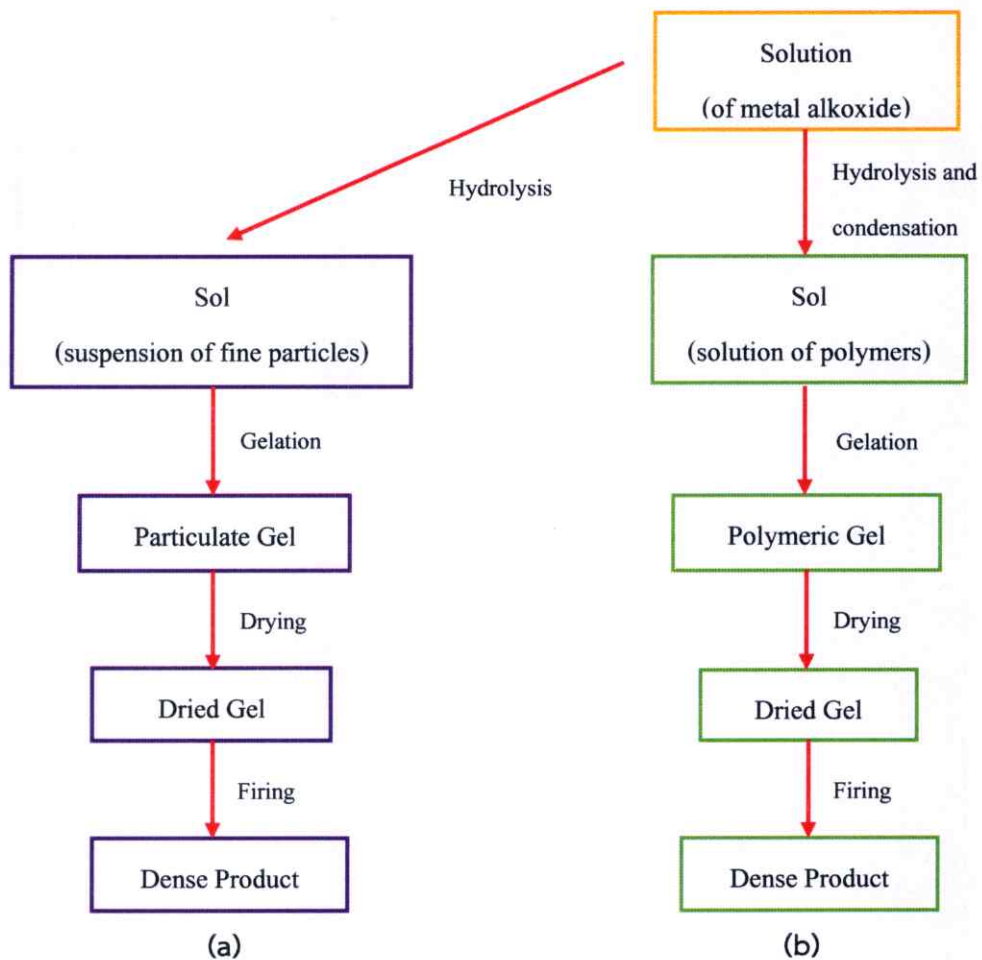


Figure 2.17 Basic flow charts for sol-gel processing using (a) a suspension of fine particles and (b) a solution. [11]

Polymerization of the species formed by the hydrolysis and condensation reactions, together with interlinking and cross-linking of the polymer chains, eventually leads to a marked increase in the viscosity of the reaction mixture and production of a gel. The gel has a continuous solid network and finite shear modulus. Normally, excess water and alcohol are used in the reactions, so that the amount of solid matter in the gel (i.e., the content of solids of the gel) can be quite low; being 5–10 vol% in many cases. The remainder of the volume consists of liquid that must be removed prior to firing. Gel drying can be the most time consuming and a difficult step in the overall fabrication route, especially when a monolithic material is required directly from the gel. Normally, the liquid is present in fine channels, typically 2–50 nm in diameter. Removal of the liquid by evaporation has two main consequences: large capillary stresses are generated, and the gel undergoes considerable shrinkage under the action of capillary stress.

2.6 Nanofiber Preparation [12, 13]

The technological attraction of ceramic nanomaterials originates from improved and/or novel properties arising from their high surface-to-volume ratio. In addition, when the particle size reduces to nanometer level, their bonding characteristics deviate from those of bulk material, thus allowing for opportunities to manipulate the surface structure for applying devices. The increased surface area of nanomaterials is beneficial in many ways for technological applications. For example, should nanometer sized particles be the active elements in a lasing medium, the increased surface area results in faster removal of heat in a laser cavity, thus, improving the power output. This phenomenon led to the concept of fiber lasers, and because of this, high power fiber lasers with an output of 10 kW have been realized and are now available commercially. Furthermore, as nanostructured materials are much smaller than the wavelength of visible light, they can be integrated conveniently with the present glass and optoelectronic industry because their reflective, refractive and light emission properties can be attuned by control of size. Such glass ceramics are now available routinely on the open market and used for many applications such as optical amplifiers for optical communication and signal processing, glass lasers, filters, etc.

Ceramic nanofibers have great potential for testing the concepts of fundamental quantum mechanics and playing a vital role in various applications such as photonics, nanoelectronics, and data storage. In addition, many unique and fascinating properties have been proposed and demonstrated for this class of materials, including superior mechanical toughness, higher luminescence efficiency, and enhancement of the thermoelectric figure of merit. Electrospinning is a mature technique used to fabricate nanofibers.

A number of processing techniques such as drawing, template synthesis, phase separation and self-assembly have been used to prepare polymer nanofibers in recent years. However, these methods have disadvantages such as material limitation, time-consumption and complicated processing systems. Regarding electrospinning, it is not only a simple one-step top-down process for fabricating nanofibers, but also the co-processor of polymer mixtures, and chemical cross-linking can be performed to provide a variety of pathways for controlling the chemical composition of nanofibers. These benefits provide a wide range of properties such as strength, weight, elasticity, porosity and charged surface areas. In addition, electrospinning also provides the capacity to intertwine different types of nanoparticles or nanofillers that can be encapsulated into a nanofiber matrix. Functional micro/nano particles may be dispersed in polymer solutions, which are then electrospun to form composites in the form of continuous nanofibers and nanofibrous assemblies. All these aspects endow electrospinning with flexibility. Additionally, electrospinning seems to be the only method that can further current manufacturing capabilities by utilizing an easy process and capability of developing mass production of one-by-one continuous nanofibers from various polymers.

2.6.1 Electrospinning Technique [12, 13]

Electrospinning was first reported in 1934, and has been used for more than 60 years, and yet it appears under developed when studying the fabrication of continuous nanofibers. The term “electrospinning”, which derived from “electrostatic spinning”, was coined quite recently. Since the 1980s, and especially in recent years, the electrospinning process has regained more attention, probably due in part to a surging interest in nanotechnology, as ultrafine fibers or fibrous structures of various

polymers, with diameters in the submicron/nanometer range, can be fabricated easily by electrospinning.

Fabrication of one-dimensional ceramic nanofibers has gained increased interest since 2002. A novel method by which ceramic nanofibers are fabricated widely is by the combination of two conventional techniques such as electrospinning and sol-gel. Electrospinning is the process by which continuous nanofibers are produced with a high surface area to volume ratio. A polymer solution in this process is injected from a needle in the presence of an electric field. When the applied electric field overcomes the surface tension of the liquid, a continuous jet is ejected, which upon subsequent solvent evaporation and bending produces nanofibers on the collector surface. The sol-gel technique has been used to prepare ceramic nanomaterials such as ceramic nanoparticles, and is found to be versatile in preparing individual as well as mixed ceramic nanoparticles at low temperatures for applications such as thin film formation, coatings, solar cells, nanoelectronics, sensors, etc. The combination of electrospinning and sol-gel techniques provides a way to fabricate ceramic nanofibers of different sizes, compositions, and morphologies such as tubular, ribbons, and porosity in a single step. In addition, the process is relatively simple. The even distribution of materials such as catalysts and additives, and the encapsulation of insolubles into a nanofiber matrix are achieved easily by using this approach. Although a few other methods of fabricating nanofibers such as phase separation and template synthesis are reported in the literature, electrospinning is found to be unique in producing continuous nanofibers with several hundred micrometer length, flexibility, and ease of fiber production. Through this technique, different fiber assemblies such as random mats, aligned fibers, and patterned fibers; random three-dimensional architecture, can be fabricated easily. Some of these morphologies are depicted in Figure 2.18. Generally, ceramic nanofibers are made by electrospinning ceramic precursors in the presence of polymers, followed by calcination at higher temperatures. However, a few reports also are available on the fabrication of ceramic nanofibers without the addition of polymers. The electrical conductivity of ceramic precursors in polymers is found to increase drastically when compared to polymer solution. Careful preparation of the precursors is essential in order to electrospin ceramic systems accurately. Several parameters, such as solvent volatility, viscosity, surface tension, conductivity, applied voltage, etc., need to be

optimized for all systems. Sometimes, cosolvents or stabilizers are added to achieve optimum conditions for electrospinning.

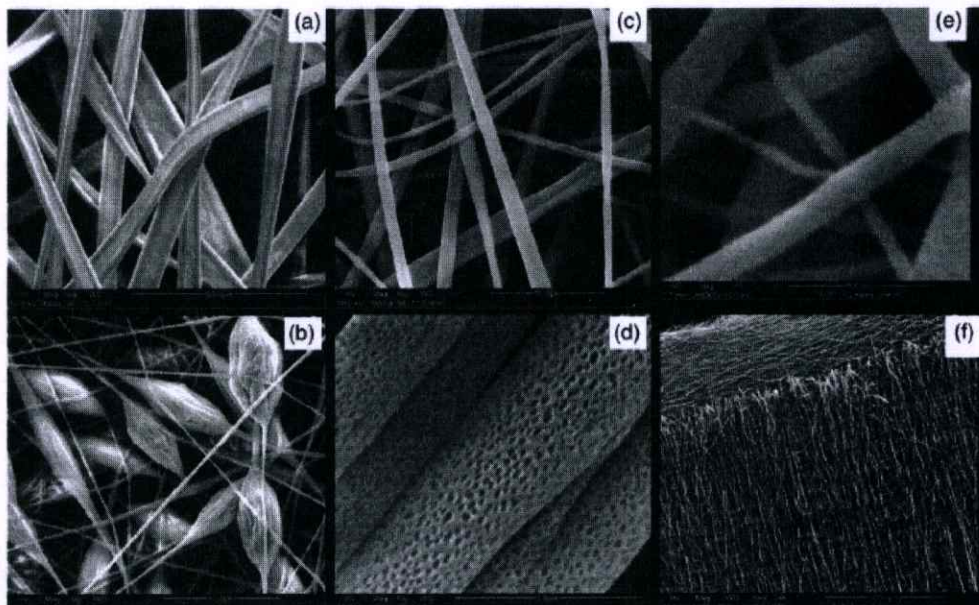


Figure 2.18 Various electrospun architecture (a) flat polymer nanofibers, (b) beaded polymer nanofibers, (c) nonporous smooth polymer nanofibers, (d) porous submicron polymer fibers, (e) randomly oriented ceramic nanofibers, and (f) aligned ceramic nanofibers. [12]

Electrospinning appears to be affected by the following parameters and variables: 1) system parameters such as molecular weight, molecular weight distribution and architecture (branched, linear, etc.) of the polymer, and polymer solution properties (viscosity, conductivity, dielectric constant, and surface tension, as well as charge carried by the spinning jet) and 2) process parameters such as electric potential, flow rate and concentration, distance between the capillary and collection screen, ambient parameters (temperature, humidity and air velocity in the chamber) and finally motion of the target screen. By appropriately varying one or more of the above parameters, nanofibers can be electrospun successfully from a rich variety of materials that include polymers, biopolymers, DNA, protein, composites, and ceramics and even relatively small macromolecules such as phospholipids.

Electrospinning, in combination with the conventional sol-gel process, has been extended recently to fabricate a variety of ceramic nanofibers. From this technique, the ceramic nanofibers and conventional sol-gel precursors are mixed with various kinds of polymers, such as poly(ethylene oxide) (PEO), poly(vinylpyrrolidone) (PVP) and poly(vinyl alcohol) (PVA), to increase viscosity.

2.6.2 Experimental Setup for E-Spinning [14, 15]

As the name suggests, e-spinning depends on electrostatic forces to form fibers. In essence, an electric field of several kilovolts is applied between a reservoir containing a complex fluid ceramic precursor and a collector. A schematic diagram of the experimental setup and a picture of a typical laboratory setup are presented in Figure 2.19. A syringe pump squeezes a small amount of complex fluid (ceramic precursor, polymer, solvent) out of a 100 mm needle. The metallic needle is attached to a high voltage source that is either positive or negative. The droplet that forms at the end of the needle will change its form as soon as a voltage is applied. Depending on experimental conditions, the jet then starts to whip close to the collector, causing it to thin to a few hundred nanometers, with lower limits in tenths of nanometers. So far, all ceramic systems and most polymers have been electrospun via solution-based e-spinning, but another processing pathway is possible that is based on melting (melt-based e-spinning). This new pathway has yet to be applied to ceramic systems, but was demonstrated successfully for polymers. The complex fluid containing ceramic precursors can consist of salt loaded polymer solutions, sol-gel systems, or nanoparticle slurries. Most of the time, a polymer is introduced to achieve the required viscosity and mechanical properties in the green state. However, it has been shown by aging the sol-gel precursor that e-spinning of ceramic systems without an organic polymer also is possible. In summary, the experimental steps for e-spinning ceramics normally are as follows:

- (1) Preparation of e-spinning solution.
- (2) E-spinning of the prepared solution and collection of the polymer/inorganic composite fibers/mat.
- (3) Calcination of the composite fibers to remove unwanted constituents (polymer, solvent) and obtain the desired ceramic phase.
- (4) Annealing for further modification of the fiber microstructure.

While collection, calcination and annealing processes are essential, arguably the most challenging step is the preparation of a suitable solution or dispersion for electrospinning, as the system requires a balance of forces that are controlled by charges, viscosity, and surface tension.

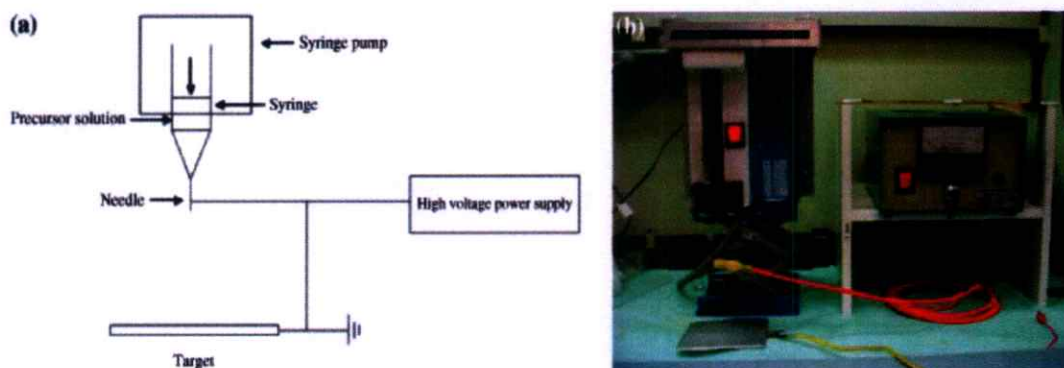


Figure 2.19 A schematic diagram of the experimental setup and picture of a typical laboratory setup. [14]

The formation of nanofibers through electrospinning is based on the uniaxial stretching of a viscoelastic solution. There are basically three components in an electrospun setup: a high voltage power supply, capillary tube with a needle and metal collector. When a sufficiently high voltage is applied to a liquid droplet, the body of the liquid becomes charged, and electrostatic repulsion counteracts the surface tension and the droplet is stretched, and a stream of liquid erupts from the surface at a critical point, which is known as the Taylor cone. If the molecular cohesion of the liquid is sufficiently high, stream breakup does not occur (if it should, the droplets would be electrospayed) and a charged liquid jet is formed. As the jet dries out in flight, the mode of current flow changes from ohmic to convective as the charge migrates to the fiber surface. The jet is then elongated by a whipping process caused by electrostatic repulsion initiated at small bends in the fiber, until it is deposited finally on the grounded collector. The elongation and thinning of the fiber result from the bending instability, which leads to the formation of uniform fibers with nanometer-scale diameters. The main advantage of the electrospinning nanomanufacturing process is its cost effectiveness when compared to most bottom-up methods. Nanofibers prepared from the electrospinning process are often uniform

and continuous and do not require expensive purification, unlike submicrometer diameter whiskers, inorganic nanorods and carbon nanotubes.

2.6.3 Characteristics of Electrospun Fibers [13]

Nanofibers have a diameter in the order of a few nanometers to over 1 μm (more typically 50~500 nm) and possess unique characteristics, such as extraordinarily high surface area per unit mass (for instance, nanofibers with ~100 nm diameter have a specific surface of ~1,000 m^2/g), coupled with remarkably high porosity, excellent structural mechanical properties, high axial strength combined with extreme flexibility, low basic weight, cost effectiveness and more.

Another interesting aspect in the use of nanofibers is the feasibility to modify not only their morphology and content (internal bulk), but also the surface structure in order to carry out various functions. Nanofibers can be post-synthetically functionalized easily (for example by chemical or physical vapour deposition). Furthermore, it is even feasible to control secondary nanofiber structures in order to prepare nanofibers with core/sheath structures, hollow interiors and porous structures.

Additionally, nanofibers have one dimension on the microscopic scale and another macroscopically. This unique characteristic endows nanofiber mats with both the merits possessed by functional materials on the nanometer scale, and these have advantages over conventional solid membrane such as easy processing, ease of packaging and shipping.

These outstanding properties make polymer nanofibers good candidates for many applications. Polymer nanofiber mats are being considered for use in composite material reinforcement, sensors, filtration, catalysis, protective clothing, biomedical applications (including wound dressing and scaffolds for tissue engineering, implants, membranes and drug delivery systems), space applications such as solar cells, and micro- and nano optoelectronic devices such as light emitting diodes (LEDs) and photocells.

2.7 Polymer-Ceramic Composite Materials [16]

Polymer-piezoelectric ceramic composites have been investigated extensively for piezoelectric and pyroelectric transducer application. Although many

piezoelectric ceramic materials have good piezoelectric and pyroelectric properties and high dielectric constants (ϵ_r), they represent a large leakage of current, low dielectric strength and generally natural brittleness. In addition, relatively high density, high acoustic impedance and mechanical stiffness limit their applications. On the other hand, polymeric materials exhibit very high dielectric strengths and low leakage of current, and they have acoustic impedance well matched to water and biological issues. However, polymers generally show small dielectric constants ($\epsilon_r=2\sim 12$). Flexible piezoelectric composite is considered as a solution to the problem. This element offers several advantages over single-phase piezoelectric materials. It consists of a ceramic material embedded in a flexible polymer matrix, with a certain connectivity pattern, and exhibits good piezoelectric and pyroelectric properties, low densities, low leakage of current, high breakdown strength and mechanical flexibility.

The properties of ceramic-polymer composites are determined by the number of phases and connectivity between phases in composite materials. Additionally, the filler particle size, interfacial properties, percolation level, and effects of porosity also can play a role in composite properties.

2.7.1 Design of Composites - Connectivity Models [17]

Properties of the components, amount of each phase present, and how they are interconnected, viz connectivity, are important for fabricating a composite. Newnham et al., 1978 and Tressler et al., 1999 proposed the concept of connectivity. Any phase in a mixture can be self-connected in zero, one, two, and three dimensions. For example, inclusions dispersed in a polymer host material shall have connectivity 0, while host polymer shall have connectivity 3. Thus, the term composite with connectivity 0-3 or 0-3 composites can be used. In a two phase composite system, there can be ten different connectivities, i.e. 0-0, 0-1, 0-2, 0-3, 1-1, 1-2, 1-3, 2-2, 2-3, and 3-3 (Figure 2.20). In this format, the first digit denotes the connectivity of inclusions and the second one the host. Generally, the host is a polymer in the case of polymer composites.

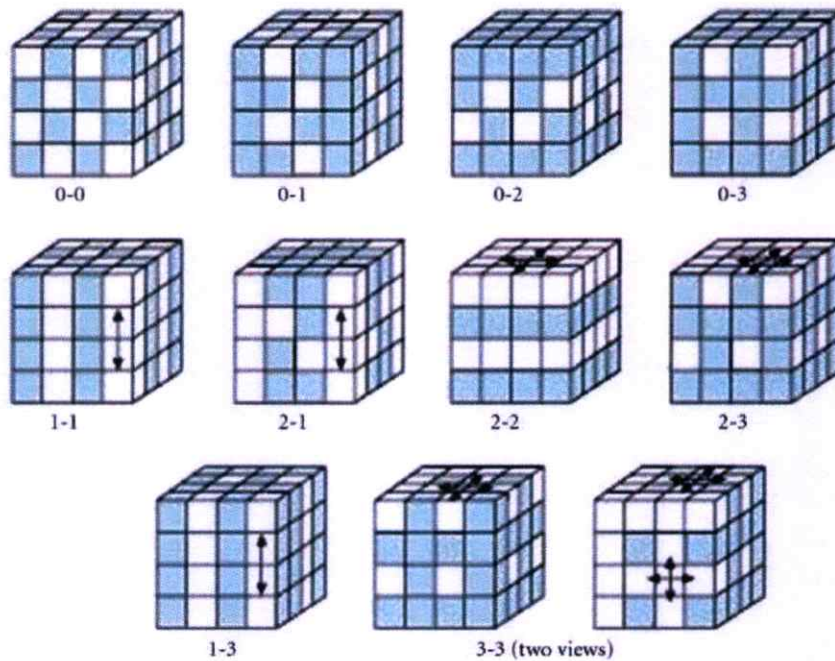


Figure 2.20 Connectivity Models. [18]

2.7.2 Fabrication of Polymer-Ceramic Composites [1]

In a diphasic composite, there are 10 different ways in which the materials can be oriented in three dimensional (3D) space. The possible connectivity patterns are 0-0, 1-0, 2-0, 3-0, 1-1, 2-1, 3-1, 2-2, 3-2, and 3-3. As a matter of convention, the first and second numbers in the connectivity denote continuity of the piezoelectric and polymer phases, respectively. The important connectivity patterns are 0-3, 1-3, 3-3, and 2-2. The 0-3 composites are made with a homogeneous distribution of piezoelectric ceramic particles within the polymer matrix. The primary advantage of these composites is the ability to form them into shapes, while remaining piezoelectrically active. The disadvantage is that 0-3 composites cannot be poled sufficiently because the ceramic phase is not self-connected in the poling direction. On the other hand, 3-0 composites, which are simply the ceramic matrix with low concentration of polymer inclusions or voids, can be poled effectively and exhibit hydrostatic properties superior to that of single phase PZT. The piezoceramic and polymer phases in composite with connectivity 3-3 are continuous in three dimensions in the form of two interlocking skeletons having intimate contact with each other. The first composite with connectivity 3-3 was formed by the replamine

process using a coral skeleton. Another effective method of making 3–3 composites is called BUR nedout Plastic Spheres (BURPS) with properties similar to the replamine composites. A mixture of PZT powder and burnable plastic spheres are used to fabricate the PZT–polymer composites. Other techniques, such as relic processing and distorted reticulated ceramics, have been developed to fabricate 3–3 composites. Recently, fused deposition modeling (FDM) and fused deposition of ceramics (FDC) have been used to make ladder and 3D honeycomb composites. In the FDM technique, a 3D plastic mold is prepared and filled with PZT slurry. The FDC process directly deposits a mixture of PZT and polymer in the form of a 3D ladder structure. Either structure is heat-treated to burn the organic, sintered PZT, and embed it in the epoxy polymer. The most extensively studied and used transducer applications are composites with connectivity 1–3. They consist of individual PZT rods, or fibers, aligned parallel to the poling, and embedded in a polymer matrix. Decoupling d_h , d_{33} and d_{31} responses of the PZT elements significantly enhance. The rod diameters, spacing between them, composite thickness, volume fraction of PZT, and polymer compliance, influences the composite performance. The most common methods of forming 1–3 composites are the dice and fill technique and injection molding. In the former method, the composite is fabricated by dicing deep grooves perpendicularly into a solid sintered block of poled PZT. The grooves are backfilled with polymer and the base is removed via either grinding or cutting. In the latter method, a thermoplastic mixture of ceramic powder and organic binder is injected into a cooled mold. The process can be used to form composites with a variety of rod sizes, shapes, and spacing.

2.7.3 Properties of Piezoelectric-Polymer Composites [18, 19]

Based on connectivity designs, several important piezoelectric ceramic/polymer composites were developed. Figure 2.21 represents the schematic diagram of different piezoelectric ceramic/polymer composites. All of them showed improved piezoelectric properties when compared to single phase piezoelectric ceramics. Their d_{hg} figures of merit are compared in Figure 2.22.

Piezocomposites comprised of piezoelectric ceramics and polymers are promising materials because of their excellent tailored properties. The geometry of two-phase composites can be classified into 10 structures; 0-0, 0-1, 0-2, 0-3, 1-1, 1-2,

1-3, 2-2, 2-3, and 3-3 according to the connectivity of each phase (0, 1, 2, or 3 dimensionality). The 1-3 piezocomposite or PZT-rod/polymer-matrix composite is a most promising candidate. Its advantages are high coupling factors, low acoustic impedance (square root of its product density and elastic stiffness), good match to water or human tissue, mechanical flexibility, broad bandwidth in combination with low mechanical quality factor, and the possibility of making undiced arrays by structuring only the electrodes. The thickness-mode electromechanical coupling of the composite can exceed the k_t (0.40–0.50) of constituent ceramic and almost approach the value of the rod-mode electromechanical coupling, k_{33} (0.70–0.80), of that ceramic. The acoustic match to tissue or water (1.5 Mrayls) of typical piezoceramics (20–30 Mrayls) has improved significantly by forming a composite structure and replacing a heavy, stiff ceramic with a light, soft polymer. Piezoelectric composite materials are used especially for underwater sonar and medical diagnostic ultrasonic transducers.

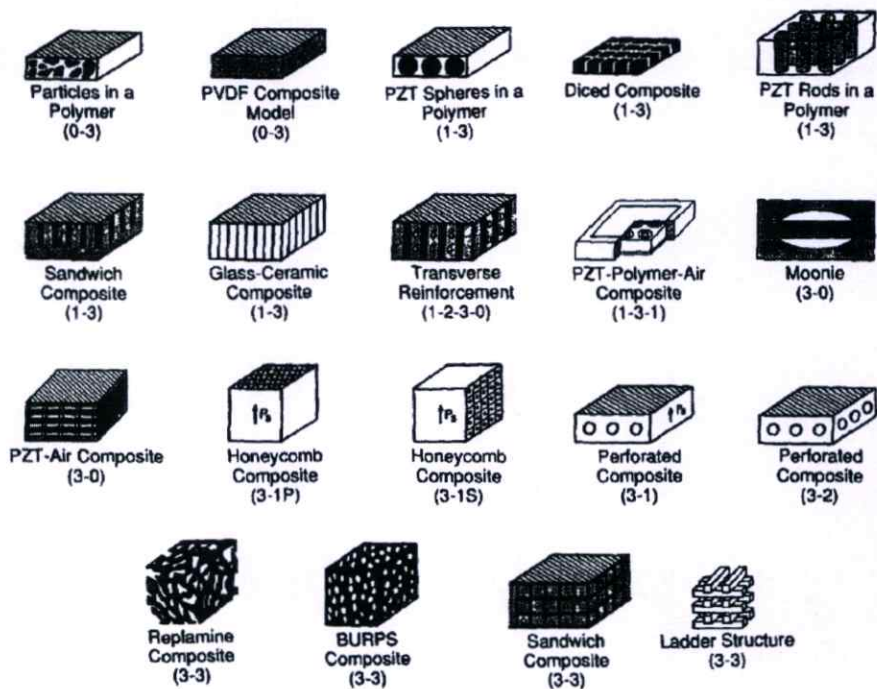


Figure 2.21 Schematic diagram of different piezoelectric ceramic/polymer composites. [18]

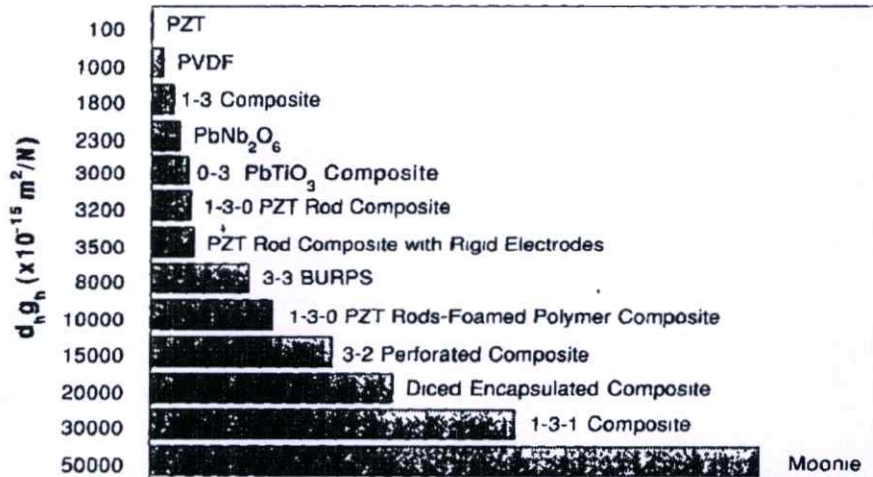


Figure 2.22 The $d_h g_h$ figures of merit of these composites. [18]

2.7.4 Dielectric Properties of Polymer–Ceramic Composites [19, 20]

The dielectric characteristics of the composites for the same filler ceramic loading were found to depend strongly on the type of polymer. Polar polymers increase the ϵ_r of the composites at low frequencies, but they have hardly any effect at microwave frequencies. The tangent loss of the composites peaks at an intermediate frequency, indicating the relaxation behavior of the polymer matrix. The dielectric properties of the composites are influenced not only by the relative permittivity of the components, but also other factors such as the morphology, dispersion, and interactions between the two phases. Therefore, predicting the relative permittivity of the composite from that of the components and volume fraction of the filler is very important, but this is a difficult task for electronic packaging applications.

However, while different models have been developed, usually little or no experimental evidence was provided to support the derived equations. Therefore, the ambiguity prevails as to which model is more useful for the prediction of an effective dielectric constant of the composites. Polymers filled with ceramics have been studied for use as dielectric materials in thick film capacitors. Ceramic particle size influences the effective dielectric constant of a composite dramatically. Precise prediction of the effective dielectric constant of polymer/ceramic nanocomposites forms a focal point for the design of composite materials. Many theoretical models have been proposed in the literature for simulating the electrical properties of the

composites. Mostly, composite dielectrics are statistical mixtures of several components. The models mentioned are empirical ones that describe the polymer/ceramic nanocomposite property. Other efforts also have been made to predict the dielectric properties of a composite using the percolation theory. The major interest in the physics of disordered materials lies in relating the macroscopic property of interest such as permittivity, conductivity, etc. The effective medium theory (EMT) also is used to set up a numerical model that can predict the dielectric constant of a polymer/ceramic nanocomposite precisely. The major factors affecting the dielectric properties of barium titanate ceramics are the grain size, phase contents and types of dopants used. Thus, the dielectric property of a composite can be treated in terms of an effective medium, from which dielectric permittivity can be obtained by suitably averaging its two constituents. The perovskite-type barium titanate for polymer/ceramic composites is in the powder instead of sintered form. Removing grain boundaries, eliminating constrained forces from neighboring grains and dropping domain density, due to decreased particle size, reduces the dielectric constant of barium titanate (BT) powders. Furthermore, it was seen that inorganic ceramic materials need to be compatible with the polymer matrix. Therefore, as ceramic material is required to be compatible with the polymer matrix, it needs surface modification for increased compatibility.

2.8 Polymer Matrix [21]

Properties of different polymers will determine the application to which they are appropriate. The chief advantages of polymers as a matrix are low cost, easy processability, good chemical resistance, and low specific gravity. On the other hand, low strength, low modulus, and low operating temperatures limit their use. Varieties of polymers for composites are thermoplastic polymers, thermosetting polymers, elastomers, and their blends.

Thermoplastic polymers: Thermoplastics consist of linear or branched chain molecules that have strong intramolecular bonds, but weak intermolecular bonds. They can be reshaped by applying heat and pressure and are either semicrystalline or amorphous in structure. Examples include polyethylene, polypropylene,

polystyrene, nylons, polycarbonate, polyacetals, polyamide-imides, polyether ether ketone, polysulfone, polyphenylene sulfide, polyether imide, and so on.

Thermosetting polymers: Thermosets have cross-linked or network structures with covalent bonds in all molecules. They do not soften but decompose on heating. Once solidified by the cross-linking process they cannot be reshaped. Common examples are epoxies, polyesters, phenolics, ureas, melamine, silicone, and polyimides.

Elastomers: An elastomer is a polymer with the property of viscoelasticity, and in general notably low Young's modulus and a high yield strain when compared with other materials. The term, elastomer, derived from elastic polymer, and is often used interchangeably with the term, rubber, although the latter is preferred when referring to vulcanizates. Each monomer that links to form the polymer is made usually of carbon, hydrogen, oxygen, and silicon. Elastomers are amorphous polymers that exist above their glass transition temperature, so that considerable segmental motion is possible. At ambient temperatures, rubbers are relatively soft ($E \sim 3\text{MPa}$) and deformable, and they are used primarily for seals, adhesives, and molded flexible parts. Some examples of elastomers are as follows: natural rubber, synthetic polyisoprene, polybutadiene, chloroprene rubber, butyl rubber, ethylene propylene rubber, epichlorohydrin rubber, silicone rubber, fluoroelastomers, thermoplastic elastomers, polysulfide rubber, and so on.

2.8.1 Poly(vinylidenedifluoride) (PVDF) [1]

PVDF or PVF_2 is a piezoelectric when stretched during fabrication. It has superior piezoelectric properties when compared with other types of polymeric materials, due to its polar crystalline structure. Thin sheets of the cast polymer are drawn and stretched in the plane of the sheet in at least one direction and also frequently in a perpendicular direction to convert the material into its microscopically polar phase. Crystallization from a melt forms the nonpolar α -phase, which can be converted into another polar β -phase by uniaxial or biaxial drawing; and these dipoles are then reoriented by electric poling. Large sheets can be manufactured and thermally formed into complex shapes. Copolymerization of vinylidenedifluoride with trifluoroethylene (TrFE) results in a random copolymer (PVDF-TrFE) that has a stable, polar β -phase. This polymer does not need to be

stretched; it can be poled directly as formed. The thickness-mode coupling coefficient of 0.30 has been reported. Such piezoelectric polymers are used for directional microphones and ultrasonic hydrophones.

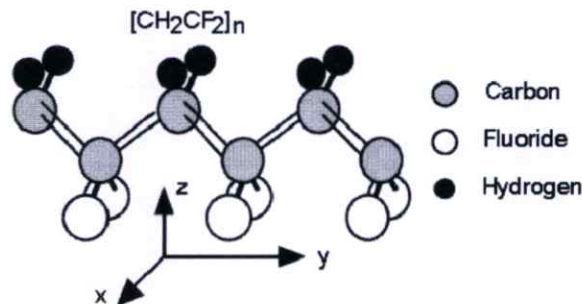


Figure 2.23 Structure of polyvinylidenedifluoride (PVDF). [1]

2.9 Carbon Nanotubes (CNT) based Composites [22-24]

2.9.1 Carbon Nanotubes [22]

Carbon nanotubes (CNTs) have remarkable electrical and mechanical properties such as extremely high conductance and Young's modulus. They are found to be attractive on account of their potential for applications in nanoscale devices. Their use in nanocomposites as a filler material can be viewed as one of the most promising areas driving toward commercial applications. CNT/polymer composites are of particular interest because a small amount of conductive CNTs added to an otherwise insulating polymer matrix results in nanocomposites with highly enhanced electrical conductivity. The critical content of CNTs, which characterizes a drastic increase in conductivity, is termed commonly as the electrical percolation threshold (EPT). Classical percolation theories have been proposed, which essentially examine the formation of conductive pathways inside the polymer matrix in the form of uninterrupted clusters of connected CNTs. Some other studies also indicate the importance of considering quantum effects such as electronic tunneling between neighboring CNTs to explain EPT as well as conductivity. CNT/polymer nanocomposites are thus an alluring avenue for research because of their potentially functional applications in optoelectronic devices and organic light-emitting diodes, which probe EPT in nanocomposites; and many theoretical and numerical studies based on different methods such as continuum mechanics and

Monte Carlo simulations have been carried out. Monte Carlo methods, in particular, have been used extensively for numerical studies of electrical percolation and formation of percolation networks, as well as effects of varying parameters on the threshold. With the help of simulations based on simple two dimensional (2D) modeling of randomly dispersed fillers, Natsuki et al. investigated the relationship between percolation behavior and orientation as well as the aspect ratio of fillers. In general, exponential decrease is found in the percolation threshold with an increased aspect ratio. Regarding CNT films, Behnam et al. also found that film conductivity depends on the alignment of nanotubes, in that the highest conductivity is obtained at partially aligned CNTs. Other studies extended 3D simulations further and revealed qualitatively similar features. High aspect ratio nanotubes are seen to have the tendency to curl up in composites, and taking the effect of waviness into account is therefore important. By employing 3D models with randomly distributed curved fibers of finite width, the critical volume fraction was found to increase with an increase in the degree of waviness, and reduction of electrical conductivity was an accompanying effect. Hu et al. also emphasized that poor dispersion of nanotubes in the matrix, which can lead to the formation of agglomerates, significantly raises the percolation threshold.

2.9.2 Dispersion of Carbon Nanotubes [23]

Carbon nanotubes tend to aggregate together inside the solution and form ropes, due to the strong van der Waals attraction forces between them, and they usually have highly entangled network structures. That is why dispersion of CNT inside the polymers becomes difficult. However, by careful procedure these two components can be mixed without severe aggregation of nanotubes. The attractive forces also arise, due to an entropic effect inside the polymer matrix. Polymer chains in the region of the colloidal filler suffer an entropic penalty, since roughly half of their configurations are precluded. Therefore, the polymer in this region is depleted, resulting in an osmotic pressure forcing the filler particles to come together.

The method of functionalizing nanotubes is a good choice. It requires chemical modifications of their surrounding surface, supported by mechanical agitation methods such as ultrasonication and shear mixing. Several functionalization methods have been reported already. They are mainly based on the covalent

(grafting-to and grafting-from), and non-covalent (polymer wrapping, π - π stacking interaction) functionalization. The adsorption and coupling of surfactants and functionalities to CNTs are described as follows:

(A) Covalent functionalization: Covalent methods refer to a treatment that involves bond breaking across the surface of CNTs (e.g. by oxidation), which disrupts the delocalized π -electron systems and fracture of σ -bonds, and hence leads to incorporation of other species across the CNT surface. Introducing defects to the CNT shell significantly alters the optical, mechanical and electrical properties of the nanotubes and leads to an inferior performance of the composites. The advantage is that this kind of modification may improve the efficiency of bonding between nanotubes and the host material (cross-linking). Therefore, the interfacial stress transfer between the matrix and CNTs may be enhanced, thus leading to a better mechanical performance.

(B) Non-covalent functionalization: This modification of carbon nanotubes is of great advantage because no disruption of the sp^2 graphene structure occurs, and the CNT properties are preserved. Its disadvantage concerns weak forces between wrapped/coupled molecules that may lower the load transferred in the composite. Various approaches for the fabrication of CNT/polymer composites were shown, including different functionalization and dispersion methods of nanotubes. The most important were:

(1) Solution processing of composites: The most common method is based on mixing CNTs and a polymer in a suitable solvent before evaporating the solvent to form a composite film. Dispersing components in a solvent, mixing, and evaporating are often supported by mechanical agitation (e.g. ultrasonication, magnetic stirring and shear mixing).

(2) Melt processing of bulk composites: This method concerns polymers that are insoluble in any solvent, like thermoplastic polymers. It involves melting polymers to form viscous liquids to which CNTs can be added and mixed.

(3) Melt processing of composite fibers: CNTs are added to the polymer melts. Formation of CNT/polymer fibers from their melts occurs through, for example, the melt-spinning process.

(4) Composites based on thermosets: A thermoset polymer does not melt when heated, such as epoxy resins. The composite is formed from a monomer

(usually liquid) and CNTs, and the mixture is cured with cross-linking/catalyzing agents.

(5) Layer-by-layer (LBL) assembly: CNTs and polyelectrolytes are used to form a highly homogeneous composite, with good dispersion, good interpenetration, and a high concentration of CNTs. This method involves alternating monolayer adsorptions of the components, which are attracted to each other by electrostatic interactions, resulting in a uniform growth of the films.

(6) In-situ polymerization: The polymer macromolecules are grafted directly onto the walls of carbon nanotubes. This technique is often used for insoluble and thermally unstable polymers, which cannot be processed by melt. Polymerization occurs directly on the surface of CNTs. In general, these different techniques give various results in terms of nanotube dispersion efficiency, interfacial interaction between components, properties of the composites, and possible promising applications.

2.9.3 Properties, Manufacturing, and Application [23, 24]

These nanocomposite based polymers have been used widely for various products from automotive parts and electronics to commodities, due to the wealth of polymers suitable for each specific application. Nanotube based, particularly CNT based, polymer composites have a very rich application in the technological field, due to their strength, stiffness and heat resistance. These properties depend upon the aspect ratios of fillers and the adhesive strength between the filler and polymer matrix. Outstanding thermal and electrical conductivity make the carbon nanotubes promising filling material for fabricating new advanced composite systems for a broad range of technological applications. Efficient chemical functionalization of CNTs, homogeneous dispersions in solvents and supporting media, as well as good interconnectivity with the matrix, remain very important issues that must be considered in order to achieve heterostructures with enhanced or even new properties. There are numerous methods and approaches for the functionalization and more efficient dispersion of carbon nanotubes in different media.

Most researchers have incorporated nanotubes into thermoplastic polymers, due to their ease in processing. This allows fibers or films to be made and other objects easily melt processed into molded parts. Research has been performed using

both amorphous and semicrystalline polymers, with varying degrees of success. Nanotubes have been shown to toughen and stiffen amorphous brittle materials, like polymethyl methacrylate (PMMA), as well as semicrystalline polymers such as polypropylene (PP). In addition to the effects of toughening and stiffening, morphological changes are the subject of discussion for semicrystalline polymers such as PP. Research literature has suggested that nanotubes act as nucleating agents in these materials, leading to new crystallographic morphologies and ultimately increased strength. Although most polymer/nanotube composite research has utilized thermoplastic matrices, research has been conducted also with thermosetting materials. The change in viscosity as a function of cross-linking can be problematic in optimizing dispersion and orientation. Research has been carried out to study mechanical and thermal thermosetting polymer/nanotube composites and their properties with varying results. Of the various thermosetting polymers that have been reported in the literature, epoxies were used most commonly.

2.10 Literature Review

In recent years, fine scale piezoelectric fibers have received extensive attention because of their potential applications as building blocks in various nanotechnologies, which include mechanics, photonics, electronics, and sensing. The high surface-to-volume ratio is an attractive characteristic that can be achieved from nanofibers, and more attention has been paid to this area. With miniaturization of electronic devices, nanofibers of piezoelectric material are currently attracting a great deal of interest in the design of smart materials, due to their novel properties that are significantly different from their bulk, such as physical and chemical properties.

In 2003, Qiu et al. [25] studied the fabrication of piezoelectric ceramic fibers by the extrusion of $\text{Pb}(\text{Zr},\text{Ti})\text{O}_3$ powder and $\text{Pb}(\text{Zr},\text{Ti})\text{O}_3$ sol mixture. Green fibers with diameters of 300 μm and lengths of over 10 m were extruded successfully with the sol and powder mixture (powder:sol= 5–8:1). The extruded fibers, sintered at 1,200°C, had microstructures consisting of 2–6 μm grains, and no pores or cracks. Figure 2.25 shows the displacement behavior of 1–3 composite with fibers sintered at 1,200°C. The curve is atypical butterfly-like hysteretic loop of piezoelectric materials. The maximum strain of about 0.17% is at the same level as that of bulk materials

with the same composition, in which the maximum strain is about 0.18% in the strain versus electric field hysteretic curve. The above results provided evidence that these fibers, fabricated from a mixture of sol and powder, have the desired piezoelectric properties.

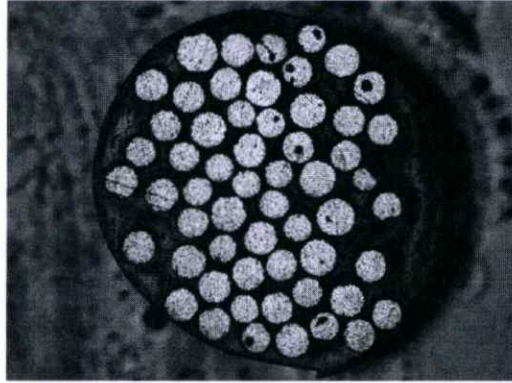


Figure 2.24 A photograph of the piezoelectric fiber composite. [25]

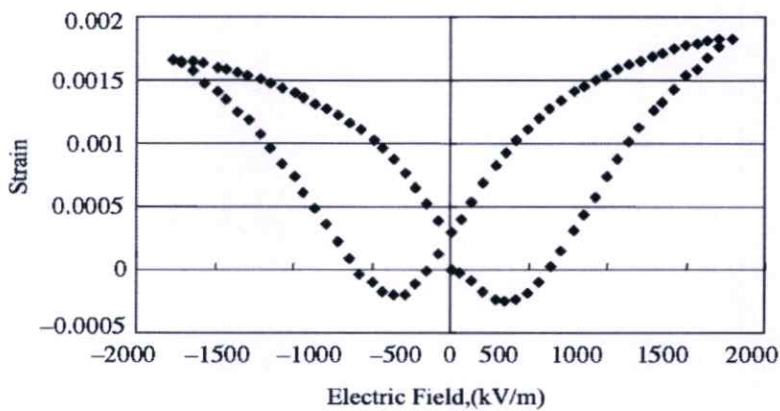


Figure 2.25 Displacement behavior of the 1-3 composite with polymer and PZT fibers fired at 1,200 °C. [25]

In 2003, Dan Li and Younan Xia [26] reported a procedure based on electrospinning for generating nanofibers of anatase with controllable diameters and porous structures. When an ethanol solution containing both poly(vinyl pyrrolidone) (PVP) and titanium tetraisopropoxide was injected through a needle under a strong electrical field, composite nanofibers made of PVP and amorphous TiO_2 were formed. These nanofibers could be converted subsequently into anatase without

changing their morphology via calcination in air at 500°C. The average diameter of these ceramic nanofibers could be controlled in a range from 20 to 200 nm by varying a number of parameters such as the ratio between PVP and titanium tetraisopropoxide, their concentrations in alcohol solution, the strength of the electric field, and the feeding rate of the precursor solution.

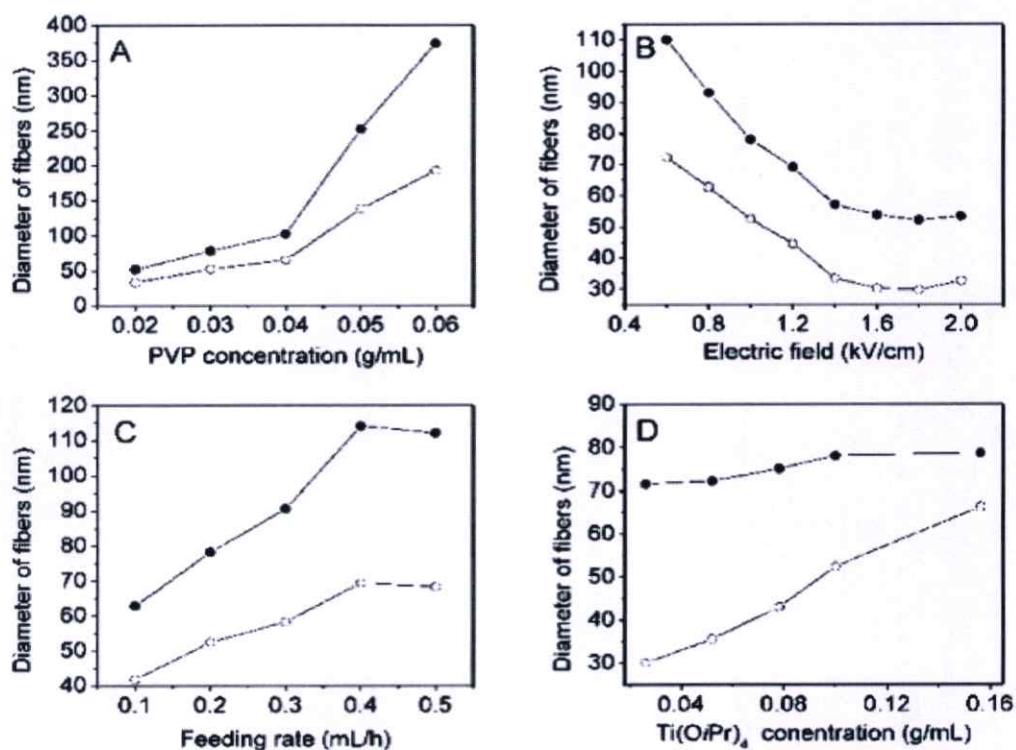


Figure 2.26 The dependence of nanofiber diameter on various processing parameters: (A) concentration of PVP; (B) electric field strength; (C) feeding rate of the ethanol solution; and (D) concentration of $\text{Ti}(\text{O}i\text{Pr})_4$. The solid and open dots represent measurements taken from nanofibers before and after they had been calcined (in air at 500°C for 3 h), respectively. [26]

As shown in Figure 2.26, the nanofibers increased in diameter as the PVP concentration was increased. The strength (E) of the electric field was another key factor that determined the morphology and diameter of the electrospun fibers. If the electric field was lower than 0.6 kV/cm, no stable liquid jets were observed. When E was increased, thinner nanofibers were obtained as the final product. At 1.6 kV/cm, anatase nanofibers as thin as 30 ± 7 nm were generated. However, when E was greater

than 1.6 kV/cm, the spinning jets became unstable, and the average diameter was found to increase slightly with increasing E . The feeding rate of the PVP solution also influenced the diameter of the fibers. Faster feeding rates often resulted in thicker fibers, but the jets became unstable if the feeding rate exceeded 0.5 mL/h. The concentration of $\text{Ti}(\text{O}i\text{Pr})_4$ in the precursor solution had minor impact on the diameter of TiO_2/PVP composite fibers, but played a significant role in determining the size of calcined anatase nanofibers. In general, the use of $\text{Ti}(\text{O}i\text{Pr})_4$ at lower concentrations led to the formation of thinner ceramic nanofibers.

In 2006, Li et al. [27] reported a simple and versatile technique for producing ceramic nanofibers and nanotubes. In addition to the ease and simplicity associated with the polymer-assisted spinning process for producing ceramic nanofibers, it is also feasible to control the diameter of resulting fibers. As shown in Figure 2.27, the diameter of TiO_2 nanofibers could be varied from tens of nanometers to several micrometers with relatively narrow size distributions by simply altering the concentration of PVP and/or the ratio of alkoxide precursor to PVP. By adjusting the composition of precursor solution as well as spinning parameters, researchers have demonstrated that TiO_2 nanofibers thinner than 20 nm could be prepared routinely.

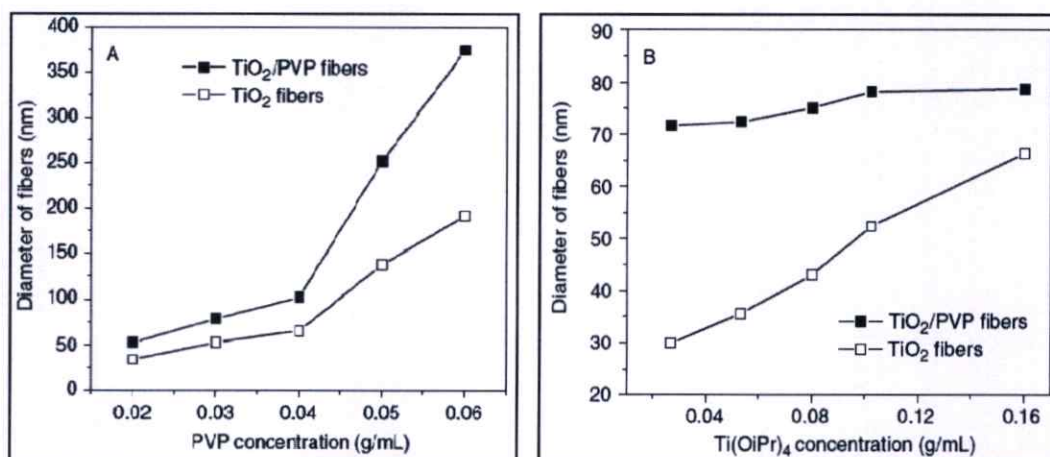


Figure 2.27 Plots demonstrating the ability to control the diameter of electrospun nanofibers by simply adjusting the composition of spinning solutions. [27]

In 2009, Liao et al. [28] reported the fabrication of $\text{Bi}_{3.15}\text{Nd}_{0.85}\text{Ti}_3\text{O}_{12}$ (BNT) nanofibers by the sol-gel process and electrospinning. BNT nanofibers exhibit an

effective piezoelectric coefficient of 89 pm/V (Figure 2.28) and a Curie temperature of 500°C, which are higher than those of the BNT bulk.

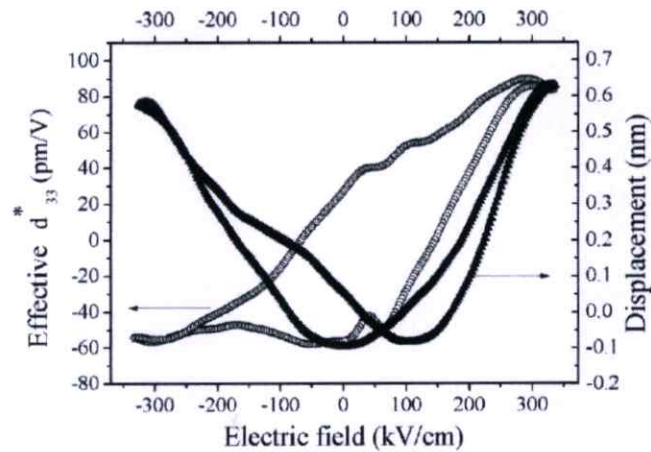


Figure 2.28 Local piezoelectric response as a function of the electric field applied for a single BNT nanofiber. [28]

Antiferroelectric materials have attracted much research interest, due to their potential applications in microactuators and energy conversion devices. Lead zirconate (PbZrO_3 ; PZ) is a well known antiferroelectric material that can be processed into various forms such as bulk ceramics, thin films, and fibers. The hysteresis characteristics of antiferroelectric PbZrO_3 regions are well suited for either power-storage or actuator applications. Furthermore, the extremely large charge released from the FE to AFE state may be useful as alternate capacitor material in DRAMs.

In 1998, Kim et al. [29] reported the characteristics of antiferroelectric PbZrO_3 thin films by using reactive magnetron co-sputtering, followed by rapid thermal annealing. From observations by scanning electron microscopy, the grains were found to have a columnar structure, and the average grain size was $0.3 \pm 0.5 \mu\text{m}$. An electric-field-forced transformation from the antiferroelectric to ferroelectric phase was observed at room temperature and it had a maximum polarization value of $41 \mu\text{C}/\text{cm}^2$. The average field for exciting the ferroelectric state and that for reversing to the antiferroelectric state, as measured by charge versus voltage curves, was 357

kV/cm and 207 kV/cm, respectively. The dielectric constant was 196, with an associated dissipation factor of 0.043 at 100 kHz, as shown in Figure 2.29.

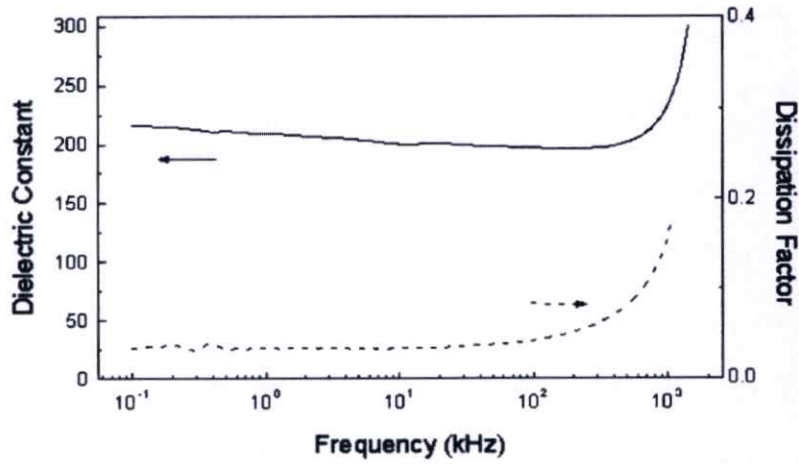


Figure 2.29 The frequency-dependent dielectric constant and dissipation factor of a PbZrO_3 film with a thickness of 300 nm. [29]

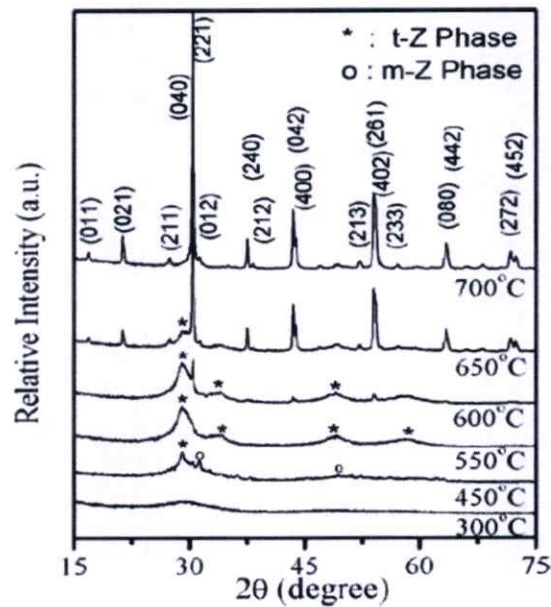


Figure 2.30 X-ray diffraction (XRD) pattern of PZ gel powder calcined at 300, 450, 550, 600, 650 and 700 °C, consecutively, for 1 h. [30]

In 2009, Singh et al. [30] fabricated an orthorhombic structure of PZ nanoparticles by a novel sol-gel method based on diol-based solution. Initially, PZ was crystallized with intermediate m-Z and t-Z phases in a temperature range from 400-550°C and started transforming to an orthorhombic structure at around 600°C, before finally transforming into a pure orthorhombic PZ phase at about 700°C (Figure 2.30).

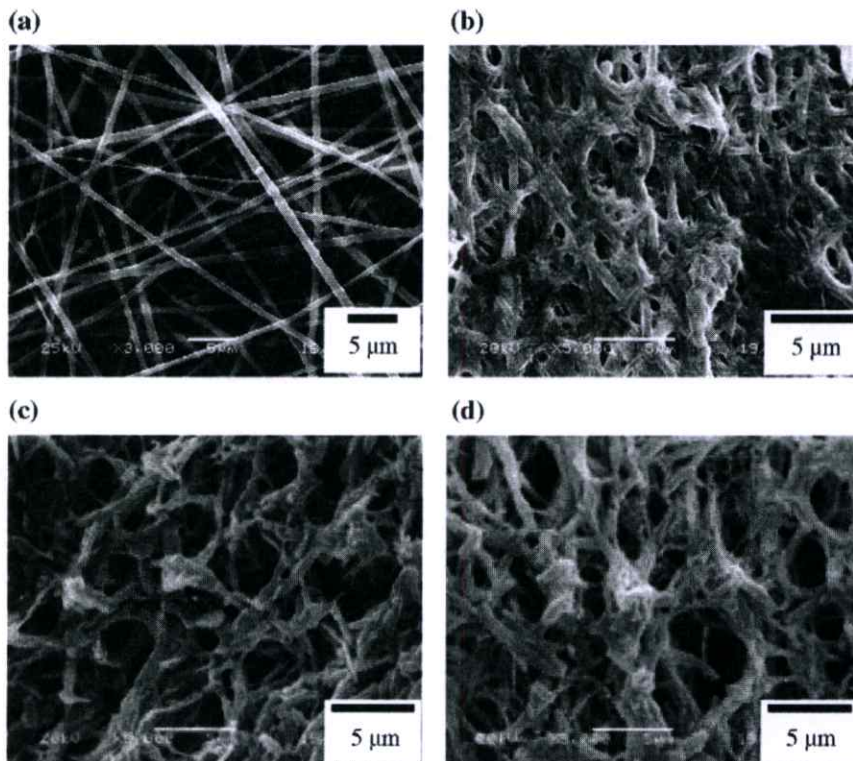


Figure 2.31 Scanning electron microscope (SEM) images of PZT nanofibres: (a) as-prepared composite fibres, (b) fibres calcinated at 550°C, (c) fibres calcinated at 650°C, and (d) fibres calcinated at 700°C. [31]

In 2005, Dharmaraj et al. [31] reported the preparation of ferroelectric $\text{Pb}(\text{Zr}_{0.5}\text{Ti}_{0.5})\text{O}_3$ nanofibres by electrospinning. $\text{Pb}(\text{Zr}_{0.5}\text{Ti}_{0.5})\text{O}_3$ (PZT) nanofibres with diameters ranging from 200–300 nm have been synthesized by calcination of the electrospun PZT/polyvinyl acetate composite fibres. Formation of the perovskite PZT phase was observed at temperatures as low as 550°C. Sol-gel processing resulted in low perovskite crystallization temperature (550°C), as compared to other conventional synthesis methods. However, when reducing the fiber diameter to nanoscale by the

electrospinning method, fiber fusion and continuous fibers could not be formed after annealing at high temperature, as shown in Figure 2.31, which presents fiber mats with a soldering-like attachment of nanofibers at their junction after calcinations at 550°C.

In 2008, Xie et al. [32] reported a strategy to hybrid multiferroicity at nanoscale. Multiferoic $\text{CoFe}_2\text{O}_4\text{-Pb}(\text{Zr}_{0.52}\text{Ti}_{0.48})\text{O}_3$ nanofibers are synthesized by the sol-gel process and electrospinning. Butterfly loops that are typical for ferroelectric materials were observed in the composite nanofibers; and the field induced displacement, as well as symmetry of the butterfly loops, increased with the increased composition of PZT. The effective piezoelectric coefficient, d_{33}^* , is estimated to be about 125, 140, and 157 pm/V for composite nanofibers with $\text{CoFe}_2\text{O}_4\text{-Pb}(\text{Zr}_{0.52}\text{Ti}_{0.48})\text{O}_3$ molar ratios of 1.25:1, 1:1, and 0.75:1, respectively, which is larger than that of pure PZT thin film (93 pm/V). The remnant magnetization is several times higher than CFO film and the corresponding coercivity is much lower than that of the CFO nanowire. Thus, multiferoicity in the one-dimensional composite nanofibers is confirmed with excellent ferroelectricity and ferromagnetism.

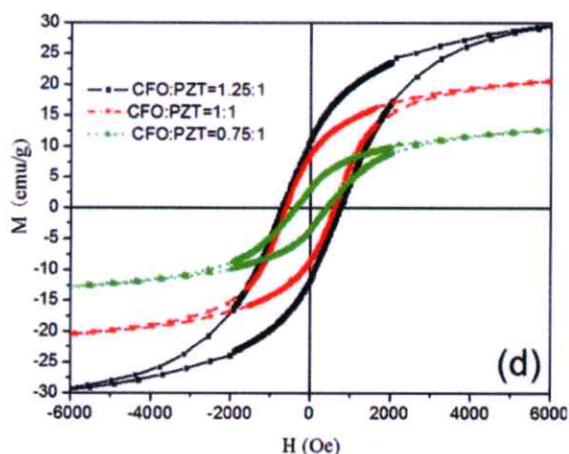


Figure 2.32 Magnetic hysteresis loops for the CFO-PZT composite nanofibers. [32]

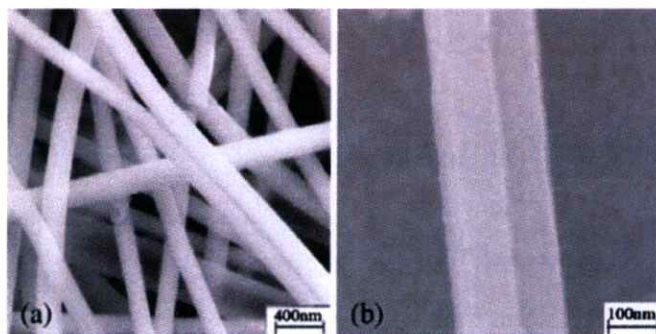


Figure 2.33 SEM images of composite CFO-PZT nanofibers with a 1:1 molar ratio. (a) CFO-PZT-PVP nanofibers before calcination and (b) selected fine CFO-PZT nanofibers calcined at 550°C. [32]

In 2008, Xie et al [33] reported a strategy for hybrid multiferroicity at nanoscale. Multiferroic $\text{NiFe}_2\text{O}_4\text{-Pb}(\text{Zr}_{0.52}\text{Ti}_{0.48})\text{O}_3$ composite nanofibers were synthesized by a sol-gel process and electrospinning, with fiber diameters ranging from 100 to 400 nm. The remnant magnetization for the nanofibers and nanoparticles is 13.80 and 11.62 emu/g, respectively, while the corresponding coercive fields are 197 and 134 Oe, respectively (Figure 2.34). Thus, multiferroicity is confirmed with good ferroelectricity and ferromagnetism in one-dimensional nanofibers rather than nanoparticles.

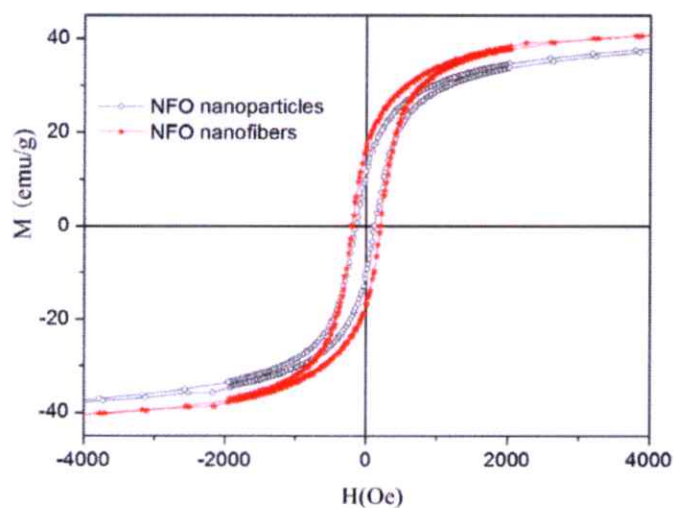


Figure 2.34 Magnetic hysteresis loops for NiFe_2O_4 nanoparticles and nanofibers. [33]

In addition, many researchers also focus on lead-free ferroelectric material. Barium titanate (BaTiO_3 ; BT), with perovskite structure, is a common ferroelectric

material with a high dielectric constant and low characteristic loss. This material is very attractive in the field of electroceramics and microelectronics, due to its good characteristics. It is utilized widely to manufacture electronic components such as multilayer capacitors (MLCs), positive temperature coefficient (PTC) thermistors, piezoelectric transducers, and a variety of electro-optic devices. Based on its excellent dielectric and ferroelectric properties, there is an enormous amount of literature on the preparation of this material.

In 2005, Yuh et al. [34] reported stand-alone electrospun complex oxide ferroelectric nanofiber for the first time. Barium titanate nanofibers, with a perovskite structure, were synthesized by electrospinning utilizing sol-gel precursors. Based on the conventional sol-gel process, barium acetate and titanium isopropoxide were used as starting materials. After dissolution of all compounds, the precursor solution was mixed with a solution consisting of poly(vinyl pyrrolidone) [PVP] dissolved in ethanol. Polycrystalline barium titanate fibers were obtained after annealing at 750°C for 1 h. The typical diameter of fiber was between 80 and 190 nm, with fiber lengths exceeding 0.1 mm. It is demonstrated herein that the electrospinning technique offers a simple and versatile method for synthesizing long nanofibers of complex ferroelectric ceramics.

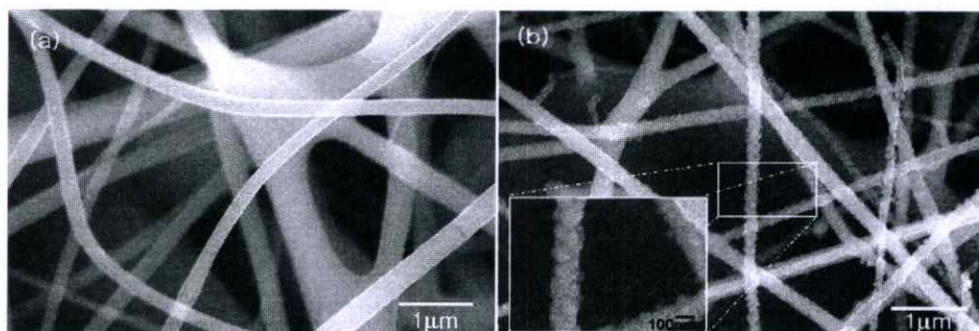


Figure 2.35 (a) SEM image of as-synthesized barium titanium and PVP composite nanofibers (b) SEM image of BaTiO₃ nanofibers annealed at 750°C for 1 h. The inset shows the morphology of polycrystalline fiber. [34]

In 2009, Li et al. [35] reported the fabrication of BaTiO₃ nanofibers by electrospinning. BaTiO₃ nanofibers with diameters ranging from 92 to 182 nm have been prepared successfully. Besides, the diameter of fibers was decreased when the

annealing temperature increased from 500°C to 600°C, but at an elevated temperature of higher than 600°C, the fibers became thicker and also exhibited a rougher surface feature. The electrospun BaTiO₃ nanofibers have much higher T_c (220°C) than bulk BaTiO₃ ceramics, which are induced by smaller internal stresses that result from smaller grain size.

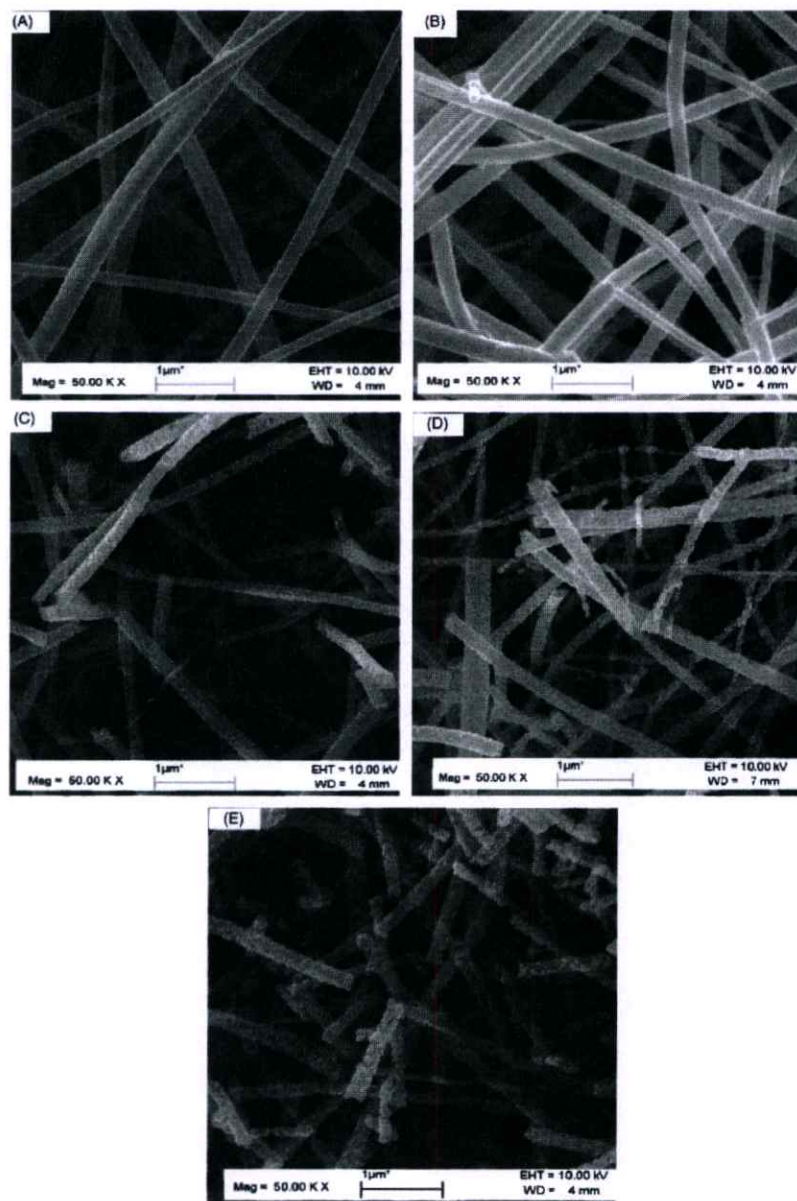


Figure 2.36 SEM images of BaTiO₃ nanofibers under different conditions: (A) heat treated at 550°C for 10 h, (B) 570°C for 10 h, (C) 600°C for 10 h, (D) 700°C for 10 h, and (E) 800°C for 10 h. [35]

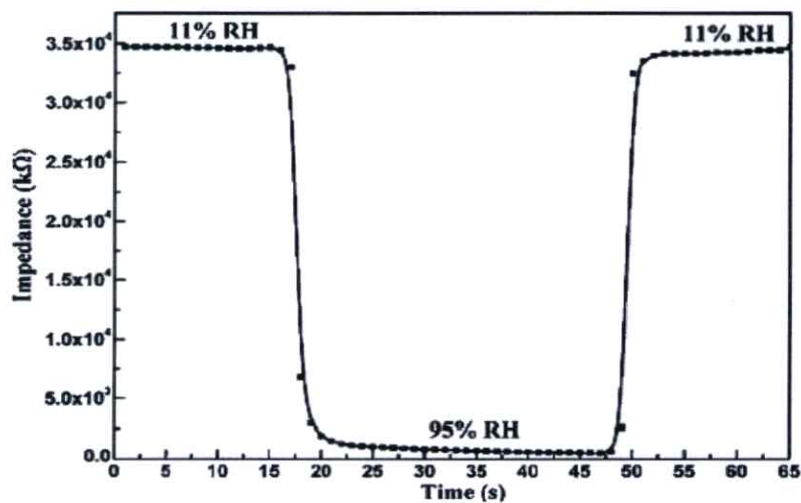


Figure 2.37 Response and recovery properties. The test condition was AC 1V, 100 Hz. The response and recovery time was less than 5 and 4 s, respectively. [36]

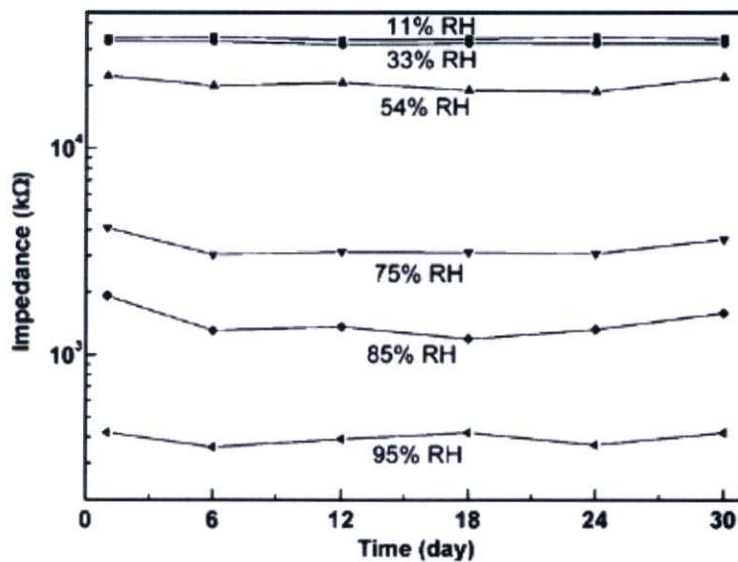


Figure 2.38 Long-term stable property. The test condition was AC 1V, 100 Hz. The sensor was exposed in air for 30 days, with measurements repeated weekly. [36]

In 2010, He et al. [36] reported the fabrication of barium titanate (BaTiO_3) nanofiber. In their research, barium titanate nanofiber was synthesized via electrospinning, which offered a simple but versatile method for synthesizing long ceramic nanofiber. After annealing at 800°C for 2 h, nanofiber with a perovskite

structure was obtained. Its average diameter was 80–200 nm, and its length over 0.1 mm. An impedance-type humidity sensor was then fabricated based on this BaTiO₃ nanofiber. It was surprising to find that such a sensor exhibited a fast response and recovery, which were 5 and 4 s between 11% and 95% relative humidity, respectively (Figure 2.37). The long stability and humidity of the hysteresis properties of this sensor also were tested, and found to be the optimum (Figure 2.38). These excellent sensing characteristics prove that BaTiO₃ nanofiber is applicable for high-performance humidity sensors.

In the last few decades, piezoelectric ceramic-polymer composites have been studied intensively because of their considerable potential for applications such as pyroelectric sensors, ultrasonic transducers, and hydrophones. Piezoelectric ceramics have been used extensively, due to their large dielectric constant, high piezoelectric strain and high electromechanical coupling coefficient. However, high leakage of current, low dielectric strength and mechanical stiffness limit their applications. On the other hand, polymeric materials exhibit very high dielectric strength and low leakage of current, but their polymers generally show small dielectric constants. Polymer based composite is considered as a solution to the problem by providing good opportunity for the development of a high dielectric constant, low leakage and high breakdown strength of the materials.

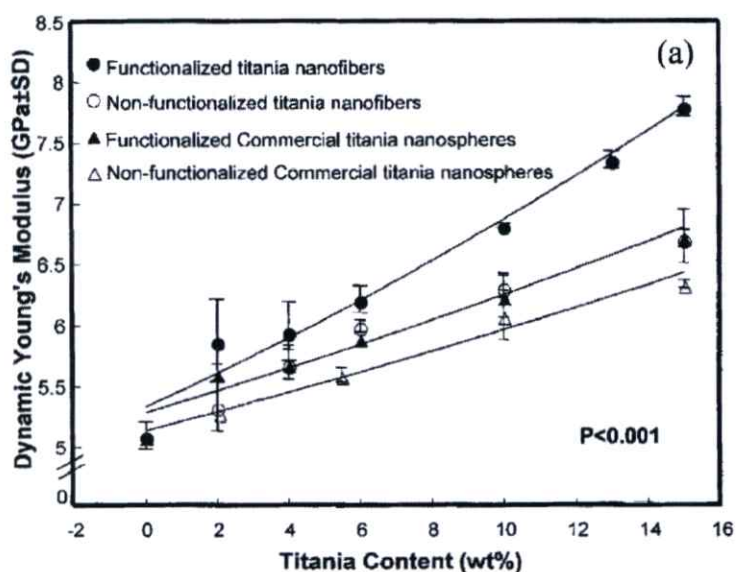


Figure 2.39 Mechanical properties of (a) dynamic Young's modulus versus weight percentage of the TiO₂ nanofillers. [37]

In 2007, Khaled et al [37] studied the synthesis of TiO_2 -PMMA nanocomposite. In their study, TiO_2 fiber-PMMA nanocomposites, with chemical bonding between the filler and polymer matrix, were synthesized for the first time using the coupling agent, methacrylic acid. The composites, with functionalized titania nanofibers, exhibited significantly higher elastic moduli than those with nonfunctionalized fibers at $p < 0.001$ (Figure 2.39). In addition, the nanofiber structure provided higher elastic properties in the PMMA matrix than those prepared using a commercial nanospherical structure.

In 2011, Chen et al [38] presented a self-powered Nanoscale Active Fiber Composite (NAFC) based Acoustic Emission (AE) sensor with high sensitivity. The aligned PZT nanofiber, with a diameter and length of approximately 80 nm and 500 μm respectively, was electrospun on a silicon substrate. Interdigitated electrodes were deposited on the PZT nanofibers and packaged by spinning a thin soft polymer layer on the top of the sensor (Figure 2.40). The polymer also serves as an acoustic couplant. The tiny sensor was imbedded in an epoxy structure and the voltage output transmitted acoustically to the sensor from distant periodic impacts measured over 30 mVolts, as shown in Figure 2.41. Figure 2.42 shows the hysteresis loop of PZT NFACs, and these hysteresis loops display the typical shape of a ferroelectric. However, it is difficult to determine the coercive field and remnant polarization.

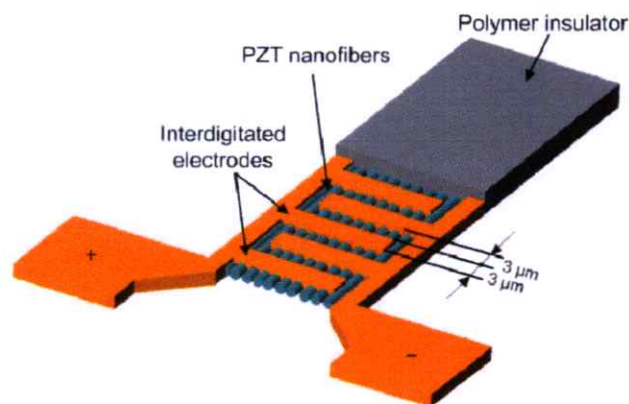


Figure 2.40 Schematic view of the PZT NAFCAE sensor. [38]

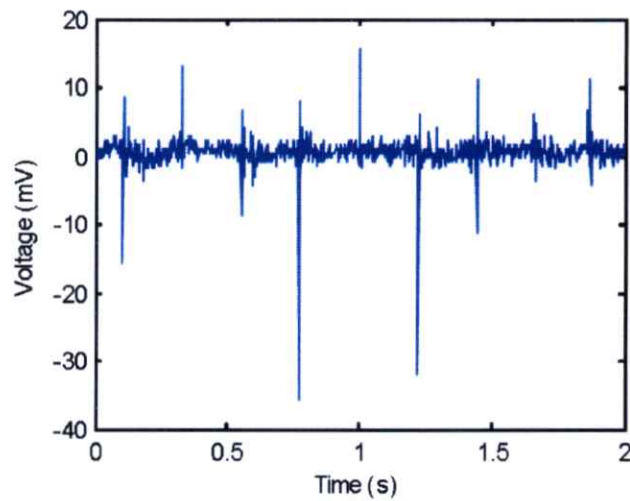


Figure 2.41 Output signal from the sensor cell of acoustic surface energy. [38]

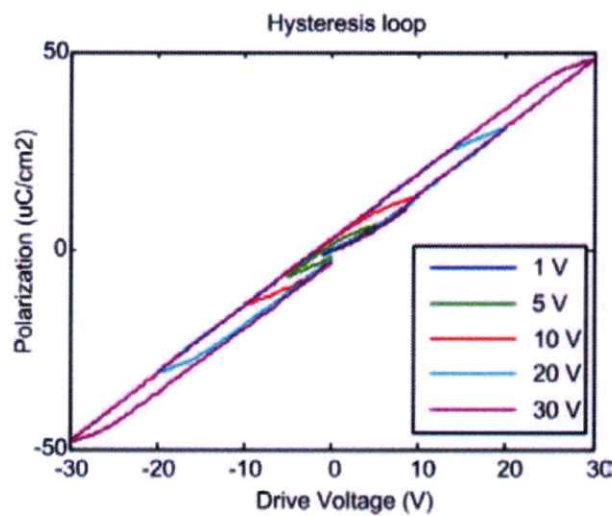


Figure 2.42 Hysteresis loop of PZT NFACs. [38]

In 2010, Chen et al [39] demonstrated a new piezoelectric nanogenerator based on PZT nanofibers, which had a diameter and length of approximately 60 nm and 500 μm , respectively, and were aligned on interdigitated electrodes of platinum fine wires and packaged using a soft polymer on a silicon substrate. The flexible PZT nanofibers were embedded in a soft polydimethylsiloxane (PDMS) polymer matrix, which helped prevent damage to the PZT nanofibers, thereby extending the life cycle of the nanogenerator. The simple fabrication and assembly process allows facile mass production of this type of nanogenerator.

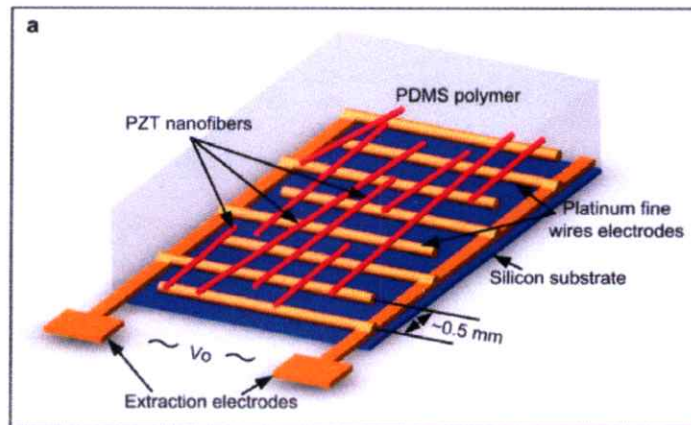


Figure 2.43 Schematic view of the PZT nanofiber generator. [39]

This nanogenerator presents several advantages over others recently reported. The measured voltage output and power under periodic stress applied to the soft polymer was 1.63 V and 0.03 μW , respectively. The piezoelectric voltage constant and dielectric constant of PZT nanofibers were much higher than those of the semiconductor type of piezoelectric nanowires and nanofibers, making this material ideal for nanogenerator or nanobattery applications.

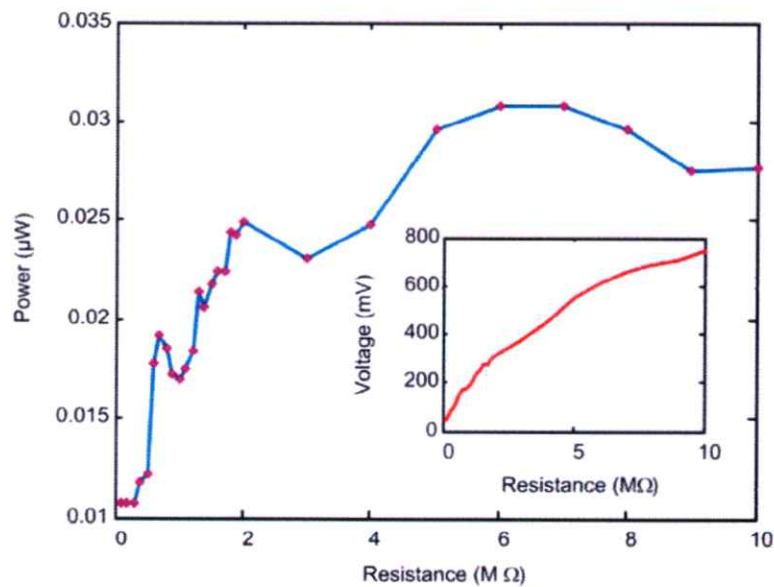


Figure 2.44 Power delivered to the load resistors versus load resistance. Inset in (d) shows voltage output versus load resistance. [39]

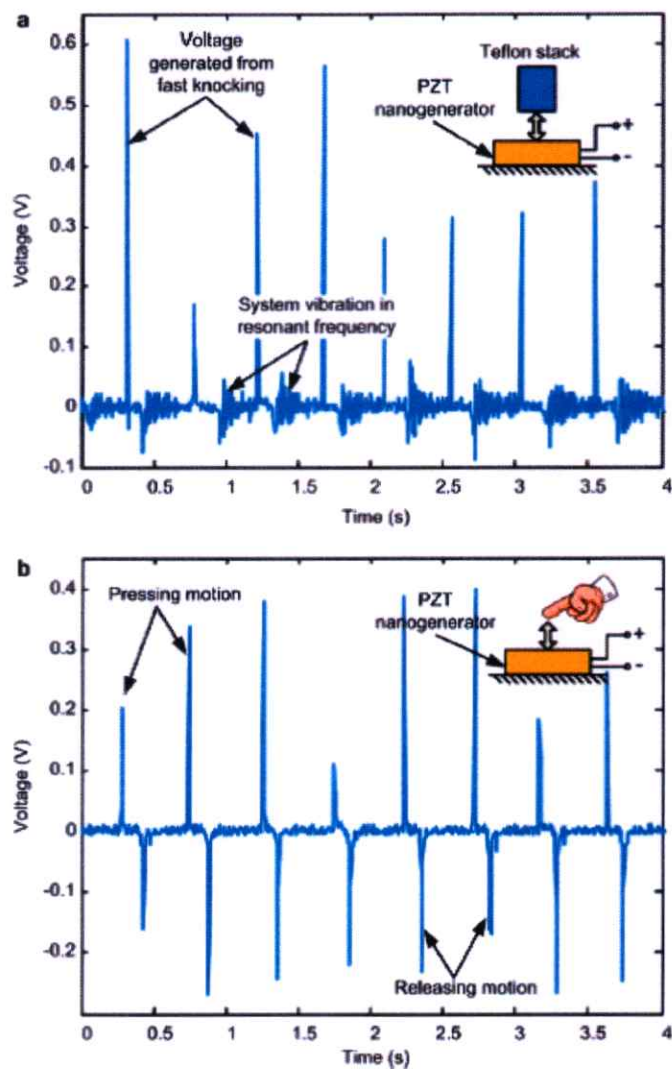


Figure 2.45 Measurements of voltage output from a PZT nanofiber generator. (a) Voltage output measured when a small Teflon stack was used to impart an impulsive load on top of the PZT nanofiber generator. Inset in (a) shows a schematic of the Teflon stack tapping on the nanogenerator. (b) Voltage output measured by using a finger to apply a dynamic load on top of the generator. Inset in (b) shows a schematic of a finger applying the dynamic load. [39]

In 2010, Chang et al [40] reported the piezoelectric polymeric nanogenerator with high energy conversion efficiency. In their work, near-field electrospinning was used to direct-write poly(vinylidene fluoride) (PVDF) nanofibers with in situ mechanical stretch and electrical poling characteristics to produce piezoelectric

properties. Under mechanical stretching, nanogenerators have shown repeatable and consistent electrical outputs with energy conversion efficiency, and an order of magnitude higher than that made of PVDF thin films. Typical electrical outputs of more than 50 tested nanogenerators were 5-30 mV and 0.5-3 nA (Figure 2.46). Early onset of nonlinear domain wall motion behavior has been identified as a mechanism responsible for the apparently high piezoelectricity in nanofibers, rendering them potentially advantageous for sensing and actuation applications.

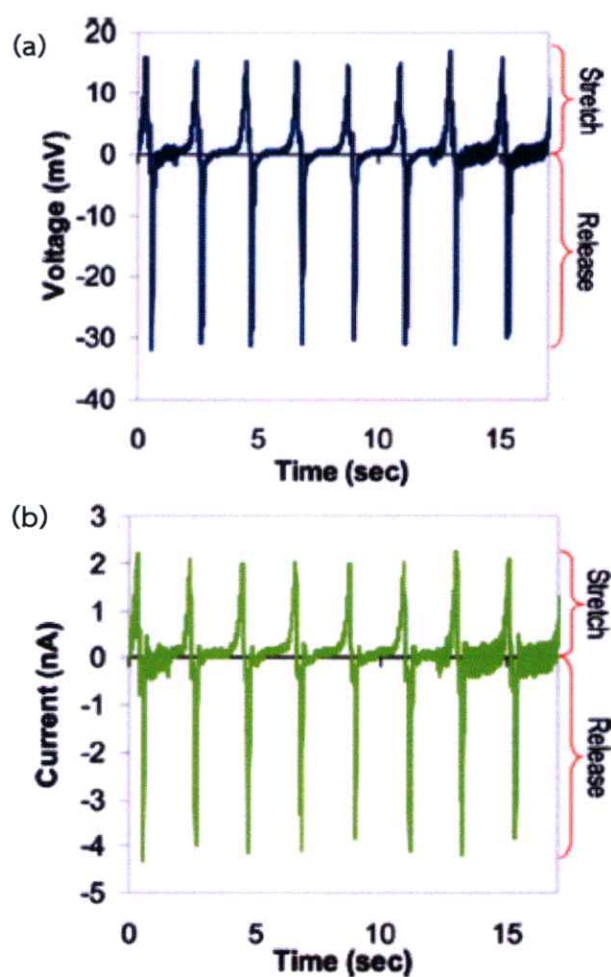


Figure 2.46 Piezoelectric PVDF nanogenerator. (a) Output voltage measured with respect to time under an applied strain at 2 Hz. (b) Current output measured with respect to time under applied strain at 2 Hz. [40]

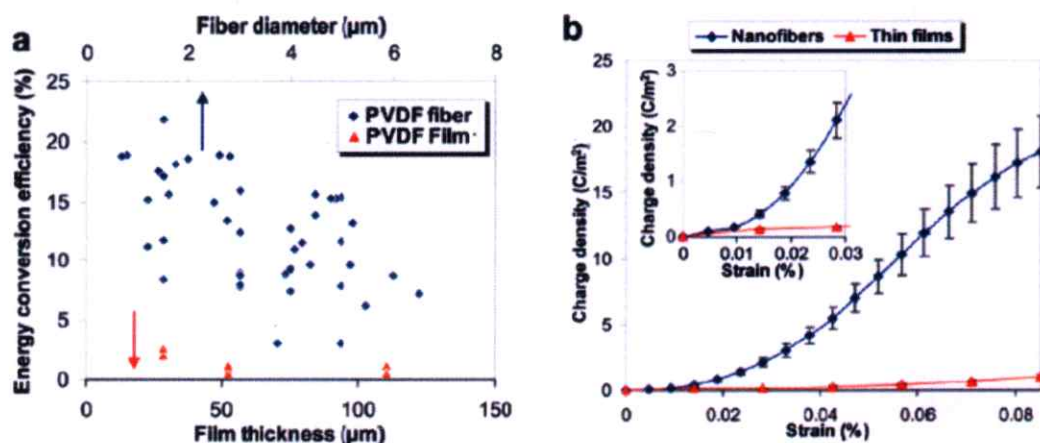


Figure 2.47 Energy conversion efficiency of a piezoelectric PVDF nanogenerator. (a) Plots of measured energy conversion efficiency of PVDF nanogenerators and thin films with different feature sizes. (b) Experimental results of PVDF thin film and nanofiber charge density (generated charges divided by electrode area) with respect to an applied strain. The charge density of PVDF nanofiber increases nonlinearly when the applied strain is greater than 0.01%. The inset shows details under small strains. [40]

In 2010, Dang et al [41] reported a three-phase [nanosized BaTiO_3 (NBT)-multiwall carbon nanotube (MWNT)/polyvinylidene fluoride (PVDF) nanocomposite], with a significantly enhanced dielectric constant (643 at 103 Hz) and gradually decreased loss, which was extremely hard to realize at the same time for composites filled only by conductive MWNT filler. Adjustable dielectric properties were discovered by employing the three-phase system, due to change of the nanocomposite microstructure. The CNT was chosen as an excellent candidate for acquiring high dielectric constant polymer matrix composites, according to the percolation theory. However, its nanometer-scale dimension causes it to form bundles naturally, which makes it difficult to use. Compared with chemical modification of the MWNT, the incorporation of a third component, NBT particles, into MWNT/polymer composites realizes the uniform dispersion of the MWNT, without sacrificing its inherent properties.

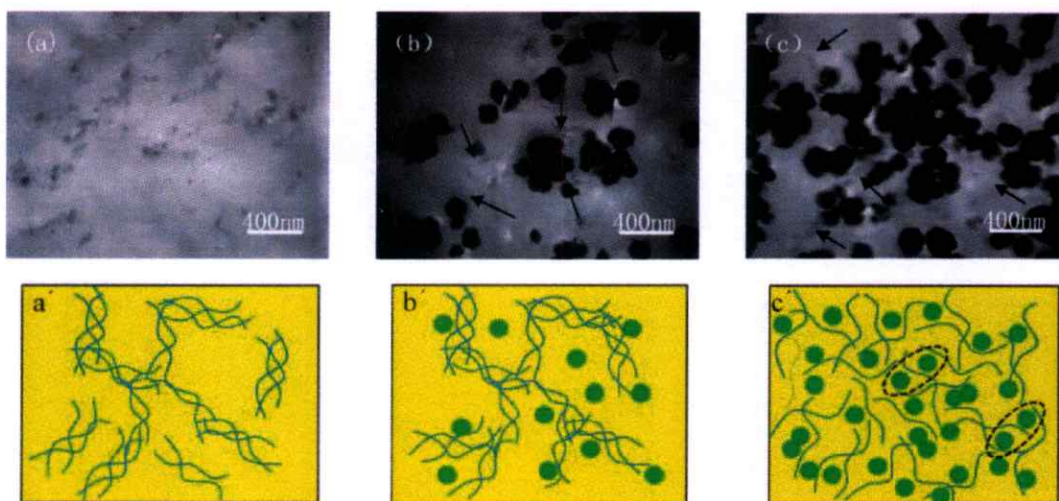


Figure 2.48 Transmission electron microscope (TEM) images of the freeze-fractured (NBT-MWNT)/PVDF composites with matrix at (a) $f_{\text{NBT}} = 0$, (b) $f_{\text{NBT}} = 0.05$, and (c) $f_{\text{NBT}} = 0.20$, and schematic illustration of the microstructure of (NBT-MWNT)/PVDF composites, in which the gray lines stand for the MWNTs and the green balls NBTs. [41]

In 2012, Park et al [42] fabricated the nanocomposite generator (NCG) device, based on piezoelectric BaTiO_3 nanopowders (NPs) and universal graphitic carbons. The BaTiO_3 NPs are mixed with one of the carbon nanomaterials (SW/MW-CNTs or RGO) to prepare the polymer-nanocomposite (p-NC). The NCG device is obtained by the spin-casting/bar-coating method and converts mechanical deformation and even tiny biomechanical movements into electric energy, which measures the outputs generated by the NCG device during the periodic bending and unbending motion of the bending stage. The results are shown in Figure 2.49. When a measuring instrument is forward connected to the device, the NCG device generates a positive voltage and current upon the bending states. The alternating energy generated from an NCG device is stored in capacitors and used subsequently to turn on a commercial LED device. This result innovatively expands the feasibility of self-powered energy systems for application in consumer electronics, sensor networks, and energy harvesting in indoor environments.

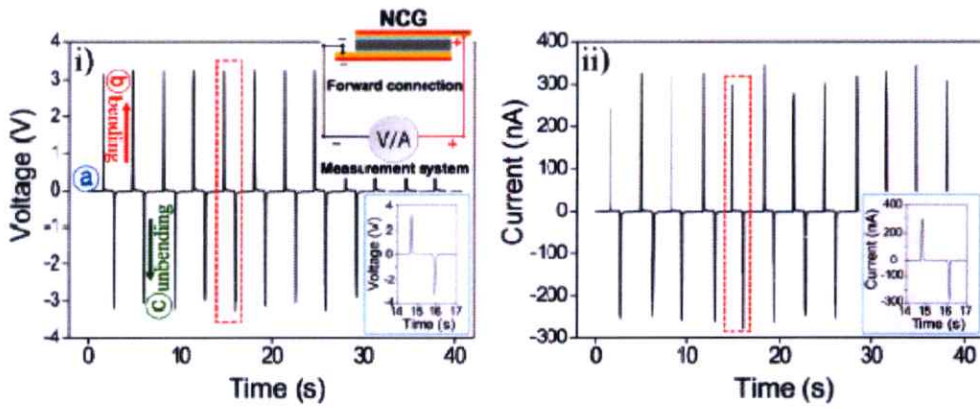


Figure 2.49 The measured voltage output and current signals of the NCG device in forward connection during periodic bending and unbending motions. [42]

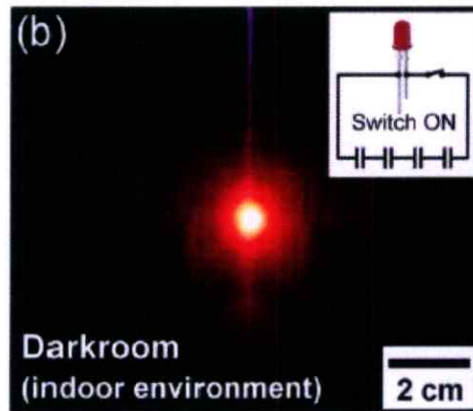


Figure 2.50 A captured photograph showing an LED lit by electric energy generated from a NCG device. [42]

REFERENCE

- [1] Uchino, K., and Ito, Y. 2009. "Smart Ceramics: Transducers, Sensors, and Actuators." in Schwartz, M., (editors). **Smart Materials**. Taylor & Francis Group, LLC.
- [2] Vijatovic, M. M., Bobic, J. D., and Stojanovic, B. D. 2008. "History and Challenges of Barium Titanate: Part I." **Sci. Sinter**. 40 : 155-165.
- [3] Haertling, G. H. 1999. "Ferroelectric Ceramics: History and Technology." **J. Am. Ceram. Soc.** 82[4] : 797-818.
- [4] Vijatovic, M. M., Bobic, J. D., and Stojanovic, B. D. 2008. "History and Challenges of Barium Titanate: Part II." **Sci. Sinter**. 40 : 235-244.
- [5] Yoon, D. H. 2006. "Tetragonality of Barium Titanate Powder for a Ceramic Capacitor Application." **J. Ceram. Process. Res.** 7[4] : 343-354.
- [6] Kim, I., Bae, S., Kim, K., Kim, H., Lee, J. S., Jeong, J., and Yamakawa, K. "Characteristics of Antiferroelectric PbZrO₃ Thin Films." **J. Korean Phys. Soc.** 33[2] : 180-183.
- [7] Movahedi, B. 2012. "A Solid State Approach to Synthesis Advanced Nanomaterials for Thermal Spray Applications." pp. 189-218. in Jazi, H. (editor). **Advanced Plasma Spray Applications**. In Tech. [Online]. Available : <http://www.intechopen.com/books/advanced-plasma-spray-applications/a-solid-state-approach-to-synthesis-advanced-nanomaterials-for-thermal-spray-applications>.pp. 189-218.
- [8] Ozaki, Y. 1983. "Ultrafine Electroceramic Powder Preparation from Metal Alkoxides." **Ferroelectrics**. 49 : 285-296.
- [9] Rahaman, M. N. 2003. "Synthesis of powders." *Ceramic Processing and Sintering: Second edition*. New York: Marcel Dekker, Inc.
- [10] Devaraju, M. K., and Honma, I. 2012. "Hydrothermal and Solvothermal Process Towards Development of LiMPO₄ (M = Fe, Mn) Nanomaterials for Lithium-Ion Batteries." **Adv. Energy. Mater.** 2 : 284-297.
- [11] Riedel, R., Ionescu, E., and Chen, I. W. 2008. "Modern Trends in Advanced Ceramics." pp. 15-18. in Riedel, R., and Chen, I. W. (editors). **Ceramics Science**

- and Technology Vol.1: Structures.** Weinheim: WILEY-VCH Verlag GmbH & Co. KGaA..
- [12] Ramaseshan, R., Sundarrajan S., and Jose, R. 2007. "Nanostructured Ceramics by Electrospinning." **J. Appl. Phys.** 102 : 111101.
- [13] Yu, D. G., Zhu, L. M., White, K., and Branford-White, C. 2009. "Electrospun Nanofiber-Based Drug Delivery Systems." **Health.** 1[2] : 67-75.
- [14] Sigmund, W., Yuh, J., Park, H., Maneeratana, V., Pyrgiotakis, G., Daga, A., Taylor, J., and Nino, J. C. 2006. "Processing and Structure Relationships in Electrospinning of Ceramic Fiber Systems." **J. Am. Ceram. Soc.** 89 [2] : 395-407.
- [15] Kumar, A., and Deka, M. 2010. "Nanofiber Reinforced Composite Polymer Electrolyte Membranes." pp. 13-38. in Kumar, A. (editor). **Nanofibres.** India: Intech..
- [16] Nawani, C. Rerkratn, A., Seeharaj, P., and Vittayakorn, N. 2013. "Characterization and Dielectric Properties of Nanocomposite Made of Lead Zirconate Nanofibers and Polyvinylidene Fluoride Improved with Carbon Nanotubes." **Integr. Ferroelectr.** 149 : 18-24.
- [17] Guggilla, P., and Batra, A. K. 2011. "Novel Electroceramic: Polymer Composites - Preparation, Properties and Applications." in Cuppoletti, J. (editor). **Nanocomposites and Polymers with Analytical Methods.** Intech.
[Online]. Available : <http://www.intechopen.com/books/nanocomposites-and-polymers-with-analytical-methods/Novel-electroceramic-polymer-composites-preparation-properties-and-applications>.
- [18] Safari, A. 1994. "Development of piezoelectric composites for transducers." **J. Phys. III Fiance.** 4 : 129-1149.
- [19] Tressler, J. F., Alkoy, S., and Newnham, R. E. 1998. "Piezoelectric Sensors and Sensor Materials." **J, Electroceram.** 2[4] : 257-272.
- [20] Sebastian, M. T. 2010. "Polymer-Ceramic Composites of 0-3 Connectivity for Circuits in Electronics: A Review." **Int. J. Appl. Ceram. Technol.** 7 [4] : 415-434.
- [21] Jose, J. P., Malhotra, S. K., Thomas, S., Joseph, K., Goda, K., and Sreekala, M. S. 2012. "Advances in Polymer Composites: Macro- and Microcomposites." in Thomas, S., Joseph, K., Malhotra, S. K., Goda, K., and Sreekala, M. S. (editors). **Polymer Composites: Volume 1, First Edition.** Wiley-VCH Verlag GmbH & Co. KGaA.

- [22] Zeng, X., Xu, X., Shenai, P. M., Kovalev, E., Baudot, C., Mathews, N., and Zhao, Y. 2011. "Characteristics of the Electrical Percolation in Carbon Nanotubes/Polymer Nanocomposites." **J. Phys. Chem. C.** 115 : 21685–21690.
- [23] Pradhan, N. R. 2010. "Thermal Conductivity of Nanowires, Nanotubes and Polymer-Nanotube Composites." Doctor of Philosophy, Worcester Polytechnic Institute.
- [24] Hussain, F., Hojjati, M., Okamoto, M., and Gorga, R. E. 2006. "Review article: Polymer-matrix Nanocomposites, Processing, Manufacturing, and Application: An Overview." **J. Composite Materials.** 40 [17] : 1511-1575.
- [25] Qiu, J., Tani, J., Kobayashi, Y., Um, T. Y., and Takahashi, H. 2003. "Fabrication of Piezoelectric Ceramic Fibers by Extrusion of $\text{Pb}(\text{Zr,Ti})\text{O}_3$ Powder and $\text{Pb}(\text{Zr,Ti})\text{O}_3$ Sol Mixture." **Smart Mater. Struct.** 12 : 331-337.
- [26] Li, D., and Xia, Y. 2003. "Fabrication of Titania Nanofibers by Electrospinning." **Nano Lett.** 3[4] : 555-560.
- [27] Li, D., McCann, J. T., and Xia, Y. 2006. "Electrospinning: A Simple and Versatile Technique for Producing Ceramic Nanofibers and Nanotubes." **J. Am. Ceram. Soc.** 89[6] : 1861-1869.
- [28] Liao, M., Zhong, X. L., Wang, J. B., Xie, S. H., and Zhou, Y. C. 2010. "Structure and Electrical Properties of $\text{Bi}_{3.15}\text{Nd}_{0.85}\text{Ti}_3\text{O}_{12}$ Nanofibers Synthesized by Electrospinning and Sol-Gel Method." **App. Phys. Lett.** 96 : 012904.
- [29] Kim, I., Bae, S., Kim, K., and Kim, H. 1998. "Characteristics of Antiferroelectric PbZrO_3 Thin Films". **J. Korean Phys. Soc.** 33[2] : 180-183.
- [30] Singh, S., and Krupanidhi, S. B. 2009. "Fabrication and Phase Transformation in Crystalline Nanoparticles of PbZrO_3 Derived by Sol-Gel." **Curr. Nanosci.** 5 : 489-492.
- [31] Dharmaraj, N., Kim, C.H., and Kim, H.Y. 2005. " $\text{Pb}(\text{Zr}_{0.5}, \text{Ti}_{0.5})\text{O}_3$ Nanofibres by Electrospinning." **Mater. Lett.** 59 : 3085–3089.
- [32] Xie, S. H., Li, J. Y., Qiao, Y., Liu, Y. Y., Lan, L. N., Zhou, Y. C., and Tan, S. T. 2008. "Multiferroic CoFe_2O_4 - $\text{Pb}(\text{Zr}_{0.52}\text{Ti}_{0.48})\text{O}_3$ Nanofiber by Electrospinning." **App. Phys. Lett.** 92 : 062901.
- [33] Xie, S. H., Li, J. Y., Liu, Y. Y., Lan, L. N., Jin, G., and Zhou, Y. C. 2008. "Electrospinning and Multiferroic Properties of NiFe_2O_4 - $\text{Pb}(\text{Zr}_{0.52}\text{Ti}_{0.48})\text{O}_3$ Composite Nanofibers." **J. App. Phys.** 104 : 024115.

- [34] Yuh, J., Nino, J. C., and Sigmund, W. M. 2005. "Synthesis of Barium titanate (BaTiO_3) Nanofibers via Electrospinning." **Materials Letters**. 59 : 3645–3647.
- [35] Li, H., Wu, H., Lin, D., and Pan, W. 2009. "High T_C in Electrospun BaTiO_3 Nanofibers." **J. Am. Ceram. Soc.** 92[9] : 2162-2164.
- [36] He, Y., Zhang, T., Zheng, W., Wang, R., Liu, X., Xia, Y., and Zhao, J. 2010. "Humidity Sensing Properties of BaTiO_3 Nanofiber Prepared via Electrospinning." **Sens. Actuators B**. 146 : 98–102.
- [37] Khaled, S. M., Sui, R., Charpentier, P. A., and Rizkalla, A. S. 2007. "Synthesis of TiO_2 -PMMA Nanocomposite: Using Methacrylic Acid as a Coupling Agent." **Langmuir**. 23 : 3988-3995.
- [38] Chen, X., Galos, R., and Shi, Y. 2011. "A Self Powered PZT Nanofiber Composite Sensor for Structural Health Monitoring." **The 6th International Workshop on Advanced Smart Materials and Smart Structures Technology ANCRISST2011**. Dalian, China.
- [39] Chen, X., Xu, S., Yao, N., and Shi, Y. 2010. "Nanogenerator for Mechanical Energy Harvesting Using PZT Nanofibers." **Nano Lett.** 10 : 2133–2137.
- [40] Chang, C., Tran, V. H., Wang, J., Fuh, Y.-K., and Lin, L. 2010. "Direct-Write Piezoelectric Polymeric Nanogenerator with High Energy Conversion Efficiency." **Nano Lett.** 10 : 726-731.
- [41] Dang, Z. M., Yao, S. H., Yuan, J. K., and Bai, J. 2010. "Tailored Dielectric Properties based on Microstructure Change in BaTiO_3 -Carbon Nanotube/Polyvinylidene Fluoride Three-Phase Nanocomposites." **J. Phys. Chem. C**. 114[31] : 13204–13209.
- [42] Park, K., Lee, M., Liu, Y., Moon, S., Hwang, G. T., Zhu, G., Kim, J. E., Kim, S. O., Kim, D. K., Wang, Z. L., and Lee, K. J. 2012. "Flexible Nanocomposite Generator Made of BaTiO_3 Nanoparticles and Graphitic Carbons." **Adv. Mater.** 201200105.

CHAPTER 3

RESEARCH METHODOLOGY

This chapter describes the experimental procedures and techniques used for the preparation of nanofibers and fabrication of nanocomposite materials. In addition, characterization techniques and electrical measurement are mentioned as follows.

3.1 Sample Preparation

3.1.1 Preparation of Fibers

In this study, synthesis of the nanofiber lead zirconate (PZ) system was of interest. A systematic investigation of piezoceramic nanofiber was conducted using two synthesis routes, namely the sol-gel and electrospinning process, followed by calcinations at high temperature. The concentration, volume ratio of precursor solution to polymer, feeding rate, calcination temperature, polymer type [such as polyethyleneoxide (PEO), polyvinylpyrrolidone (PVP), and Glutinous Rice Starch (GRS)], were varied. The electrospinning setup is demonstrated in Figure 3.1. Detailed descriptions are given in Chapter 4.

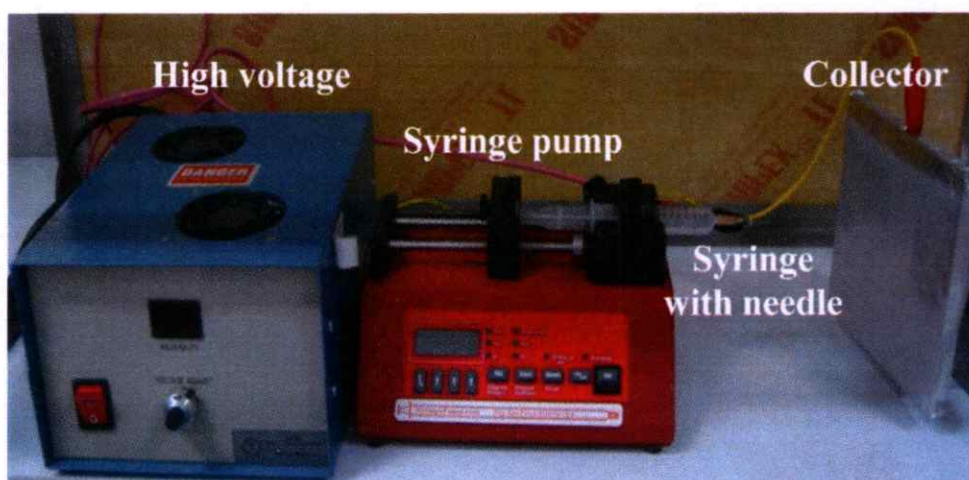


Figure 3.1 Electrospinning setup

3.1.2 Fabrication of Nanocomposite Materials

A two phase nanocomposite of lead zirconate (PZ) system was prepared by the solvent casting technique by dispersing the disperse phase into the polymer matrix phase. In addition, a three-phase nanocomposite of lead zirconate (PZ) system modified with carbon nanotube (CNT) was prepared. For more detail are descript in Chapter 7 and 8.

3.2 Characterization Techniques

The characterization of ferroelectric materials requires exploration for its different properties using different analytical techniques. Structural characterization of the samples was carried out using X-ray Diffraction (XRD), and microstructure and particle sizes were characterized using Scanning Electron Microscopy (SEM) and Transmission Electron Microscopy (TEM). The presence of functional bonds was confirmed by Fourier Transform Infrared Spectroscopy (FT-IR) and Raman techniques. Detailed description of the techniques used for analysis is given below.

3.2.1 Structural Characterization

3.2.1.1 X-Ray Diffraction (XRD) [1]

The X-ray powder diffraction method is best suited for characterization and identification of polycrystalline materials and their different phases. It is a rapid analytical technique used primarily for identifying phases in crystalline materials and providing information about unit cell dimensions. When X-rays interact with a crystalline substance, they become diffracted and a diffraction pattern is obtained. The X-ray diffraction pattern of a pure substance is therefore like a fingerprint of the substance. Today, more than 50,000 inorganic and around 25,000 organic single components, with crystalline phase diffraction patterns, have been collected and stored as standards on magnetic or optical media.

As illustrated in Figure 3.2(a), a crystal lattice consists of a regular arrangement of atoms, with layers of high atomic density existing throughout the crystal structure. Planes of high atomic density mean planes of high electron density. Scattering occurs between impinging X-ray photons and loosely bound outer orbital atomic electrons when a monochromatic beam of radiation falls onto high atomic density layers. In order to satisfy the requirement for constructive interference, it is

necessary that the scattered waves originate from individual atoms, and the scattering points should be in phase with one another. The geometric conditions for this situation to occur are illustrated in Figure 3.2(b). Here, a series of parallel rays strike a set of crystal planes at the angle, θ , and are scattered as previously described. Reinforcement occurs when difference in the path lengths of two interfering waves is equal to a whole number of wavelengths. This path length difference is $2d \sin \theta$, where d is the inter-planar spacing; hence the overall condition for reinforcement is as follows:

$$2d \sin \theta = n\lambda \quad (3.1)$$

where θ is the angle of incidence

d is the inter planer spacing

n is the order of reflection, and

λ is the wavelength of the incident beam used.

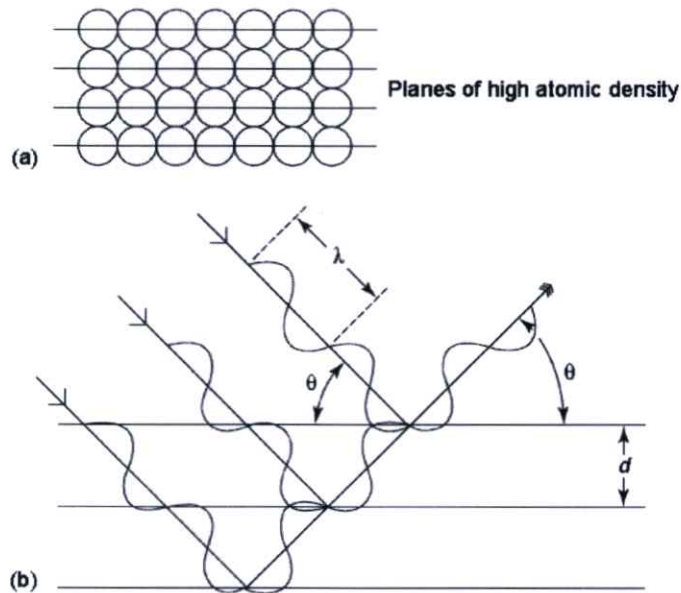


Figure 3.2 Scatter and diffraction from an ordered arrangement of atoms. [1]

Equation (3.1) is a statement of Bragg's law. Diffraction experiments are made generally at a fixed wavelength, thus a measure of the diffraction angles allows associated d -spacings to be calculated. Bragg's law is also important in wavelength

dispersive spectrometry, since each unique wavelength is diffracted at a unique diffraction angle when using a crystal of fixed $2d$. Thus, measuring the diffraction angle, 2θ , allows determination of the wavelength (inter-planar spacing), if the d -spacing of the crystal is known. Since there is a simple relationship between wavelength and atomic number, the atomic number(s) of the element(s) from which the wavelengths were emitted can be established.

3.2.1.2 Fourier Transform Infrared Spectroscopy (FT-IR) [2, 3]

Infrared spectroscopy is a technique based on the atom vibrations of a molecule. An infrared spectrum is obtained usually by passing infrared radiation through a sample, and determining what fraction of the radiation incident is absorbed at a particular energy. The energy at which any peak in an absorption spectrum appears corresponds to frequency of the vibrational part of a sample molecule.

The infrared spectrum can be divided into three main regions: the far-infrared ($< 400 \text{ cm}^{-1}$), mid-infrared ($4,000\text{--}400 \text{ cm}^{-1}$) and near-infrared ($13,000\text{--}4,000 \text{ cm}^{-1}$). Many infrared applications employ the mid-infrared region, but the near- and far-infrared regions also provide important information about certain materials. Generally, there are fewer infrared bands in the $4,000\text{--}1,800 \text{ cm}^{-1}$ region, but many bands between $1,800$ and 400 cm^{-1} . Sometimes, the scale is changed to contract the region between $4,000$ and $1,800 \text{ cm}^{-1}$ and expand that between $1,800$ and 400 cm^{-1} in order to emphasize features of interest.

The basic components of an FT-IR spectrometer are shown schematically in Figure 3.3. The radiation emerging from the source is passed through an interferometer to the sample before reaching a detector. Upon amplifying the signal, in which a filter eliminates high-frequency contributions, the data are converted to digital form by an analog-to-digital converter and transferred to the computer for Fourier-transformation.

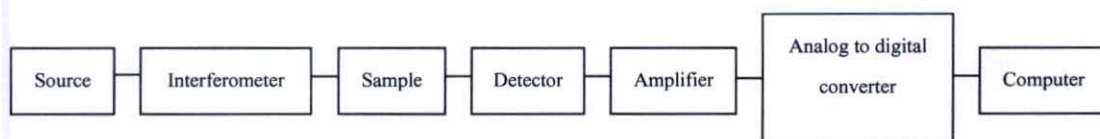


Figure 3.3 Basic components of an FT-IR spectrometer. [2]

3.2.1.3 Raman Spectroscopy [4]

Raman spectroscopy is a spectroscopic technique used in condensed matter physics and chemistry to study vibrational, rotational, and other low-frequency modes in a system. It relies on inelastic scattering, or Raman scattering of monochromatic laser light. The laser light interacts with phonons or other excitations in the system, resulting in energy of the laser photons being shifted up or down. The shift in energy gives information about the phonon modes in the system.

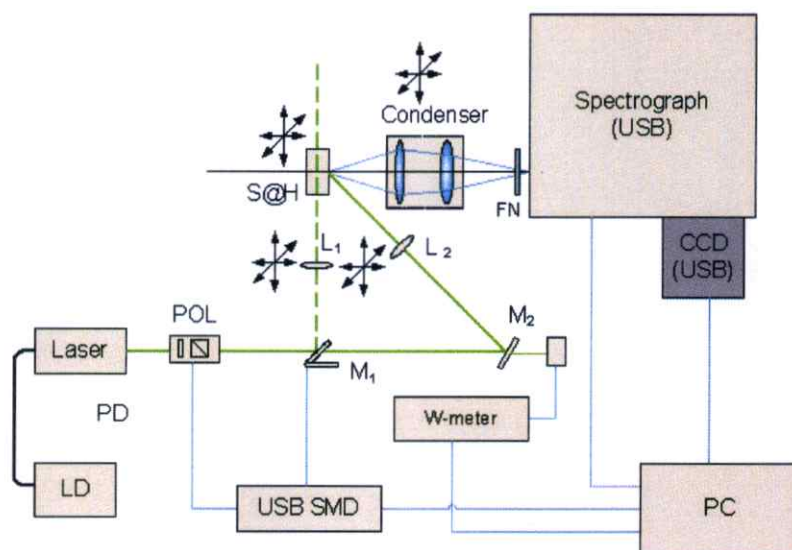


Figure 3.4 Schematic diagram of the Raman spectrometer. [4]

The effect of Raman occurs when light impinges upon a molecule, which interacts with its own electron cloud bonds, and a photon incident excites one of the electrons into a virtual state. To achieve a spontaneous effect from Raman, the molecule becomes excited from the ground state to a virtual energy state, and relaxes into a vibrational excited state, which generates Stokes Raman scattering. Should the molecule already be in an elevated vibrational energy state, Raman scattering is called anti-Stokes Raman scattering. A molecular polarizability change, or degree of deforming the electron cloud, with respect to the vibrational coordinate, is required to enable the molecule to exhibit the effect of Raman. The amount of polarizability change determines Raman scattering intensity, whereas the Raman shift is equal to the vibrational level involved.

3.2.2 Morphology

3.2.2.1 Scanning Electron Microscopy (SEM) [4]

The scanning electron microscope (Figure 3.5) can create images of the sample surface by scanning it with a high energy beam of electrons. Conventional light microscopes use a series of glass lenses to bend light waves and create a magnified image, while the scanning electron microscope creates magnified images by using electrons instead of light waves.

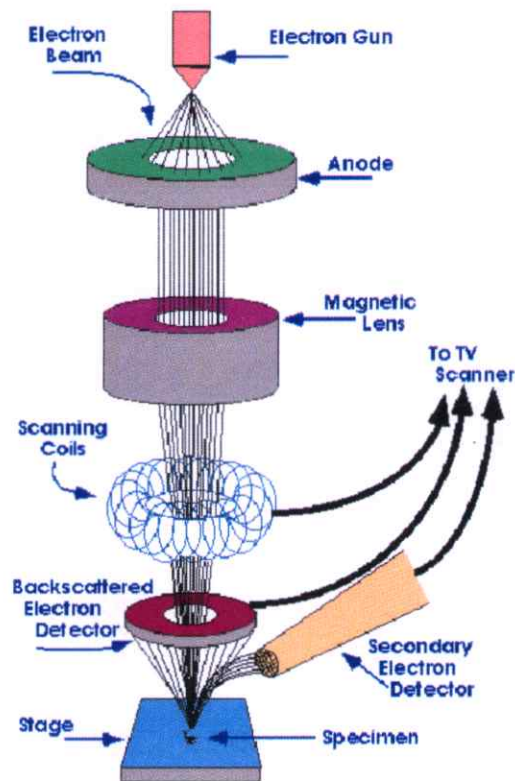


Figure 3.5 Schematic diagram of the SEM. [4]

When the beam of electrons strikes the surface of the specimen and interacts with the atoms of the sample, signals form as secondary electrons, and back scattered electrons and characteristic X-rays generate to contain information about the surface topography, composition, etc., of the sample. SEM can produce very high-resolution images of a sample surface, revealing details of about 1-5 nm in size in its primary detection mode, i.e. secondary electron imaging. Characteristic X-rays are the second most common imaging mode used in SEM. These characteristic X-rays are used to identify the elemental composition of the sample by a technique

known as energy dispersive X-ray (EDX). Back-scattered electrons (BSE) that come from the sample also may be used to form an image. BSE images are used often in analytical SEM together with the spectra made from characteristic X-rays, as clues to the elemental composition of the sample.

SEM requires the specimens to be conductive in order that the electron beam can scan the surface, and electrons have a path to ground for conventional imaging. Non-conductive solid specimens are coated generally with a layer of conductive material by low vacuum sputter coating or high vacuum evaporation. This is performed to prevent accumulation of static electric charge on the specimen during electron irradiation. Non-conducting specimens also may be imaged uncoated, by using specialized SEM instrumentation such as the "Environmental SEM" (ESEM) or field emission gun (FEG) SEM, which is operated at low voltage, high vacuum or low vacuum, high voltage.

3.2.2.2 Transmission Electron Microscopy (TEM) [4, 5]

Transmission electron microscopy is a technique for transmitting a beam of electrons through an ultra thin specimen, while interacting as it passes through the sample. An image is formed from the electrons transmitted through the specimen, and magnified and focused on an objective lens to appear on an imaging screen.

The contrast in a TEM image is not like that from a light microscope. In TEM, the crystalline sample interacts with the electron beam mostly by diffraction rather than absorption. The intensity of diffraction depends on the orientation of the atom planes in a crystal, which are relative to the electron beam, and diffracted strongly from the axis of the incoming beam, while the beam is transmitted mostly at other angles. Modern transmission electron microscopes are equipped with specimen holders that allow them to tilt the specimen in a range of angles in order to obtain specific diffraction conditions. Therefore, a high contrast image can be formed by blocking electrons deflected away from the optical axis of the microscope through placing the aperture to allow only unscattered electrons through. This produces variation in electron intensity that reveals information on the crystal structure. The TEM technique is particularly sensitive to extended crystal lattice defects by a particular crystal plane, which is known as a dark field image.

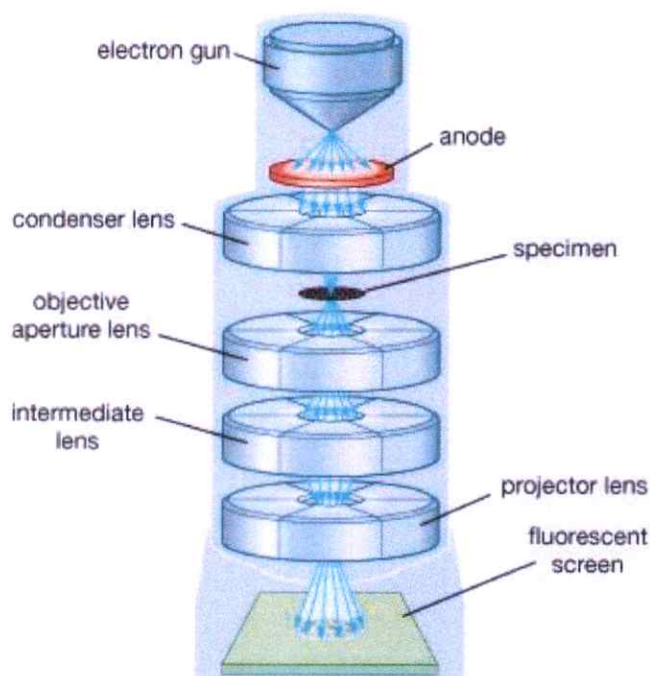


Figure 3.6 The schematic outline of a TEM. [6]

The specimen must be prepared as a thin foil so that the electron beam can penetrate. Materials that have dimensions small enough to be electron transparent, such as powders or nanotubes, can be produced quickly by the deposition of a diluted sample containing the specimen on support grids. As polymeric nanocomposites, or textile samples, are not as hard as metals, they are cut into thin films (<100 nm) using an ultra-microtome with diamond knife in cryogenic condition (in liquid nitrogen).

3.3 Thermal Analysis

3.3.1 Differential Thermal Analysis (DTA) [7]

The structure of a classical differential thermal analyzer is illustrated in Figure 3.7. The sample holder assembly is placed in the center of a furnace. One holder is filled with the sample and the other with an inert reference material, such as α -alumina. Thermocouples inserted in each holder measure the temperature difference between the sample and reference, as the temperature of the furnace is controlled by a temperature programmer. When the sample holder assembly is heated at a programmed rate, the temperatures of both (the sample and the

reference material) increase uniformly. The furnace temperature is recorded as a function of time. If the sample undergoes a phase change, energy is absorbed or emitted, and a temperature difference between the sample and reference is detected. The minimum temperature difference, which can be measured by DTA, is 0.01 K.

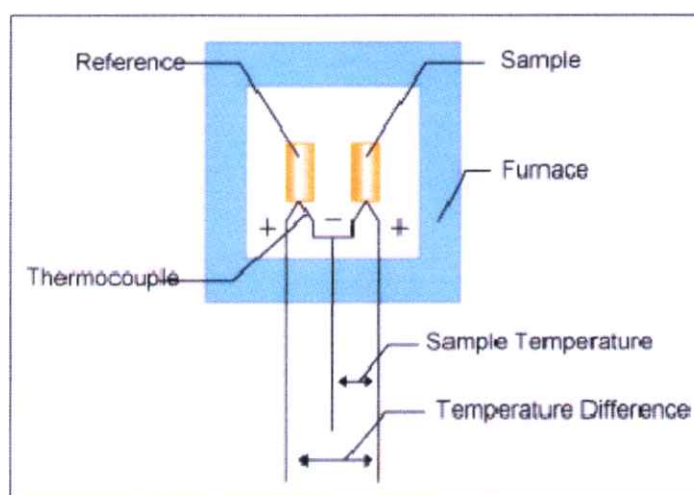


Figure 3.7 Block diagram of DTA. [8]

A DTA curve plots the temperature difference as a function of temperature (scanning mode) or time (isothermal mode). During a phase transition, the programmed temperature ramp cannot be maintained, owing to heat absorption or emission by the sample. This situation is illustrated in Figure 3.8, where the temperature of the sample holder increases above the programmed value during crystallization, owing to the exothermic heat of crystallization. In contrast, the temperature of the sample holder does not increase in response to the temperature programmer during melting because heat flows from the sample holder to the sample. Therefore, the true temperature scanning rate of the sample is not constant over the entire temperature range of the experiment. Temperature calibration is achieved using standard reference materials, of which transition temperatures are well characterized and in the same temperature range as transition in the sample. The transition temperature can be determined by DTA, but the enthalpy of transition is difficult to measure because non-uniform temperature gradients in the sample are not easy to quantify, due to the structure of the sample holder.

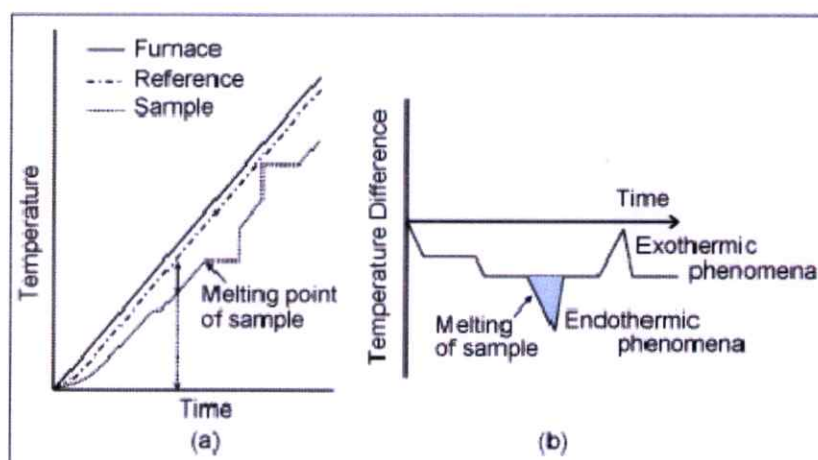


Figure 3.8 Measurement principles of DTA. [8]

3.3.2 Thermogravimetry (TG) [7]

Thermogravimetry (TG) is the branch of thermal analysis that examines the mass change of a sample as a function of temperature in the scanning mode, or function of time in the isothermal mode. TG is used to characterize the decomposition and thermal stability of materials under various conditions and examine the kinetics of the physicochemical processes occurring in the sample. The mass change in characteristics of a material is strongly dependent on the experimental conditions employed. Factors such as sample mass, volume and physical form, shape and nature of the sample holder, nature and pressure of the atmosphere inside the sample chamber and scanning rate all have important influence on the characteristics of a recorded TG curve. TG curves are plotted normally with the mass change (D_m) expressed in percentage on the vertical axis, and temperature (T) or time (t) on the horizontal axis.

A schematic representation of a 1-stage reaction process observed in scanning mode is shown in Figure 3.9. The reaction is characterized by two temperatures, T_i and T_f which are called the procedural decomposition and final temperature, respectively. T_i merely represents the lowest temperature at which the onset of a mass change can be detected for a given set of experimental conditions. Similarly, T_f represents the lowest temperature needed to complete the process responsible for the mass change. The values of T_i and T_f have no absolute significance, as both the reaction temperature and the reaction interval ($T_i - T_f$) have

no definitive value, but they depend on experimental conditions. Interpretation of TG data is often facilitated by comparison with data from other experimental techniques.

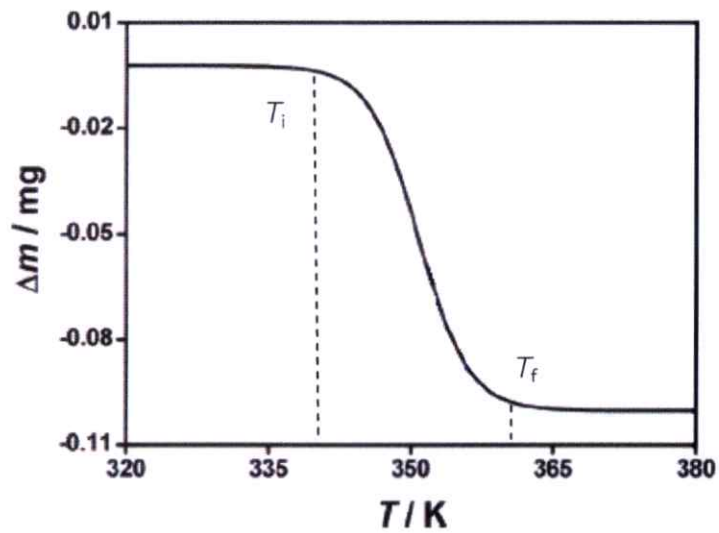


Figure 3.9 Schematic single-stage TG curve. [7]

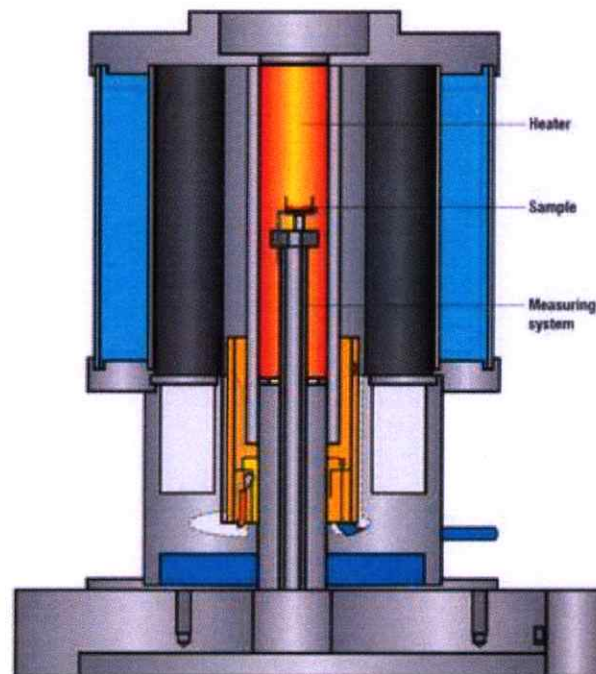


Figure 3.10 Structure of the TG instrument. [8]

3.3.3 Differential Scanning Calorimetry (DSC) [7]

A differential scanning calorimeter employs a different operating principle from the DTA systems presented earlier. A block diagram of the DSC instrument is shown in Figure 3.11. The base of the sample holder assembly is placed in a reservoir of coolant. The sample and reference holders are equipped individually with a resistance sensor, which measures the temperature of the holder's base and a resistance heater. If a temperature difference is detected between the sample and reference, due to a phase change in the sample, energy is supplied until the temperature difference is less than a threshold value, which is typically < 0.01 K. The energy input per unit time is recorded as a function of temperature or time. A simplified idea on the thermal properties of this configuration shows that the energy input is proportional to the heat capacity of the sample. Temperature and energy calibration is achieved by using standard reference materials. Isothermal experiments, annealing (single- and multi-step) and heat capacity measurements can be performed more readily by using a power compensation-type instrument. Maintaining the baseline linearity of the instrument is a problem at high temperatures or in sub-ambient mode. Moist condensation on the sample holder must be avoided during a sub-ambient operation.

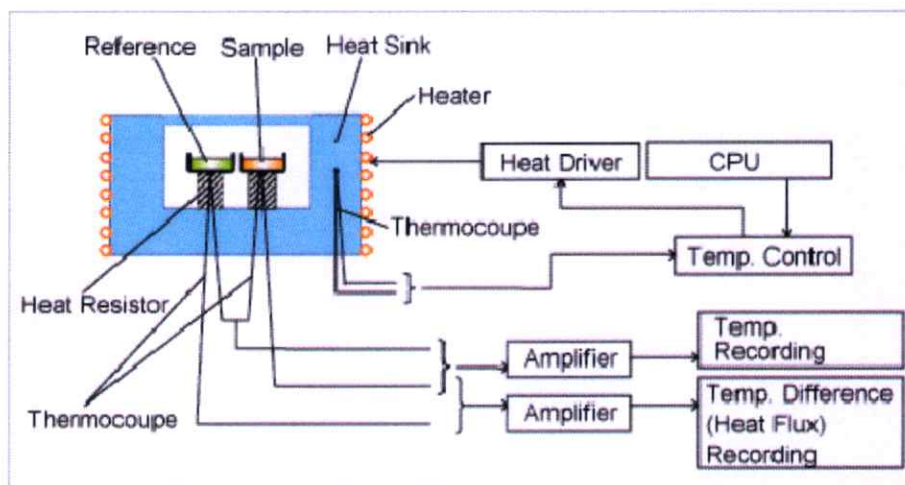


Figure 3.11 Block diagram of Heat Flux DSC. [9]

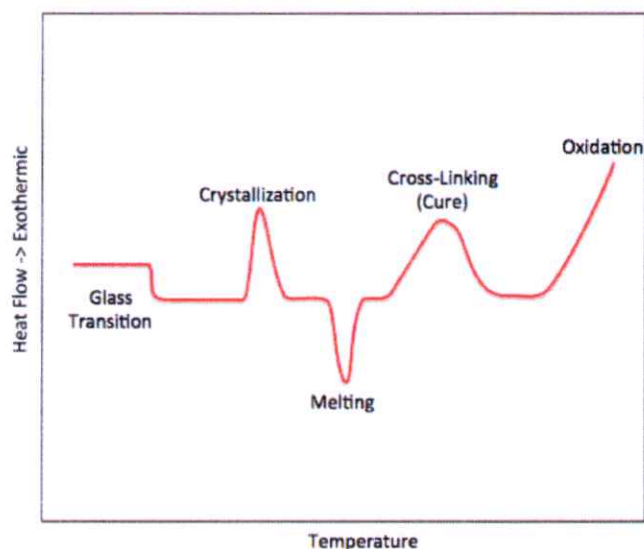


Figure 3.12 An idealized DSC curve showing the shapes associated with particular phase transitions. [10]

3.4 Dielectric Measurement [11, 12]

Study of the electrical and other related properties of dielectric materials, in relation to their chemical composition and structure, plays a vital role in understanding the physical mechanism of phase transition, as well as its practical utility for device applications. Under the electrical properties of ferroelectric or nonlinear dielectric materials, this author was concerned mainly with the study of dielectric properties such as dielectric constant and dielectric loss. These electric measurements can be carried out easily using an LCR meter. A brief theoretical account of dielectric properties is mentioned as follows.

3.4.1 Dielectric Constant [12]

The dielectric constant is the measure of a material's influence on the electric field. The net capacitance increases or decreases depending on the type of dielectric material. Permittivity relates to the ability of a material to transmit an electric field. Increased permittivity in capacitors allows the same charge to be stored with a smaller electric field, which leads to increased capacitance. Capacitance depends on the geometry of the conductors, and not on an external source of charge or potential difference. The space between the two plates of the capacitor is covered with dielectric material. In general, the value of capacitance is determined

by the dielectric material, distance between the plates, and area of each plate. The capacitance of a capacitor can be expressed in terms of its geometry and dielectric constant as follows:

$$C = \frac{\epsilon_r \epsilon_0 A}{d} \quad (3.2)$$

where C is the capacitance in farads (F)

ϵ_r is the relative static permittivity (dielectric constant) of the material between the plates

ϵ_0 is the permittivity of free space, which is equal to 8.854×10^{-12} F/m

A is the area of each plate, in square meters. and

d is the distance (in meters) that separates the two plates.

According to Equation 3.2, the capacitance is proportional to the amount of dielectric constant. As the dielectric constant between the capacitive plates of a capacitor rises, the capacitance increases accordingly. Capacitance can be stated in terms of the dielectric constant, as follows:

$$C = \epsilon_r C_0 \quad (3.3)$$

where C_0 is the capacitance in the absence of the dielectric constant.

3.4.2 Dielectric Loss [13]

The dielectric loss factor measures the amount of energy that a material dissipates when subjected to an alternating electrical field. The value of the loss factor is always greater than zero, but usually less than the value of relative permittivity.

According to the phase diagram of current and voltage in a capacitor energized by alternating voltage; should the power not be dissipated at all in the dielectrics of the capacitor (ideal dielectrics), then the phasor current I passing through the capacitor would be ahead of the phasor voltage V by precisely 90° , and the current would be purely reactive (Figure 3.13). However, in actual practice, the phase angle, Φ , is slightly less than 90° and the total current I passing through the capacitor can be resolved in two components (the active current I_a and reactive current I_r). Thus, the phase angle describes a capacitor from the viewpoint of losses

in dielectrics (power losses in the capacitor plates and leads are neglected). Since the phase angle is very close to 90° in a capacitor, with a high quality dielectrics, the angle, δ , is a more descriptive parameter, which when added to the angle, Φ , brings the angle, Φ , to 90° .

$$\delta = 90 - \Phi \quad (3.4)$$

The angle, δ , is called the dielectric loss angle and its tangent is equal to the ratio between the active and reactive currents.

$$\tan \delta = I_a/I_r \quad (3.5)$$

where $\tan \delta$ can be defined also in terms of power, and is defined as the ratio of active power (power loss) P to reactive power P_q .

$$\tan \delta = P/P_q \quad (3.6)$$

The dielectric loss angle is an important parameter for dielectric material, and the quality factor of an insulated portion is determined as follows:

$$Q = 1/\tan \delta = \cot \delta \quad (3.7)$$

For good quality dielectrics, $\tan \delta$ maybe in the order of $1/10^{-3}$ or $1/10^{-4}$. The value of dielectric constant depends on frequency of the applied voltage. The time required is very small for electronic or ionic polarization to set-in, as compared with the time needed for voltage sign change, i.e. half of the period or more.

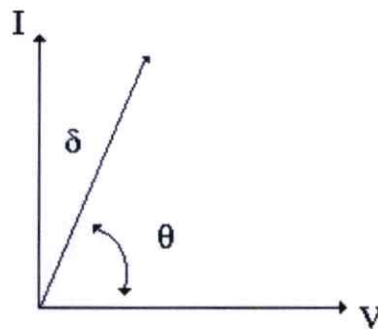


Figure 3.13 Phase diagram of current and voltage in a capacitor energized by an alternating voltage. [13]

REFERENCE

- [1] Jenkins, R. 2000. "X-ray Techniques: Overview." pp. 13269–13288. in Meyers, R.A. (editor). **Encyclopedia of Analytical Chemistry**. Chichester: John Wiley & Sons Ltd.
- [2] Stuart, B. 2004. **Infrared Spectroscopy: Fundamentals and Applications**. John Wiley & Sons Ltd.
- [3] Coates, J. 2000. "Interpretation of Infrared Spectra, A Practical Approach." pp. 10815–10837. in Meyers, R.A. (editor). **Encyclopedia of Analytical Chemistr.** Chichester: John Wiley & Sons Ltd.
- [4] Joshi, M., Bhattacharyya, A., and Wazed Ali, S. 2008. "Characterization techniques for nanotechnology applications in textiles." **Indian J. Fibre Text. Res.** 33 : 304-317.
- [5] Voutou, B., and Stefanaki. E. C. 2013. **Electron Microscopy: The Basics**. [Online]. Available : <https://optiki.files.wordpress.com/2013/03/electron-microscopythe-basics.pdf>.
- [6] Shannon, R. R. 2015. **Microscope Instrument**. Encyclopaedia Britannica, Inc. [Online]. Available : <http://www.britannica.com/technology/microscope>.
- [7] Hatakeyama, T., and Quinn, F.X. 1999. "Thermal Analysis." **Fundamentals and Applications to Polymer Science**; Second Edition. England: John Wiley & Sons Ltd.
- [8] LINSEIS. 2012. **Thermal analysis**. [Online]. Available : http://www.lookfordiagnosis.com/mesh_info.php?term=Thermogravimetry&lang=1
- [9] Hitachi High-Technologies Corporation. 2001, 2015. **Thermal Analysis**. [Online]. Available : <http://www.hitachi-hightech.com/global/products/science/tech/ana/thermal/descriptions/dsc.html/>
- [10] Barron, A. R. 1999-2015. Physical Methods in Chemistry and Nano Science, Rice University. [Online]. Available: http://cnx.org/contents/ba27839d-5042-4a40-afcf-c0e6e39fb454@20.16:31/Physical_Methods_in_Chemistry_
- [11] Rabih, A. A. S., Begam, K. M., Ibrahim, T., and Burhanudin, Z. A. 2013. "Dielectric Properties of Properly Slaughtered and Non-properly Slaughtered Chicken." **J. Med. Res. Dev.** 3[1] : 107-120.

- [12] Terzic, E., Terzic, J., Nagarajah, and R., Alamgir, M. 2012. "A Neural Network Approach to Fluid Quantity Measurement in Dynamic Environments." pp. 11-37. **Capacitive Sensing Technology**. London: Springer-Verlag.
- [13] Joshi, N. J. 2012. "Studies of nano-sized high dielectric constant materials." Doctor of Philosophy, The Maharaja Sayajirao University of Baroda, Gujarat, India.

CHAPTER 4

SYNTHESIS AND PHASE EVOLUTION OF ELECTROSPUN ANTIFERROELECTRIC LEAD ZIRCONATE (PbZrO₃) NANOFIBERS

Based on article published in *Materials Science and Engineering B*
177 (2012) 1009–1016

This chapter reported the synthesis and phase evolution of electrospun antiferroelectric lead zirconate (PbZrO₃; PZ) nanofibers. In this study, lead zirconate fibers were synthesized by the electrospinning method using a solution that contained 5 wt% poly(ethylene oxide) (PEO) in ethanol and a sol-gel solution of PZ. Some parameters varied, for example, the ratio between PEO and PZ, concentrations of the precursor solution, flow rate, and calcination temperature. The as-spun and calcined PZ/PEO composite fibers were characterized by TG-DTA, X-ray diffraction, FT-IR, SEM and TEM. PZ fibers were obtained successfully with a welldeveloped perovskite structure after as-spun PZ/PEO composite fibers were calcined using the PZ/PEO volume ratio of 10:3 at a PZ concentration of 1.0 M at 650°C for 4 h. Stable nanofibers were produced with an average diameter of 300±64 nm. Additionally, the PZ fibers showed a Curie temperature that rose by nearly 13°C, when comparing with a normal PZ particle.

4.1 Introduction

In recent years, fine scale piezoelectric fibers have received extensive attention because of their potential applications as building blocks in various nanotechnologies, which include mechanics [1], photonics [2], electronics [3], and sensing [4]. The high surface to volume ratio is an attractive characteristic that can be achieved from nanofibers, and more attention has been paid to this area. With miniaturization of electronic devices, nanofibers of piezoelectric material are currently attracting a great deal of interest in the design of smart materials, due to

their novel properties that are significantly different from their bulk, such as physical and chemical properties [5]. Mai et al. [6] reported the preparation of piezoelectric lead zirconate titanate (PZT) fibers, with diameters ranging from 10 μm to 40 μm , and revealed their ferroelectric property. When heat-treated at 1,000°C, the permittivity and dielectric loss of these fibers was 581 and 0.01, respectively, at 10 kHz. Furthermore, electrospun PZT nanofibers exhibited an extremely high piezoelectric voltage constant ($g_{33} = 0.079 \text{ Vm/N}$), high bending flexibility, and high mechanical strength, as demonstrated by Chen et al. [7]. However, when reducing the fiber diameter to nanoscale by the electrospinning method, fiber fusion and continuous fibers could not be formed after annealing at high temperature, as reported in many researches. Dharmaraj et al. [8] reported the preparation of ferroelectric $\text{Pb}(\text{Zr}_{0.5}\text{Ti}_{0.5})\text{O}_3$ nanofibres by electrospinning, which presented fiber mats with a soldering-like attachment of nanofibers at their junction after calcinations at 550°C. Wu and Coffey [9] reported the preparation of erbium-doped silicon and germanium oxide nanofibers, and found a partially deformed nanofiber structure with some interfiber connections forming after calcinations at 700°C. In addition, Tuttle et al. [10] reported that the surface of fabricated aluminum acetate/PVP fibers became rough, and the fibers broke to a short length, after calcinations at 1,200°C. This demonstrated that preparation of ceramic nanofibers is fairly difficult when obtaining a continuous and smooth surface without forming interfiber connections. Furthermore, most studies of ceramic electrospinning to date have reported the synthesis of metal oxide fibers in the ferroelectric (e.g. PZT, BT) [7, 11] and multiferroic system (e.g. NF-PZT, CoF-PZT) [12,13]. In this study, synthesis of the nanofiber antiferroelectric system by electrospinning, followed by calcinations at high temperature, was of interest.

Antiferroelectric lead zirconate (PbZrO_3 : PZ) ceramics have received increasing attention as potential applications in microactuators and high energy storage capacitors [14]. The free energy difference between the antiferroelectric (AFE) and ferroelectric (FE) phase enables phase switching from the AFE to FE phase by applying an electric field [15]. PZ at room temperature has an orthorhombic structure with the lattice parameters, $a = 5.884 \text{ \AA}$, $b = 11.768 \text{ \AA}$ and $c = 8.22 \text{ \AA}$ [16]. The orthorhombic unit cell consists of eight formula units and eight primitive cells with a tetragonal structure [17]. Over the past few decades, PZ and PZ-based

systems have been synthesized and utilized massively in forms of bulk ceramics or crystalline films [18]. Based on our knowledge, there has been no previous report on the fabrication of antiferroelectric PZ fibers by electrospinning. Furthermore, fibrous antiferroelectric PZ has the potential for utilizing high performance hydrophones, and high electromechanical actuator and nanogenerator applications.

4.2 Experimental Procedure

In the preparation of lead zirconate (PZ) solution by a sol-gel process, lead acetate trihydrate [$\text{Pb}(\text{CH}_3\text{COO})_2 \cdot 3\text{H}_2\text{O}$, puriss; Sigma-Aldrich] and zirconium (IV) propoxide solution (~70% in propanol; Fluka) were used as precursors, and 2-methoxyethanol (puriss; Sigma-Aldrich) was selected as a solvent. The process for preparing PZ fibers is illustrated in Figure 4.1. Firstly, lead acetate trihydrate was dissolved in 2-methoxyethanol, which could act as didentate chelating ligands that allowed the sol to stabilize for a long period of time at room temperature. Then, this solution was stirred for 30 min at 70°C, with 3 mol% excess lead acetate trihydrate added to compensate for evaporation during high temperature calcination, whereas, zirconium (IV) propoxide was dissolved in 2-methoxyethanol while stirring for 30 min at room temperature. Next, the two solutions were mixed together by heating and stirring to form a sol. Acetic acid was added to the sol in order to prevent precipitation of the precursor solution, which had various final concentrations of 0.3, 0.5, 0.7, 0.9 and 1.0 M, obtained after stirring at 70°C for 1 h. In preparing lead zirconate/poly(ethylene oxide) (PZ/PEO) solution for electrospinning, the proper solution parameter had to be found for producing lead zirconate nanofibers, after which the precursor solution was mixed with poly(ethylene oxide) (PEO, MW = 300,000; Aldrich) solution (5 wt.% in ethanol) in volume ratios of 10:1, 10:2, and 10:3, consecutively. After stirring at room temperature for 1 h, the mixture was loaded into a plastic syringe, which was connected to a metallic needle and linked to a syringe pump (NE-1000, New Era Pump Systems, Inc. Wantagh, NY) in order to control the feeding rate of the solution. The positive terminal of high voltage power supply (ES30P-5 W, Gamma High Voltage Research Inc., Ormond Beach, FL) was connected to the needle tip of the syringe, while the aluminum plate collector, covered with aluminum foil, worked as a

counter electrode. The distance between the needle tip of the syringe and collector was fixed at 15 cm, and the feeding rate of the solution varied. When the voltage applied between two electrodes reached 10 kV, a non-woven mat of PZ/PEO composite fibers collected on the surface of the aluminum plate, which was wrapped with aluminum foil. The reaction of the as-spun composite nanofibers, which took place during heat treatment, was investigated by differential thermal analysis (DTA; Shimadzu) and thermogravimetry analysis (TGA; Shimadzu), using a heating rate of 10°C/min in air that ranged from room temperature to 1,300°C. X-ray diffraction (XRD; Bruker-D8 Advance) using $\text{CuK}\alpha$ radiation was used to determine the phases formed and optimum firing temperatures for formation of the desired phase. A room-temperature FT-IR spectrum ranging from 4,000 to 370 cm^{-1} was recorded by a PerkinElmer Spectrum GX FT-IR/FT-Raman spectrometer, with eight scans and a resolution of 4 cm^{-1} using KBr pellets. Phase transition of the fibers was investigated, using a differential scanning calorimeter (DSC 2920, TA Instrument) between room temperature and 300°C at a heating rate of 10°C/min. Finally, a scanning electron microscope (SEM, JEOL JSM5910LV) and transmission electron microscopy (TEM, JEOL JEM-2100) were used to observe the morphology of the PZ fibers.

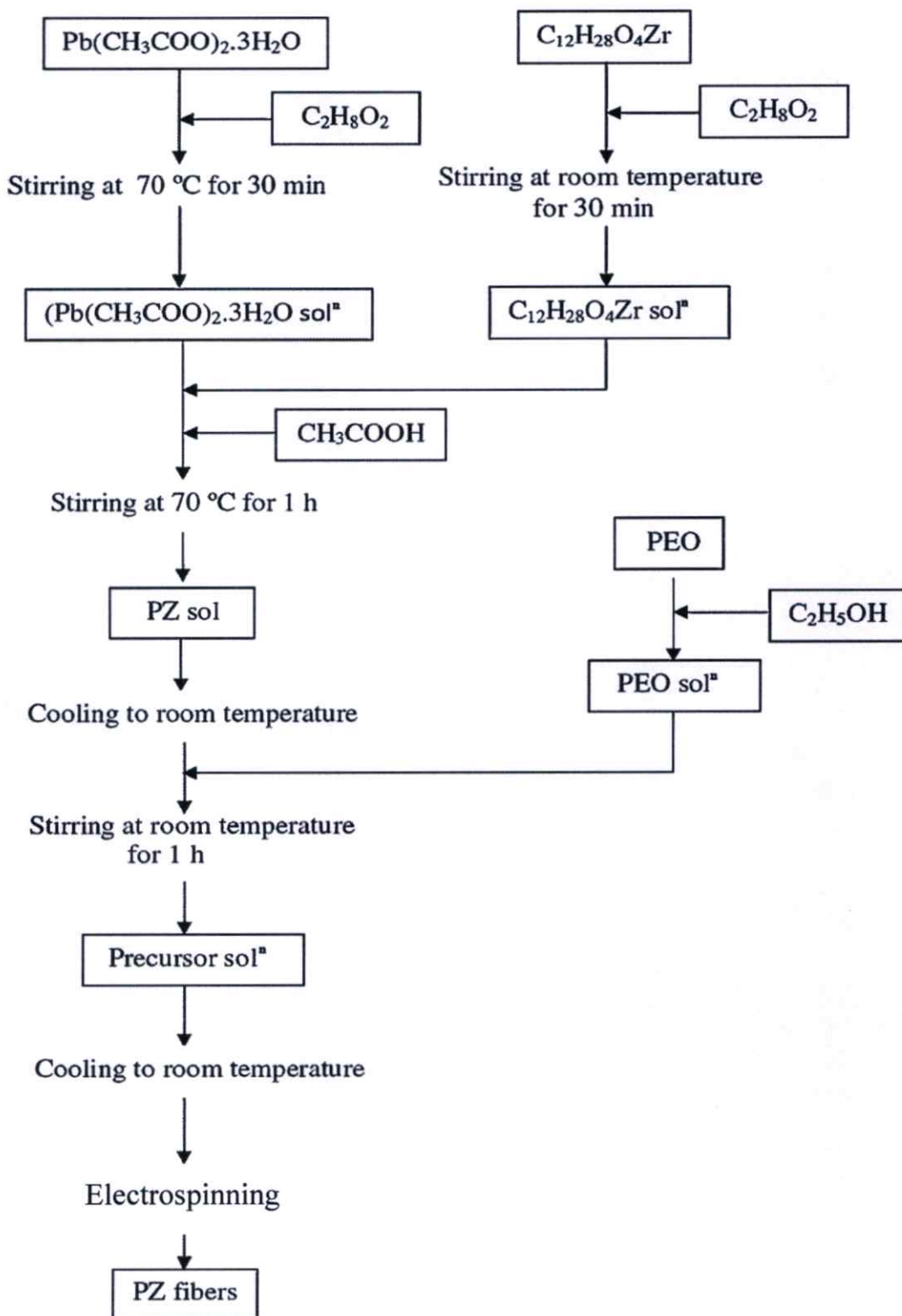


Figure 4.1 Process for the preparation of PZ fibers.

4.3 Results and Discussion

4.3.1 Effect of PZ/PEO Volume Ratios

Figure 4.2 shows the SEM photographs of the as-spun PZ/PEO composite, with a PZ concentration of 0.7 M using the PZ/PEO volume ratios of 10:1, 10:2 and 10:3, consecutively. Figure 4.2(a) indicates that continuous fibers could not form, as the jet broke up into droplets, due to the low viscosity of the precursor solution. With the polymer in highly diluted solution, each polymer chain was so far apart, most of them were separated. When the amount of PEO increased, the viscosity rose, due to individual polymer chains becoming entangled, thus creating more resistance to the electric field, and resulting in a more stable jet. In general, chain entanglement causes a significant impact on the electrospinning process by determining whether the jet breaks up into droplets, beads, or fibers and if it affects the geometry of fiber formations [19]. The formation of beads was observed in low viscosity solution, as presented in Fig. 4.2(b), whereas, continuous fibers and smooth surface with uniform diameter were obtained in high viscosity solution, which indicated a smooth injection of PZ sol dispersed in the polymer matrix during electrospinning [Figure 4.2(c)]. A remarkable correlation was observed when comparing with the optimum conditions determined from solution with a PZ/PEO volume ratio of 10:3. That is to say, the PEO content of the solution is important in obtaining continuous and bead-free fiber mats, but the real controlling factor appears to be the viscosity of the polymer solution. The PEO content is believed to be merely adjustment of the polymer viscosity. However, when a solid polymer is dissolved in a solvent; the more the solution viscosity is proportional to the polymer concentration, the larger the resulting nanofiber diameters, according to a power law relationship [19].

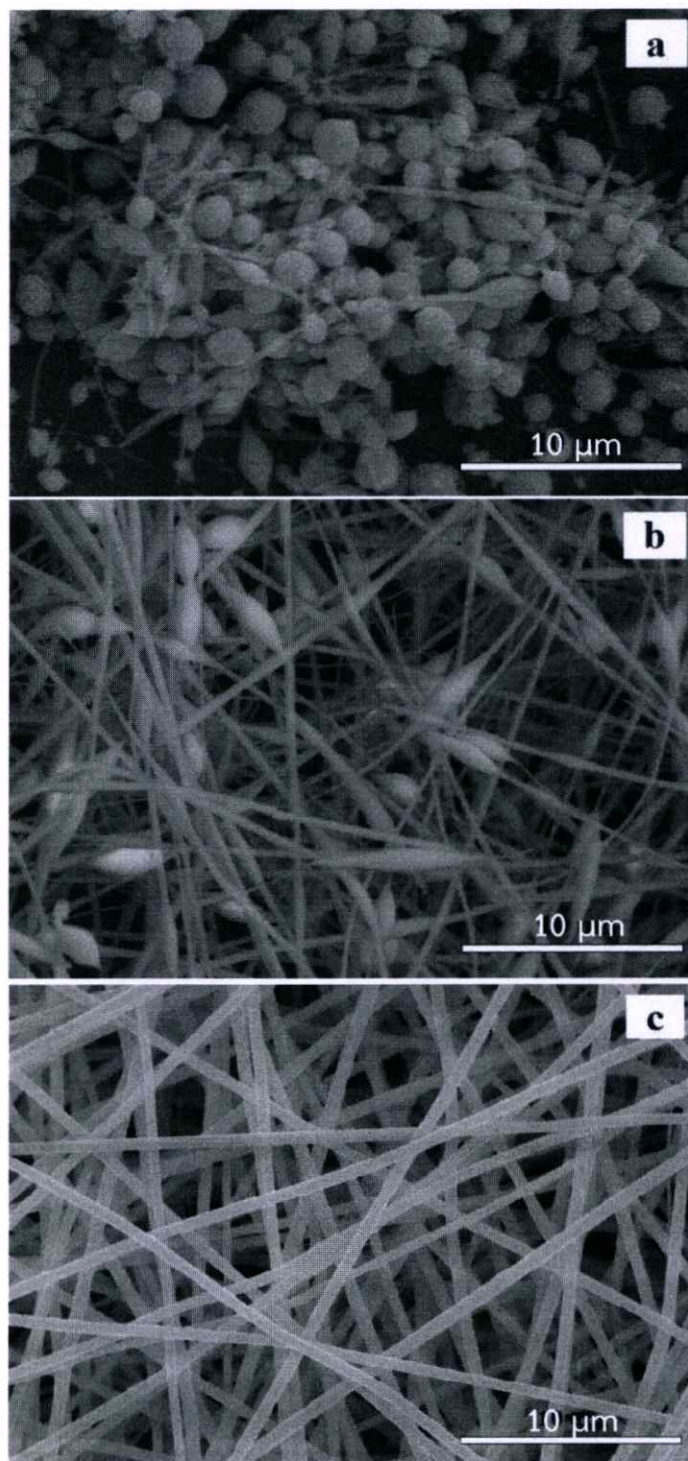


Figure 4.2 SEM micrographs of the as-spun PZ/PEO nanofibers with a PZ concentration of 0.7 M at the PZ/PEO volume ratio of (a) 10:1, (b) 10:2 and (c) 10:3, consecutively.

4.3.2 Effect of PZ Concentrations

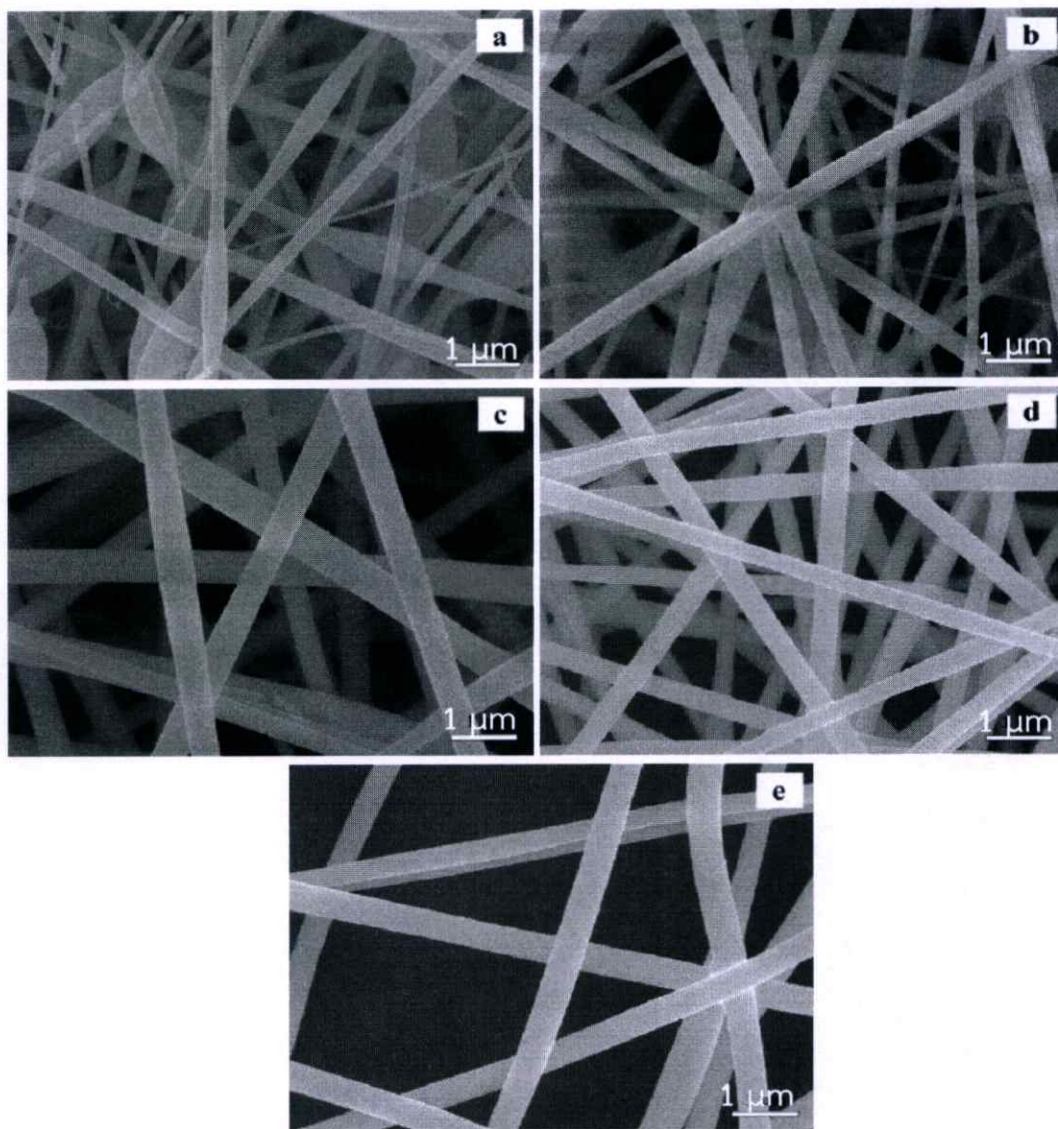


Figure 4.3 SEM micrograph of the as-spun PZ/PEO volume ratio of 10:3 at PZ concentrations of (a) 0.3, (b) 0.5, (c) 0.7 (d) 0.9 and (e) 1.0 M, consecutively.

Figure 4.3 shows the SEM micrograph of the as-spun PZ/PEO volume ratio of 10:3 at PZ concentrations of 0.3, 0.5, 0.7, 0.9 and 1.0 M, consecutively. When comparing between Figure 4.3(a), (b), (c), (d) and (e), the formation of beads can be seen to decrease with increased PZ concentration, and the as-spun PZ/PEO composite fibers, with PZ concentrations of 0.7, 0.9 and 1.0 M, have relative uniformity and a smooth surface, which indicates that the PZ was dispersed uniformly in the PEO medium. Beads or agglomerated fibers could not be observed. Furthermore, it can be seen that the average fiber diameter increases with increased PZ concentration. Decreases in the concentration of precursor solution cause the surface tension to dominate the electrostatic force, which results in thinner fibers or bead formation along the fibers. As the concentration increases, higher electrical charges induce more jet solution to collect on the aluminum plate; thus, fibers form with a larger diameter, which averages 266 ± 92 , 300 ± 51 , 354 ± 33 , 364 ± 38 and 439 ± 74 nm with a PZ concentration of 0.3, 0.5, 0.7, 0.9 and 1.0 M, respectively.

Thermal analysis was carried out to investigate the decomposition process of the fiber. The result of TG and DTA analyses of the as-spun PZ/PEO composite fibers are shown in Figure 4.4. The endothermic peak in the DTA curve, and weight loss (~24%) in the TGA curve, were observed below 350°C , which indicates a loss of moisture and trapped solvent in the as-spun fibers [20]. Despite bending instability during the electrospinning process, the jet path length increased enormously, which provided passage for the solvent to evaporate and the fibers to solidify, but a small amount of solvent still remained on the fiber surface. Whereas, an endothermic peak and a weight loss (~3%) in the range of $400\text{--}550^{\circ}\text{C}$ were due to the degradation of PEO, and there was no change here in the weight loss range of $550\text{--}900^{\circ}\text{C}$. On the other hand, there was an exothermic peak at 850°C in the DTA thermograph, which possibly corresponded to formation of the perovskite phase. In addition, the endothermic peaks in the DTA curve and weight loss (~7%) in the TGA curve, in temperatures ranging from 900°C to $1,000^{\circ}\text{C}$, were due to the loss of PbO at high temperature. Based on the TG-DTA results, the mixture was calcined at various temperatures ranging from 550°C to 850°C , with dwell times of 4 h and heating/cooling rates in a closed alumina crucible ranging around $5^{\circ}\text{C}/\text{min}$, in order to investigate the perovskite phase formation.

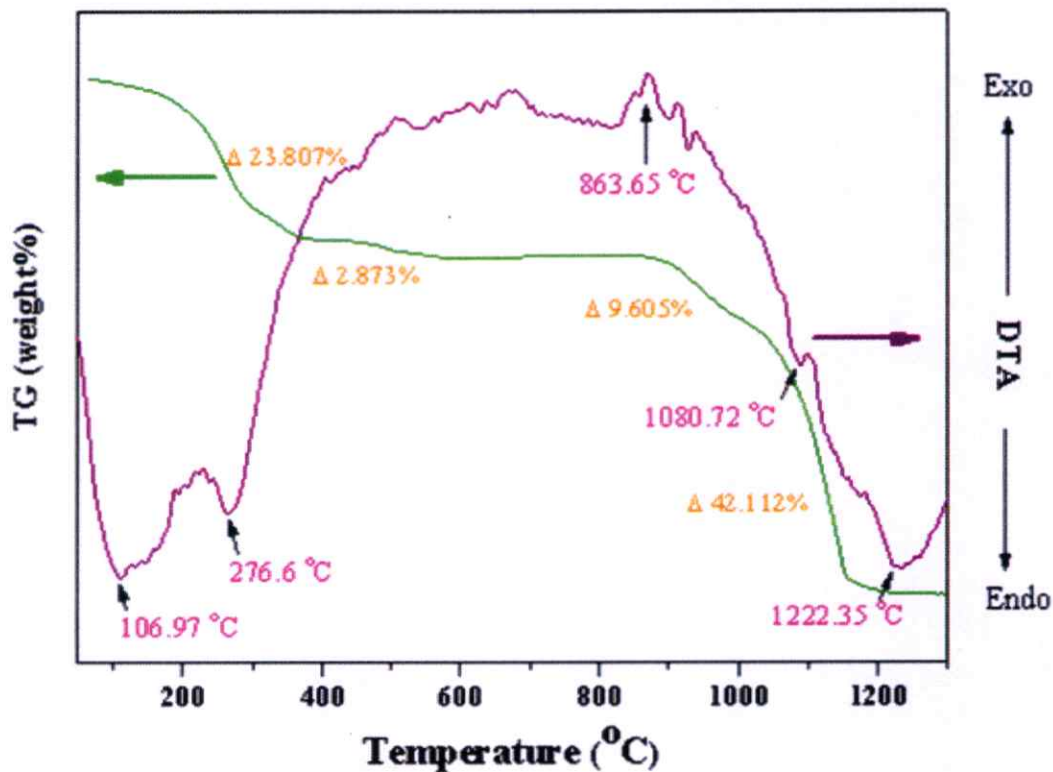


Figure 4.4 TG-DTA curves of thermal decomposition of the as-spun PZ/PEO composite nanofiber.

The crystalline phases of PZ fibers at various calcined temperatures were determined by X-ray diffraction spectra. Figure 4.5 shows the XRD patterns of PZ/PEO composite fibers calcined at different temperatures. After calcinations of as-spun PZ/PEO composite fibers at 550°C for 4 h, it was revealed that crystallization of the perovskite phase began to form. However, the main peak intensity of the PZ phase was weak, and a broad diffraction peak appeared at around $2\theta = 28^\circ$, which implied that the fiber was not fully crystallized and, to some extent, had an amorphous phase. When the calcination temperature was 650°C, the crystalline PZ fibers, with a well-developed perovskite structure, were obtained successfully. According to JCPDS card no.75-1607, the diffraction peaks can be indexed as an orthorhombic perovskite structure of lead zirconate. No other peaks could be observed in the XRD patterns, which indicated that the sample is free from lead oxide or any other crystalline

materials. By increasing the calcination temperature, the intensities of the peaks increase, and the full width at half maximum of the (1 2 2) main peak decreases, which indicates that crystallization of the PZ nanofibers has improved. The relative intensity of (h k l) peaks to that of the (1 2 2) peak in nanofibers increases with increased calcination temperature, which agrees well with the results of PZ films [21]. The lattice parameter calculated from the XRD pattern comprised $a = 5.8824 \text{ \AA}$, $b = 11.7711 \text{ \AA}$ and $c = 8.2294 \text{ \AA}$, which are close to reported values [13]. Furthermore, the PEO decomposes at 450°C , according to its thermal properties, and this study guarantees that its sample was free from PEO polymer.

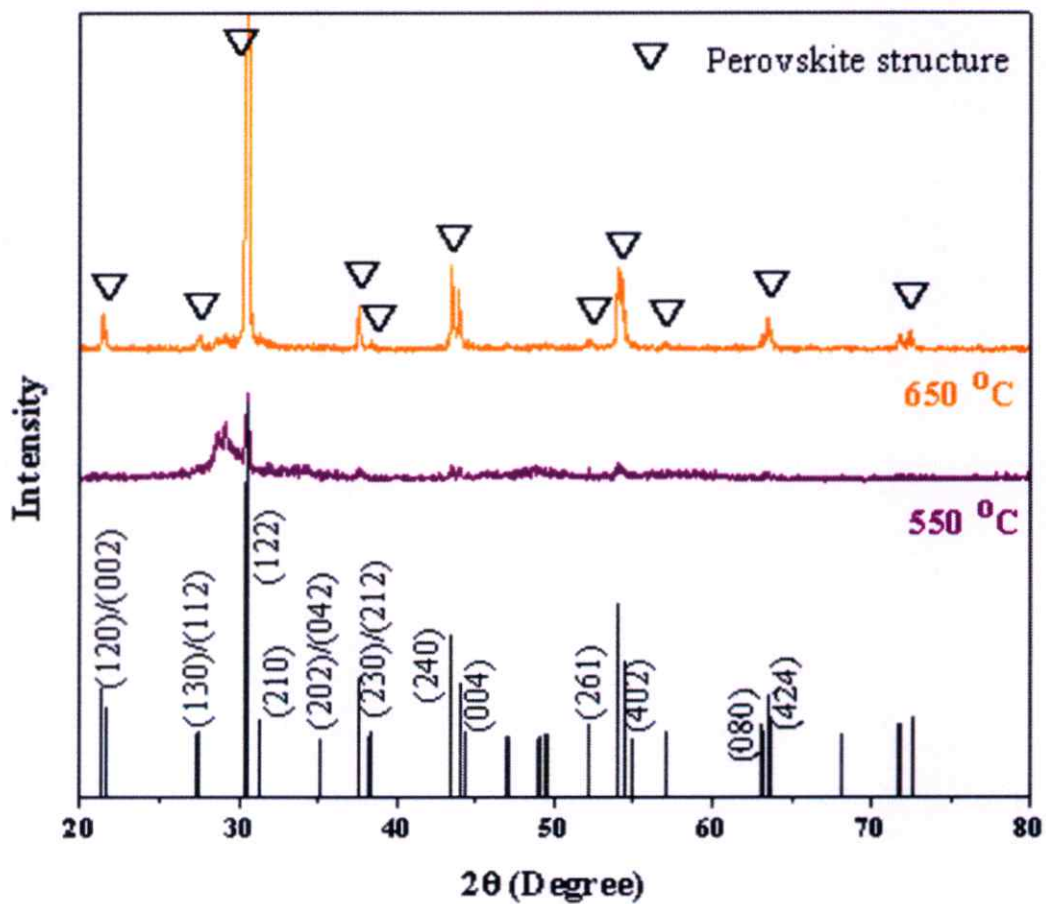


Figure 4.5 XRD patterns of electrospun PZ/PEO composite nanofibers calcined in air for 4 h at different temperatures.

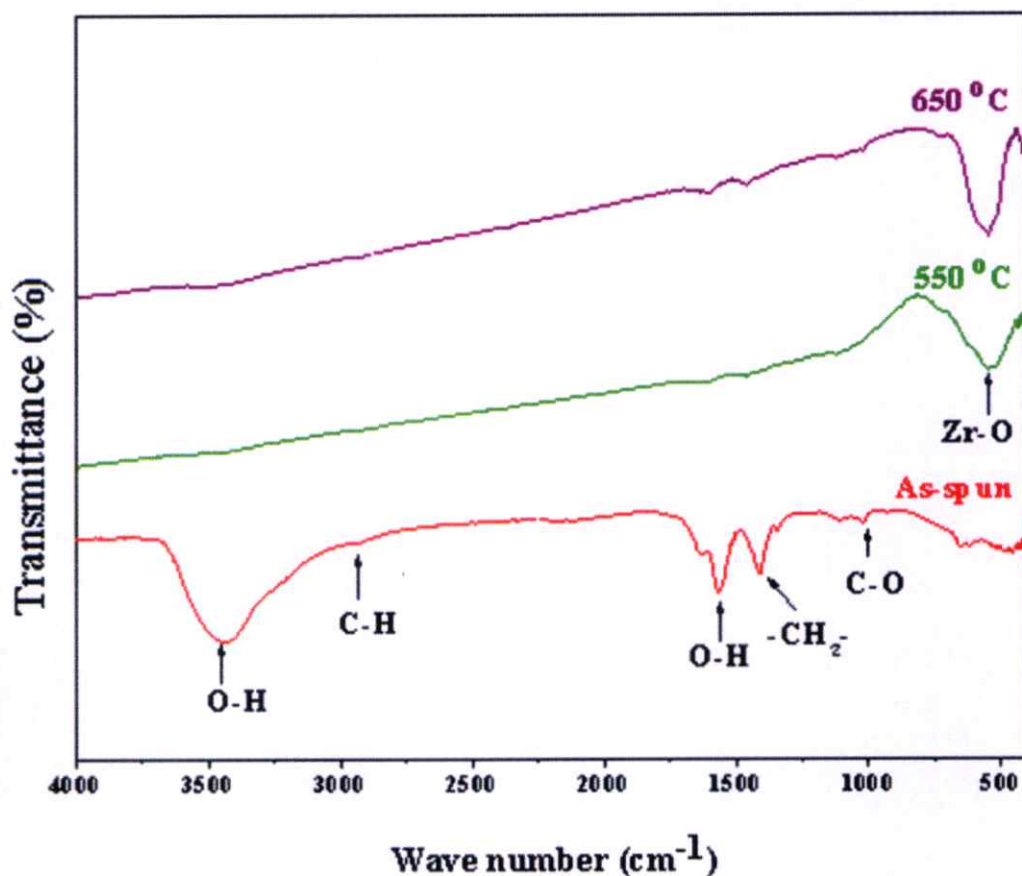


Figure 4.6 FT-IR spectra of electrospun PZ/PEO composite nanofibers calcined in air for 4h.

Formation of the perovskite structure in the calcined PZ fibers was supported further by FT-IR spectra, as shown in Figure 4.6. The spectrum of the PZ/PEO composite fibers shows multiple absorption bands in the region $1,000\text{--}4,000\text{ cm}^{-1}$, which correspond to the stretching and bending vibrations of PEO and moisture. Of these, peaks of around $1,450\text{ cm}^{-1}$ correspond to the aliphatic CH group vibrations of the CH_2 mode [22]. The band of $1,337\text{ cm}^{-1}$ has been attributed to the deformed vibration of CH_3 groups [6]. Peaks at $1,020$ and $1,048\text{ cm}^{-1}$ are assigned for stretching the C-O bond of 2-methoxyethanol and/or rocking vibration of CH_3 groups [23]. The wave number at $\sim 1,600\text{ cm}^{-1}$ and broad peak at around $3,400\text{ cm}^{-1}$ correspond to and are assigned for O-H stretching vibration, respectively, and the

shoulder at $2,900\text{ cm}^{-1}$ is related to the stretching vibration of C-H bonds [23]. After calcinations at 550°C for 4 h, it was found that these peaks almost disappear, indicating that most of the PEO and other organics have been removed. The appearance of an absorption peak at $\sim 548\text{ cm}^{-1}$ is attributed to Zr-O stretching vibration [24], which corresponds to the polycrystalline fiber obtained. As the calcination temperature increases to 650°C , the absorption peak of Zr-O bonds becomes narrower and more intense, which indicates that the crystallization of the PZ fibers improves with increasing calcination temperature, and the PEO is fully decomposed, as suggested in the XRD results.

In general, the formation of PZ fibers from composite ones should involve three main processes: evaporation of the polymer (PEO); nucleation and growth of PZ nanocrystals; and directional mass transport of the PZ crystal to form continuous fibers [25]. Figure 4.7(a)–(f) shows scanning electron microscopy (SEM) and transmission electron microscopy (TEM) images of the PZ fibers calcined at 650°C , with the PZ/PEO volume ratio of 10:3 at PZ concentrations of 0.7, 0.9 and 1.0 M, consecutively. The average diameter of fibers was 270 ± 38 , 294 ± 48 and 300 ± 64 nm with a PZ concentration of 0.7, 0.9 and 1.0 M, respectively, after calcination. SEM images of these fibers present a uniform and smooth surface [in Figure 4.7(a)–(c)], whereas, TEM images (Figure 4.7(d)–(f)) show that PZ fibers with a higher PZ concentration have improved fiber structure. It is evident from the TEM images that the mutual boundary tends to minimize forming a “neck” in the array of grains, which represents grain boundaries arranged by grain to grain unit cell clusters. The linearity of grains indicates good crystallographic coherence. This result differs from those in other researches, in which several agglomerates are composed of small grains. Wang et al. reported the fabrication of WO_3 Nanofibers, when the TEM image of the sample showed a grained fiber structure after calcination [26]. Kumar et al. reported the “fabrication of TiO_2 nanofibers by electrospinning”, when observing that the micrograph of nanofibers consisted of several agglomerated grains when heated at 650°C [27]. A higher PZ concentration improves the structure of PZ fibers, due to each highly concentrated PZ molecule being closer together than those with a low concentration. When the temperature is high enough to eliminate the polymer between molecules, PZ molecules will connect more easily between crystals at a higher concentration.

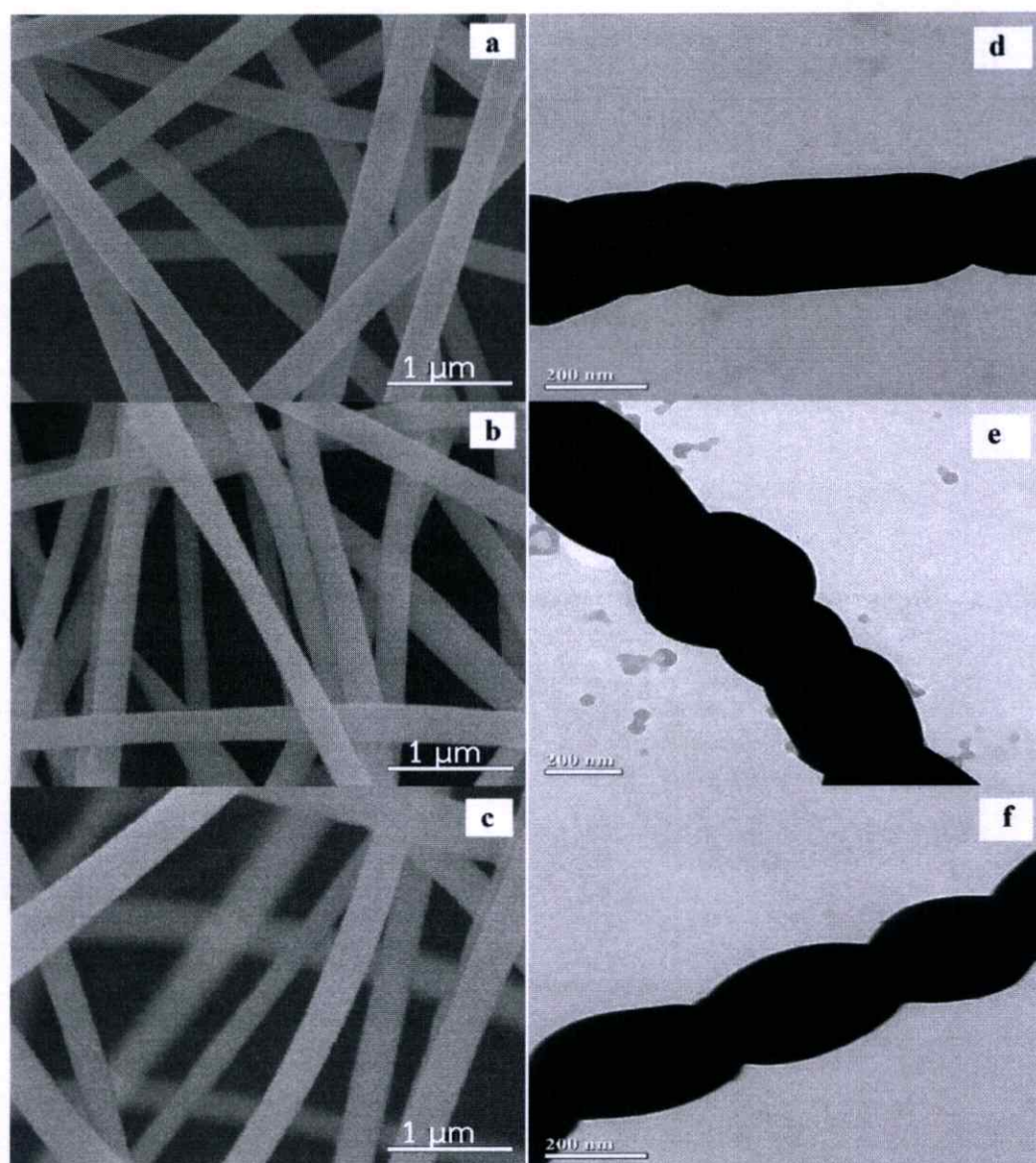


Figure 4.7 (a)–(c) SEM micrographs and (d)–(f) TEM micrographs of the PZ fibers calcined at 650°C with the PZ/PEO volume ratio of 10:3 at PZ concentrations of 0.7, 0.9 and 1.0 M, consecutively.

4.3.3 Effect of Calcination Temperature

Figure 4.8(a)–(h) shows SEM images of the as-spun and PZ fibers, with the volume ratio of 10:3 at PZ concentrations of 1.0 M, and calcined at 650°C, 750°C and 850°C, consecutively. All the calcined samples present non-woven fabrics, with interconnected continuous free space between the fibers to form a structure of

packed particles or crystallites. While the PEO was removed selectively during calcinations at 650°C, the fiber structures remained continuous, with an average diameter of 300 ± 64 nm, as seen in Figure 4.8(b). The diameter of the fibers, following calcinations at various temperatures, appeared smaller on average than the as-spun fibers, for example, the average fiber diameter was decreased from 439 ± 74 nm [Figure 4.8(a)] to 300 ± 64 nm after calcination at 650°C. The reduction in size of the nanofibers should be attributed to their loss of PEO and the crystallization of PbZrO_3 . The fibrous material is considerably more brittle and delicate than the as-spun materials. The decrease in the flexibility of the fibers may result from a high fraction of crystallinity and/or cross-linking between fibers during calcination. Whereas, after calcinations at 750°C and 850°C [Figure 4.8(c) and (d)], the fibers became rough and presented a detailed non-woven electrospun mat, and through interpenetration and entanglement of molecular chains after annealing, a soldering-like attachment of the nanofibers was visualized at their junction points, when the average diameter of the fibers was 471 ± 60 and 516 ± 69 nm, consecutively. The enhancement of this fiber diameter is due to grain growth by temperature.

In addition, the effect of feeding rate on the fiber was studied as well, and showed that when decreasing the feeding rate from 2 ml/h to 0.5 ml/h, the average fiber diameter was decreased from 439 ± 74 nm to 378 ± 43 nm. This result corresponded with the research of Rutledge and co-workers [28], in which the jet solution became thinner when the feeding rate decreased. Furthermore, it was observed that the nature of nanofibers was changed dramatically, and a necklace-like structure of packed particles or crystallites became prominent when decreasing the feeding rate of the precursor solution from 2 ml/h [Figure 4.8(a)–(d)] to 0.5 ml/h [Figure 4.8(e)–(h)]. It is clear from these results that the feeding rate has a strong effect on the morphology of calcined PZ/PEO, which are composite nanofibers. This was due to a lower feeding rate, which acts as a function of aging that allows for a greater orientation period of the crystallites, and suggests improvement in crystallization of the PZ nanofibers. In addition, the fiber diameter was decreased when reducing the feeding rate, i.e. the diameter of PZ fiber was decreased from 516 ± 69 nm [Figure 4.9(d)] to 370 ± 39 nm when calcined at 850°C [Figure 4.8(h)]. This may be due to a lower feeding rate by allowing more time for chain entanglement, which causes individual molecules to close up and result in a smaller fiber diameter.

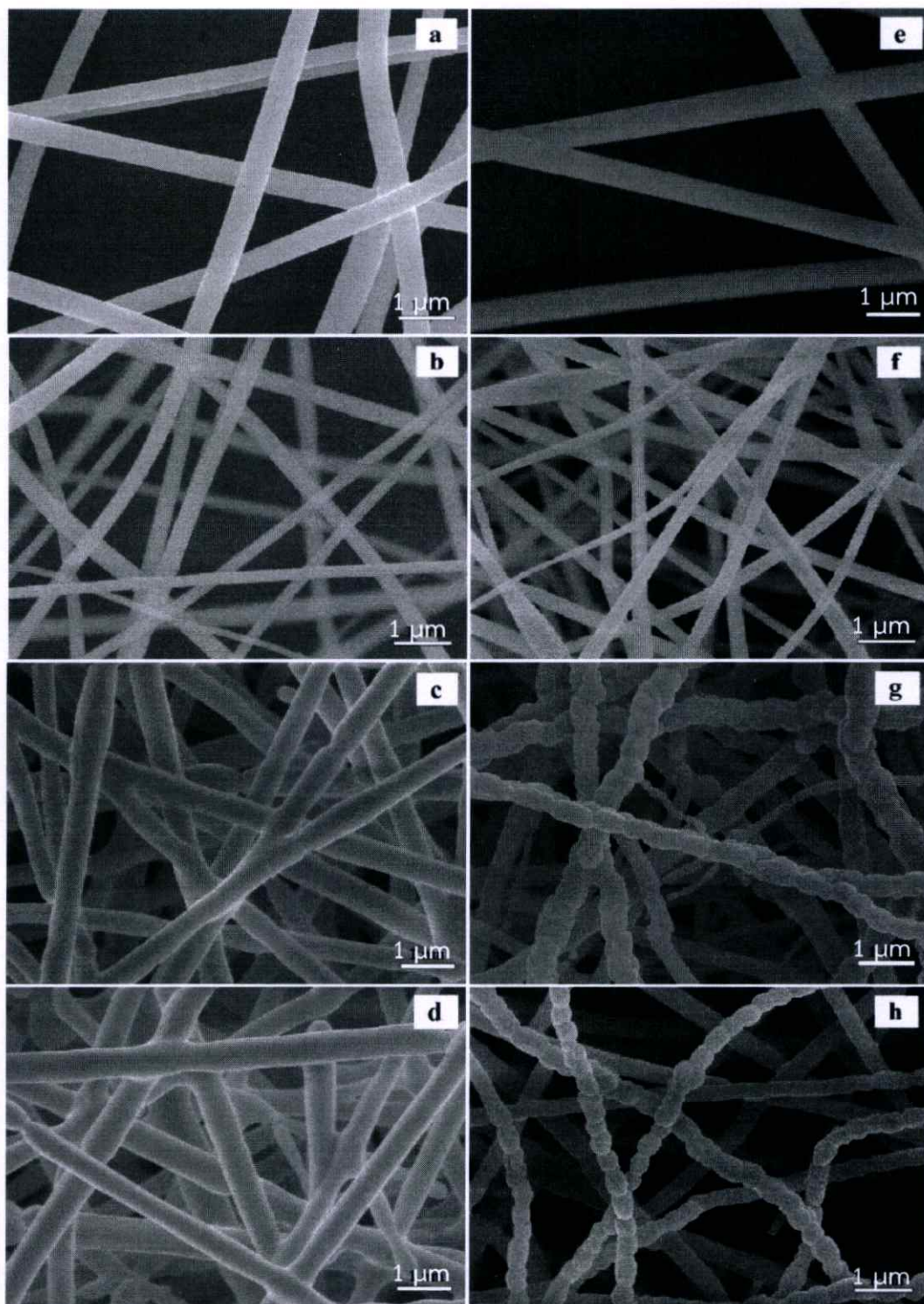


Figure 4.8 SEM micrograph of the fibers using: (a)–(d) feeding rate of 2 ml/h and (e)–(h) feeding rate of 0.5 ml/h of the as-spun fibers with the volume ratio of 10:3 at PZ concentrations of 1.0 M, and PZ fibers calcined in air for 4 h at 650°C, 750°C and 850°C, consecutively.

4.3.4 Thermal Properties

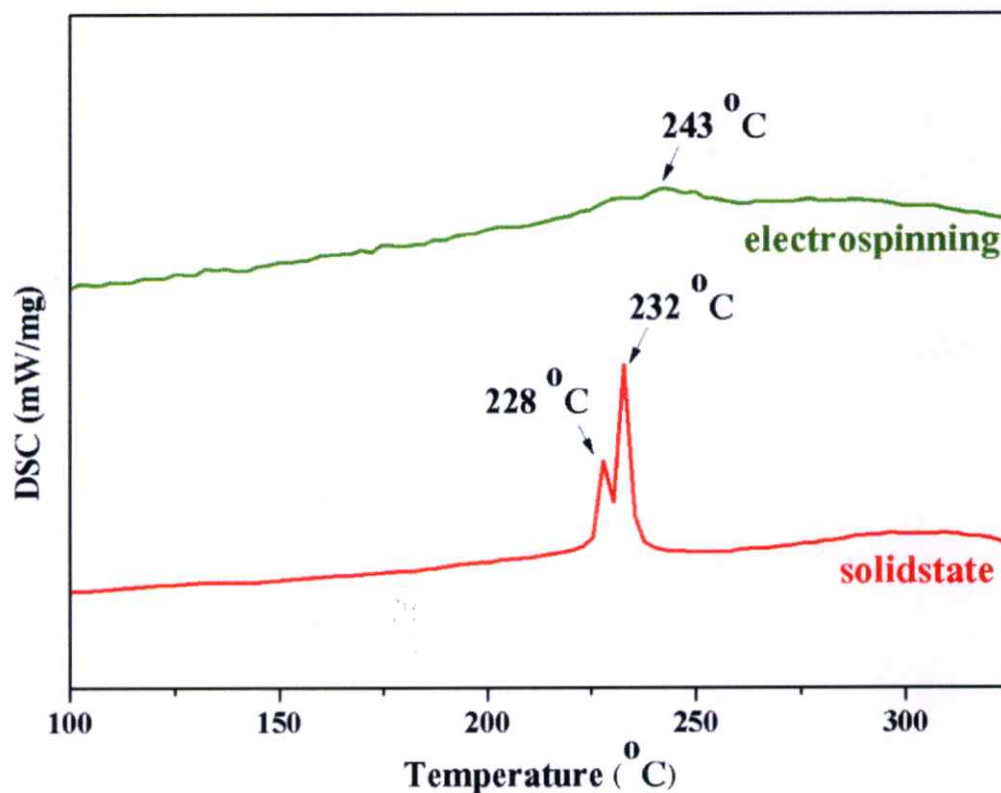


Figure 4.9 Typical DSC curves for PZ fibers and PZO particles.

Figure 4.9 shows results of the DSC for the PZ particle and PZ fibers from using the solid state and electrospinning method, respectively. The DSC result of the PZ particle shows two sharp and distinct endothermic peaks, which become closer together. The lower temperature corresponds to the transition temperature of the antiferroelectric (AFE) \rightarrow ferroelectric (FE) phase transition, while the higher temperature corresponds to the FE \rightarrow paraelectric (PE) phase transition. Whereas, the FE intermediate phase is not established in PZ fibers. However, the AFE-PE phase transition becomes broader progressively. This result is likely in line with the research of Lu et al. [29], who present the DSC curve with neither a transition phase nor an endothermic peak when synthesized BT is in nanosize. It is clear from the figure that the PZ fibers undergo a successive phase transition from orthorhombic to cubic

phase at 243°C, showing a Curie temperature rise of nearly 13°C, when comparing with a normal PZ particle. It is well known that the grain sizes in PZ particles are usually in micrometer range, which is more than 100 times larger than those of PZ fibers. The reduced grain size in electrospun PZ fibers causes larger grain boundary areas, and relieves internal stresses further in materials, due to grain boundary sliding. Smaller internal stresses, which are relaxed by grain boundaries, could decrease the free energy of the antiferroelectric phase, thus increasing the Curie temperature. Therefore, nanostructured PZ fibers have a higher T_c than PZ particles.

4.4 Summary

In summary, this study successfully prepared PZ fibers by the electrospinning method. The as-spun PZ/PEO composite fibers were relatively uniform and had a smooth surface. Beads or agglomerated nanofibers were not observed. The PZ nanofibers, with a well-developed perovskite structure, were obtained successfully at the calcination temperature of 850°C for 4 h. Furthermore, it is clear that the PZ fibers undergo a successive phase transition from orthorhombic to cubic phase at 243°C, showing a Curie temperature rise of nearly 13°C, when comparing with a normal PZ particle.

REFERENCE

- [1] Khaled, S.M., Sui, R., Charpentier, P. A., and Rizkalla, A. S. 2007. "Synthesis of TiO₂-PMMA Nanocomposite: using Methacrylic Acid as a Coupling Agent." *Langmuir*. 23[7] : 3988-3995.
- [2] Zhao, J., Jia, C., Duan, H., Sun, Z., Wang, X., and Xie, E. 2008. "Structural and Photoluminescence Properties of Europium-doped Titania Nanofibers Prepared by Electrospinning Method." *J. Alloys Compd.* 455[1-2] : 497-500.
- [3] Pukird, S., Chamninok, P., Polsongkram, D., Inchidjuy, P., Tipparach, U., and Chow, L. 2008. "Synthesis of ZnO Nanowires and Nanobelts by Thermal Evaporation." *CMU J. Nat. Sci.:* Special Issue on Nanotechnology. 7 [1] : 95-98.
- [4] Liu, Q., Li, B., Gong, J., Sun, Y., and Li, W. 2008. "Preparation and Luminescent Properties of One-Dimensional [Ru(Bphen)₂dppz]Cl₂/PVP Composite Fibers by Electrospinning." *J. Alloys Compd.* 466 : 314-318.
- [5] Cai, Z., Li, J., Wang, Y. 2010. "Fabrication of Zinc Titanate Nanofibers by Electrospinning Technique." *J. Alloys Compd.* 489 : 167-169.
- [6] Mai, M., Lin, C., Xiong, Z., Xue, H., and Chen, L. 2009. "Preparation and Characterization of Lead Zirconate Titanate Ceramic Fibers with Alkoxide-Based Sol-Gel Route." *J. Phys.: Conference Series*. 152 : 012077.
- [7] Chen, X., Galos, R., and Shi, Y. 2011. "A Self Powered PZT Nanofiber Composite Sensor for Structural Health Monitoring." The 6th International Workshop on Advanced Smart Materials and Smart Structures Technology ANCRISST2011. Dalian, China.
- [8] Dharmaraj, N., Kim, C.H., and Kim, H.Y. 2005. "Pb(Zr_{0.5}Ti_{0.5})O₃ Nanofibres by Electrospinning." *Mater. Lett.* 59 : 3085-3089.
- [9] Wu, J., and Coffey, J.L. 2007. "Emissive Erbium-Doped Silicon and Germanium Oxide Nanofibers Derived from an Electrospinning Process." *Chem. Mater.* 19 : 6266-6276.
- [10] Tuttle, R.W., Chowdury, A., Bender, E.T., Ramsier, R.D., Rapp, J.L., and Espe, M.P. 2008. "Electrospun Ceramic Fibers: Composition, Structure and the Fate of Precursors." *Appl. Surf. Sci.* 254 : 4925-4929.

- [11] Li, H., Sun, Y., Zhang, W., and Pan, W. 2010. "Preparation of Heterostructured Ag/BaTiO₃ Nanofibers via Electrospinning." **J. Alloys Compd.** 508 : 536-539.
- [12] Xie, S.H., Li, J.Y., Liu, Y.Y., Lan, L.N., Jin, G., and Zhou, Y.C. 2008. "Electrospinning and Multiferroic Properties of NiFe₂O₄-Pb(Zr_{0.52}Ti_{0.48})O₃ Composite Nanofibers". **J. Appl. Phys.** 104 : 024115.
- [13] Chen, W., Chen, X.F., Wang, Z.H., Zhu, W., and Tan, O.K. 2009. "Microstructures, Ferromagnetic, and Ferroelectric Properties in Polyvinylpyrrolidone-Assisted CoFe₂O₄/Pb(Zr_{0.53}Ti_{0.47})O₃ Multiferroic Composite Thick Films." **J. Mater. Sci.** 44 : 4939-4943.
- [14] Tang, X.G., Ding, A.L., and Luo, W.G. 2001. "Surface Morphology and Chemical States of Highly Oriented PbZrO₃ Thin Films Prepared by a Sol-Gel Process." **Appl. Surf. Sci.** 174 : 148-154.
- [15] Liu, Y., Hao, X., Zhou, J., Xu, J., and An, S. 2011. "Effects of Raw Materials on Microstructure and Dielectric Properties of PbZrO₃ Antiferroelectric Thin Films Prepared via Sol-Gel Process." **J. Alloys Compd.** 509 : 8779-8782.
- [16] Vittayakorn, N., and Boonchom, B. 2011. "Effect of BiAlO₃ Modification on the Stability of Antiferroelectric Phase in PbZrO₃ Ceramics Prepared by Conventional Solid State Reaction." **J. Alloys Compd.** 509 : 2304-2310.
- [17] Cakare, L., Kosec, M., and Malic, B. 2000. "Sol-Gel Processing of PbZrO₃ Thin Films." **J. Sol-Gel Sci. Technol.** 19 : 603-606.
- [18] Charoonsuk, P., Wirunchit, S., Muanghlua, R., Niemcharoen, S., Boonchom, B. and Vittayakorn, N. 2010. "The Phase Evolution with Temperature in 0.94PbZrO₃-0.06Pb(Mg_{1/2}W_{1/2})O₃ Antiferroelectric Ceramic." **J. Alloys Compd.** 506[1] : 313-316.
- [19] He, J.H., Wan, Y.Q., and Yu, J.Y. 2008. "Effect of Concentration on Electrospun Polyacrylonitrile (PAN) Nanofibers." **Fiber. Polym.** 9[2] : 140-142.
- [20] Maensiri, S., Nuansing, W., Klinkaewnarong, J., Laokul, P., and Khemprasit, J. 2006. "Nanofibers of Barium Strontium Titanate (BST) by Sol-Gel Processing and Electrospinning." **J. Colloid Interface Sci.** 297 : 578-583.
- [21] Ion, E.D., Malic, B., and Kosec, M. 2007. "Characterization of PbZrO₃ Prepared using an Alkoxide-Based Sol-Gel Synthesis Route with Different Hydrolysis Conditions." **J. Eur. Ceram. Soc.** 27 : 4349-4352.

- [22] Zhang, Z., Li, X., Wang, C., Wei, L., Liu, Y., and Shao, C. 2009. "ZnO Hollow Nanofibers: Fabrication from Facile Single Capillary Electrospinning and Applications in Gas Sensors." **J. Phys. Chem.** 113 : 19397-19403.
- [23] Kitaoka, K., Kozuka, H., and Yoko, T. 1998. "Preparation of Lead Lanthanum Zirconate Titanate (PLZT, (Pb,La)(Zr,Ti)O₃) Fibers by Sol-Gel Method." **J. Am. Ceram. Soc.** 81[5] : 1189-1196.
- [24] Wang, Y., and Santiago-Aviles, J.J. 2004. "Synthesis of Lead Zirconate Titanate Nanofibres and the Fouriertransform Infrared Characterization of Their Metallo-Organic Decomposition Process." **Nanotechnology.** 15 : 32-36.
- [25] Le Viet, A., Reddy, M.V., Jose, R., Chowdari, B. V. R., and Ramakrishna, S. 2010. "Nanostructured Nb₂O₅ Polymorphs by Electrospinning for Rechargeable Lithium Batteries." **J. Phys. Chem.** 114 : 664-671.
- [26] Wang, G., Ji, Y., Huang, X., Yang, X., Gouma, P.I., and Dudley, M. 2006. "Fabrication and Characterization of Polycrystalline WO₃ Nanofibers and Their Application for Ammonia Sensing." **J. Phys. Chem. B.** 110 : 23777-23782.
- [27] Kumar, A., Jose, R., Fujihara, K., Wang, J., and Ramakrishna, S. 2007. "Structural and Optical Properties of Electrospun TiO₂ Nanofibers." **Chem. Mater.** 19 : 6536-6542.
- [28] Rutledge, G.C., and Fridrikh, S.V. 2007. "Formation of Fibers by Electrospinning." **Adv. Drug Deliver. Rev.** 59[14] : 1384-1391.
- [29] Lu, S.W., Lee, B.I., Wang, Z.L., and Samuels, W.D. 2000. "Hydrothermal Synthesis and Structural Characterization of BaTiO₃ Nanocrystals." **J. Crystal Growth.** 219 : 269-276.

CHAPTER 5

THE EFFECT OF THAI GLUTINOUS RICE STARCH ON THE SYNTHESIS OF LEAD ZIRCONATE (PbZrO₃) NANOFIBERS VIA THE ELECTROSPINNING METHOD

Based on article published in *Journal of Nanoscience and Nanotechnology* 13 (2013) 3700–3704

This study synthesized blended lead zirconate (PbZrO₃; PZ)/poly(ethylene oxide)(PEO)/Glutinous rice starch (GRS) nanofibers by the electrospinning method. A number of parameters such as the ratio between PEO and GRS and calcination temperature have been studied. The as-spun PZ/PEO/GRS composite and PZ fibers were characterized by TG-DTA, X-ray diffraction, FT-IR and SEM, respectively. SEM results showed that smooth and continuous fibers were obtained at the volume ratio of 10:2:1, PZ/PEO/GRS. After calcination of the as-spun PZ/PEO/GRS composite nanofibers at 650°C for 4 h, PZ nanofibers with perovskite structure were obtained successfully. The fibers had a uniform and smooth surface without grain boundaries. However, when the calcinations temperature increased to 750°C and 850°C, the fiber represented a necklace-like structure with grain boundaries arranged by grain to grain unit cell clusters.

5.1 Introduction

In recent years, one-dimensional nanostructures of metal oxides and related materials, such as nanowires and nanofibers, have been a subject of intense research because of their potential applications as building blocks in various nanotechnologies, which include mechanics, photonics, electronics, and sensing [1]. Over the past few decades, PZ and PZ-based systems have been synthesized and utilized massively in forms of bulk ceramics or crystalline films [2]. In addition, there has been no previous report in the literature on the fabrication of PZ fibers by electrospinning. The high surface to volume ratio is an attractive characteristic that

can be achieved from nanofibers. With miniaturization of electronic devices, nanofibers of piezoelectric material are currently attracting a great deal of interest in the design of smart materials, due to their novel properties that are significantly different from their bulk, such as mechanical and electrical property [3]. Antiferroelectric lead zirconate (PbZrO_3 : PZ) materials have received increasing attention as potential applications in micro-actuators and high energy storage capacitors [4]. The free energy difference between the antiferroelectric (AFE) and ferroelectric (FE) phase makes it possible to force phase switching from the AFE to FE phase by applying an electric field [5]. At room temperature, PZ has an orthorhombic structure with the lattice parameters, $a = 5.884 \text{ \AA}$, $b = 11.768 \text{ \AA}$ and $c = 8.22 \text{ \AA}$ [6]. Electrospinning is a simple and convenient method for producing fibers with polymeric, composite or ceramic compositions. Electrospinning, in combination with the conventional sol-gel process, has been extended recently to fabricate a variety of ceramic nanofibers [7]. From this technique, the ceramic nanofibers and conventional sol-gel precursors are mixed with various kinds of polymers, such as poly(ethylene oxide) (PEO), poly(vinylpyrrolidone) viscosity [8]. However, these polymers are fairly expensive. Starch is a natural high molecular weight polysaccharide composed of glucose units. Most starches consist of two components: a linear glucose polymer amylose, and a branched polymer amylopectin. Amylose most likely accounts for the disintegrant properties of starch by containing up to 6,000 glucose units connected by α -1,4 linkage. On the other hand, amylopectin is a good binder. It has a highly branched structure consisting of short linear chains with a degree of polymerization ranging from 10 to 60 glucose units, which are connected to each other by α -1,6 linkage [9]. Glutinous rice is of a kind commonly cultivated in Thailand, which has low cost, high viscosity and high amylopectin (99.70%). Glutinous rice starch (GRS) is used widely in food industries, but few of its applications have been reported in the electronics business. Therefore, this study synthesized lead zirconate fibers by the electrospinning method using solution that contained PEO, Thai GRS and a sol-gel precursor solution of PZ. The ratio between PEO, GRS and PZ concentrations of the precursor solution, which could result in formation of PZ fibrils, was varied.

5.2 Experimental Procedure

In the preparation of PZ solution by a sol-gel process, lead acetate trihydrate [$\text{Pb}(\text{CH}_3\text{COO})_2 \cdot 3\text{H}_2\text{O}$, puriss; Sigma- Aldrich], and zirconium (IV) propoxide solution (~70% in propanol; Fluka) were used as precursors, and 2-methoxyethanol (puriss; Sigma-Aldrich) was selected as a solvent. Firstly, lead acetate trihydrate was dissolved in 2-methoxyethanol, which could act as didentate chelating ligands. This allowed the sol to be stable for a long period of time at room temperature. Then, this solution was stirred for 30 minutes at 70°C, with 3 mol% excess lead acetate trihydrate added to compensate for evaporation during calcination at high temperature, whereas, zirconium (IV) propoxide was dissolved in 2-methoxyethanol at room temperature for 30 minutes while stirring. Next, these two solutions were mixed together by heating and stirring to form a sol, with acetic acid added to it in order to prevent precipitation of the precursor solution. The precursor solution, which had final concentrations of 1.0 M, was obtained after stirring at 70°C for 1 h. In preparing PZ/PEO/GRS solution for electrospinning, the proper solution parameter had to be found for producing lead zirconate nanofibers, after which the precursor solution was mixed with poly(ethylene oxide) (PEO, MW = 300,000; Aldrich) solution (5 wt.% in ethanol) and Glutinous rice starch (GRS; Newgrade, packed and distributed by Thai Wah Food Products Public Company Limited) solution (5 wt.% in water) in volume ratios of 10:2:1, 10:1.5:1.5, 10:1:2, and 10:0:3, consecutively. The viscosity of GRS solution was measured by a Brookfield viscometer (LVT 71420, Brookfield Engineering Laboratories, Inc. Stoughtonma, 02072, USA). After stirring at room temperature for 1 h, the mixture was loaded into a plastic syringe, which was connected to a metallic needle and linked to a syringe pump (NE-1000, New Era Pump Systems, Inc. Wantagh, NY) to control the feeding rate of the solution. The positive terminal of high voltage power supply (ES30P-5W, Gamma High Voltage Research Inc., Ormond Beach, FL) was connected to the needle tip of the syringe, while the collector covered with aluminum foil worked as a counter electrode. The distance between the needle tip of the syringe and collector was fixed at 15 cm, and the feeding rate of the solution was 0.5 mL/h. When the voltage applied between two electrodes reached 10 kV, non-woven mat of PZ/PEO/GRS composite fibers accumulated on the surface of the aluminum foil. The reaction of the as-spun

composite nanofibers, which took place during heat treatment, was investigated by differential thermal analysis (DTA; Shimadzu) and thermogravimetry analysis (TGA; Shimadzu), using a heating rate of 10°C/min in air that ranged from room temperature to 1,300°C. X-ray diffraction (XRD; Bruker-D8 Advance) using $\text{CuK}\alpha$ radiation was used to determine the phases formed and optimum firing temperatures for formation of the desired phase. The room-temperature FT-IR spectrum range of 4,000–370 cm^{-1} was recorded by a Perkin Elmer Spectrum GX FT-IR/FT-Raman spectrometer, with 8 scans and a resolution of 4 cm^{-1} using KBr pellets. Finally, a scanning electron microscope (SEM, JEOL JSM5910LV) was used to observe the microstructures of the PZ fibers.

5.3 Results and Discussion

The morphology of the as-spun and calcined PZ/PEO/GRS composite fibers was revealed by scanning electron microscopy (SEM). Figure 5.1 shows SEM photographs of the as-spun PZ/PEO/GRS volume ratio of 10:2:1 compared to the as-spun PZ/PEO volume ratio of 10:2, with a PZ concentration of 1.0 M. Comparison between Figure 5.1(a) and (b) shows that the formation of beads decreases when adding GRS into the solution. The as-spun PZ/PEO/GRS composite fibers were relatively uniform, with a smooth surface and average diameter of 395 ± 59 nm. Therefore, it can be said that the addition of GRS improves the appearance of the fiber, but the real controlling factor is the viscosity of the polymer solution. Viscosity of the polymer solution was measured at the same weight ratio by a Brookfield viscometer, which found that viscosity of GRS solution (575 centipoise) is greater than that of PEO solution (175 centipoise). The higher viscosity of GRS solution resulted from chain entanglement, which causes a significant impact on the electrospinning process [10]. GRS is a naturally high molecular weight polysaccharide composed of glucose units. It contains two types of glucose polymers, i.e., amylose and amylopectin. Amylose is a linear polymer containing up to 6,000 glucose units. Amylopectin has a highly branched structure consisting of short linear chains, with a degree of polymerization ranging from 10 to 60 glucose units [9]. Therefore, adding GRS into the solution can enhance the chain entanglement of the molecular chain, which makes the viscosity increase.

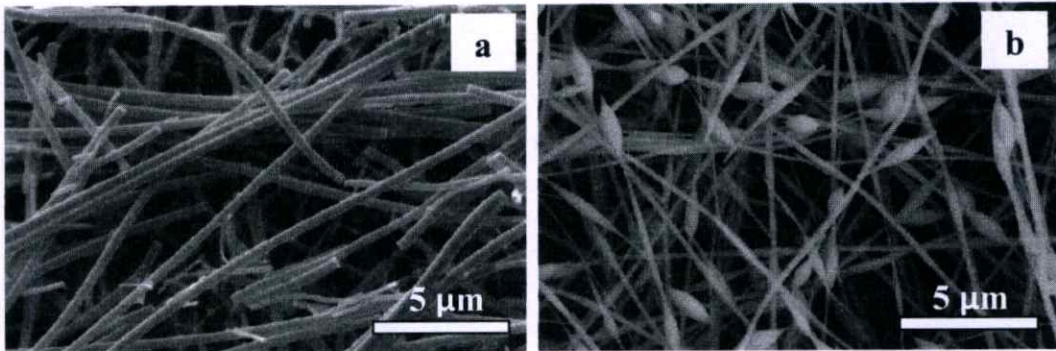


Figure 5.1 SEM photographs of the as-spun PZ/PEO/GRS volume ratios of 10:2:1 (a) compared with the as-spun PZ/PEO volume ratios of 10:2 (b), with a PZ concentration of 1.0 M.

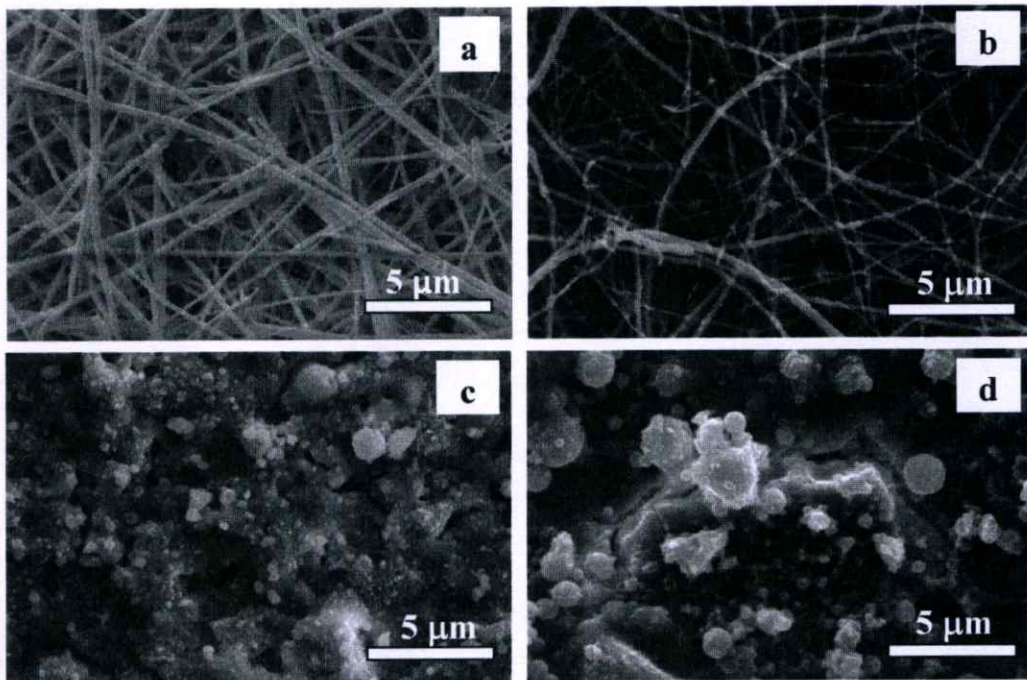


Figure 5.2 SEM micrographs of the as-spun PZ/PEO/GRS nanofibers with a PZ concentration of 1.0 M at the PZ/PEO/GRS volume ratios of (a) 10:2:1, (b) 10:1.5:1.5, (c) 10:1:2 and (d) 10:0:3, consecutively.

Figure 5.2 shows SEM photographs of the as-spun PZ/PEO/GRS composite, with a PZ concentration of 1.0 M, using the PZ/PEO/GRS volume ratios of 10:2:1, 10:1.5:1.5, 10:1:2 and 10:0:3, consecutively. Figures 5.2(a) and 5.2(b) illustrate that the fibers present a detailed non-woven electrospun mat. When the amount of GRS increased and that of PEO decreased, the fiber diameter was reduced and formation of beads observed. Figures 5.2(c) and 5.2(d) indicate that continuous fibers could not form, as the jet broke up into droplets. This may be due to the compatibility of GRS and precursor solution, which is still not completely compatible. Thus, optimum conditions determined from the solution had a PZ/PEO/GRS volume ratio of 10:2:1.

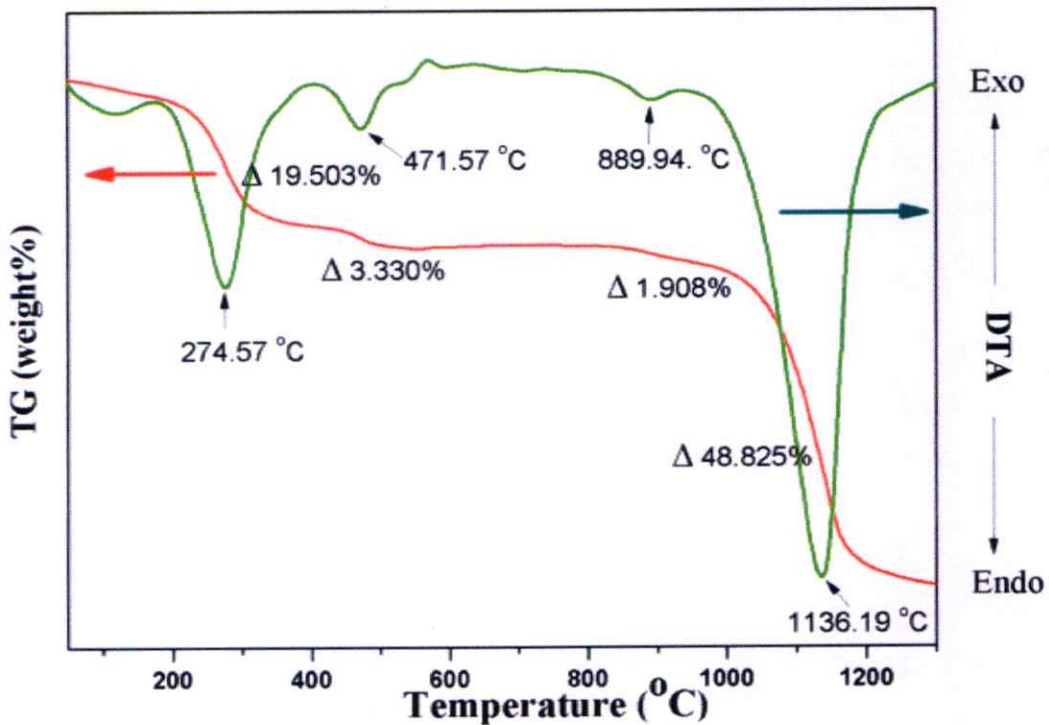


Figure 5.3 TG-DTA curves of thermal decomposition of the as-spun PZ/PEO/GRS composite nanofiber, with a PZ concentration of 1.0 M at the PZ/PEO volume ratio of 10:2:1.

Thermal analysis was carried out to investigate the decomposition process of the fiber. The results of TG and DTA analyses of the as-spun PZ/PEO/GRS composite fibers are shown in Figure 5.3. The endothermic peak in the DTA curve, and weight loss (~3%) in the TGA curve, were observed below 200°C, which indicated a loss of moisture [11]. The endothermic peak and a weight loss (~20%) in the range of 200°C to 350°C occurred through a loss of trapped solvent and GRS in the as-spun fibers, whereas, an endothermic peak and a weight loss (~3%) in the range of 400°C to 550°C were due to the degradation of PEO. According to their thermal properties, GRS and PEO decomposed at a temperature of about 300°C and 450°C, respectively, which supported the loss of GRS and PEO, consecutively. The TG and DTA curve indicated no change in the weight loss range from 550°C to 850 °C, which possibly corresponded to formation of the perovskite phase.

Based on the TG–DTA results, the mixture was calcined at various temperatures ranging from 550°C to 850°C, with dwell times of 4 h, and the heating/cooling rates ranged around 5°C/min in a closed alumina crucible, in order to investigate the perovskite phase formation. The crystalline phases of PZ fibers were revealed at various calcined temperatures by X-ray diffraction spectra. Figure 5.4 shows the XRD patterns of PZ/PEO/GRS composite fibers calcined at different temperatures. As-spun PZ/PEO/GRS composite fibers calcined at 550°C for 4 h revealed that crystallization of the perovskite phase began to form. However, the main peak intensity of the PZ phase was weak, which implied that the fiber was not fully crystallized. When the calcination temperature was 650°C, the crystalline PZ fibers were obtained successfully with a well-developed perovskite structure. According to JCPDS card no. 75-1607, the diffraction peaks can be indexed as an orthorhombic perovskite structure of lead zirconate. No other peaks could be observed in the XRD patterns, which indicated that the sample is free from lead oxide or any other crystalline materials. However, when increasing the calcinations temperature to 750°C, intensities of the main peaks decreased. This behavior is similar to the XRD result of TiO₂ nanofibers [12] and PZT fibers [13] that show lower diffraction intensity when increasing calcinations temperature. This may be due to the enhancement of driving energy that caused the orientation of atoms to cluster, whereas, after calcination at 850°C, the peak intensity increased again, as a result of grain growth by temperature [14].

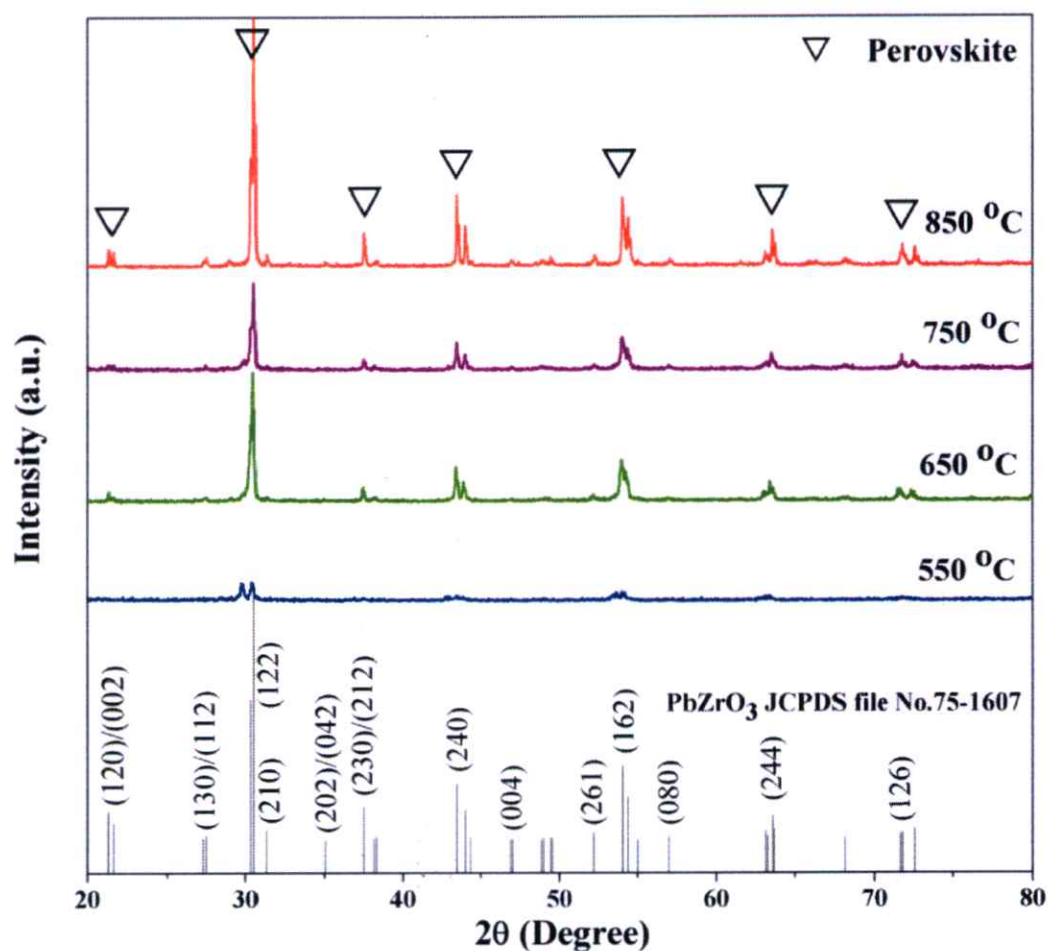


Figure 5.4 XRD patterns of electrospun PZ/PEO/GRS composite nanofibers, with a PZ concentration of 1.0 M at the PZ/PEO volume ratio of 10:2:1, calcined in air for 4 h at different temperatures.

Formation of the calcined PZ nanofibers was confirmed further by the FT-IR spectra, as shown in Figure 5.5. The spectrum of the as-spun PZ/PEO/GRS composite fibers shows multiple absorption bands in the region of $1,000$ to $4,000\text{ cm}^{-1}$, which corresponds to the stretching and bending vibrations of polymers, organic solvent and moisture. Peaks of around $1,450\text{ cm}^{-1}$ correspond to the aliphatic CH group vibrations of the CH_2 mode [15]. The wave number at $\sim 1,600\text{ cm}^{-1}$ and broad peak at around $3,400\text{ cm}^{-1}$ both correspond to the O-H stretching vibration [16]. After calcination at 550°C for 4 h, it was found that these peaks almost disappear,

indicating that most of the polymers and other organics have been removed. This study can guarantee that its sample was free from GRS and PEO polymer. As the calcination temperature increases to 650°C, 750°C and 850°C, the appearance of an absorption peak at $\sim 548\text{ cm}^{-1}$ is attributed to Zr-O stretching vibration [17], which corresponds to the polycrystalline fiber obtained.

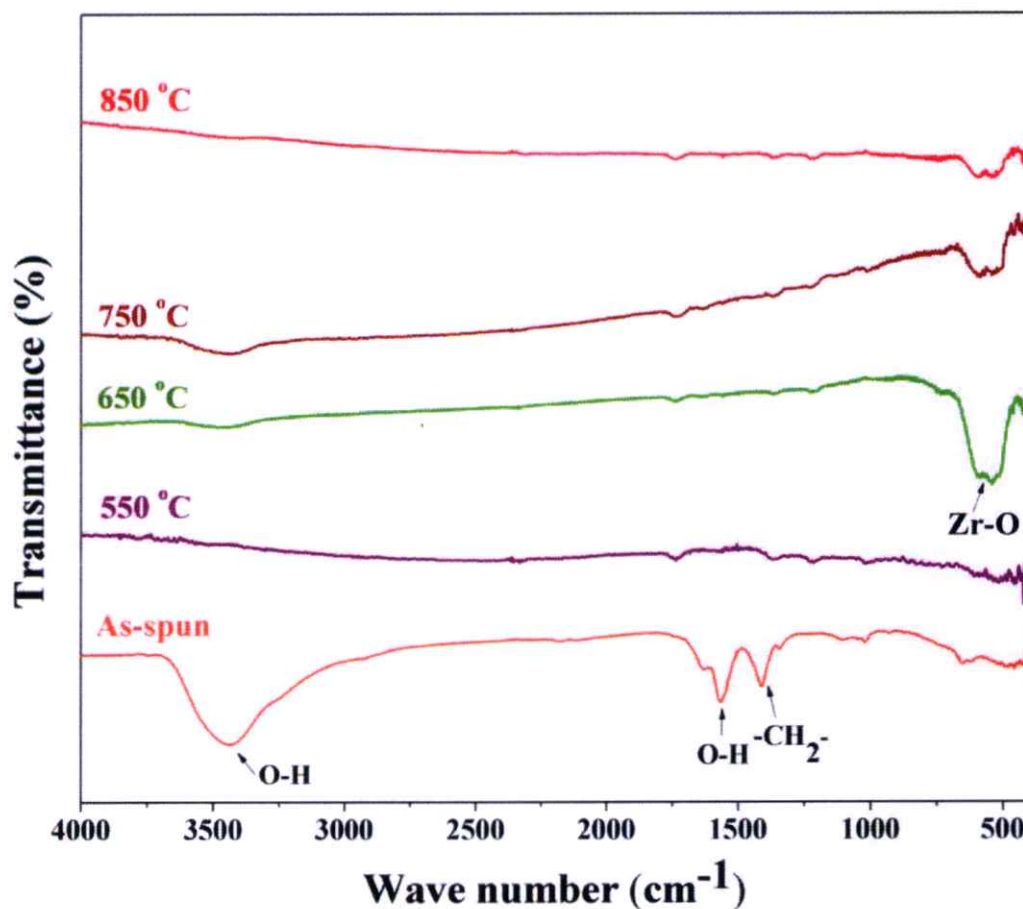


Figure 5.5 FTIR spectra of electrospun PZ/PEO/GRS composite nanofiber, with a PZ concentration of 1.0 M at the PZ/PEO volume ratio of 10:2:1, calcined in air for 4 h at different temperatures.

Figure 5.6 shows SEM images of the as-spun and PZ fibers, with a volume ratio of 10:2:1 at PZ concentrations of 1.0 M, calcined at 650°C, 750°C and 850°C, consecutively. All the calcined samples present non-woven fabrics and form a structure of packed particles or crystallites. Those calcined at 650°C [Figure 5.6(b)] represent a uniform and smooth surface, with a diameter of 229 ± 46 nm. From this figure, grain boundaries were not observed at all, which suggests that there is a highly ordered arrangement in the fiber, as shown in Figure 5.7(a). The result was consistent with the XRD pattern that showed a high intensity of XRD peak. Furthermore, this result is different from those in other researches that had a soldering-like attachment of nanofibers at their junction after annealing [18]. After calcination at 750°C [Figure 5.6(c)] the fiber remained as continuous structures with a diameter of 252 ± 63 nm. It can be seen that following calcinations, the diameter of the fibers appears smaller on average than that of the as-spun fibers (395 ± 59 nm) [Figure 5.6(a)]. The reduction in size of the nanofibers should be attributed to their loss of PEO and GRS and the crystallization of PbZrO_3 . The fiber represents a necklace-like structure, which may be due to the enhancement of driving energy by increasing temperature, resulting from the macroscopic migration of the grain boundary, in the direction that reduces the energy of the system [19]. This is shown in Figure 5.7(b) that represents grain boundaries arranged by grain to grain unit cell clusters, which is consistent with XRD results showing a peak with lower intensity than the fabrication of TiO_2 nanofibers of Shao et al [12]. Their results exhibited a necklacelike structure that represented lower diffraction intensity after calcinations at a higher temperature. However, after calcinations at 850°C [Figure 5.6(d)], the nature of nanofibers was changed dramatically, and a necklace-like structure of packed particles or crystallites was prominent. Furthermore, the average fiber diameter increased with increased calcination temperature, for example, the average fiber diameter at 650°C and 850°C is 229 ± 46 nm and 453 ± 103 nm, respectively, after calcination. The enhancement of this fiber diameter is due to the grain growth by temperature [12, 20]. As a result, the peak intensity of the XRD pattern increased.

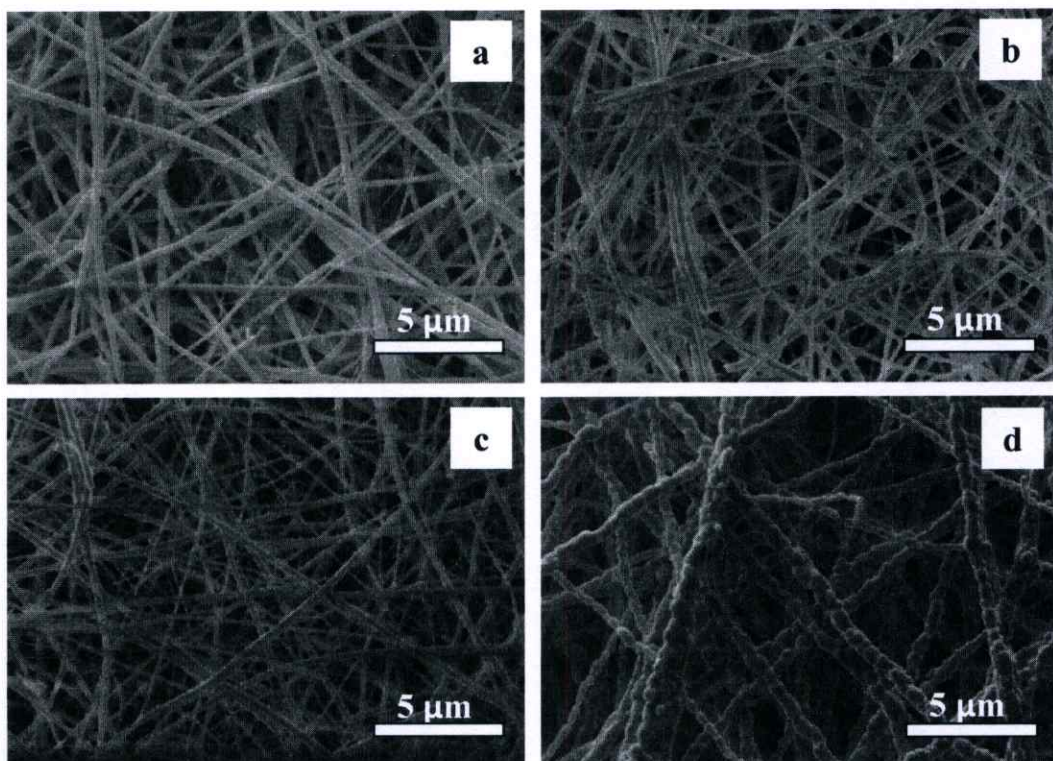


Figure 5.6 SEM micrograph of (a) the as-spun and PZ fibers calcined in air for 4 h at (b) 650°C, (c) 750°C and (d) 850°C.

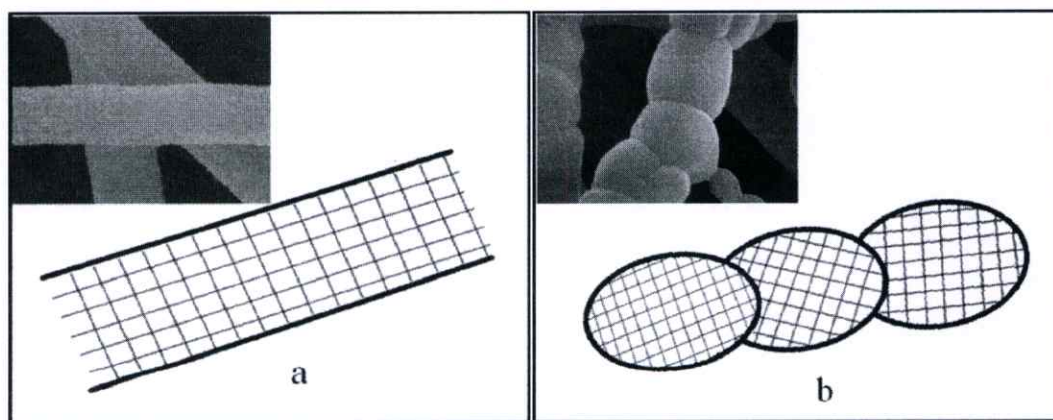


Figure 5.7 Schematic diagram of (a) PZ fibers calcined at 650°C and (b) PZ fibers calcined at 750°C.

5.4 Summary

In summary, this study prepared PZ/PEO/GRS fibers successfully by the electrospinning method. The as-spun PZ/PEO/GRS composite fibers were relatively uniform with a smooth surface. Beads or agglomerated nanofibers could not be observed. The PZ nanofibers, with a welldeveloped perovskite structure, were obtained successfully at the calcination temperature of 650°C for 4 h, while a necklace-like structure of packed particles or crystallites was obtained after calcination at 850°C. Furthermore, the cost of the process can be reduced by successfully putting glutinous rice starch into the solution.

REFERENCE

- [1] Li, D., and Xia, Y. 2003. "Fabrication of Titania Nanofibers by Electrospinning." **Nano Lett.** 3[4] : 555-560.
- [2] Cakare, L., Kosec, M., and Malic, B. 2000. "Sol-Gel Processing of PbZrO₃ Thin Films." **J. Sol-Gel Sci. Tech.** 19 : 603-606.
- [3] Zou, C.W., and Gao, W. 2010. "Fabrication, Optical Properties and Photocatalytic Applications of Metallic Oxides Composite Nanostructures." **Trans. Electr. Electron. Mater.** 11 : 1-10
- [4] Tang, X.G., Ding, A.L., and Luo, W.G. 2001. "Surface Morphology and Chemical States of Highly Oriented PbZrO₃ Thin Films Prepared by a Sol-Gel Process." **Appl. Surf. Sci.** 174 : 148-154.
- [5] Vittayakorn, N., Charoonsuk, P., Kasiansin, P., Wirunchit, S., and Boonchom, B. 2009. "Dielectric Properties and Phase Transition Behaviors in (1-x)PbZrO₃-xPb(Mg_{1/2}W_{1/2})O₃ Ceramics." **J. Appl. Phys.** 106 : 064104.
- [6] Jona, F., Shirane, G., Mazzi, F., and Pepinsky, R. 1957. "X-Ray and Neutron Diffraction Study of Antiferroelectric Lead Zirconate, PbZrO₃." **Phys. Rev.** 105, 849 (1957).
- [7] Sigmund, W., Yuh, J., Park, H., Maneeratana, V., Pyrgiotakis, G., Daga, A., Taylor, J., and Nino, J.C. 2006. "Processing and Structure Relationships in Electrospinning of Ceramic Fiber Systems." **J. Am. Ceram. Soc.** 89[2] : 395-407.
- [8] Yuh, J., Perez, L., Sigmund, W.M., and Nino, J.C. 2007. "Sol-Gel Based Synthesis of Complex Oxide Nanofibers." **J. Sol-Gel Sci. Techn.** 42 : 323-329.
- [9] Peerapattana, J., Phuvarit, P., Srijesdaruk, V., Preechagoon, D., and Tattawasart, A. 2010. "Pregelatinized Glutinous Rice Starch as a Sustained Release Agent for tablet preparations." **Carbohydr. Polym.** 80[2] : 453-459.
- [10] He, J.H., Wan, Y.Q., and Yu, J.Y. 2008. "Effect of concentration on electrospun polyacrylonitrile (PAN) nanofibers." **Fiber. Polym.** 9[2] : 140-142.
- [11] Wang, T., and Kumar, S. 2006. "Electrospinning of Polyacrylonitrile Nanofibers." **J. Appl. Polym. Sci.** 102 : 1023-1029.

- [12] Zhao, J., Jia, C., Duan, H., Li, H., and Xie, E. 2008. "Structural Properties and Photoluminescence of TiO_2 Nanofibers were Fabricated by Electrospinning." *J. Alloy. Compd.* 461, 447-450.
- [13] Meyer, R., Jr., Shrout, T., and Yoshikawa, S. 1998. "Ultra-Fine Lead Zirconate Titanate Fibers Derived From Sol-Gel Technology," *J. Am. Ceram. Soc.* 81[4] : 861-868.
- [14] Thomas, R., Mochizuki, S., Mihara, T., and Ishida, T. 2003. "Preparation of Ferroelectric $\text{Pb}(\text{Zr}_{0.5}\text{Ti}_{0.5})\text{O}_3$ Thin Films by Sol-Gel Process: Dielectric and Ferroelectric Properties." *Mater. Lett.* 57[13] : 2007-2014.
- [15] Maensiri, S., Nuansing, W., Klinkaewnarong, J., Laokul, P., Khemprasit, J. 2006. "Nanofibers of Barium Strontium Titanate (BST) by Sol-Gel Processing and Electrospinning." *J. Colloid Interface Sci.* 297: 578-583.
- [16] Zhang, Z., Li, X., Wang, C., Wei, L., Liu, Y., and Shao, C. 2009. "ZnO Hollow Nanofibers: Fabrication from Facile Single Capillary Electrospinning and Applications in Gas Sensors." *J. Phys. Chem.* 113 : 19397-19403.
- [17] Mai, M., Lin, C., Xiong, Z., Xue, H., and Chen, L. 2009. "Preparation and Characterization of Lead Zirconate Titanate Ceramic Fibers with Alkoxide-Based Sol-Gel Route." *J. Phys.: conference series* 152 : 012077.
- [18] Dharmaraj, N., Kim, C.H., Kim, H.Y. 2005. " $\text{Pb}(\text{Zr}_{0.5}\text{Ti}_{0.5})\text{O}_3$ Nanofibres by Electrospinning." *Mater. Lett.* 59 : 3085-3089.
- [19] Thompson, C.V. 1990. "Grain Growth in Thin Films." *Annu. Rev. Mater. Sci.* 20, 245-268.
- [20] Lai, J.K. L., Shek, C.H., and Lin, G.M. 2003. "Grain Growth Kinetics of Nanocrystalline SnO_2 for Long-Term Isothermal Annealing." *Scripta Mater.* 49, 441-446.

CHAPTER 6

EFFECT OF CHEMICAL TREATMENT ON PHASE TRANSITION OF LEAD ZIRCONATE NANOFIBERS

Based on article published in *Ferroelectrics* 450 (2013) 49–56

This chapter studied the effect of chemical treatment on phase transition of lead zirconate nanofibers. In this study, lead zirconate (PZ) nanofibers were treated by the solvothermal method in the presence of dimethyl formamide (DMF) solution in order to investigate the effect of chemical treatment on phase transition of PZ nanofibers. The influences of temperature and reaction time are described. The crystal structure, phase transition and morphology of the powders were analyzed by X-ray diffraction (XRD), fourier-transform infrared spectroscopy (FT-IR), differential scanning calorimetry (DSC), and scanning electron microscopy (SEM). The results of DSC confirmed that chemical treatment with DMF could effect the AFE-PE phase transition of PZ nanofibers efficiently. Significant changes of fiber size and morphology after chemical treatment are shown by SEM images.

6.1 Introduction

Lead zirconate (PbZrO_3 ; PZ) material plays an ever-increasing role in electrical and electronic applications including micro-actuators, microelectromechanical systems and high energy storage capacitors [1]. It has a perovskite structure and shows an antiferroelectric nature. At room temperature, bulk lead zirconate has an orthorhombic structure that changes to a cubic one at 230°C [2]. However, antiferroelectric-to-ferroelectric switching properties have not been investigated in detail for highly oriented lead zirconate nanofibers. Nanosize materials with peculiar properties are not expected in a bulk phase and have led already to a breakthrough in various fields of science and technology, owing to their peculiar physical and electrical behavior [3, 4]. Our previous study investigated the phase transformation of lead zirconate nanofibers, and the lack of a sharply defined phase transition in

nanosized samples was observed by using differential scanning calorimetry. This result is consistent with those reported by Lu et al. [5], who did not observe phase transition or endothermic peak if hydrothermally synthesized barium titanate particles were nanosized. Smith et al. [6] reported the absence of an enthalpy peak around the Curie point of nanosized samples. Regarding bulk barium titanate, the DSC trace showed a peak near 130°C, which was indicative of phase transition. However, similar features were not observed in the DSC of nanoparticle samples. It is true that the DSC technique is not very sensitive to the presence of phase transition in nanosized samples. The literature has documented that the developed solvothermal technique, which involves the use of organic solvent instead of water, may provide an alternative to producing low defect materials, and give display of a narrower transition region when compared with normal samples. Badheka et.al [7] examined the phase transformation in barium titanate nanoparticles from metastable cubic to ferroelectric tetragonal phase using solvothermal treatment. The DSC result clearly presented an endothermic peak at 130°C after solvothermal treatment for 24 h at 170°C, using dimethyl formamide as an effective solvent. The solvothermal method is used to synthesize inorganic materials in organic media at elevated temperatures (200°C to 300°C) under autogenous pressure of the organics. The term “solvothermal” means reactions in liquid or supercritical media at temperatures higher than the boiling point of the medium [8]. Dimethyl formamide is a dipolar aprotic solvent with a boiling point at 153°C. It is largely basic and has high dielectric constants. Due to the high basicity of these solvents, cations are highly solvated, but anions are left unsolvated. Therefore, anions in these solvents have high reactivity [8]. Very few papers have dealt with the effect of these solvents in inorganic synthesis. Therefore, this study examined the phase transformation in lead zirconate nanofibers from the paraelectric to antiferroelectric phase by using solvothermal treatment. The optimum condition of chemical treatment for the phase transition in lead zirconate fibers was determined at different temperatures and times using dimethyl formamide as an effective solvent. The different temperatures and times were chosen according to the boiling point of the solvent. The influence of solvothermal treatment with dimethyl formamide solution on the fibers obtained is described and discussed.

6.2 Experimental Procedure

Lead zirconate nanofibers were synthesized by an electrospinning method, which utilized a solution that contained poly (ethylene oxide) (PEO, MW ~ 300,000; Aldrich) and sol-gel precursor solution of lead zirconate as mention in Topic 4.2 After obtaining the lead zirconate fiber mats, chemical treatment was performed by mixing lead zirconate fiber (1 g) with 20 ml of dimethyl formamide solution. This mixture was then transferred to a Teflon reactor (autoclave), which was sealed and placed in an oven (Whirlpool XT-25ES/S, 900 W, 2.45 GHz). The reaction was performed under autogenous pressure developed by heating for 6 and 24 hours at two difference temperatures of 170°C and 200°C. After cooling to room temperature, the resulting powder was recovered by filtration and washed several times with a mixture of water/alcohol (50:50 by volume). Finally, the sample was dried for 24 h at 80°C. X-ray diffraction (XRD; Bruker-D8 Advance) using $\text{CuK}\alpha$ radiation was used to determine the phases formed. The fourier-transform infrared spectroscopy (FT-IR) spectrum (range 4,000–370 cm^{-1}) was recorded at room temperature by a Perkin Elmer Spectrum GX FT-IR/FT-Raman spectrometer, with 8 scans and a resolution of 4 cm^{-1} using KBr pellets. A scanning electron microscope (SEM, JEOL JSM5910LV) was used to observe the microstructures of the PZ nanofibers before and after chemical treatment. Differential scanning calorimetry (DSC) was performed on a Perkin-Elmer Pyris DSC at a heating rate of 10°C/min under a nitrogen gas flow from 50°C to 400°C in order to investigate phase transition.

6.3 Results and Discussion

The morphology of lead zirconate fibers was revealed by scanning electron microscopy. Figure 6.1 shows SEM micrographs of comparison between lead zirconate fibers treated with dimethyl formamide as solvent and untreated lead zirconate fibers. This Figure 6.1 reveals that morphological fiber change is provided by chemically treated fibers. The samples before chemical treatment present non-woven fabrics, with a structure of packed particles or crystallites. The fibers present continuous structures without grain boundaries [Figure 6.1(a)]. After chemical treatment for 6 and 24 h at both 170°C and 200°C, the lead zirconate fibers still had continuous structures. However, the nature of the nanofibers was changed

dramatically. The surface of the nanofibers had become rough, as seen in Figure 6.1(b–e), because when the solvent molecules or additives were adsorbed preferentially on (or had specific interaction with) a certain surface of the products, surface growth was prohibited and, therefore, solvothermal reaction may form products with unique morphologies [8]. Figure 6.1 revealed by heat treatment that grain boundaries were prominent, due to reduced internal stress. The average diameter of fibers before solvothermal treatment was 300 ± 64 nm and after solvothermal treatment at $170^{\circ}\text{C}/6$ h, $170^{\circ}\text{C}/24$ h, $200^{\circ}\text{C}/6$ h, $200^{\circ}\text{C}/24$ h were 274 ± 64 , 344 ± 99 , 369 ± 93 , 420 ± 81 nm, respectively. It was revealed that the diameter size of the fibers decreased slightly after the dimethyl formamide chemical treatment. This is consistent with the research of Badheka et al. [7], who reported that after chemical treatment, the particle size was reduced in order to alleviate the lattice strain. However, increasing the temperature and time caused the diameter to increase, due to grain growth.

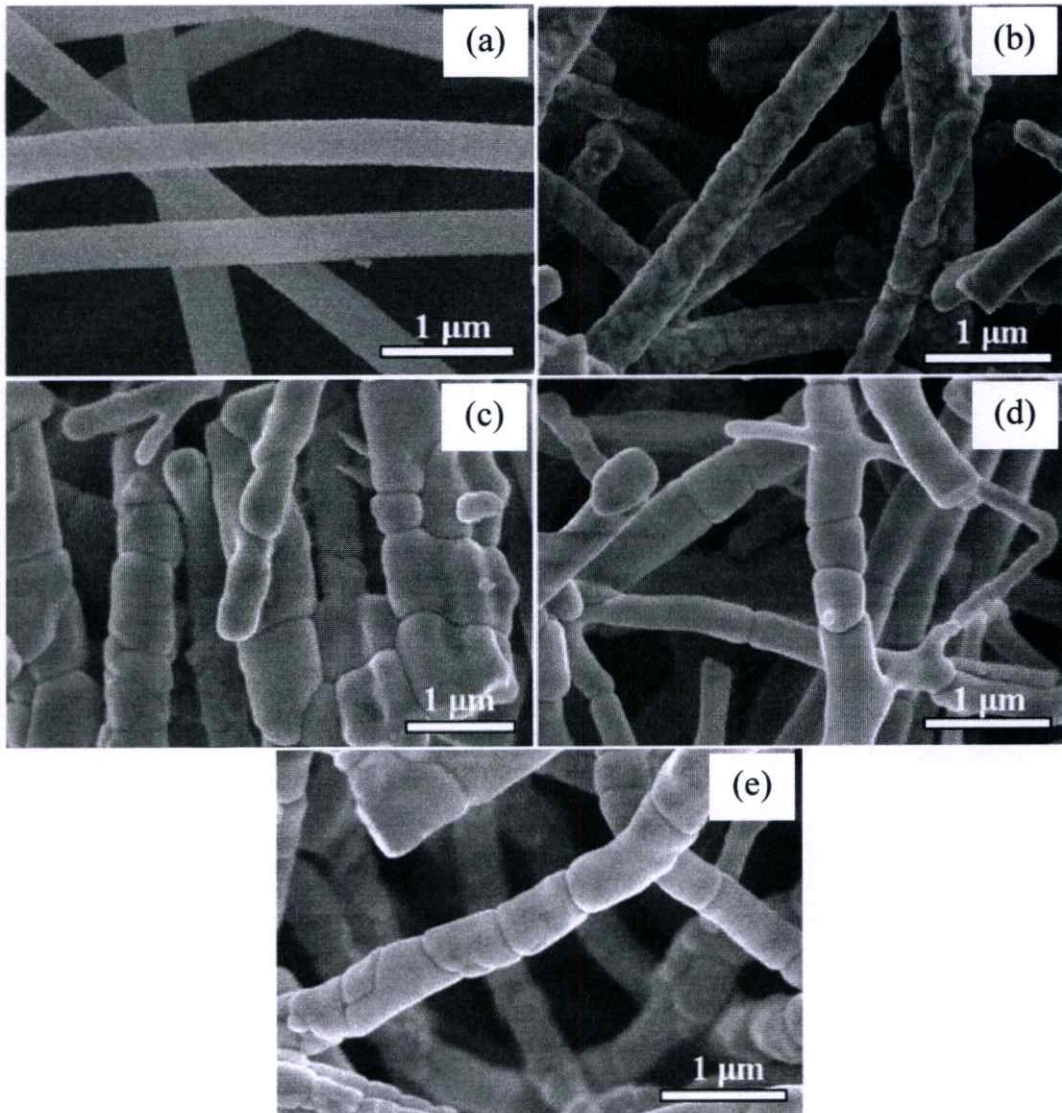


Figure 6.1 SEM micrographs of the PZ fibers (a) before and after chemical treatment for (b) 6 h at 170°C (c) 24 h at 170°C (d) 6 h at 200°C and (e) 24 h at 200°C, consecutively.

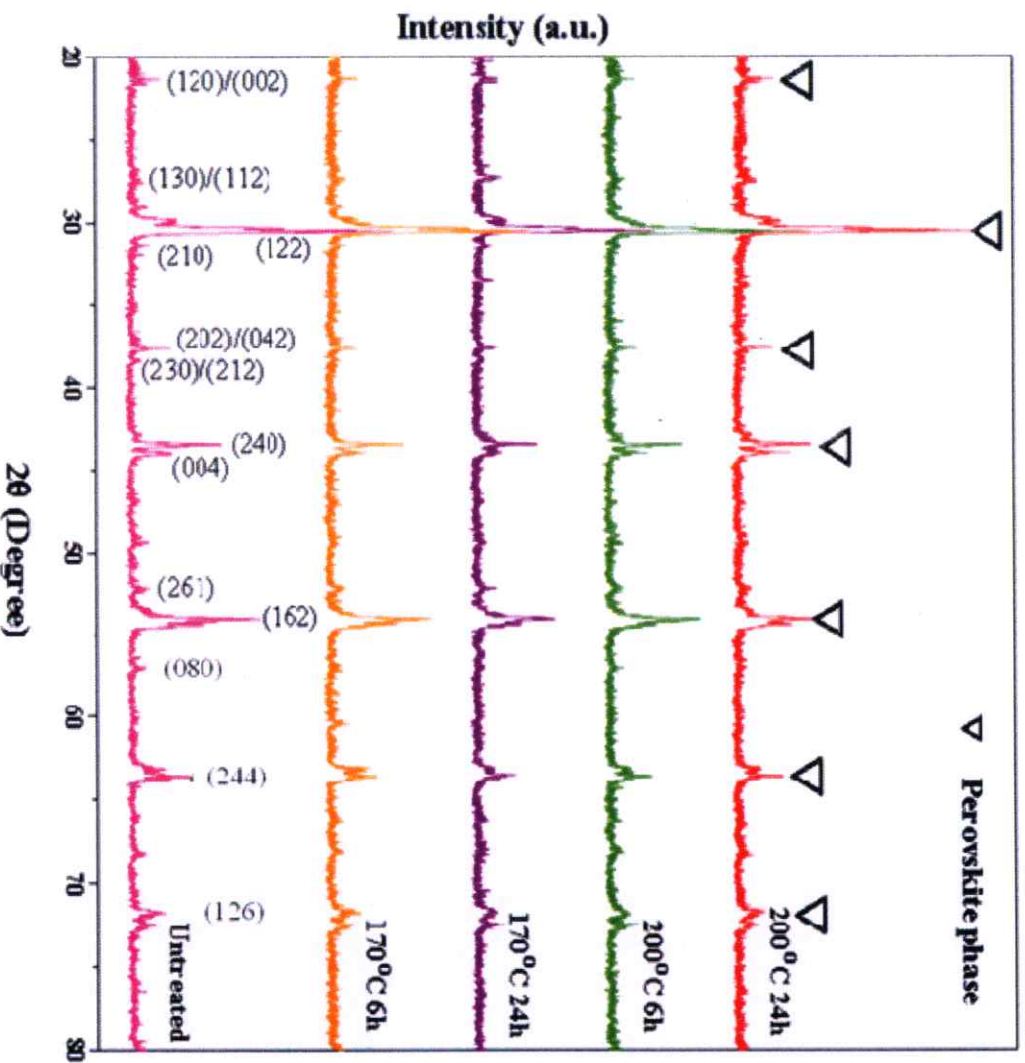


Figure 6.2 XRD patterns of the PZ particles compared with those of the PZ nanofibers before and after chemical treatment.

Figure 6.2 shows comparison between X-ray diffraction patterns of lead zirconate nanofibers that were treated chemically with dimethyl formamide for 6 and 24 h at both 170°C and 200°C and those of untreated lead zirconate nanofibers. The JCPDS file no. 75-1607 shows that all patterns fit well with the peak positions of standard lead zirconate. All of the chemically treated lead zirconate nanofibers could be indexed readily as the orthorhombic phase. XRD patterns show that there is no change in the phase transition after chemical treatment by increasing the temperature above the boiling point of the solvent and giving more time. The XRD

results show that after chemical treatment for 24 h at 200°C, the lattice parameter with the refined cell parameters, $a = 5.7652 \text{ \AA}$, $b = 11.6855 \text{ \AA}$ and $c = 8.2760 \text{ \AA}$, are close to reported values [10].

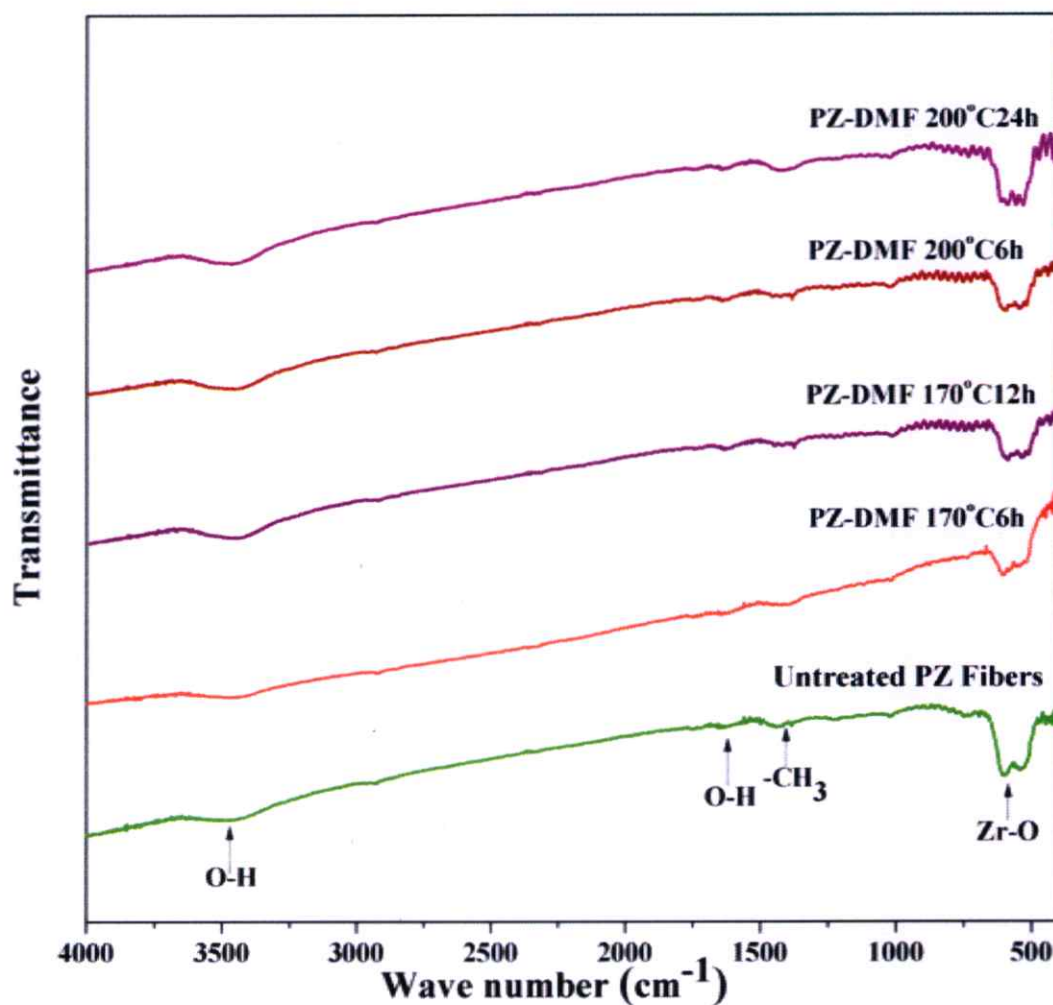


Figure 6.3 FT-IR spectra of the PZ particles compared with those of the PZ nanofibers before and after chemical treatment.

Formation of the perovskite structure in the lead zirconate fibers before and after chemical treatment was supported further by FT-IR spectra, as shown in Figure 6.3. The spectrum shows an absorption peak at $\sim 548 \text{ cm}^{-1}$, which attributed to Zr-O stretching vibration [11]. This corresponds to the occurrence of polycrystalline lead

zirconate fiber. It was found from the Figure that the spectrum of lead zirconate fibers did not change after dimethyl formamide chemical treatment, which indicates that the crystallization of the lead zirconate fibers also remained, as suggested in the XRD results. In addition, the spectrum shows multiple absorption bands in the region $1,000$ to $4,000\text{ cm}^{-1}$, which corresponds to the stretching and bending vibrations of moisture and organic solvent. Of these vibrations, peaks of around $1,450\text{ cm}^{-1}$ correspond to the aliphatic CH group vibrations of the CH_2 mode [12]. The wave number at $\sim 1,600\text{ cm}^{-1}$ and broad peak at around $3,400\text{ cm}^{-1}$ are assigned for O-H bending and O-H stretching vibration [13], respectively.

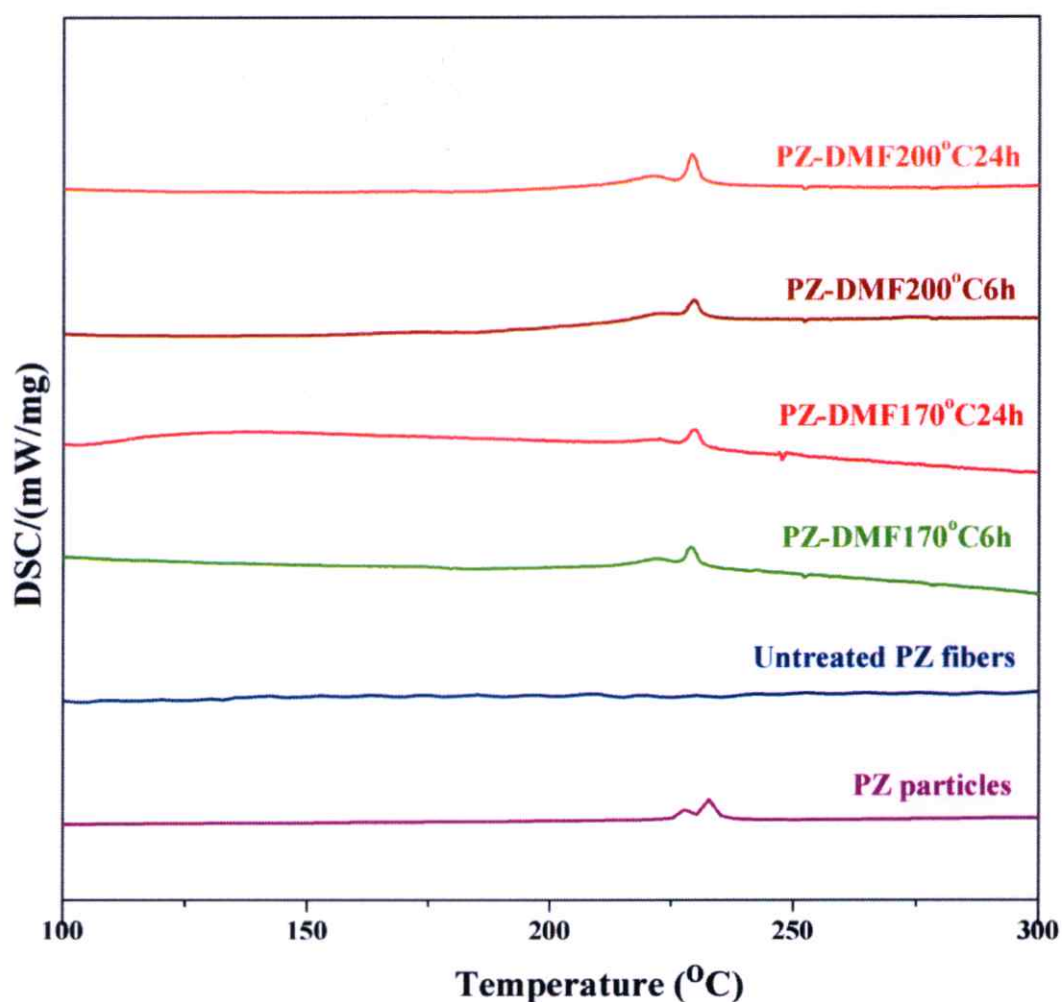


Figure 6.4 DSC results for the PZ particles compared with those for PZ nanofibers before and after chemical treatment.

Figure 6.4 shows results from the solid state method of DSC for the lead zirconate particles, and compares with the electrospinning and solvothermal method of that for the lead zirconate nanofibers and lead zirconate nanofibers treated with dimethyl formamide, respectively. The DSC result of the lead zirconate particles shows two distinct endothermic peaks that are closer together at around 230°C. The lower temperature corresponds to the transition temperature of the antiferroelectric (AFE) \rightarrow ferroelectric (FE) phase transition, while the higher temperature corresponds to the ferroelectric (FE) \rightarrow paraelectric (PE) phase transition. It was found from the Figure that when lead zirconate is fabricated in nanosize by the electrospinning method, there is no phase transition or endothermic peak at around 230°C. This result is very similar to those in other researches. Lu et al. [5] reported that if barium titanate particles are synthesized hydrothermally in nanosize, there is no phase transition or endothermic peak at around 130°C. This is because the nanocrystals are so small that structural defects in the particles prevent the completion of structural transition, leading to high strains within the crystals. Frey et al. [14] suggested that strains in the crystallites are related to defects in the lattice. Lin et al. [15] reported that coarse grained ceramics have internal stress caused by phase transition, which can be relieved by formation of 90° domains. With grain size decreasing further, the single domain becomes favorable energetically. Consequently, in fine-grained ceramics, the contribution of stress should be taken into account, due to the absence of 90° domains [15], whereas, after chemical treatment with dimethyl formamide, the lead zirconate nanofibers clearly show an endothermic transition on heating at 230°C, as seen in Figure 6.4. This corresponds to the orthorhombic to cubic phase transition at the Currie point of lead zirconate. This may be due to the effect of grain boundaries, because the SEM micrograph of lead zirconate fibers treated with dimethyl formamide shows the structure with grain boundaries, as mentioned earlier. Areas around impure ions within grains have a strong field of elastic strain, while those around impure ions at grain boundaries have an open structure and a low strain field. Therefore, impure ions will diffuse from grains into grain boundaries to form segregation in order to reduce strain energy and eliminate or release stress [16]. According to the DSC curve, increased intensity of endothermic peak with increasing temperature and time in the solvothermal process is seen clearly. Additionally, enthalpy (Δ) values calculated from the DSC curve also

increased. Increased temperature leads to greater thermal vibration of the atoms in a material, and on to increase the average distance separating adjacent atoms [17]. With increasing temperature, stress is relieved gradually in order that free energy of the antiferroelectric phase could decrease and allow enthalpy values to increase. The enthalpy (Δ) values of lead zirconate fibers after chemical treatment at 170°C/6 h, 170°C/24 h, 200°C/6 h, 200°C/24 h were 1.9469 J/g, 2.0259 J/g, 2.5334 J/g and 2.6879 J/g, respectively.

6.4 Summary

The thermal properties of lead zirconate fibers, using dimethyl formamide solvent before and after solvothermal treatment were investigated by the DSC method. The results suggested that the antiferroelectric-paraelectric phase transition was found after chemical treatment at 170°C for 6 h. Furthermore, the enthalpy values for the orthorhombic-cubic transition increased with increasing temperature and time, due to reduction of internal stresses. Microstructures were observed by SEM, which revealed grain boundaries that were prominent through heat treatment. The diameter size of the fibers decreased slightly after dimethyl formamide chemical treatment and increased with increasing temperature and time.

REFERENCE

- [1] Uchino, K. 2000. **Ferroelectric Devices**. Dekker, New York.
- [2] Oren, E.E., Taspinar, E., and Tas, A.C. 1997. "Preparation of Lead Zirconate by Homogeneous Precipitation and Calcination." **J. Am. Ceram. Soc.** **80**[10] : 2714–2716.
- [3] Xu, L.R., Li, L., Lukehart, C.M., and Kuai, H. 2007. "Mechanical Characterization of Nanofiber-Reinforced Composite Adhesives." **J. Nanosci. Nanotechnol.** **7** : 1–3.
- [4] Safari, A. 1994. "Development of Piezoelectric Composites for Transducers." **J. Phys. III Fiance.** **4** : 1129–1149.
- [5] Lu, S.W., Lee, B.I., Wang, Z.L., and Samuels, W.D. 2000. "Hydrothermal Synthesis and Structural Characterization of BaTiO₃ Nanocrystals." **J. Crystal Growth.** **219**, 269–276.
- [6] Smith, M. B., Page, K., Siegrist, T., et al. 2008. "Crystal Structure and the Paraelectric-to-Ferroelectric Phase Transition of Nanoscale BaTiO₃." **J. Am. Chem. Soc.** **130** : 6955–6963.
- [7] Badheka, P., Qi, L., and Lee, B.I. 2006. "Phase Transition in Barium Titanate Nanocrystals by Chemical Treatment." **J. Eur. Ceram. Soc.** **26** : 1393–1400.
- [8] Inoue, M. 2005. "Solvothelmal Synthesis." **Chemical Processing of Ceramics**. 2nd Ed. pp. 22–56.
- [9] Nawani, C., Boonchom, B., Prachayawarakorn, J., Vittayakorn, W., and Vittayakorn, N. 2012. "Synthesis and Phase Evolution of Electrospun Antiferroelectric Lead Zirconate (PbZrO₃) Nanofibers." **Mater. Sci. Eng. B.** **177** : 1009–1016.
- [10] Vittayakorn, N., Charoonsuk, P., Kasiansin, P., Wirunchit, S., and Boonchom, B. 2009. "Dielectric Properties and Phase Transition Behaviors in (1-x)PbZrO₃-xPb(Mg_{1/2}W_{1/2})O₃ Ceramics." **J. App. Phys.** **106** : 064104.
- [11] Mai, M., Lin, C., Xiong, Z., Xue, H., and Chen, L. 2009. "Preparation and Characterization of Lead Zirconate Titanate Ceramic Fibers with Alkoxide-Based Sol–Gel Route." **J. Phys.; conference series.** **152** : 012077.
- [12] Zhang, Z., Li, X., Wang, C., Wei, L., Liu, Y., and Shao, C. 2009. "ZnO Hollow Nanofibers: Fabrication from Facile Single Capillary Electrospinning and Applications in Gas Sensors." **J. Phys. Chem.** **113** : 19397.

- [13] Maensiri, S., Nuansing, W., Klinkaewnarong, J., Laokul, P., and Khemprasit, J. 2009. "Nanofibers of Barium Strontium Titanate (BST) by Sol–Gel Processing and Electrospinning." *J. Colloid Interface Sci.* 297 : 578.
- [14] Frey, M.H., and Payne, D.A. 1996. "Grain-Size Effect on Structure and Phase Transformations for Barium Titanate." *Phys. Rev. B.* 54[5] : 3158–3167.
- [15] Lin, S., Lu, T., Jin, C., and Wang, X. 2006. "Size Effect on the Dielectric Properties of BaTiO₃ Nanoceramics in a Modified Ginsburg-Landau-Devonshire Thermodynamic Theory." *Phys. Rev. B.* 74 : 134115.
- [16] Yin, Q., Zhu, B., and Zeng, H. 2009. "Microstructure." **Property and Processing of Functional Ceramics.** Metallurgical Industry Press, Beijing and Springer-Verlag GmbH Berlin Heidelberg. pp. 1–168.
- [17] Xiao, C. J., Li, Z. X., and Deng, X. R. 2011. "Grain-Size Effects on Thermal Properties of BaTiO₃ Ceramics." *Bull. Mater. Sci.* 34[4] : 963–966.

CHAPTER 7
PREPARATION AND DIELECTRIC PROPERTIES OF 3-3
LEAD ZIRCONATE / POLYVINYLIDENE FLUORIDE
NANOCOMPOSITE

Based on article published in *Ferroelectrics Letters Section*
40 (2013) 94–100

Composites made of electroactive ceramics and a ferroelectric polymer are very attractive for applications since they exhibit good piezoelectric and pyroelectric properties, low densities and their properties can be tailored to various requirements. Here, we reported the preparation and dielectric properties of 3-3 PZ/PVDF nanocomposites by infusion of polyvinylidenedifluoride (PVDF) into the PZ nanofiber mat followed by heating of the composite at 80°C. The 3-3 PZ/PVDF composites were characterized by X-ray diffraction, FT-IR, SEM and LCR meter. The dielectric constant of the PZ/PVDF nanocomposite are relatively stable in the range of 21.98–18.21 within the measurement frequencies from 100 Hz to 2 MHz. This value is higher than the dielectric constant of the polyvinylidene fluoride. Moreover, the dielectric loss of the composite is below 0.09 at low frequencies.

7.1 Introduction

Piezoelectric ceramic-polymer composites were intensively studied within the last decades because of their considerable potential for applications such as pyroelectric sensors, ultrasonic transducers, and hydrophones [1]. Piezoelectric ceramics have high piezoelectric strain coefficient and high electromechanical coupling coefficient [2]. However, the relatively high density, high acoustic impedance and mechanical stiffness limit their applications. On the other hand, piezoelectric polymers have acoustic impedance well matched to water and biological tissues, but their piezoelectric strain coefficient and electromechanical coupling coefficient, are lower than those of piezoelectric ceramics [3]. Thus, in many

applications, one might optimize conflicting requirements by combining the most useful properties of two or more phases that do not ordinarily appear together in nature. Therefore, different kinds of composites such as porous ceramics and ceramic-polymer composites are typically developed.

Antiferroelectric materials have attracted much research interest due to their potential applications in microactuators and energy conversion devices [4]. Lead zirconate, PbZrO_3 (PZ), is a well known antiferroelectric materials. This material can be processed into various forms such as bulk ceramics, thin films, and fibers, depending on the application area. The hysteresis characteristics of Antiferroelectric PbZrO_3 regions are well suited for either power-storage or actuator applications. Moreover, the extremely large charge which is released from the FE state to the AFE state may be useful as alternate capacitor materials in DRAMs [5]. In recent years, researchers have focused on synthesizing nanosized PZ fibers to improve desired properties. Fibrous PZ have potential for utilization in high performance electric-mechanical application such as actuators, sensors, high energy storage capacitors and microelectromechanical systems (MEMS). Due to the high surface-to-volume ratio and their novel properties that are significantly different from their bulk, such as mechanical [6] and electrical property [7]. Nanoscale PZ fibers incorporated into a piezoelectric polymer are expected to obtain smart piezocomposite structures and to find wide applications, particularly in nanoelectronics, photonics, sensors, and actuators. Both kinds of materials show different piezoelectric properties, such as resonance frequencies and electromechanical coupling coefficients because of differences in their microscopic structures, their elastic properties and their typical transducer geometries [8]. Due to such special qualities, piezoelectric polymers have been increasingly used in a rapidly expanding range of applications such as electromechanical transducers, position sensors and vibration control actuators [9]. Often piezo- and pyroelectric polymers such as nylon [10], polyvinyl chloride (PVC) [3] and polyvinylidene fluoride (PVDF) [11] were used as matrix. Based on our knowledge, there has been no previous report on the fabrication of PZ fibers/PVDF composite. Polyvinylidene fluoride (PVDF) is a piezoelectric polymer that has been used in many applications including microphones, transducers, sensors and actuators, due to its high piezo-, pyro- and ferroelectric properties [12]. The PVDF has low permittivity, low thermal conductivity and is flexible and relatively low in cost [13]. In

addition, it is exceptionally sensitive, for example, sensors based on PVDF film have been applied even in erosive media to detect pressure, in biological environments to aid minimally invasive surgery, test and characterize fabrics, and monitor human health [12]. Therefore this study fabricated 3-3 PZ/PVDF nanocomposite using PZ fibers embedded in PVDF matrix. The crystal structure and morphology were investigated. Moreover, the dielectric properties of the resultant 3-3 PZ/PVDF nanocomposite was characterized.

7.2 Experimental Procedure

PZ nanofibers were synthesized by an electrospinning method utilizing a solution which contained poly(ethylene oxide) (PEO, MW ~ 300,000; Aldrich), and sol-gel precursor solution of PZ as mention in Chapter 4. After obtaining the PZ fiber mats, PZ/PVDF nanocomposite samples were prepared. Firstly, Polyvinylidene fluoride (PVDF; MW~534,000; Aldrich) powder was dissolved in DMF solvent to obtain the polymer matrix of the composite. This solution was poured on to the calcined PZ fiber mat and this sample was kept under vacuum for 10 min to eliminate trapped air. Then, the sample was dried 24 h at 80°C. X-ray diffraction (XRD; Bruker-D8 Advance) using $\text{CuK}\alpha$ radiation was used to determine the phases formed. The room-temperature FTIR spectrum ranging 4,000–370 cm^{-1} was recorded by a Perkin Elmer Spectrum GX FTIR/FT-Raman spectrometer, with 8 scans and a resolution of 4 cm^{-1} using KBr pellets. A scanning electron microscope (SEM, JEOL JSM5910LV) was used to observe the microstructures of the PZ/PVDF nanocomposite. Finally, dielectric properties of the PZ/PVDF nanocomposites were measured from 100 Hz to 2 MHz using a precision LCR meter HP-4284A (Hewlett-Packard, Palo Alto, CA). The samples were prepared into thin, rectangular, parallel plates, and the dielectric measurements were taken by placing the samples between two parallel metal plates of the sample holder.

7.3 Results and Discussion

PZ/PVDF nanocomposite achieved from embedded PZ nanofibers in PVDF polymer has a smooth surface, with no buckling or folding over, thus indicating that the solvent evaporated uniformly. The morphology of the PZ/PVDF composite was

revealed by scanning electron microscopy (SEM). Figure 7.1 shows SEM photographs of the composite. From Figure 7.1(a), it is shown that the polymer matrix phase was infiltrated thoroughly into the fiber network, and an intimate mixture of two phases was obtained. Figure 7.1(b) shows the backscattering electrons SEM image of the composite section, in which the PZ phase is visible with a bright-white contrast, and the PVDF phase is identifiable as the darker-gray region. The microgeometry of the inclusion and the interface between the filler and the matrix could be important. The mixing rules of a given property are controlled by the connectivity of the individual phases [13]. From the Figure, it reveals that the composite has 3-3 connectivity by using Newnham's convention on connectivity of piezocomposites, in which the active PZ and polymer matrix phases are both connected in three dimensions in the micrometer scale [7].

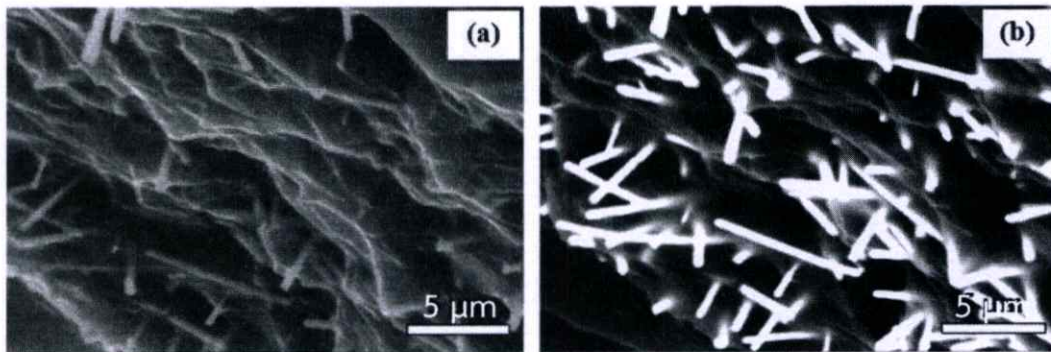


Figure 7.1 SEM micrograph of the composite structure of 3-3 PZ/PVDF nanocomposite.

The crystalline phases of 3-3 PZ/PVDF composite was revealed by X-ray diffraction spectra. Figure 7.2 shows the XRD patterns of the 3-3 PZ/PVDF composite compared with PZ fibers and PVDF powder. From the Figure, it is revealed that crystalline PZ/PVDF composite were obtained. According to JCPDS card no.75-1607, the diffraction peaks can be indexed as an orthorhombic perovskite structure of lead zirconate. Moreover, peaks of polyvinylidene fluoride (PVDF) could be observed in the XRD patterns of the composite, because of PVDF is a semi-crystalline polymer

with typical crystallinity of 50%. The spectra of the PVDF polymer are also seen to have well defined peaks at $2\theta = 20.3^\circ$, referent to the sum of the diffractions in plane (110) and (200) characteristic of the β phase. Peak at $2\theta = 26.64^\circ$ referent to the diffractions in planes (021), which characteristic of α phase [15].

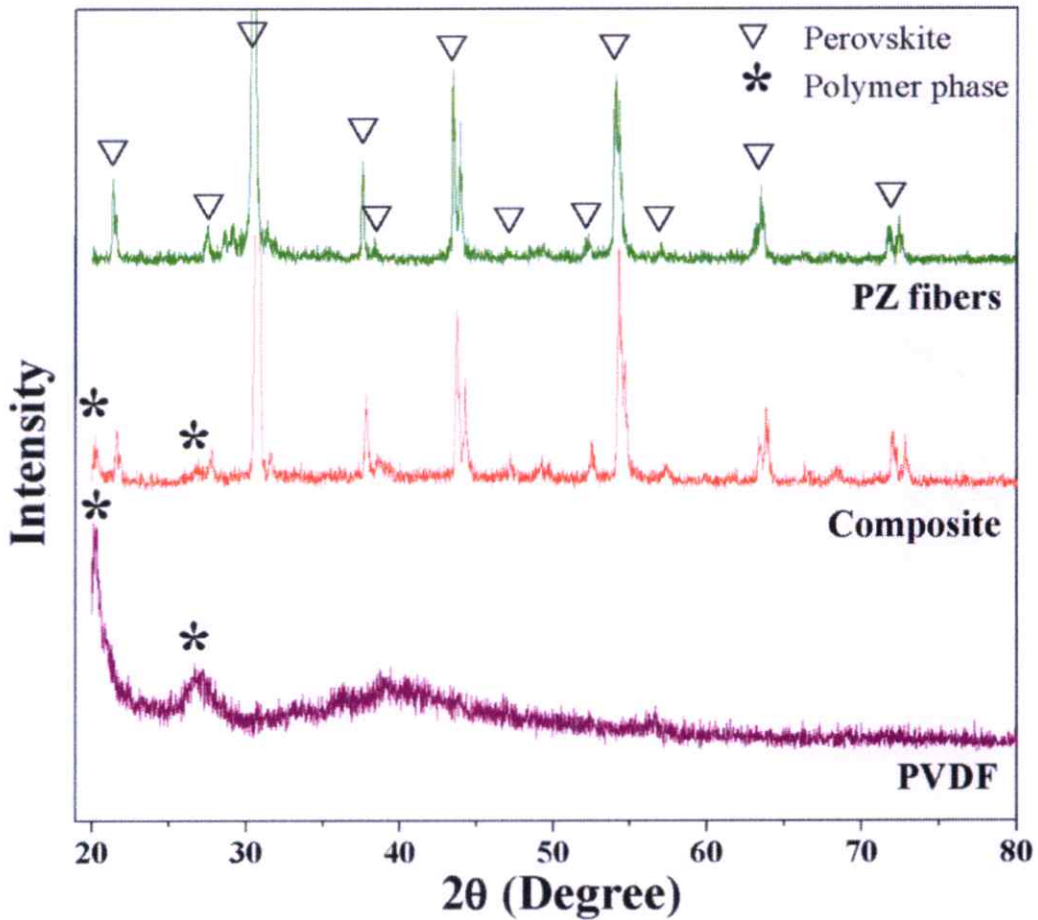


Figure 7.2 XRD patterns of 3-3 PZ/PVDF nanocomposite compared with PZ fibers and PVDF powder

Formation of the 3-3 PZ/PVDF composite was confirmed further by the FTIR spectra, as shown in Figure 7.3. The spectrum of the 3-3 PZ/PVDF composite shows multiple absorption bands in the region of 400 to $4,000\text{ cm}^{-1}$, which corresponds to the stretching and bending vibrations of ceramic, polymers and moisture. Peaks of

around $1,450\text{ cm}^{-1}$ correspond to the aliphatic CH group vibrations of the CH_2 mode of PVDF polymer [9]. The wave number at $\sim 1,600\text{ cm}^{-1}$ and broad peak at around $3,400\text{ cm}^{-1}$ both correspond to the O-H stretching vibration of moisture [10]. The symmetric and asymmetric CH stretching vibration of PVDF is observed at $2,900\text{ cm}^{-1}$ [16]. The absorption band at 480, 530, 612, 764, 797, 855, 976 and $1,410\text{ cm}^{-1}$ correspond to large amount of α crystal phase, whereas peak at $1,226\text{ cm}^{-1}$ indicates β phase of vinylidene group of polymer [15, 17]. In addition, the absorption peak at $\sim 548\text{ cm}^{-1}$ is attributed to Zr-O stretching vibration [11], which corresponds to the polycrystalline PZ fiber. This study can guarantee that its sample consists of two phases, including ceramic and polymer phases.

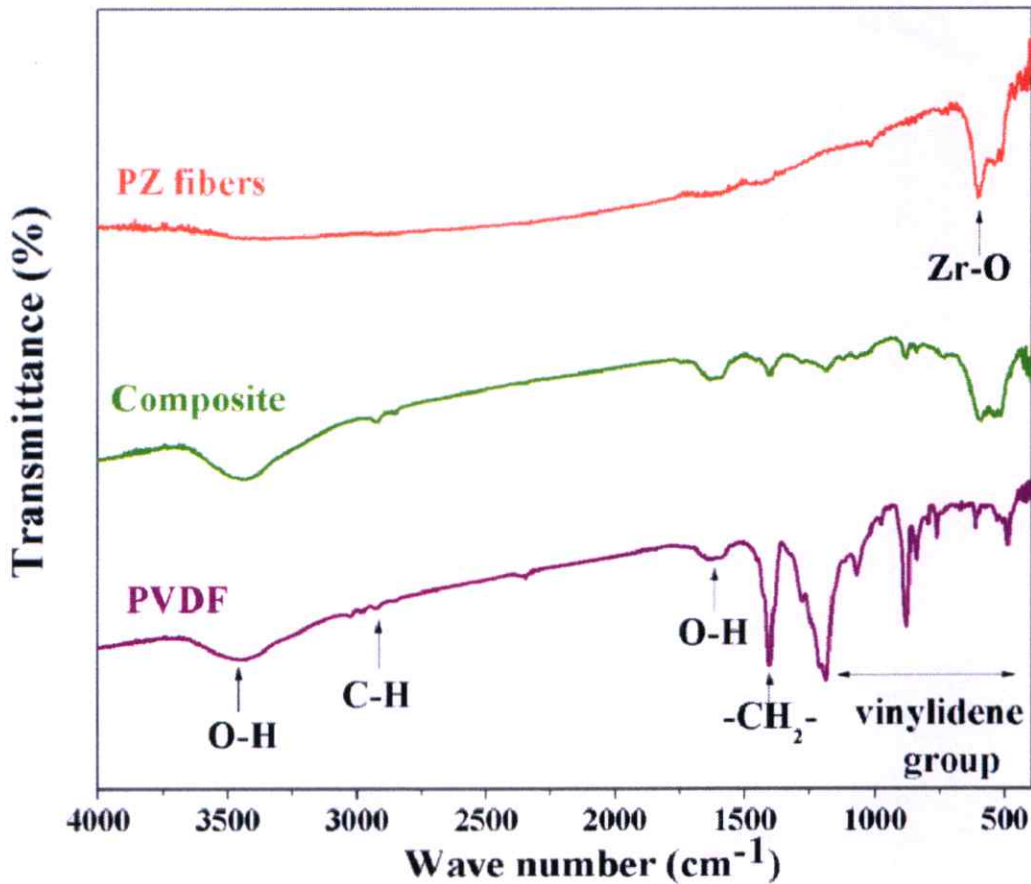


Figure 7.3 FT-IR spectra of 3-3 PZ/PVDF nanocomposite

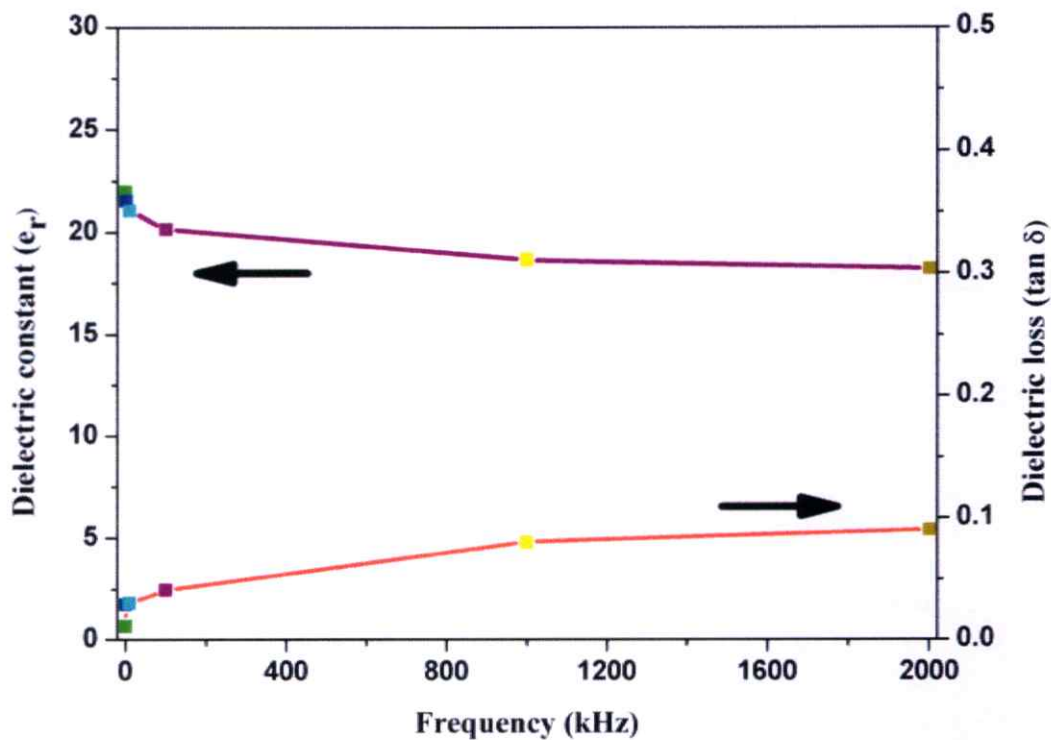


Figure 7.4 Dielectric properties of 3-3 PZ/PVDF nanocomposite within the measurement frequencies from 100 Hz to 2 MHz.

Dielectric properties of the resultant 3-3 PZ/PVDF nanocomposite was characterized by LCR meter. The dielectric constant of the 3-3 composite was found to be relatively stable in the range of 21.98–18.21 within the measurement frequencies from 100 Hz to 2 MHz (Figure 7.4). This value is higher than the dielectric constant of the polyvinylidene fluoride, which was measured as 13.14 (at 2 MHz) in this study. This is due to the increasing contribution of PZ to the dielectric properties of the composites, because PZ has a substantially higher dielectric constant ($\epsilon_r = 116$ at room temperature [18]) than the polymer. This result demonstrated that, a particular response of a composite to an external field may depend either on the corresponding response of individual phases or may result in a property not existent in the phases composing the material. In addition, a particular property of the composite may depend on several properties of the individual phase [19]. The

polymer phase in the composite was burnt out at 600°C, and the weight of the sample was recorded. From the theoretical density of PZ (8.085 g/cm³) and PVDF (0.6 g/cm³), the volume fraction of the PZ fibers in this composite structure was determined to be about 10%. Using the rule of mixtures according to equation (7.1) and dielectric constants of the constituent phases, polyvinylidene fluoride and PZ, the calculated dielectric constant of the composite was 23.43. [20]

$$\epsilon'_{composite} = \epsilon'_{polymer} V_{polymer} + \epsilon'_{ceramic} V_{ceramic} \quad (7.1)$$

The calculated value is higher than the measured value, this may be due to the porosity and its contribution to the dielectric constant of the composite. The dielectric loss of the composite is below 0.09 at low frequencies.

7.4 Summary

In summary, this study prepared 3-3 PZ/PVDF nanocomposite successfully by infiltrating a polyvinylidene fluoride (PVDF) polymer into the PZ nanofiber mat. The composite has relatively smooth surface. The PZ/PVDF composite consists of two phases, including ceramic phase with orthorhombic perovskite structure and polymer phases. The dielectric constant of the composite measured at room temperature is higher than the polymer matrix and reasonably agrees with the prediction from the rule of mixtures.

REFERENCE

- [1] Petchsuk, A., Supmak, W. and Thanaboonsombut, A. 2009. "A Series of 0-3 Composites of Lead Zirconate Titanate and Ferroelectric Nylon77: Preparation and Electrical Properties." *J. Appl. Polym. Sci.* 114 : 1048–1054.
- [2] Wu, M., Huang, H., Chu, W., Guo, L., Qiao, L., Xu, J., and Zhang, T.Y. 2010. "Tuning the Ferroelectric and Piezoelectric Properties of $0.91\text{Pb}(\text{Zn}_{1/3}\text{Nb}_{2/3})\text{O}_3$ - 0.09PbTiO_3 Single Crystals and Lead Zirconate Titanate Ceramics by Doping Hydrogen." *J. Phys. Chem. C.* 114 : 9955-9960.
- [3] Xiaofang, L., Chuanxi, X., Huajun, S., Lijie, D., Rui, L. and Yang, L. 2005. "Characterization of PZT/PVC Composites Added with Carbon Black." *J. Wuhan University of Technology-Mater. Sci. Ed.* 20[4] : 60.
- [4] Lou, X. J. and Wang, J. 2010. "Unipolar and Bipolar Fatigue in Antiferroelectric Lead Zirconate Thin Films and Evidences for Switching-Induced Charge Injection Inducing Fatigue." *Appl. Phys. Lett.* 96 : 102906.
- [5] Kim, I., Bae, S., Kim, K., Kim, H., Lee, J. S., Jeong, J., and Yamakawa, K. 1998. "Characteristics of Antiferroelectric PbZrO_3 Thin Films." *J. Korean Phys. Soc.* 33[2] : 180-183.
- [6] Xu, L.R., Li, L., Lukehart, C.M., and Kuai, H. 2007. "Mechanical Characterization of Nanofiber-Reinforced Composite Adhesives." *J. Nanosci. Nanotechnol.* 7 : 2546-2548.
- [7] Safari, A. 1994. "Development of Piezoelectric Composites for Transducers." *J. Phys. III France.* 4 : 1129-1149.
- [8] Arlt, K. and Wegener, M. 2010. "Piezoelectric PZT/PVDF-Copolymer 0-3 Composites: Aspects on Film Preparation and Electrical Poling." *IEEE.* 1178.
- [9] Vinogradov, A.M., Schmidt, V.H., Tuthill, G.F., and Bohannon, G. W. 2004. "Damping and Electromechanical Energy Losses in the Piezoelectric Polymer PVDF." *Mech. Mater.* 36 : 1007-1016.
- [10] Petchsuk, A., Supmak, W., and Thanaboonsombut, A. 2009. "A Series of 0-3 Composites of Lead Zirconate Titanate and Ferroelectric Nylon77: Preparation and Electrical Properties." *J. Appl. Polym. Sci.* 114 : 1048.

- [11] Chan, H.L.W., Chan, W.K., Zhang, Y., and Choy, C.L. 1998. "Pyroelectric and Piezoelectric Properties of Lead Titanate/Polyvinylidene Fluoride-Trifluoroethylene 0-3 Composites." *IEEE: Transactions on Dielectrics and Electrical Insulation*. 5[4].
- [12] Wang, Y.R., Zheng, J.M., Ren, G.Y., Zhang, P.H., and Xu, C. 2011. "A Flexible Piezoelectric Force Sensor Based on PVDF Fabrics." *Smart Mater. Struct.* 20 : 045009.
- [13] Hajeesaeh, S., and Muensit, S. 2007. "Theory and Measurements for 0-3 BaTiO₃/PVDF Composites." *Songklanakarin J. Sci. Technol.* 29.
- [14] Nawani, C., Boomchom, B., Prachayawarakorn, J., Vittayakorn, W. C. and Vittayakorn, N. 2012. "Synthesis and Phase Evolution of Electrospun Antiferroelectric Lead Zirconate (PbZrO₃) Nanofibers." *Mater. Sci. Eng. B.* 177: 1009–1016.
- [15] Ostasevicius, V., Milasauskaite, I., Dauksevicius, R., Baltrusaitis, V., and Grigaliunas, V., and Prosycevas, I. 2010. "Experimental Characterization of Material Structure of Piezoelectric PVDF Polymer." *Mechanika*. 6[86] : 1392-1207.
- [16] Kitaoka, K., Kozuka, H. and Yoko, T. 1998. "Preparation of Lead Lanthanum Zirconate Titanate (PLZT, (Pb,La)(Zr,Ti)O₃) Fibers by Sol-Gel Method." *J. Am. Ceram. Soc.* 81[5] : 1189-1196.
- [17] Kumar, A. and Deka, M. 2010. "Nanofiber Reinforced Composite Polymer Electrolyte Membranes." *Nanofibers*. pp. 438.
- [18] Vittayakorn, N., Charoonsuk, P., Kasiangsin, P., Wirunchit, S. and Boonchom, B. 2009. "Dielectric Properties and Phase Transition Behaviors in (1-x)PbZrO₃-xPb(Mg_{1/2}W_{1/2})O₃ Ceramics." *J. Appl. Phys.* 106, 064104 (2009).
- [19] Hilczer, B., Kutek, J., Markiewicz, E., Kosec, M., and Mali, B. 2002. "Dielectric Relaxation in Ferroelectric PZT-PVDF Nanocomposites." *J. Non-Cryst. Solids*. 305 : 167-173.
- [20] Alkoy, E. M., Dagdeviren, C., and Papila, M. 2009. "Processing Conditions and Aging Effect on the Morphology of PZT Electrospun Nanofibers, and Dielectric Properties of the Resulting 3-3 PZT/Polymer Composite." *J. Am. Ceram. Soc.* 92[11] : 2566-2570.

CHAPTER 8

CHARACTERIZATION AND DIELECTRIC PROPERTIES OF NANOCOMPOSITE MADE OF LEAD ZIRCONATE NANOFIBERS AND POLYVINYLIDENE FLUORIDE IMPROVED WITH CARBON NANOTUBES

Based on article published in *Integrated Ferroelectrics* 149 (2013) 18–24

This chapter studied the characterization and dielectric properties of nanocomposite made of lead zirconate nanofibers and polyvinylidene fluoride improved with carbon nanotubes. A three-phase PZ/CNT/PVDF nanocomposite comprising lead zirconate (PZ) nanofibers, polyvinylidene fluoride (PVDF) and a small volume fraction of carbon nanotubes (CNT) was prepared by the solvent casting technique followed by composite heating at 80°C. The PZ/CNT/PVDF composites were characterized by X-ray diffraction, FT-IR and scanning electron microscopy (SEM). The dielectric properties of the composite were studied as a function of the frequency by an LCR meter. The dielectric constant of the PZ/CNT/PVDF nanocomposite was found to be in the range of 18–61 within the measurement frequencies from 100 Hz to 2MHz. This value is higher than the dielectric constant of the PZ/PVDF nanocomposite. The measured dielectric properties demonstrate that the addition of CNT can improve the dielectric property appearance of the composite.

8.1 Introduction

Composites made of electroactive ceramics and a ferroelectric polymer are very attractive for applications, since they exhibit low densities and good piezoelectric and pyroelectric properties that can be tailored to various requirements. Piezoelectric ceramics have been used extensively, due to their large dielectric constant, high piezoelectric strain and high electromechanical coupling

coefficient [1]. However, the high leakage current, low dielectric strength and mechanical stiffness limit their applications [2], whereas, polymeric materials exhibit very high dielectric strength and low leakage current, but polymers generally show small dielectric constants ($\epsilon_r = 2\sim 12$) [2]. Polymer based composite is considered as a solution to the problem by providing good opportunity for the development of a high dielectric constant, low leakage and high breakdown strength materials. Antiferroelectric materials have attracted much research interest due to their potential applications in microactuators and energy conversion devices. Lead zirconate [PbZrO_3 (PZ)] is a well known antiferroelectric material that can be processed into various forms such as bulk ceramics, thin films, and fibers. The hysteresis characteristics of antiferroelectric PbZrO_3 regions are well suited for either power-storage or actuator applications. Furthermore, the extremely large charge released from the FE to AFE state may be useful as alternate capacitor materials in DRAMs. In recent years, researchers have focused on synthesizing nanosized PZ fibers by the electrospinning technique and incorporated that into a piezoelectric polymer to obtain smart piezocomposite structures, using polyvinylidene fluoride (PVDF) as a matrix. This is because PVDF has superior piezoelectric properties when compared with other types of polymeric materials, due to its polar crystalline structure. This research reports the preparation and dielectric properties of PZ/PVDF nanocomposite, with modification of the carbon nanotube (CNT). PZ/PVDF nanocomposite was chosen as an excellent candidate for acquiring high dielectric constant polymer matrix composites, according to the percolation theory, which is formation of long-range connectivity in random systems. Carbon nanotubes (CNTs) have remarkable electrical and mechanical properties such as extremely high conductance and Young's modulus [3]. They are found to be attractive on account of their potential for applications in nanoscale devices [4]. The PZ-CNT/PVDF composites were characterized using different techniques. Morphological studies were carried out using scanning electron microscopy (SEM), with the crystal structures determined by X-ray diffraction (XRD). The functional groups and dielectric properties of the composite were confirmed using FT-IR and an LCR meter, respectively.

8.2 Experimental Procedure

PZ nanofibers were synthesized by an electrospinning method, which utilized a solution that contained poly (ethylene oxide) (PEO, MW \sim 300,000; Aldrich), and sol-gel precursor solution of PZ. After obtaining the PZ fiber mats, three-phase PZ/CNT/PVDF nanocomposite samples were prepared. Firstly, polyvinylidene fluoride (PVDF; MW \sim 534,000; Aldrich) powder was dissolved in dimethyl formamide (DMF) solvent to obtain the polymer matrix of the composite, before mixing in carbon nanotubes in specific proportions (compositions of 1 wt% CNTs). After stirring for 1 hr, the mixture was poured onto the calcined PZ fiber mat for the final polymer nanocomposite product, and this sample was kept under vacuum for 10 min to eliminate trapped air. Then, the sample was dried for 24 h at 80°C. X-ray diffraction (XRD; Bruker-D8 Advance) using $\text{CuK}\alpha$ radiation was used to determine the phases formed. The room-temperature FT-IR spectrum ranging 4,000–370 cm^{-1} was recorded by a Perkin Elmer Spectrum GX FT-IR/FT-Raman spectrometer, with 8 scans and a resolution of 4 cm^{-1} using KBr pellets. A scanning electron microscope (SEM, JEOL JSM5910LV) was used to observe the microstructures of the PZ/PVDF nanocomposite. Finally, dielectric properties of the PZ/PVDF nanocomposite were measured from 100 Hz to 2 MHz using an HP 4194A Impedance Analyzer (Santa Clara, CA). Samples of thin, rectangular, parallel plates were prepared and placed between two parallel metal plates of the sample holder for dielectric measurements.

8.3 Results and Discussion

Morphology of the PZ fiber and the three-phase PZ/CNT/PVDF nanocomposite were revealed by scanning electron microscopy (SEM). Figure 8.1 reveals that the continuous PZ nanofibers with average diameter of 300 ± 64 nm. Figure 8.2 shows SEM micrographs of the secondary electron [Figure 8.2(a)] and backscattering electrons [Figure 8.2(b)] images of the PZ/CNT/PVDF nanocomposite. In Figure 8.2(b), the backscattering electrons image of the composite cross section shows that the polymer matrix phase thoroughly infiltrates the fiber network. The intimate mixture of three phases was obtained, in which the PZ phase and CNTs were visible in bright-white contrast, and the PVDF phase was identifiable as a darker-gray region. The

figure revealed that the composite has 3-3 connectivity by using Newnham's convention [6] on connectivity of piezocomposites, in which the active PZ, CNT and polymer matrix phases are connected in three dimensions in the nanometer scale.

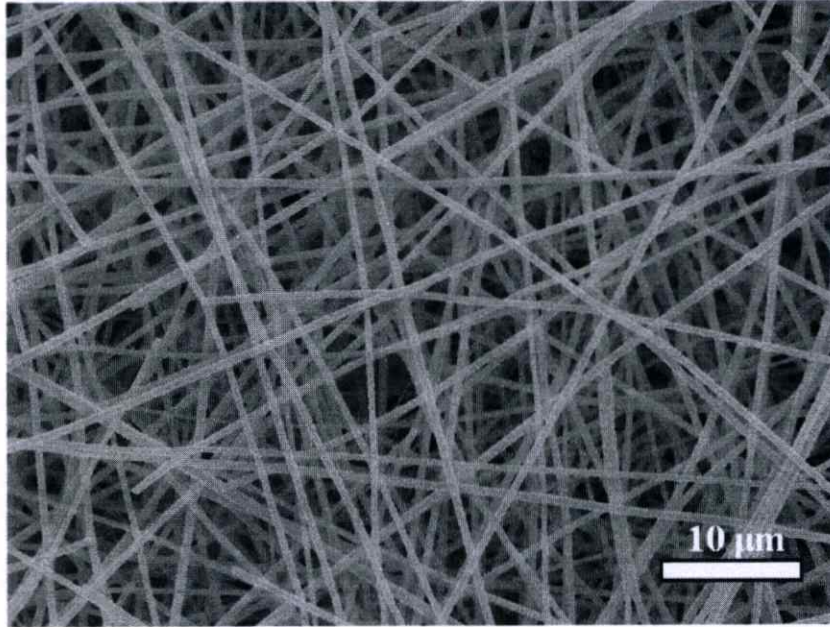


Figure 8.1 SEM micrograph of the PZ fibers.

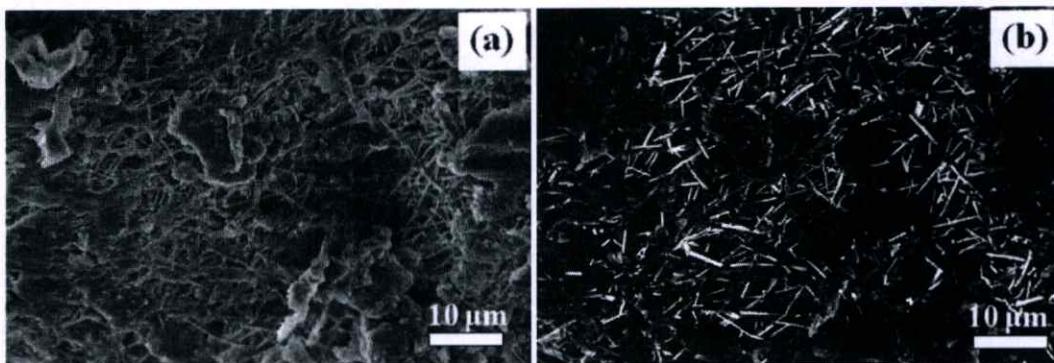


Figure 8.2 SEM micrographs of the (a) secondary electron and (b) backscattering electrons images of the PZ/CNT/PVDF nanocomposite.

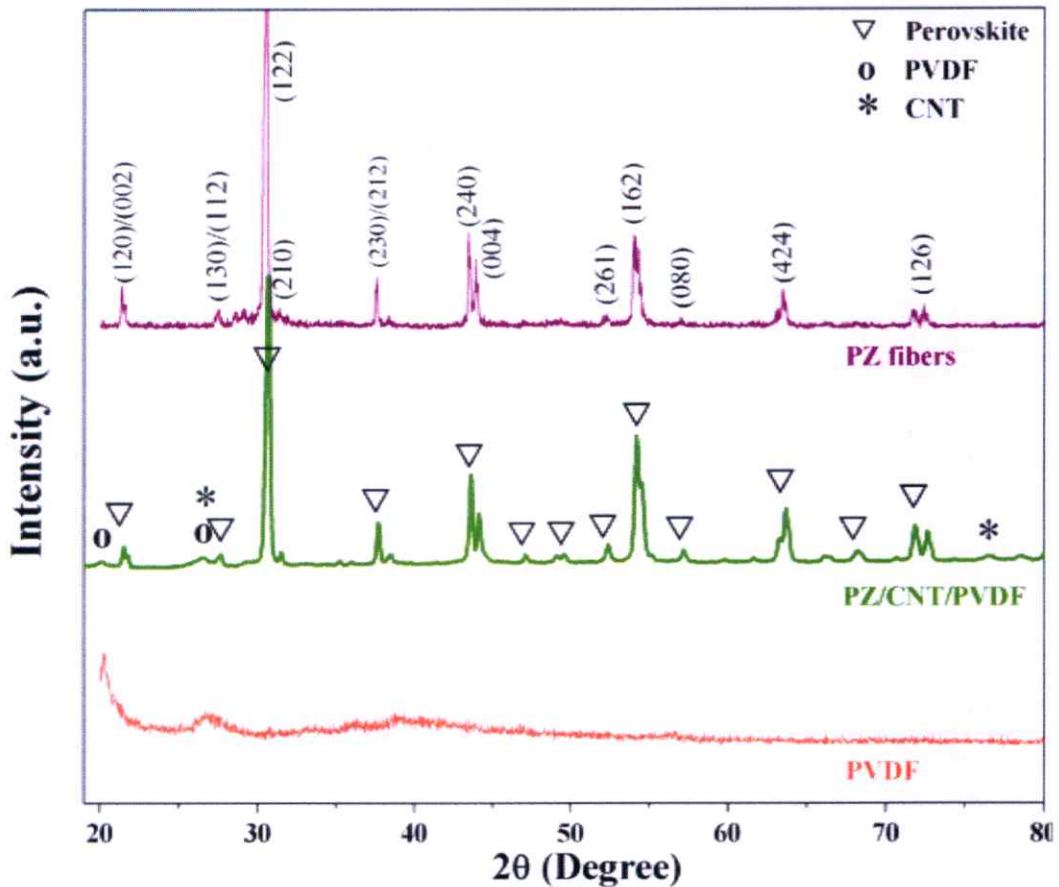


Figure 8.3 XRD patterns of PZ/CNT/PVDF nanocomposite compared with those of PZ fibers.

The crystalline phases of PZ/CNT/PVDF nanocomposite were revealed by X-ray diffraction (XRD) spectra. Figure 8.3 shows the XRD patterns of the PZ/CNT/PVDF nanocomposite compared with those of PZ fibers. The figure revealed that crystalline PZ/CNT/PVDF nanocomposite was obtained. The strong diffraction peaks at 2θ values of 21.47, 30.66, 37.81, 43.58, 54.02, 63.69 and 71.95 corresponding to (120), (122), (202), (240), (162), (424) and (126) crystal planes, respectively, indicating the formation of lead zirconate. According to JCPDS card no.75-1607, the diffraction peaks can be indexed as an orthorhombic perovskite structure. In addition, peaks of polyvinylidene fluoride (PVDF) could be observed in the XRD patterns of the composite, because PVDF is a semi-crystalline polymer with typical crystallinity of

50% [7]. Spectra of the PVDF polymer are seen at $2\theta = 26^\circ$ when referring to the diffractions in planes (021), which are characteristic of the α -phase [7]. The α -phase is the dominant crystalline phase most common upon crystallization from the melt [8], while the peak at $2\theta = 20^\circ$ refers to the sum of diffractions in plane (110) and (200), which are characteristic of the β -phase [7]. The β -phase exhibits the most piezoelectric, pyroelectric and ferroelectric activities. The latter form endues PVDF with great potential for various device applications [8]. The spectra also show that the (002) peak at 26° and (110) peak at 77° correspond to a crystal structure of graphite [9]. This study guarantees that the sample consists of three phases, including lead zirconate, carbon nanotubes and polymer phases.

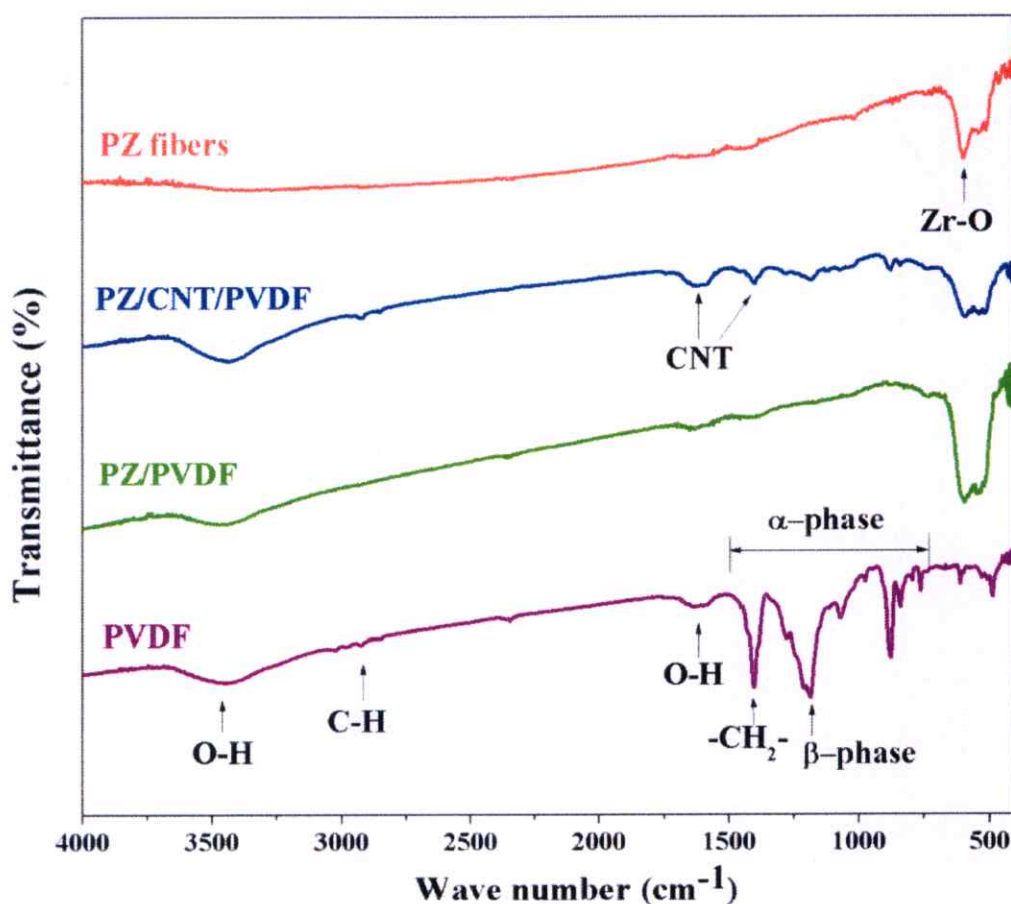


Figure 8.4 FT-IR spectra of PZ/CNT/PVDF nanocomposite compared with those of PZ fibers.

FT-IR is used to characterize the functional group of the PZ/CNT/PVDF nanocomposite. Figure 8.4 shows the FT-IR spectra in the range of $400\text{--}4,000\text{ cm}^{-1}$. At $\sim 548\text{ cm}^{-1}$, the absorption peak is attributed to Zr-O stretching vibration [10], which corresponds to the polycrystalline PZ fiber. The broad peak at around $3,400\text{ cm}^{-1}$ corresponds to the O-H stretching vibration of moisture [10]. Peaks of around $1,450\text{ cm}^{-1}$ correspond to the aliphatic CH group vibrations of the CH_2 mode of PVDF polymer [11]. The symmetric and asymmetric CH stretching vibration of PVDF is observed at $2,900\text{ cm}^{-1}$ [11]. The absorption band at $760, 800, 860, 980$ and $1,400\text{ cm}^{-1}$ corresponds to a large amount of α crystal phase, whereas a peak at $\sim 1,220\text{ cm}^{-1}$ indicates β phase of the vinylidene group of polymer [12]. A small peak at around 1650 cm^{-1} is associated with the C-C stretching of CNT [4].

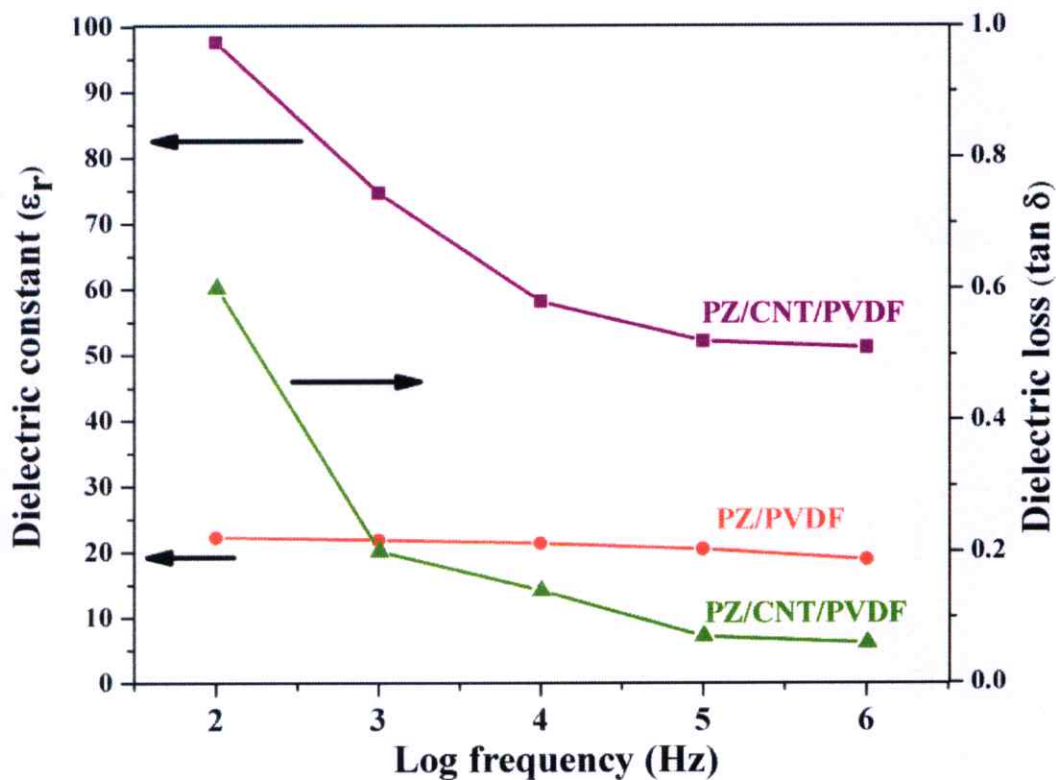


Figure 8.5 Dielectric constant and dielectric loss of PZ/CNT/PVDF nanocomposite compared with that of PZ/PVDF nanocomposite as a function of log frequencies.

A dielectric property of the PZ/CNT/PVDF nanocomposite was characterized by an LCR meter. Figure 8.5 presents frequency dependence of the dielectric constant (ϵ_r) of the PZ/CNT/PVDF nanocomposite at room temperature, and comparing with that of PZ/PVDF nanocomposite. It was found that the dielectric constant of the PZ/CNT/PVDF nanocomposite was in the range of 97–49, within the measurement frequencies from 100 Hz to 2 MHz. This value is higher than the dielectric constant of the PZ/PVDF nanocomposite measured as 18.21 (at 2 MHz), which may be due to the PZ fibers being well distributed by forming a complex mixture with CNT networks. This is in accordance with the percolation theory [13], which is the formation of long-range connectivity in random systems. This phenomenon is depicted in the schematic illustrations of Figure 8.6, which demonstrates the sample with [Figure 8.6(b)] and without [Figure 8.6(a)] CNT. Since the CNT in Figure 8.6(b) is mixed well and entangled with PZ fibers in the PVDF matrix, the task of dispersing PZ fibers uniformly inside the composite for a high-performance material is challenging. As a result, a high dielectric constant is generated. Furthermore, the conduction paths formed by the CNT networks can reduce the internal resistance of nanocomposite material [14]. Dang et al. [13] reported that CNTs reinforced by composites possess a much lower percolation threshold than those of composites containing conventional spherical fillers, such as metallic particles or carbon black. This is due to high-aspect ratio conductive fillers easily producing percolation (a conducting network) at a lower volume fraction. Thus, the CNT can act as dispersant and conduct functional material in nanocomposite. Additionally, it is noticeable that a low dielectric loss was obtained together with a high dielectric constant, as shown in Figure 8.5. The minimum value of loss is 0.02 and the maximum value is still less than 0.6, which is attractive for practical applications.

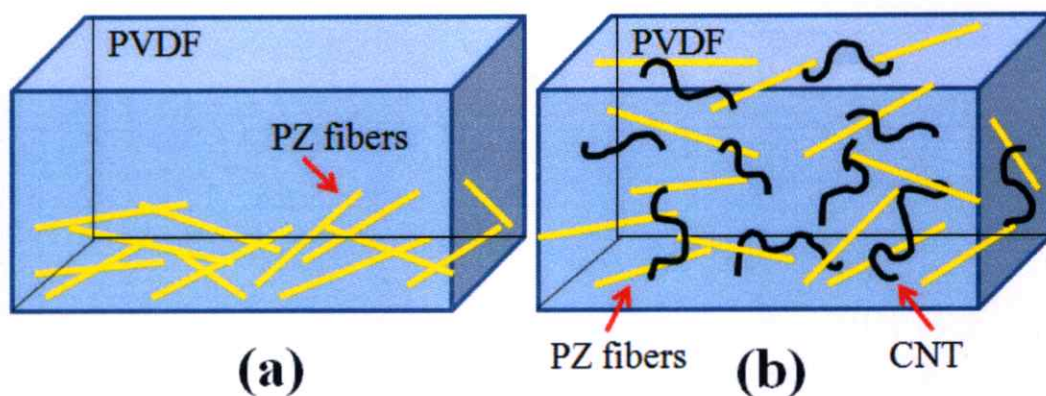


Figure 8.6 Schematics of the cross-sectional structure of PZ/PVDF nanocomposite (a) without CNT and (b) with CNT.

8.4 Summary

In summary, three-phase PZ/CNT/PVDF nanocomposite in carbon nanotubes filled with PZ/PVDF mixture was prepared via a simple casting technique using PZ fibers from the electrospinning process. The effects of CNT on the dielectric properties of PZ/PVDF nanocomposite were examined. The dielectric constant of the PZ/CNT/PVDF nanocomposite measured at room temperature was found to be in the range of 97–49, within the measurement frequencies from 100 Hz to 2 MHz, and higher than the PZ/PVDF nanocomposite without CNT. This result agrees reasonably well with the percolation theory of CNT. Thus, adjustable dielectric properties were discovered by employing the three-phase system.

REFERENCE

- [1] Wu, M., Huang, H., and Chu, W., et al. 2010. "Tuning the Ferroelectric and Piezoelectric Properties of $0.91\text{Pb}(\text{Zn}_{1/3}\text{Nb}_{2/3})\text{O}_3$ - 0.09PbTiO_3 Single Crystals and Lead Zirconate Titanate Ceramics by Doping Hydrogen." **J. Phys. Chem. C.** 114 : 9955–9960.
- [2] Joshi, N. J. 2012. "Studies of Nano-Sized High Dielectric Constant Materials." The Maharaja Sayajirao University of Baroda Vadodara, Gujarat India.
- [3] Zeng, X., Xu, X., Shenai, P. M., Kovalev, E., Baudot, C., Mathews, N., and Zhao, Y. 2011. "Characteristics of the Electrical Percolation in Carbon Nanotubes/Polymer Nanocomposites." **J. Phys. Chem. C.** 115(44), 21685–21690 (2011).
- [4] Ramesh, B. P., Blau, W. J., Tyagi, P. K., Misra, D. S., Ali, N., Gracio, J., Cabral, G., and Titus, E. 2006. "Thermogravimetric Analysis of Cobalt-Filled Carbon Nanotubes Deposited by Chemical Vapour Deposition." **Thin Solid Films.** 494 : 128–132.
- [5] Nawani, C., Boonchom, B., Prachayawarakorn, J., Vittayakorn, W., and Vittayakorn, N. 2012. "Synthesis and Phase Evolution of Electrospun Antiferroelectric Lead Zirconate (PbZrO_3) Nanofibers." **Mater. Sci. Eng B.** 177 : 1009–1016.
- [6] Safari, A. 1994. "Development of Piezoelectric Composites for Transducers." **J. Phys. III. France.** 4 : 1129–1149.
- [7] Ostasevicius, V., Milasauskaite, I., Dauksevicius, R., Baltrusaitis, V., Grigaliunas, V., and Prosycevas, I. 2010. "Experimental Characterization of Material Structure of Piezoelectric PVDF Polymer." **Mechanika.** 6(86) : 1392–1207.
- [8] Mago, G., Fisher, F. T., and Kalyon, D. M. 2009. "Deformation-Induce Crystallization and Associated Morphology Development of Carbon Nanotube-PVDF Nanocomposites." **J. Nanosci. Nanotechnol.** 9 : 3330–3340.
- [9] Cao, A., Xu, C., Liang, J., Wu, D., and Wei, B. 2001. "X-ray Diffraction Characterization on the Alignment Degree of Carbon Nanotubes." **Chem. Phys. Lett.** 344 : 13–17.
- [10] Wang, Y., and Santiago-Aviles, J. J. 2004. "Synthesis of Lead Zirconate Titanate Nanofibres and the Fouriertransform Infrared Characterization of Their Metallo-Organic Decomposition Process." **Nanotechnology.** 15 : 32–36.

- [11] Vinogradov, A. M., Schmidt, V. H., Tuthill, G. F., and Bohannon, G. W. 2004. "Damping and Electromechanical Energy Losses in the Piezoelectric Polymer PVDF." **Mech. Mater.** 36 : 1007–1016.
- [12] Ostasevicius, V., Milasauskaite, I., Dauksevicius, R., Baltrusaitis, V., Grigaliunas, V., and Prosycevas, I. 2010. "Experimental Characterization of Material Structure of Piezoelectric PVDF Polymer." **Mechanika.** 6(86) : 1392–1207.
- [13] Dang, Z. M., Yao, S. H., Yuan, J. K., and Bai, J. 2010. "Tailored Dielectric Properties Based on Microstructure Change in BaTiO₃-Carbon Nanotube/Polyvinylidene Fluoride Three-Phase Nanocomposites." **J. Phys. Chem. C.** 114 : 13204–13209.
- [14] Park, K. I., Lee, M., Liu, Y. et al. 2012. "Flexible Nanocomposite Generator Made of BaTiO₃ Nanoparticles and Graphitic Carbons." **Adv. Mater.** 1–6.

CHAPTER 9

CONCLUSIONS AND SUGGESTIONS

9.1 Conclusions

This study presents a characterization and dielectric properties of polymer-ceramic nanocomposites, by using lead zirconate (PZ) nanofiber as disperse phase and polyvinylidenedifluoride (PVDF) as matrix phase. A systematic investigation was conducted of piezoceramic nanofiber using two synthesis routes, namely the sol-gel and electrospinning process by varying the concentration, volume ratio of precursor solution to polymer, feeding rate, calcination temperature and polymer type. Moreover, this research examined the effect of solvothermal treatment on phase transformation in lead zirconate nanofibers. The optimum condition of chemical treatment for the phase transition in lead zirconate fibers was determined at different temperatures and times using dimethyl formamide as an effective solvent. Additionally, the dielectric properties of polymer-ceramic nanocomposites have been improved by adding carbon nanotubes (CNT). This chapter will summarize the experimental measurement done in this thesis and some of the suggestions to expand this study. The main obtained results in this work are as follows:

- (1) Synthesis of the nanofiber antiferroelectric lead zirconate system by electrospinning, followed by calcinations at high temperature was successfully prepared. The as-spun PZ fibers were relatively uniform and had a smooth surface. Beads or agglomerated nanofibers were not observed. The PZ nanofibers, with a well-developed perovskite structure, were obtained successfully at the calcination temperature of 650°C for 4 h.
- (2) The polymer content of the solution is important in obtaining continuous and bead-free fiber mats. The polymer content is believed to be merely adjustment of the solution viscosity. When the amount of polymer increased, the viscosity rose, due to individual polymer chains becoming entangled, thus creating more resistance to the electric field, and resulting in a more stable jet of fiber. Thus the real controlling factor appears to be the viscosity of the polymer solution. Additionally, the solution viscosity is

proportional to the polymer concentration. Therefore, the more the solution viscosity, the larger the resulting nanofiber diameters.

- (3) The precursor solution is strongly influenced in the fiber formation. Decrease in the concentration of precursor solution causes the surface tension to dominate the electrostatic force, which results in thinner fibers or bead formation along the fibers. As the concentration increases, higher electrical charges induce more jet solution to collect on the aluminum plate; thus, fibers form with a larger diameter. Moreover, a higher PZ concentration improves the structure of PZ fibers, as each highly concentrated PZ molecule is closer together than those in a diluted concentration.
- (4) From the TEM images, the mutual boundary of PZ fiber tends to minimize forming a neck in the array of grains after calcination at high temperature, which represents grain boundaries arranged by grain to grain unit cell clusters. The linearity of grains indicates good crystallographic coherence. This result differs from those in other researches, in which several agglomerates are composed of small grains.
- (5) The feeding rate has a strong effect on the morphology of calcined PZ fiber. The nature of nanofibers was changed dramatically, a necklace-like structure of packed particles or crystallites became prominent. This was due to a lower feeding rate, which acts as a function of aging that allows for a greater orientation period of the crystallites, and suggests improvement in crystallization of the PZ nanofibers. In addition, the fiber diameter was decreased when reducing the feeding rate.
- (6) The diameter of the fibers, following calcinations at various temperatures, appeared smaller on average than the as-spun fibers due to their loss of polymer and the crystallization of PbZrO_3 . Whereas, after calcinations at high temperature the average diameter of the fibers was increased due to grain growth by temperature.
- (7) The ferroelectric (FE) intermediate phase is not established in PZ fibers. However, the antiferroelectric (AFE) – paraelectric (PE) phase transition becomes broader progressively. It is clear that the PZ fibers undergo a successive phase transition from orthorhombic to cubic phase at 243°C ,

showing a Curie temperature rise of nearly 13°C, when comparing with a normal PZ particle.

- (8) The effect of solvothermal treatment on phase transformation in PZ nanofibers was investigated. The results suggested the PZ nanofibers clearly show an endothermic transition after solvothermal treatment at 170°C for 6 h using dimethyl formamide solvent. The enthalpy values for the orthorhombic-cubic transition increased with increasing temperature and time. With increasing temperature, stress is relieved gradually in such that free energy of the antiferroelectric phase could decrease and allow enthalpy values to increase. In addition, grain boundaries were prominent after heat treatment due to reduced internal stress. The diameter size of the fibers decreased slightly after dimethyl formamide chemical treatment and increased with increasing temperature and time.
- (9) This study prepared PZ fibers successfully by the electrospinning method using solution that contained commercial polymer combined with Thai glutinous rice starch (GRS) in order to increase viscosity and reduce cost of the precursor solution. The as-spun PZ/PEO/GRS composite fibers were relatively uniform with a smooth surface. The PZ nanofibers, with a well developed perovskite structure, were obtained successfully at the calcination temperature of 650 °C for 4 h.
- (10) The addition of GRS improves the appearance of the fiber, but the real controlling factor is the viscosity of the polymer solution. The higher viscosity of GRS solution resulted from chain entanglement, which causes a significant impact on the electrospinning process. Therefore, adding GRS into the solution can enhance the chain entanglement of the molecular chain, which makes the viscosity increase. Thus, the cost of the process can be reduced by successfully putting GRS into the solution.
- (11) The PZ/PVDF nanocomposite was successfully prepared by infiltrating a polyvinylidenedifluoride (PVDF) polymer into the PZ nanofiber mat, and an intimate mixture of two phases was obtained. The composite has 3-3 connectivity by using Newnham's convention on connectivity of piezocomposites, in which the active PZ and polymer matrix phases are both connected in three dimensions in the micrometer scale. The dielectric

constant of the PZ/PVDF composite measured at room temperature is higher than the polymer matrix and reasonably agrees with the prediction from the rule of mixtures. This is due to the increasing contribution of PZ to the dielectric properties of the composites, because PZ has a substantially higher dielectric constant than the polymer.

- (12) Three-phase PZ/CNT/PVDF nanocomposite from carbon nanotubes (CNT) filled with PZ/PVDF mixture was prepared via a simple casting technique using PZ fibers from the electrospinning process. The dielectric constant of the PZ/CNT/PVDF nanocomposite measured at room temperature was found to be in the range of 97–49, within the measurement frequencies from 100 Hz to 2 MHz. The dielectric constant of the PZ/CNT/PVDF nanocomposite is higher than the PZ/PVDF nanocomposite without CNT which may be due to the PZ fibers being well distributed by forming a complex mixture with CNT networks. Furthermore, the conduction paths formed by the CNT networks can reduce the internal resistance of nanocomposite material. As a result, a high dielectric constant is generated. Thus, the CNT can act as dispersant and conduct functional material in nanocomposite. Additionally, it is noticeable that a low dielectric loss was obtained together with a high dielectric constant.

9.2 Suggestions

A number of interesting factors and some problems also remain in the fabrication of nanopiezoelectric composite material. The electrical properties of nanocomposite in the field of piezoelectric application also need further study. Thus, this thesis work should be partly filled by the following suggestion for further work.

- (1) In the preparation of nanofiber, electrospinning appears to be affected by the following parameters and variables: 1) system parameters such as molecular weight, molecular weight distribution and architecture (branched, linear, etc.) of the polymer, and polymer solution properties (viscosity, conductivity, dielectric constant, and surface tension, as well as charge carried by the spinning jet) and 2) process parameters such as electric potential, flow rate and concentration, distance between the capillary and collection screen,

ambient parameters (temperature, humidity and air velocity in the chamber) and finally motion of the target screen. Therefore, the effect of these factors would need to be considered.

- (2) Careful preparation of the precursors is essential in order to electrospin ceramic systems accurately. Several parameters, such as solvent volatility, viscosity, surface tension, conductivity, applied voltage, etc., need to be optimized for all systems.
- (3) The fabrication of ceramic nanofiber could be applied to other ferroelectric materials.
- (4) In the preparation of composite material, inorganic ceramic materials need to be compatible with the polymer matrix. Therefore, as ceramic material is required to be compatible with the polymer matrix, it needs surface modification for increased compatibility.
- (5) Some improvement may be achieved by investigate the Copolymerization of vinylidenedifluoride with trifluoroethylene (TrFE), as this polymer does not need to be stretched; it can be poled directly as formed.
- (6) Further work on the dispersion and distribution of filler in composite material would facilitate an improvement. There are numerous methods and approaches for the functionalization and many efficient dispersion of filler in different media such as solution processing of composites, melt processing of bulk composites, melt processing of composite fibers, composites based on thermosets, Layer-by-layer (LBL) assembly, and in-situ polymerization.
- (7) Using high volume fraction of carbon nanotubes tend to aggregate together inside the solution, due to the strong van der Waals attraction forces between them, and they usually have highly entangled network structures. That is why dispersion of CNT inside the polymers becomes difficult.
- (8) The ceramic-polymer composite approach developed in this work could be applied to other electroceramic materials.

APPENDIX



Synthesis and phase evolution of electrospun antiferroelectric lead zirconate (PbZrO₃) nanofibers

Chanisa Nawani^{a,b}, Banjong Boomchom^c, Jutarat Prachayawarakorn^d, Wanwilai C. Vittayakorn^a, Naratip Vittayakorn^{a,b,d,*}

^a Electroceramic Research Laboratory, College of Nanotechnology, King Mongkut's Institute of Technology Ladkrabang, Bangkok 10520, Thailand

^b TheP Center, CHE, 328 Si Ayutthaya Rd., Bangkok 10400, Thailand

^c King Mongkut's Institute of Technology Ladkrabang, Chumphon Campus, 17/1 M. 6 Pha Thiew District, Chumphon 86160, Thailand

^d Department of Chemistry, Faculty of Science, King Mongkut's Institute of Technology Ladkrabang, Bangkok 10520, Thailand

ARTICLE INFO

Article history:

Received 13 January 2012

Received in revised form 18 April 2012

Accepted 28 May 2012

Available online 13 June 2012

Keywords:

Electrospinning

Sol-gel

Lead zirconate

ABSTRACT

Lead zirconate (PbZrO₃; PZO) fibers were synthesized by the electrospinning method using a solution that contained 5 wt% poly(ethylene oxide) (PEO) in ethanol and a sol-gel solution of PZO. Some parameters varied, for example, the ratio between PEO and PZO, concentrations of the precursor solution, flow rate, and calcination temperature. The as-spun and calcined PZO/PEO composite fibers were characterized by TG-DTA, X-ray diffraction, FT-IR, SEM and TEM. PZO fibers were obtained successfully with a well-developed perovskite structure after as-spun PZO/PEO composite fibers were calcined using the PZO/PEO volume ratio of 10:3 at a PZO concentration of 1.0 M at 650 °C for 4 h. Stable nanofibers were produced with an average diameter of 300 ± 64 nm. Additionally, the PZO fibers showed a Curie temperature that rose by nearly 13 °C, when comparing with a normal PZO particle.

© 2012 Elsevier B.V. All rights reserved.

1. Introduction

In recent years, fine scale piezoelectric fibers have received extensive attention because of their potential applications as building blocks in various nanotechnologies, which include mechanics [1], photonics [2], electronics [3], and sensing [4]. The high surface-to-volume ratio is an attractive characteristic that can be achieved from nanofibers, and more attention has been paid to this area. With miniaturization of electronic devices, nanofibers of piezoelectric material are currently attracting a great deal of interest in the design of smart materials, due to their novel properties that are significantly different from their bulk, such as physical and chemical properties [5]. Mai et al. [6] reported the preparation of piezoelectric lead zirconate titanate (PZT) fibers, with diameters ranging from 10 μm to 40 μm, and revealed their ferroelectric property. When heat-treated at 1000 °C, the permittivity and dielectric loss of these fibers was 581 and 0.01, respectively, at 10 kHz. Furthermore, electrospun PZT nanofibers exhibited an extremely high piezoelectric voltage constant ($g_{33} = 0.079$ V m/N), high bending flexibility, and high mechanical strength, as demonstrated by Chen et al. [7]. However, when reducing the fiber diameter to nanoscale by the

electrospinning method, fiber fusion and continuous fibers could not be formed after annealing at high temperature, as reported in many researches. Dharmaraj et al. [8] reported the preparation of ferroelectric Pb(Zr_{0.5}, Ti_{0.5})O₃ nanofibers by electrospinning, which presented fiber mats with a soldering-like attachment of nanofibers at their junction after calcinations at 550 °C. Wu and Coffey [9] reported the preparation of erbium-doped silicon and germanium oxide nanofibers, and found a partially deformed nanofiber structure with some interfiber connections forming after calcinations at 700 °C. In addition, Tuttle et al. [10] reported that the surface of fabricated aluminum acetate/PVP fibers became rough, and the fibers broke to a short length, after calcinations at 1200 °C. This demonstrated that preparation of ceramic nanofibers is fairly difficult when obtaining a continuous and smooth surface without forming interfiber connections. Furthermore, most studies of ceramic electrospinning to date have reported the synthesis of metal oxide fibers in the ferroelectric (e.g. PZT, BT) [7,11] and multiferroic system (e.g. NF-PZT, CoF-PZT) [12,13]. In this study, synthesis of the nanofiber antiferroelectric system by electrospinning, followed by calcinations at high temperature, was of interest.

Antiferroelectric lead zirconate (PbZrO₃:PZO) ceramics have received increasing attention as potential applications in micro-actuators and high energy storage capacitors [14]. The free energy difference between the antiferroelectric (AFE) and ferroelectric (FE) phase enables phase switching from the AFE to FE phase by applying an electric field [15]. PZO at room temperature has an orthorhombic structure with the lattice parameters, $a = 5.884$ Å, $b = 11.768$ Å

* Corresponding author at: Department of Chemistry, Faculty of Science, King Mongkut's Institute of Technology Ladkrabang, Bangkok 10520, Thailand. Tel.: +66 89 700 2136; fax: +66 2 326 4415.

E-mail address: naratipcmu@yahoo.com (N. Vittayakorn).

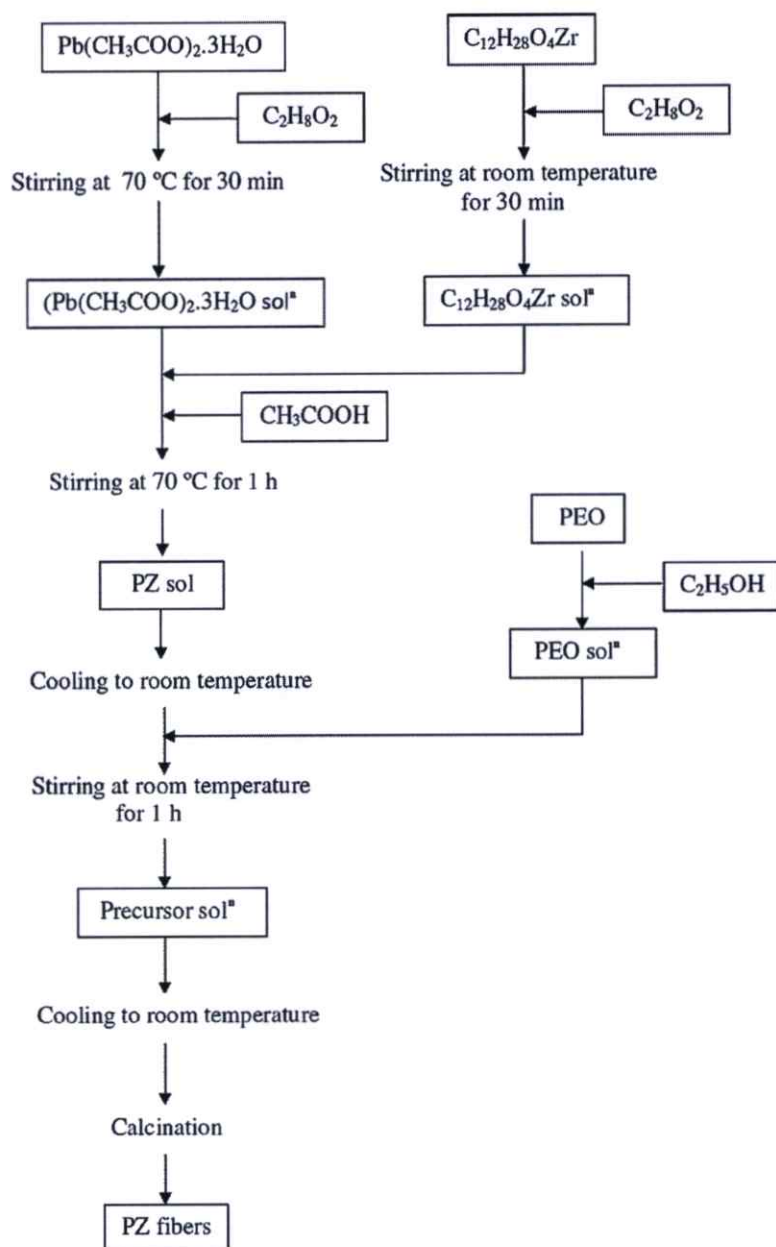


Fig. 1. Process for the preparation of PZO fibers.

and $c=8.22 \text{ \AA}$ [16]. The orthorhombic unit cell consists of eight formula units and eight primitive cells with a tetragonal structure [17]. Over the past few decades, PZO and PZO-based systems have been synthesized and utilized massively in forms of bulk ceramics or crystalline films [18]. Based on our knowledge, there has been no previous report on the fabrication of antiferroelectric PZO fibers by electrospinning. Furthermore, fibrous antiferroelectric PZO has the potential for utilizing high performance hydrophones, and high electromechanical actuator and nanogenerator applications.

2. Experimental procedure

In the preparation of lead zirconate (PZO) solution by a sol-gel process, lead acetate trihydrate $[\text{Pb}(\text{CH}_3\text{COO})_2 \cdot 3\text{H}_2\text{O}]$, puriss;

Sigma-Aldrich] and zirconium (IV) propoxide solution (~70% in propanol; Fluka) were used as precursors, and 2-methoxyethanol (puriss; Sigma-Aldrich) was selected as a solvent. The process for preparing PZO fibers is illustrated in Fig. 1. Firstly, lead acetate trihydrate was dissolved in 2-methoxyethanol, which could act as didentate chelating ligands that allowed the sol to stabilize for a long period of time at room temperature. Then, this solution was stirred for 30 min at 70 °C, with 3 mol% excess lead acetate trihydrate added to compensate for evaporation during high temperature calcination, whereas, zirconium (IV) propoxide was dissolved in 2-methoxyethanol while stirring for 30 min at room temperature. Next, the two solutions were mixed together by heating and stirring to form a sol. Acetic acid was added to the sol in order to prevent precipitation of the precursor solution, which had various final concentrations of 0.3, 0.5, 0.7, 0.9 and 1.0M, obtained after stirring at 70 °C for 1 h. In preparing

lead zirconate/poly(ethylene oxide) (PZO/PEO) solution for electrospinning, the proper solution parameter had to be found for producing lead zirconate nanofibers, after which the precursor solution was mixed with poly(ethylene oxide) (PEO, $M_v = 300,000$; Aldrich) solution (5 wt.% in ethanol) in volume ratios of 10:1, 10:2, and 10:3, consecutively. After stirring at room temperature for 1 h, the mixture was loaded into a plastic syringe, which was connected to a metallic needle and linked to a syringe pump (NE-1000, New Era Pump Systems, Inc. Wantagh, NY) in order to control the feeding rate of the solution. The positive terminal of high voltage power supply (ES30P-5 W, Gamma High Voltage Research Inc., Ormond Beach, FL) was connected to the needle tip of the syringe, while the aluminum plate collector, covered with aluminum foil, worked as a counter electrode. The distance between the needle tip of the syringe and collector was fixed at 15 cm, and the feeding rate of the solution varied. When the voltage applied between two electrodes reached 10 kV, a non-woven mat of PZO/PEO composite fibers collected on the surface of the aluminum plate, which was wrapped with aluminum foil. The reaction of the as-spun composite nanofibers, which took place during heat treatment, was investigated by differential thermal analysis (DTA; Shimadzu) and thermogravimetry analysis (TGA; Shimadzu), using a heating rate of $10^\circ\text{C}/\text{min}$ in air that ranged from room temperature to 1300°C . X-ray diffraction (XRD; Bruker-D8 Advance) using $\text{Cu K}\alpha$ radiation was used to determine the phases formed and optimum firing temperatures for formation of the desired phase. A room-temperature FT-IR spectrum ranging from 4000 to 370 cm^{-1} was recorded by a PerkinElmer Spectrum GX FT-IR/FT-Raman spectrometer, with eight scans and a resolution of 4 cm^{-1} using KBr pellets. Phase transition of the fibers was investigated, using a differential scanning calorimeter (DSC 2920, TA Instrument) between room temperature and 300°C at a heating rate of $10^\circ\text{C}/\text{min}$. Finally, a scanning electron microscope (SEM, JEOL JSM5910LV) and transmission electron microscopy (TEM, JEOL JEM-2100) were used to observe the morphology of the PZO fibers.

3. Results and discussion

3.1. Effect of PZO/PEO volume ratios

Fig. 2 shows the SEM photographs of the as-spun PZO/PEO composite, with a PZO concentration of 0.7 M using the PZO/PEO volume ratios of 10:1, 10:2 and 10:3, consecutively. Fig. 2(a) indicates that continuous fibers could not form, as the jet broke up into droplets, due to the low viscosity of the precursor solution. With the polymer in highly diluted solution, each polymer chain was so far apart, most of them were separated. When the amount of PEO increased, the viscosity rose, due to individual polymer chains becoming entangled, thus creating more resistance to the electric field, and resulting in a more stable jet. In general, chain entanglement causes a significant impact on the electrospinning process by determining whether the jet breaks up into droplets, beads, or fibers and if it affects the geometry of fiber formations [19]. The formation of beads was observed in low viscosity solution, as presented in Fig. 2(b), whereas, continuous fibers and smooth surface with uniform diameter were obtained in high viscosity solution, which indicated a smooth injection of PZO sol dispersed in the polymer matrix during electrospinning (Fig. 2(c)). A remarkable correlation was observed when comparing with the optimum conditions determined from solution with a PZO/PEO volume ratio of 10:3. That is to say, the PEO content of the solution is important in obtaining continuous and bead-free fiber mats, but the real controlling factor appears to be the viscosity of the polymer solution. The PEO content is believed to be merely adjustment of the polymer

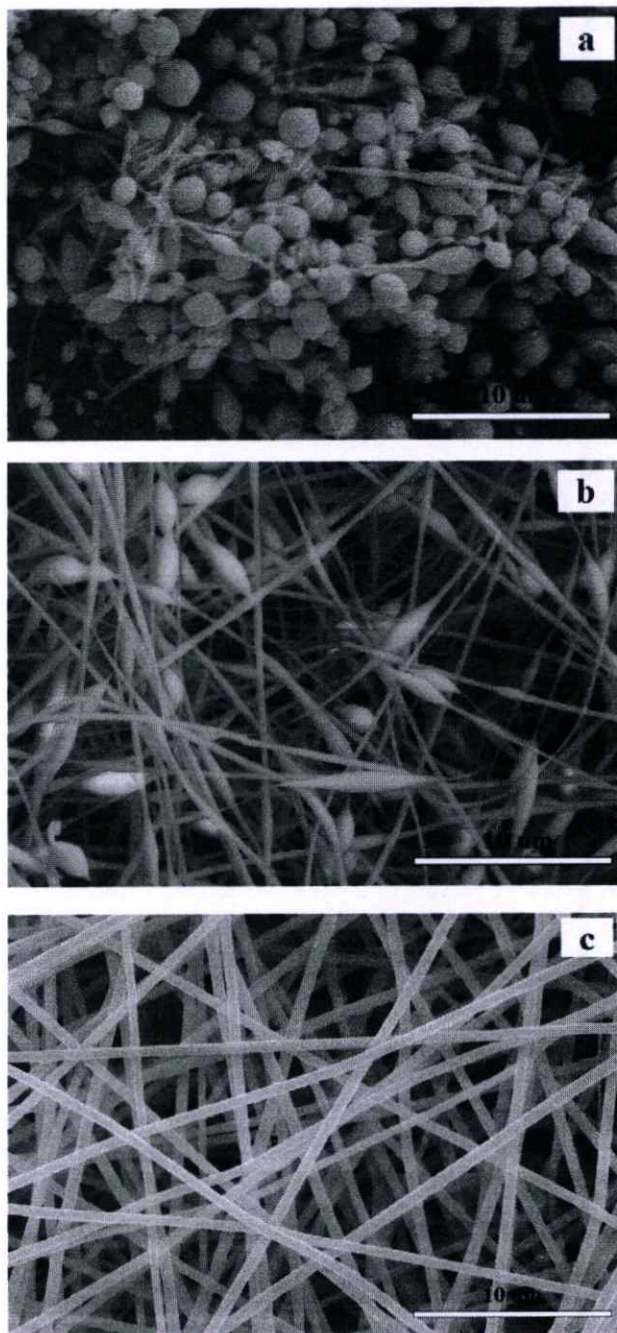


Fig. 2. SEM micrographs of the as-spun PZO/PEO nanofibers with a PZO concentration of 0.7 M at the PZO/PEO volume ratio of (a) 10:1, (b) 10:2 and (c) 10:3, consecutively.

viscosity. However, when a solid polymer is dissolved in a solvent; the more the solution viscosity is proportional to the polymer concentration, the larger the resulting nanofiber diameters, according to a power law relationship [19].

3.2. Effect of PZO concentrations

Fig. 3 shows the SEM micrograph of the as-spun PZO/PEO volume ratio of 10:3 at PZO concentrations of 0.3, 0.5, 0.7, 0.9 and 1.0 M, consecutively. When comparing between Fig. 3(a), (b), (c), (d) and (e), the formation of beads can be seen to decrease with increased

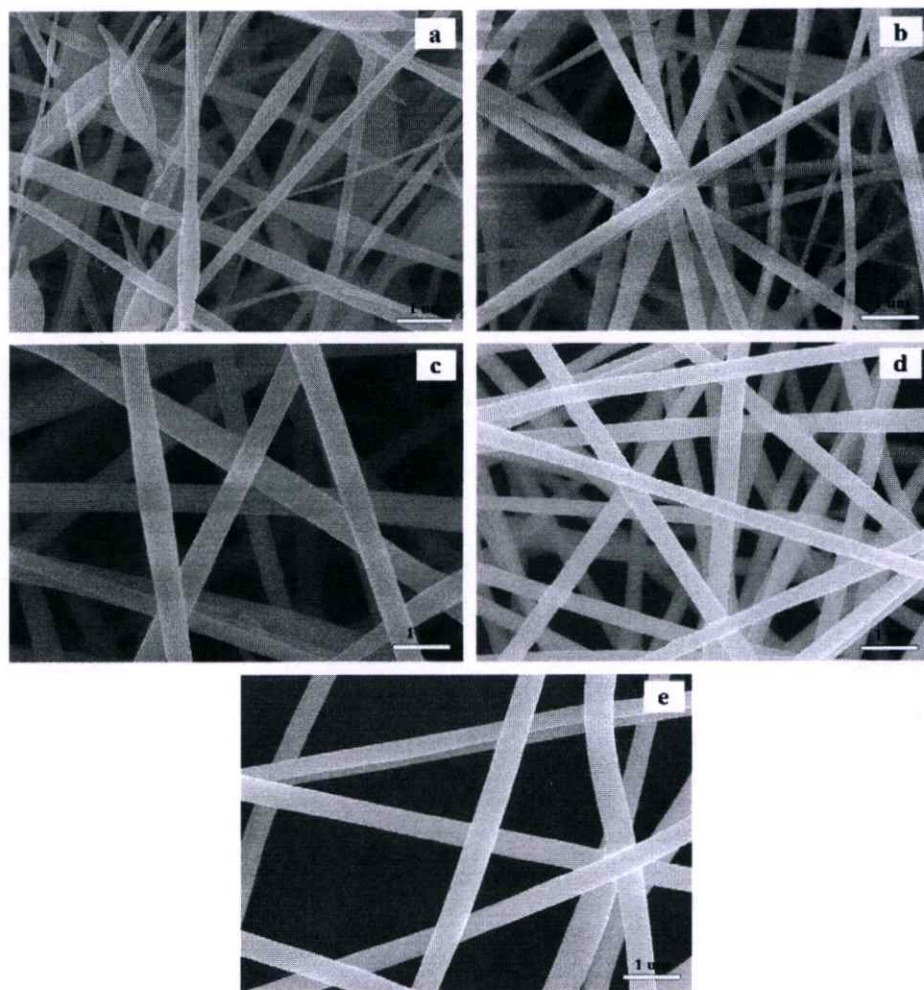


Fig. 3. SEM micrograph of the as-spun PZO/PEO volume ratio of 10:3 at PZO concentrations of (a) 0.3, (b) 0.5, (c) 0.7 (d) 0.9 and (e) 1.0 M, consecutively.

PZO concentration, and the as-spun PZO/PEO composite fibers, with PZO concentrations of 0.7, 0.9 and 1.0 M, have relative uniformity and a smooth surface, which indicates that the PZO was dispersed uniformly in the PEO medium. Beads or agglomerated fibers could not be observed. Furthermore, it can be seen that the average fiber diameter increases with increased PZO concentration. Decreases in the concentration of precursor solution cause the surface tension to dominate the electrostatic force, which results in thinner fibers or bead formation along the fibers. As the concentration increases, higher electrical charges induce more jet solution to collect on the aluminum plate; thus, fibers form with a larger diameter, which averages 266 ± 92 nm, 300 ± 51 nm, 354 ± 33 nm, 364 ± 38 nm and 439 ± 74 nm with a PZO concentration of 0.3, 0.5, 0.7, 0.9 and 1.0 M, respectively.

Thermal analysis was carried out to investigate the decomposition process of the fiber. The result of TG and DTA analyses of the as-spun PZO/PEO composite fibers are shown in Fig. 4. The endothermic peak in the DTA curve, and weight loss ($\sim 24\%$) in the TGA curve, were observed below 350°C , which indicates a loss of moisture and trapped solvent in the as-spun fibers [20]. Despite bending instability during the electrospinning process, the jet path length increased enormously, which provided passage for the solvent to evaporate and the fibers to solidify, but a small amount of solvent still remained on the fiber surface. Whereas, an endothermic peak and a weight loss ($\sim 3\%$) in the range of $400\text{--}550^\circ\text{C}$ were due to the degradation of PEO, and there was no change here in the

weight loss range of $550\text{--}900^\circ\text{C}$. On the other hand, there was an exothermic peak at 850°C in the DTA thermograph, which possibly corresponded to formation of the perovskite phase. In addition, the endothermic peaks in the DTA curve and weight loss ($\sim 7\%$) in the TGA curve, in temperatures ranging from 900°C to 1000°C , were

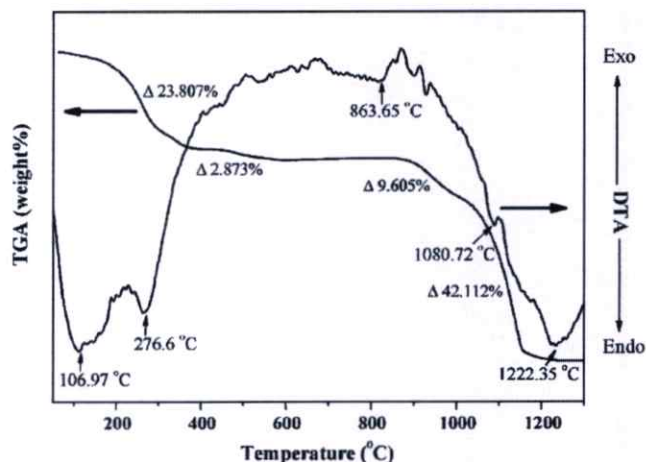


Fig. 4. TG-DTA curves of thermal decomposition of the as-spun PZO/PEO composite nanofiber.

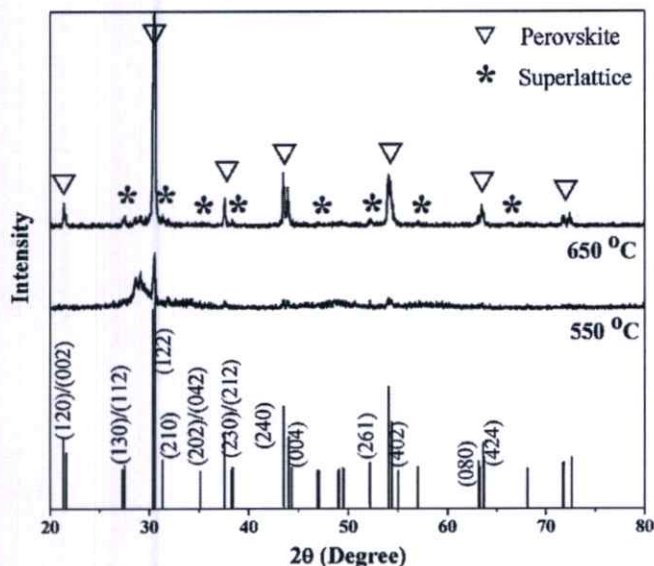


Fig. 5. XRD patterns of electrospun PZ/PEO composite nanofibers calcined in air for 4 h at different temperatures.

due to the loss of PbO at high temperature. Based on the TG-DTA results, the mixture was calcined at various temperatures ranging from 550 °C to 850 °C, with dwell times of 4 h and heating/cooling rates in a closed alumina crucible ranging around 5 °C/min, in order to investigate the perovskite phase formation.

The crystalline phases of PZO fibers at various calcined temperatures were determined by X-ray diffraction spectra. Fig. 5 shows the XRD patterns of PZO/PEO composite fibers calcined at different temperatures. After calcinations of as-spun PZO/PEO composite fibers at 550 °C for 4 h, it was revealed that crystallization of the perovskite phase began to form. However, the main peak intensity of the PZO phase was weak, and a broad diffraction peak appeared at around $2\theta = 28^\circ$, which implied that the fiber was not fully crystallized and, to some extent, had an amorphous phase. When the calcination temperature was 650 °C, the crystalline PZO fibers, with a well-developed perovskite structure, were obtained successfully. According to JCPDS card no.75-1607, the diffraction peaks can be indexed as an orthorhombic perovskite structure of lead zirconate. No other peaks could be observed in the XRD patterns, which indicated that the sample is free from lead oxide or any other crystalline materials. By increasing the calcination temperature, the intensities of the peaks increase, and the full width at half maximum of the (122) main peak decreases, which indicates that crystallization of the PZO nanofibers has improved. The relative intensity of (*hkl*) peaks to that of the (122) peak in nanofibers increases with increased calcination temperature, which agrees well with the results of PZO films [21]. The lattice parameter calculated from the XRD pattern comprised $a = 5.8824 \text{ \AA}$, $b = 11.7711 \text{ \AA}$ and $c = 8.2294 \text{ \AA}$, which are close to reported values [13]. Furthermore, the PEO decomposes at 450 °C, according to its thermal properties, and this study guarantees that its sample was free from PEO polymer.

Formation of the perovskite structure in the calcined PZO fibers was supported further by FT-IR spectra, as shown in Fig. 6. The spectrum of the PZO/PEO composite fibers shows multiple absorption bands in the region 1000–4000 cm^{-1} , which correspond to the stretching and bending vibrations of PEO and moisture. Of these, peaks of around 1450 cm^{-1} correspond to the aliphatic CH group vibrations of the CH_2 mode [22]. The band of 1337 cm^{-1} has been attributed to the deformed vibration of CH_3 groups [6]. Peaks at 1020 and 1048 cm^{-1} are assigned for stretching the C–O

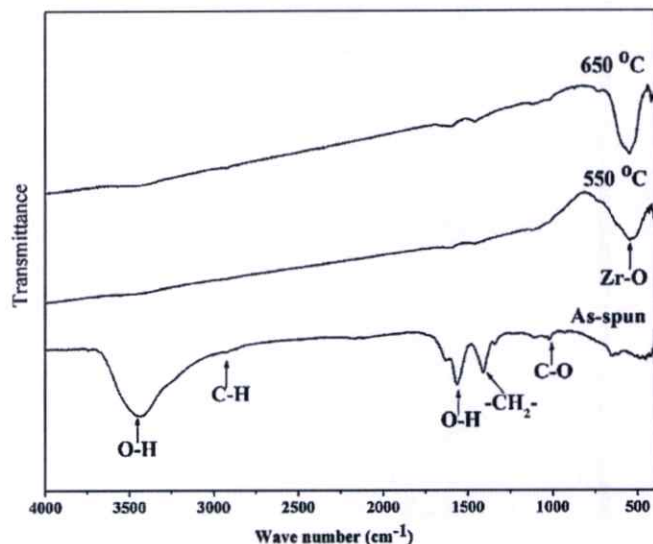


Fig. 6. FT-IR spectra of electrospun PZ/PEO composite nanofibers calcined in air for 4 h.

bond of 2-methoxyethanol and/or rocking vibration of CH_3 groups [23]. The wave number at $\sim 1600 \text{ cm}^{-1}$ and broad peak at around 3400 cm^{-1} correspond to and are assigned for O–H stretching vibration, respectively, and the shoulder at 2900 cm^{-1} is related to the stretching vibration of C–H bonds [23]. After calcination at 550 °C for 4 h, it was found that these peaks almost disappear, indicating that most of the PEO and other organics have been removed. The appearance of an absorption peak at $\sim 548 \text{ cm}^{-1}$ is attributed to Zr–O stretching vibration [24], which corresponds to the polycrystalline fiber obtained. As the calcination temperature increases to 650 °C, the absorption peak of Zr–O bonds becomes narrower and more intense, which indicates that the crystallization of the PZO fibers improves with increasing calcination temperature, and the PEO is fully decomposed, as suggested in the XRD results.

In general, the formation of PZO fibers from composite ones should involve three main processes: evaporation of the polymer (PEO); nucleation and growth of PZO nanocrystals; and directional mass transport of the PZO crystal to form continuous fibers [25]. Fig. 7(a)–(f) shows scanning electron microscopy (SEM) and transmission electron microscopy (TEM) images of the PZO fibers calcined at 650 °C, with the PZO/PEO volume ratio of 10:3 at PZO concentrations of 0.7, 0.9 and 1.0M, consecutively. The average diameter of fibers was $270 \pm 38 \text{ nm}$, $294 \pm 48 \text{ nm}$ and $300 \pm 64 \text{ nm}$ with a PZO concentration of 0.7, 0.9 and 1.0M, respectively, after calcination. SEM images of these fibers present a uniform and smooth surface (in Fig. 7(a)–(c)), whereas, TEM images (Fig. 7(d)–(f)) show that PZO fibers with a higher PZO concentration have improved fiber structure. It is evident from the TEM images that the mutual boundary tends to minimize forming a “neck” in the array of grains, which represents grain boundaries arranged by grain to grain unit cell clusters. The linearity of grains indicates good crystallographic coherence. This result differs from those in other researches, in which several agglomerates are composed of small grains. Wang et al. reported the fabrication of WO_3 Nanofibers, when the TEM image of the sample showed a grained fiber structure after calcination [26]. Kumar et al. reported the “fabrication of TiO_2 nanofibers by electrospinning”, when observing that the micrograph of nanofibers consisted of several agglomerated grains when heated at 650 °C [27]. A higher PZO concentration improves the structure of PZO fibers, due to each highly concentrated PZO molecule being closer together

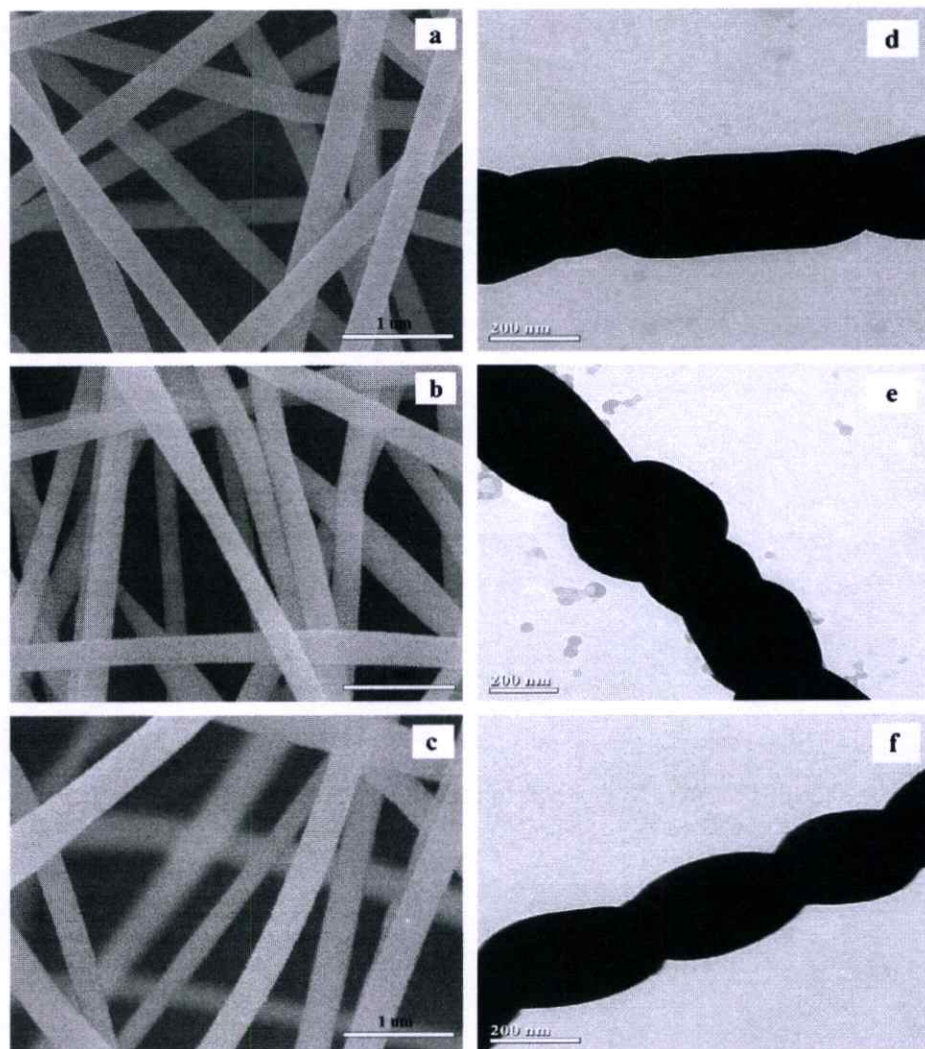


Fig. 7. (a)–(c) SEM micrographs and (d)–(f) TEM micrographs of the PZO fibers calcined at 650 °C with the PZO/PEO volume ratio of 10:3 at PZO concentrations of 0.7, 0.9 and 1.0 M, consecutively.

than those with a low concentration. When the temperature is high enough to eliminate the polymer between molecules, PZO molecules will connect more easily between crystals at a higher concentration.

3.3. Effect of calcination temperature

Fig. 8(a)–(h) shows SEM images of the as-spun and PZO fibers, with the volume ratio of 10:3 at PZO concentrations of 1.0 M, and calcined at 650, 750 and 850 °C, consecutively. All the calcined samples present non-woven fabrics, with interconnected continuous free space between the fibers to form a structure of packed particles or crystallites. While the PEO was removed selectively during calcinations at 650 °C, the fiber structures remained continuous, with an average diameter of 300 ± 64 nm, as seen in Fig. 8(b). The diameter of the fibers, following calcinations at various temperatures, appeared smaller on average than the as-spun fibers, for example, the average fiber diameter was decreased from 439 ± 74 nm (Fig. 9(a)) to 300 ± 64 nm after calcination at 650 °C. The reduction in size of the nanofibers should be attributed to their loss of PEO and the crystallization of PbZrO_3 . The fibrous material is considerably more brittle and delicate than the as-spun materials. The decrease in the flexibility of the fibers may result from a

high fraction of crystallinity and/or cross-linking between fibers during calcination. Whereas, after calcinations at 750 and 850 °C (Fig. 8(c) and (d)), the fibers became rough and presented a detailed non-woven electrospun mat, and through interpenetration and entanglement of molecular chains after annealing, a soldering-like attachment of the nanofibers was visualized at their junction points, when the average diameter of the fibers was 471 ± 60 nm and 516 ± 69 nm, consecutively. The enhancement of this fiber diameter is due to grain growth by temperature. In addition, the effect of feeding rate on the fiber was studied as well, and showed that when decreasing the feeding rate from 2 ml/h to 0.5 ml/h, the average fiber diameter was decreased from 439 ± 74 nm to 378 ± 43 nm. This result corresponded with the research of Rutledge and co-workers [28], in which the jet solution became thinner when the feeding rate decreased. Furthermore, it was observed that the nature of nanofibers was changed dramatically, and a necklace-like structure of packed particles or crystallites became prominent when decreasing the feeding rate of the precursor solution from 2 ml/h (Fig. 8(a)–(d)) to 0.5 ml/h (Fig. 8(e)–(h)). It is clear from these results that the feeding rate has a strong effect on the morphology of calcined PZO/PEO, which are composite nanofibers. This was due to a lower feeding rate, which acts as a function of aging that allows for a greater orientation period

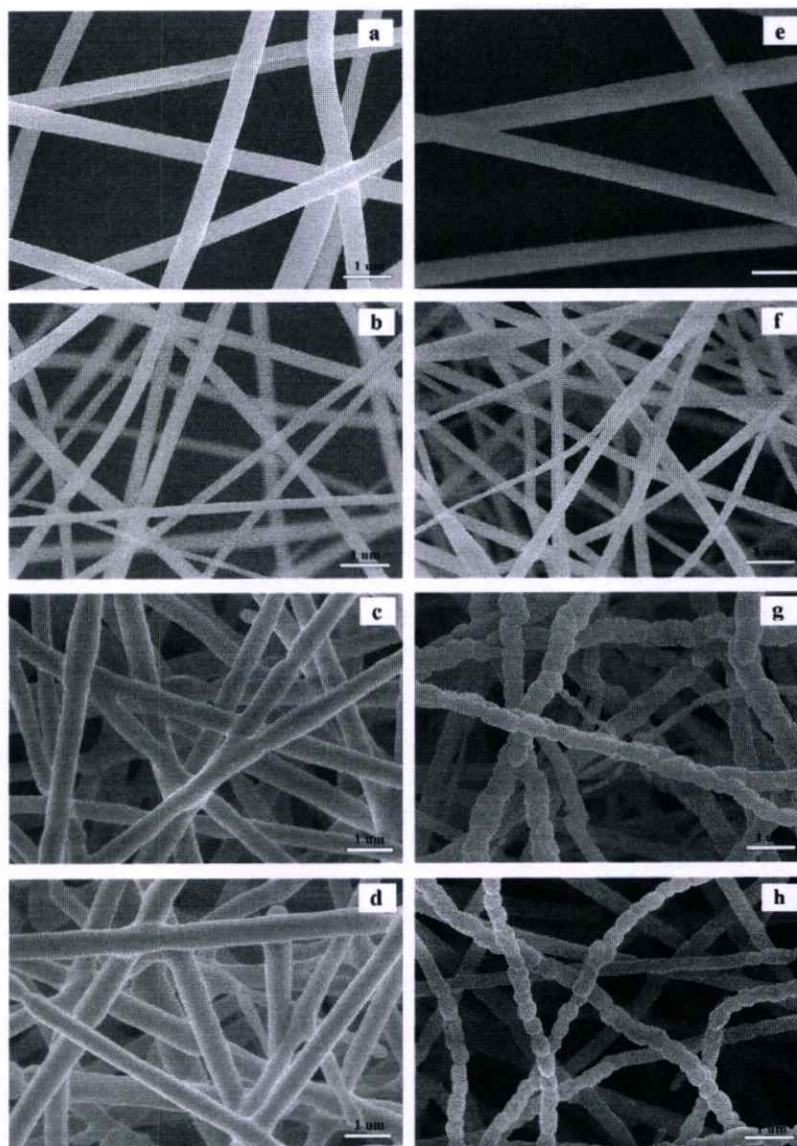


Fig. 8. SEM micrograph of the fibers using: (a)–(d) feeding rate of 2 ml/h and (e)–(h) feeding rate of 0.5 ml/h of the as-spun fibers with the volume ratio of 10:3 at PZO concentrations of 1.0 M, and PZO fibers calcined in air for 4 h at 650, 750 and 850 °C, consecutively.

of the crystallites, and suggests improvement in crystallization of the PZO nanofibers. In addition, the fiber diameter was decreased when reducing the feeding rate, i.e. the diameter of PZO fiber was decreased from 516 ± 69 nm (Fig. 8(d)) to 370 ± 39 nm when calcined at 850 °C (Fig. 8(h)). This may be due to a lower feeding rate by allowing more time for chain entanglement, which causes individual molecules to close up and result in a smaller fiber diameter.

3.4. Thermal properties

Fig. 9 shows results of the DSC for the PZO particle and PZO fibers from using the solid state and electrospinning method, respectively. The DSC result of the PZO particle shows two sharp and distinct endothermic peaks, which become closer together. The lower temperature corresponds to the transition temperature of the antiferroelectric (AFE) \rightarrow ferroelectric (FE) phase transition, while the higher temperature corresponds to the FE \rightarrow paraelectric (PE) phase transition. Whereas, the FE intermediate phase is not established in PZO fibers. However, the AFE–PE phase transition

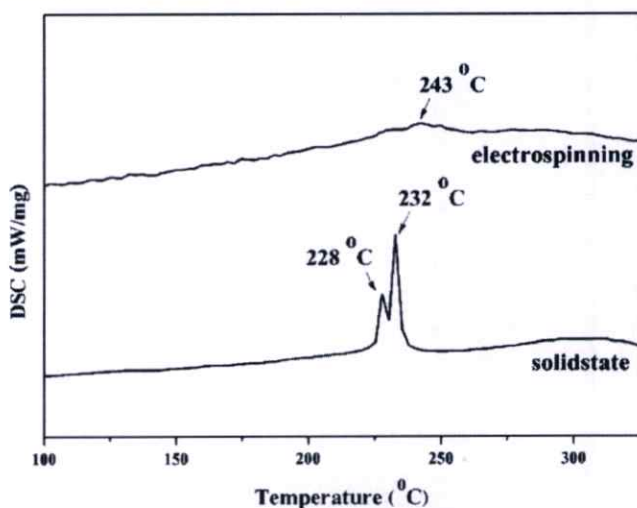


Fig. 9. Typical DSC curves for PZ fibers and PZO particles.

becomes broader progressively. This result is likely in line with the research of Lu et al. [29], who present the DSC curve with neither a transition phase nor an endothermic peak when synthesized BT is in nanosize. It is clear from the figure that the PZO fibers undergo a successive phase transition from orthorhombic to cubic phase at 243 °C, showing a Curie temperature rise of nearly 13 °C, when comparing with a normal PZO particle. It is well known that the grain sizes in PZO particles are usually in micrometer range, which is more than 100 times larger than those of PZO fibers. The reduced grain size in electrospun PZO fibers causes larger grain-boundary areas, and relieves internal stresses further in materials, due to grain boundary sliding. Smaller internal stresses, which are relaxed by grain boundaries, could decrease the free energy of the antiferroelectric phase, thus increasing the Curie temperature. Therefore, nanostructured PZO fibers have a higher T_c than PZO particles.

4. Conclusion

In summary, this study successfully prepared PZO fibers by the electrospinning method. The as-spun PZO/PEO composite fibers were relatively uniform and had a smooth surface. Beads or agglomerated nanofibers were not observed. The PZO nanofibers, with a well-developed perovskite structure, were obtained successfully at the calcination temperature of 850 °C for 4 h. Furthermore, it is clear that the PZO fibers undergo a successive phase transition from orthorhombic to cubic phase at 243 °C, showing a Curie temperature rise of nearly 13 °C, when comparing with a normal PZO particle.

Acknowledgements

The Royal Golden Jubilee Ph.D. Program (RGJ) under The Thailand Research Fund (TRF), the KMITL research fund and the National Research Council of Thailand (NRCT) supported this work.

References

- [1] S.M. Khaled, R. Sui, P.A. Charpentier, A.S. Rizkalla, *Langmuir* 23 (2007) 3988.
- [2] J. Zhao, C. Jia, H. Duan, Z. Sun, X. Wang, E. Xie, *Journal of Alloys and Compounds* 455 (2008) 497.
- [3] S. Pukird, P. Chamninok, D. Polsongkram, P. Inchidjuy, U. Tipparach, L. Chow, *CMU Journal of Nature Science Special Issue on Nanotechnology* 7 (1) (2008) 95.
- [4] Q. Liu, B. Li, J. Gong, Y. Sun, W. Li, *Journal of Alloys and Compounds* 466 (2008) 314.
- [5] Z. Cai, J. Li, Y. Wang, *Journal of Alloys and Compounds* 489 (2010) 167.
- [6] M. Mai, C. Lin, Z. Xiong, H. Xue, L. Chen, *Journal of Physics: Conference Series* 152 (2009) 012077.
- [7] X. Chen, R. Galos, Y. Shi, *The 6th International Workshop on Advanced Smart Materials and Smart Structures Technology ANCRISST2011*, July 25–26, 2011, Dalian, China, 2011.
- [8] N. Dharmaraj, C.H. Kim, H.Y. Kim, *Materials Letters* 59 (2005) 3085.
- [9] J. Wu, J.L. Coffer, *Chemistry of Materials* 19 (2007) 6266.
- [10] R.W. Tuttle, A. Chowdury, E.T. Bender, R.D. Ramsier, J.L. Rapp, M.P. Espe, *Applied Surface Science* 254 (2008) 492.
- [11] H. Li, Y. Sun, W. Zhang, W. Pan, *Journal of Alloys and Compounds* 508 (2010) 536.
- [12] S.H. Xie, J.Y. Li, Y.Y. Liu, L.N. Lan, G. Jin, Y.C. Zhou, *Journal of Applied Physics* 104 (2008) 024115.
- [13] W. Chen, X.F. Chen, Z.H. Wang, W. Zhu, O.K. Tan, *Journal of Materials Science* 44 (2009) 4939.
- [14] X.G. Tang, A.L. Ding, W.G. Luo, *Applied Surface Science* 174 (2001) 148.
- [15] Y. Liu, X. Hao, J. Zhou, J. Xu, S. An, *Journal of Alloys and Compounds* 509 (2011) 8779.
- [16] N. Vittayakorn, B. Boonchom, *Journal of Alloys and Compounds* 509 (2011) 2304.
- [17] L. Cakare, M. Kosec, B. Malic, *Journal of Sol–Gel Science and Technology* 19 (2000) 603.
- [18] P. Charoonsuk, S. Wirunchit, R. Muanghlua, S. Niemcharoen, B. Boonchom, N. Vittayakorn, *Journal of Alloys and Compounds* 506 (2010) 313.
- [19] J.H. He, Y.Q. Wan, J.Y. Yu, *Fibers and Polymers* 9 (2) (2008) 140.
- [20] S. Maensiri, W. Nuansing, J. Klinkaewnarong, P. Laokul, J. Khemprasit, *Journal of Colloid and Interface Science* 297 (2006) 578.
- [21] E.-D. Ion, B. Malic, M. Kosec, *Journal of the European Ceramic Society* 27 (2007) 4349.
- [22] Z. Zhang, X. Li, C. Wang, L. Wei, Y. Liu, C. Shao, *Journal of Physical Chemistry* 113 (2009) 19397.
- [23] K. Kitaoka, H. Kozuka, T. Yoko, *Journal of the American Ceramic Society* 81 (5) (1998) 1189.
- [24] Y. Wang, J.J. Santiago-Aviles, *Nanotechnology* 15 (2004) 32.
- [25] A. Le Viet, M.V. Reddy, R. Jose, B.V.R. Chowdari, S. Ramakrishna, *Journal of Physical Chemistry* 114 (2010) 664.
- [26] G. Wang, Y. Ji, X. Huang, X. Yang, P.I. Gouma, M. Dudley, *Journal of Physical Chemistry B* 110 (2006) 23777.
- [27] A. Kumar, R. Jose, K. Fujihara, J. Wang, S. Ramakrishna, *Chemistry of Materials* 19 (2007) 6536.
- [28] G.C. Rutledge, S.V. Fridrikh, *Advanced Drug Delivery Reviews* 59 (2007) 1384.
- [29] S.W. Lu, B.I. Lee, Z.L. Wang, W.D. Samuels, *Journal of Crystal Growth* 219 (2000) 269.



The Effect of Thai Glutinous Rice Starch on the Synthesis of Lead Zirconate (PbZrO_3) Nanofibers via the Electrospinning Method

Chanisa Nawani¹, Wanwilai Vittayakorn¹, Rangson Muanghua², Surasak Niemcharoen², Jutarat Prachayawarakorn³, and Naratip Vittayakorn^{1,3,*}

¹ *Electroceramic Research Laboratory, College of Nanotechnology, King Mongkut's Institute of Technology Ladkrabang, Bangkok 10520, Thailand*

² *Department of Electronics, Faculty of Engineering, King Mongkut's Institute of Technology Ladkrabang, Bangkok 10520, Thailand*

³ *Department of Chemistry, Faculty of Science, King Mongkut's Institute of Technology Ladkrabang, Bangkok 10520, Thailand*

This study synthesized blended lead zirconate (PbZrO_3 :PZ)/poly(ethylene oxide)(PEO)/Glutinous rice starch (GRS) nanofibers by the electrospinning method. A number of parameters such as the ratio between PEO and GRS and calcination temperature have been studied. The as-spun PZ/PEO/GRS composite and PZ fibers were characterized by TG-DTA, X-ray diffraction, FT-IR and SEM, respectively. SEM results showed that smooth and continuous fibers were obtained at the volume ratio of 10:2:1, PZ/PEO/GRS. After calcination of the as-spun PZ/PEO/GRS composite nanofibers at 650 °C for 4 h, PZ nanofibers with perovskite structure were obtained successfully. The fibers had a uniform and smooth surface without grain boundaries. However, when the calcination temperature increased to 750 °C and 850 °C, the fiber represented a necklace-like structure with grain boundaries arranged by grain to grain unit cell clusters.

Keywords: PZ, GRS, PEO, Electrospinning, Sol–Gel.

1. INTRODUCTION

In recent years, one-dimensional nanostructures of metal oxides and related materials, such as nanowires and nanofibers, have been a subject of intense research because of their potential applications as building blocks in various nanotechnologies, which include mechanics, photonics, electronics, and sensing.¹

Over the past few decades, PZ and PZ-based systems have been synthesized and utilized massively in forms of bulk ceramics or crystalline films.² In addition, there has been no previous report in the literature on the fabrication of PZ fibers by electrospinning. The high surface-to-volume ratio is an attractive characteristic that can be achieved from nanofibers. With miniaturization of electronic devices, nanofibers of piezoelectric material are currently attracting a great deal of interest in the design of smart materials, due to their novel properties that are

significantly different from their bulk, such as mechanical and electrical property.³

Antiferroelectric lead zirconate (PbZrO_3 :PZ) materials have received increasing attention as potential applications in micro-actuators and high energy storage capacitors.⁴ The free energy difference between the antiferroelectric (AFE) and ferroelectric (FE) phase makes it possible to force phase switching from the AFE to FE phase by applying an electric field.⁵ At room temperature, PZ has an orthorhombic structure with the lattice parameters, $a = 5.884 \text{ \AA}$, $b = 11.768 \text{ \AA}$ and $c = 8.22 \text{ \AA}$.⁶

Electrospinning is a simple and convenient method for producing fibers with polymeric, composite or ceramic compositions. Electrospinning, in combination with the conventional sol–gel process, has been extended recently to fabricate a variety of ceramic nanofibers.⁷ From this technique, the ceramic nanofibers and conventional sol–gel precursors are mixed with various kinds of polymers, such as poly(ethylene oxide) (PEO), poly(vinylpyrrolidone) (PVP) and poly(vinyl alcohol) (PVA), to increase

*Author to whom correspondence should be addressed.

viscosity.⁸ However, these polymers are fairly expensive. Starch is a natural high molecular weight polysaccharide composed of glucose units. Most starches consist of two components: a linear glucose polymer amylose, and a branched polymer amylopectin. Amylose most likely accounts for the disintegrant properties of starch by containing up to 6,000 glucose units connected by α -1,4 linkage. On the other hand, amylopectin is a good binder. It has a highly branched structure consisting of short linear chains with a degree of polymerization ranging from 10 to 60 glucose units, which are connected to each other by α -1,6 linkage.⁹ Glutinous rice is of a kind commonly cultivated in Thailand, which has low cost, high viscosity and high amylopectin (99.70%). Glutinous rice starch (GRS) is used widely in food industries, but few of its applications have been reported in the electronics business.

Therefore, this study synthesized lead zirconate fibers by the electrospinning method using solution that contained PEO, Thai GRS and a sol-gel precursor solution of PZ. The ratio between PEO, GRS and PZ concentrations of the precursor solution, which could result in formation of PZ fibrils, was varied.

2. EXPERIMENTAL DETAILS

In the preparation of PZ solution by a sol-gel process, lead acetate trihydrate [Pb(CH₃COO)₂ · 3H₂O, puriss; Sigma-Aldrich], and zirconium (IV) propoxide solution (~70% in propanol; Fluka) were used as precursors, and 2-methoxyethanol (puriss; Sigma-Aldrich) was selected as a solvent. Firstly, lead acetate trihydrate was dissolved in 2-methoxyethanol, which could act as didentate chelating ligands. This allowed the sol to be stable for a long period of time at room temperature. Then, this solution was stirred for 30 minutes at 70 °C, with 3 mol% excess lead acetate trihydrate added to compensate for evaporation during calcination at high temperature, whereas, zirconium (IV) propoxide was dissolved in 2-methoxyethanol at room temperature for 30 minutes while stirring. Next, these two solutions were mixed together by heating and stirring to form a sol, with acetic acid added to it in order to prevent precipitation of the precursor solution. The precursor solution, which had final concentrations of 1.0 M, was obtained after stirring at 70 °C for 1 h. In preparing PZ/PEO/GRS solution for electrospinning, the proper solution parameter had to be found for producing lead zirconate nanofibers, after which the precursor solution was mixed with poly(ethylene oxide) (PEO, $M_w = 300,000$; Aldrich) solution (5 wt.% in ethanol) and Glutinous rice starch (GRS; Newgrade, packed and distributed by Thai Wah Food Products Public Company Limited) solution (5 wt.% in water) in volume ratios of 10:2:1, 10:1.5:1.5, 10:1:2, and 10:0:3, consecutively. The viscosity of GRS solution was measured by a Brookfield viscometer (LVT 71420, Brookfield Engineering Laboratories, Inc.

Stoughtonma, 02072, USA). After stirring at room temperature for 1 h, the mixture was loaded into a plastic syringe, which was connected to a metallic needle and linked to a syringe pump (NE-1000, New Era Pump Systems, Inc. Wantagh, NY) to control the feeding rate of the solution. The positive terminal of high voltage power supply (ES30P-5W, Gamma High Voltage Research Inc., Ormond Beach, FL) was connected to the needle tip of the syringe, while the collector covered with aluminum foil worked as a counter electrode. The distance between the needle tip of the syringe and collector was fixed at 15 cm, and the feeding rate of the solution was 0.5 ml/h. When the voltage applied between two electrodes reached 10 kV, non-woven mat of PZ/PEO/GRS composite fibers accumulated on the surface of the aluminum foil. The reaction of the as-spun composite nanofibers, which took place during heat treatment, was investigated by differential thermal analysis (DTA; Shimadzu) and thermogravimetry analysis (TGA; Shimadzu), using a heating rate of 10 °C/min in air that ranged from room temperature to 1,300 °C. X-ray diffraction (XRD; Bruker-D8 Advance) using CuK α radiation was used to determine the phases formed and optimum firing temperatures for formation of the desired phase. The room-temperature FT-IR spectrum range of 4,000–370 cm⁻¹ was recorded by a Perkin Elmer Spectrum GX FT-IR/FT-Raman spectrometer, with 8 scans and a resolution of 4 cm⁻¹ using KBr pellets. Finally, a scanning electron microscope (SEM, JEOL JSM5910LV) was used to observe the microstructures of the PZ fibers.

3. RESULTS AND DISCUSSION

The morphology of the as-spun and calcined PZ/PEO/GRS composite fibers was revealed by scanning electron microscopy (SEM). Figure 1 shows SEM photographs of the as-spun PZ/PEO/GRS volume ratio of 10:2:1 compared to the as-spun PZ/PEO volume ratio of 10:2, with a PZ concentration of 1.0 M. Comparison between Figure 1(a) and (b) shows that the formation of beads decreases when adding GRS into the solution. The as-spun PZ/PEO/GRS composite fibers were relatively uniform, with a smooth surface and average diameter of 395 ± 59 nm. Therefore, it can be said that the addition of GRS improves the appearance of the fiber, but the real controlling factor is the

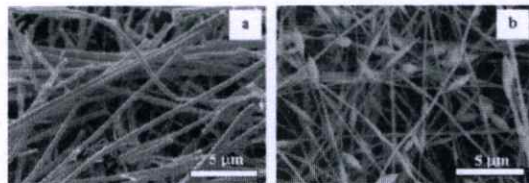


Fig. 1. SEM photographs of the as-spun PZ/PEO/GRS volume ratios of 10:2:1 (a) compared with the as-spun PZ/PEO volume ratios of 10:2 (b), with a PZ concentration of 1.0 M.

viscosity of the polymer solution. Viscosity of the polymer solution was measured at the same weight ratio by a Brookfield viscometer, which found that viscosity of GRS solution (575 centipoise) is greater than that of PEO solution (175 centipoise).

The higher viscosity of GRS solution resulted from chain entanglement, which causes a significant impact on the electrospinning process.¹⁰ GRS is a naturally high molecular weight polysaccharide composed of glucose units. It contains two types of glucose polymers, i.e., amylose and amylopectin. Amylose is a linear polymer containing up to 6,000 glucose units. Amylopectin has a highly branched structure consisting of short linear chains, with a degree of polymerization ranging from 10 to 60 glucose units.⁹ Therefore, adding GRS into the solution can enhance the chain entanglement of the molecular chain, which makes the viscosity increase. Figure 2 shows SEM photographs of the as-spun PZ/PEO/GRS composite, with a PZ concentration of 1.0 M, using the PZ/PEO/GRS volume ratios of 10:2:1, 10:1.5:1.5, 10:1:2 and 10:0:3, consecutively. Figures 2(a) and (b) illustrate that the fibers present a detailed non-woven electrospun mat. When the amount of GRS increased and that of PEO decreased, the fiber diameter was reduced and formation of beads observed.

Figures 2(c) and (d) indicate that continuous fibers could not form, as the jet broke up into droplets. This may be due to the compatibility of GRS and precursor solution, which is still not completely compatible. Thus, optimum conditions determined from the solution had a PZ/PEO/GRS volume ratio of 10:2:1.

Thermal analysis was carried out to investigate the decomposition process of the fiber. The results of TG and DTA analyses of the as-spun PZ/PEO/GRS composite fibers are shown in Figure 3. The endothermic peak in the DTA curve, and weight loss (~3%) in the TGA curve, were observed below 200 °C, which indicated a loss of moisture.¹¹ The endothermic peak and a weight loss (~20%) in the range of 200 to 350 °C occurred through

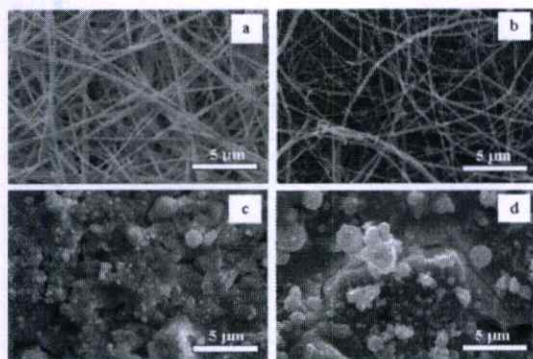


Fig. 2. SEM micrographs of the as-spun PZ/PEO/GRS nanofibers with a PZ concentration of 1.0 M at the PZ/PEO/GRS volume ratios of (a) 10:2:1, (b) 10:1.5:1.5, (c) 10:1:2 and (d) 10:0:3, consecutively.

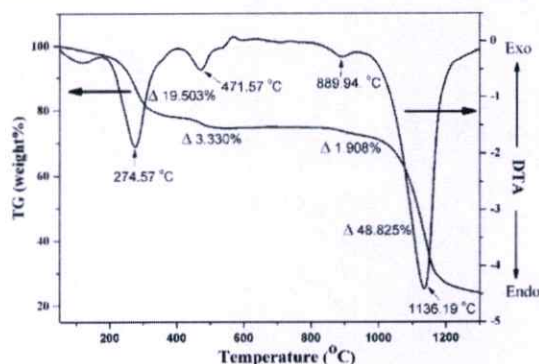


Fig. 3. TG-DTA curves of thermal decomposition of the as-spun PZ/PEO/GRS composite nanofiber, with a PZ concentration of 1.0 M at the PZ/PEO volume ratio of 10:2:1.

a loss of trapped solvent and GRS in the as-spun fibers, whereas, an endothermic peak and a weight loss (~3%) in the range of 400 to 550 °C were due to the degradation of PEO. According to their thermal properties, GRS and PEO decomposed at a temperature of about 300 °C and 450 °C, respectively, which supported the loss of GRS and PEO, consecutively. The TG and DTA curve indicated no change in the weight loss range from 550 to 850 °C, which possibly corresponded to formation of the perovskite phase. Based on the TG-DTA results, the mixture was calcined at various temperatures ranging from 550 °C to 850 °C, with dwell times of 4 h, and the heating/cooling rates ranged around 5 °C/min in a closed alumina crucible, in order to investigate the perovskite phase formation. The crystalline phases of PZ fibers were revealed at various calcined temperatures by X-ray diffraction spectra. Figure 4 shows the XRD patterns of PZ/PEO/GRS

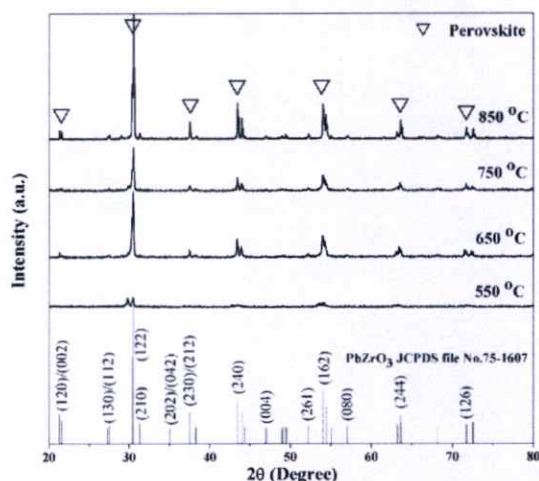


Fig. 4. XRD patterns of electrospun PZ/PEO/GRS composite nanofibers, with a PZ concentration of 1.0 M at the PZ/PEO volume ratio of 10:2:1, calcined in air for 4 h at different temperatures.

composite fibers calcined at different temperatures. As-spun PZ/PEO/GRS composite fibers calcined at 550 °C for 4 h revealed that crystallization of the perovskite phase began to form. However, the main peak intensity of the PZ phase was weak, which implied that the fiber was not fully crystallized. When the calcination temperature was 650 °C, the crystalline PZ fibers were obtained successfully with a well-developed perovskite structure. According to JCPDS card no. 75-1607, the diffraction peaks can be indexed as an orthorhombic perovskite structure of lead zirconate. No other peaks could be observed in the XRD patterns, which indicated that the sample is free from lead oxide or any other crystalline materials. However, when increasing the calcination temperature to 750 °C, intensities of the main peaks decreased. This behavior is similar to the XRD result of TiO₂ nanofibers¹² and PZT fibers¹³ that show lower diffraction intensity when increasing calcination temperature.

This may be due to the enhancement of driving energy that caused the orientation of atoms to cluster, whereas, after calcination at 850 °C, the peak intensity increased again, as a result of grain growth by temperature.¹⁴ Formation of the calcined PZ nanofibers was confirmed further by the FT-IR spectra, as shown in Figure 5. The spectrum of the as-spun PZ/PEO/GRS composite fibers shows multiple absorption bands in the region of 1,000 to 4,000 cm⁻¹, which corresponds to the stretching and bending vibrations of polymers, organic solvent and moisture. Peaks of around 1,450 cm⁻¹ correspond to the aliphatic CH group vibrations of the CH₂ mode.¹⁵ The wave number at ~1,600 cm⁻¹ and broad peak at around 3,400 cm⁻¹ both correspond to the O-H stretching vibration.¹⁶ After calcination at 550 °C for 4 h, it was found that these peaks almost disappear, indicating that most of the polymers and

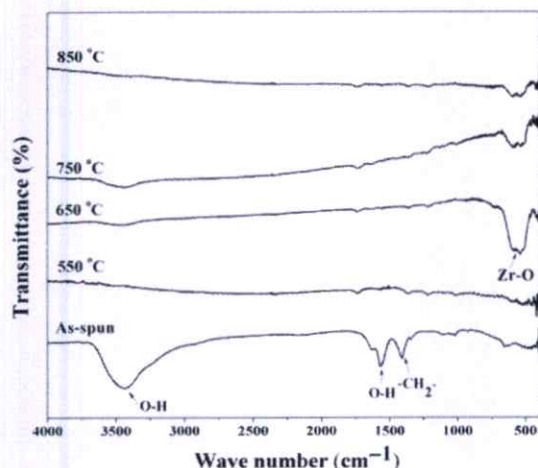


Fig. 5. FTIR spectra of electrospun PZ/PEO/GRS composite nanofiber, with a PZ concentration of 1.0 M at the PZ/PEO volume ratio of 10:2:1, calcined in air for 4 h at different temperatures.

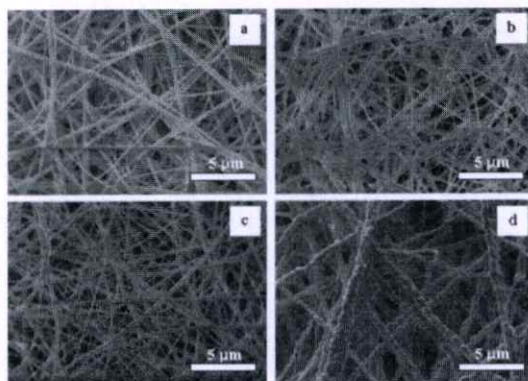


Fig. 6. SEM micrograph of (a) the as-spun and PZ fibers calcined in air for 4 h at (b) 650, (c) 750 and (d) 850 °C.

other organics have been removed. This study can guarantee that its sample was free from GRS and PEO polymer. As the calcination temperature increases to 650 °C, 750 °C and 850 °C, the appearance of an absorption peak at ~548 cm⁻¹ is attributed to Zr–O stretching vibration,¹⁷ which corresponds to the polycrystalline fiber obtained. Figure 6 shows SEM images of the as-spun and PZ fibers, with a volume ratio of 10:2:1 at PZ concentrations of 1.0 M, calcined at 650, 750 and 850 °C, consecutively. All the calcined samples present non-woven fabrics and form a structure of packed particles or crystallites.

Those calcined at 650 °C [Fig. 6(b)] represent a uniform and smooth surface, with a diameter of 229 ± 46 nm. From this figure, grain boundaries were not observed at all, which suggests that there is a highly ordered arrangement in the fiber, as shown in Figure 7(a). The result was consistent with the XRD pattern that showed a high intensity of XRD peak. Furthermore, this result is different from those in other researches that had a soldering-like attachment of nanofibers at their junction after annealing.¹⁸ After calcination at 750 °C [Fig. 6(c)] the fiber remained as continuous structures with a diameter of 252 ± 63 nm. It can be seen that following calcinations, the diameter of the fibers appears smaller on average than that of the as-spun fibers (395 ± 59 nm) [Fig. 6(a)]. The reduction in size of the nanofibers should be attributed to their loss of

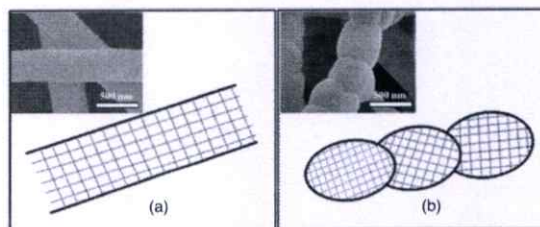


Fig. 7. Schematic diagram of (a) PZ fibers calcinations at 650 °C and (b) PZ fibers calcinations at 750 °C.

PEO and GRS and the crystallization of PbZrO₃. The fiber represents a necklace-like structure, which may be due to the enhancement of driving energy by increasing temperature, resulting from the macroscopic migration of the grain boundary, in the direction that reduces the energy of the system.¹⁹

This is shown in Figure 7(b) that represents grain boundaries arranged by grain to grain unit cell clusters, which is consistent with XRD results showing a peak with lower intensity than the fabrication of TiO₂ nanofibers of Shao et al.¹² Their results exhibited a necklace-like structure that represented lower diffraction intensity after calcinations at a higher temperature. However, after calcinations at 850 °C [Fig. 6(d)], the nature of nanofibers was changed dramatically, and a necklace-like structure of packed particles or crystallites was prominent. Furthermore, the average fiber diameter increased with increased calcination temperature, for example, the average fiber diameter at 650 °C and 850 °C is 229 ± 46 nm and 453 ± 103 nm, respectively, after calcination. The enhancement of this fiber diameter is due to the grain growth by temperature.^{12, 20} As a result, the peak intensity of the XRD pattern increased.

4. CONCLUSION

In summary, this study prepared PZ/PEO/GRS fibers successfully by the electrospinning method. The as-spun PZ/PEO/GRS composite fibers were relatively uniform with a smooth surface. Beads or agglomerated nanofibers could not be observed. The PZ nanofibers, with a well-developed perovskite structure, were obtained successfully at the calcination temperature of 650 °C for 4 h, while a necklace-like structure of packed particles or crystallites was obtained after calcination at 850 °C. Furthermore, the cost of the process can be reduced by successfully putting glutinous rice starch into the solution.

Acknowledgment: This research has supported by The Royal Golden Jubilee Ph.D. Program (RGJ) under The Thailand Research Fund (TRF), The KMITL research fund and the National Research Council of Thailand (NRCT).

References and Notes

1. D. Li and Y. Xia, *Nano Lett.* 3, 555 (2003).
2. L. Cakar, M. Kosec, and B. Malic, *J. Sol-Gel Sci. Technol.* 19, 603 (2000).
3. C. W. Zou and W. Gao, *TEEM* 11, 1 (2010).
4. X. G. Tang, A. L. Ding, and W. G. Luo, *Appl. Surf. Sci.* 174, 148 (2001).
5. N. Vittayakorn, P. Charoonsuk, P. Kasiansin, S. Wirunchit, and B. Boonchom, *J. Appl. Phys.* 106, 064104 (2009).
6. F. Jona, G. Shirane, F. Mazzi, and R. Pepinsky, *Phys. Rev.* 105, 849 (1957).
7. W. Sigmund, J. Yuh, H. Park, V. Maneerata, G. Pyrgiotakis, A. Daga, J. Taylor, and J. C. Nino, *J. Am. Ceram. Soc.* 89, 395 (2006).
8. J. Yuh, L. Perez, W. M. Sigmund, and J. C. Nino, *J. Sol-Gel Sci. Technol.* 42, 323 (2007).
9. J. Peerapattana, P. Phuvarit, V. Srijesdaruk, D. Preechagoon, and A. Tattawasart, *Carbohydrate Polym.* 80, 453 (2010).
10. J. H. He, Y. Q. Wan, and J. Y. Yu, *Fibers and Polymers* 9, 140 (2008).
11. T. Wang and S. Kumar, *J. Appl. Polym. Sci.* 102, 1023 (2006).
12. J. Zhao, C. Jia, H. Duan, H. Li, and E. Xie, *J. Alloy. Compd.* 461, 447 (2008).
13. R. Meyer Jr, T. Shroud, and S. Yoshikawa, *J. Am. Ceram. Soc.* 81, 861 (1998).
14. R. Thomas, S. Mochizuki, T. Mihara, and T. Ishida, *Mater. Lett.* 57, 2007 (2003).
15. S. Maensiri, W. Nuansing, J. Klinkaewnarong, P. Laokul, and J. Khemprasit, *J. Colloid Interface Sci.* 297, 578 (2006).
16. Z. Zhang, X. Li, C. Wang, L. Wei, Y. Liu, and C. Shao, *J. Phys. Chem.* 113, 19397(2009).
17. M. Mai, C. Lin, Z. Xiong, H. Xue, and L. Chen, *J. Phys., Conference Series* 152, 012077 (2009).
18. N. Dharmaraj, C. H. Kim, and H. Y. Kim, *Mater. Lett.* 59, 3085 (2005).
19. C. V. Thompson, *Annu. Rev. Mater. Sci.* 20, 245 (1990).
20. J. K. L. Lai, C. H. Shek, and G. M. Lin, *Scripta Mater.* 49, 441 (2003).

Received: 27 October 2011. Accepted: 12 April 2012.

Effect of Chemical Treatment on Phase Transition of Lead Zirconate Nanofibers

CHANISA NAWANIL,^{1,2} APINAI RERKRATN,³
PANPAILIN SEEHARAJ,⁴ AND NARATIP VITTAYAKORN^{1,2,4,*}

¹College of KMITL Nanotechnology, King Mongkut's Institute of Technology Ladkrabang, Bangkok 10520, Thailand

²ThEP Center, CHE, 328 Si Ayutthaya Rd., Bangkok 10400, Thailand

³Department of Instrumentation and Control Engineering, Faculty of Engineering, King Mongkut's Institute of Technology Ladkrabang, Bangkok 10520, Thailand

⁴Advanced Materials Research Unit, Department of Chemistry, Faculty of Science, King Mongkut's Institute of Technology Ladkrabang, Bangkok 10520, Thailand

Lead zirconate (PZ) nanofibers were treated by the solvothermal method in the presence of dimethyl formamide (DMF) solution in order to investigate the effect of chemical treatment on phase transition of PZ nanofibers. The influences of temperature and reaction time are described. The crystal structure, phase transition and morphology of the powders were analyzed by X-ray diffraction (XRD), fourier-transform infrared spectroscopy (FT-IR), differential scanning calorimetry (DSC), and scanning electron microscopy (SEM). The results of DSC confirmed that chemical treatment with DMF could effect the AFE-PE phase transition of PZ nanofibers efficiently. Significant changes of fiber size and morphology after chemical treatment are shown by SEM images.

Keywords Lead zirconate (PZ); dimethyl formamide (DMF); solvothermal method

1. Introduction

Lead zirconate (PbZrO_3 ; PZ) material plays an ever-increasing role in electrical and electronic applications including micro-actuators, microelectromechanical systems and high energy storage capacitors [1]. It has a perovskite structure and shows an antiferroelectric nature. At room temperature, bulk lead zirconate has an orthorhombic structure that changes to a cubic one at 230°C [2]. However, antiferroelectric-to-ferroelectric switching properties have not been investigated in detail for highly oriented lead zirconate nanofibers. Nanosize materials with peculiar properties are not expected in a bulk phase and have led already to a breakthrough in various fields of science and technology, owing to their peculiar physical and electrical behavior [3, 4]. Our previous study investigated the phase transformation of lead zirconate nanofibers, and the lack of a sharply defined phase transition in nanosized samples was observed by using differential scanning calorimetry. This result is consistent with those reported by Lu et al. [5], who did not observe phase transition or endothermic

Received December 11, 2012; in final form March 5, 2013.

*Corresponding author. E-mail: naratipcmu@yahoo.com

peak if hydrothermally synthesized barium titanate particles were nanosized. Smith et al. [6] reported the absence of an enthalpy peak around the Curie point of nanosized samples. Regarding bulk barium titanate, the DSC trace showed a peak near 130°C, which was indicative of phase transition. However, similar features were not observed in the DSC of nanoparticle samples. It is true that the DSC technique is not very sensitive to the presence of phase transition in nanosized samples.

The literature has documented that the developed solvothermal technique, which involves the use of organic solvent instead of water, may provide an alternative to producing low defect materials, and give display of a narrower transition region when compared with normal samples. Badheka et al. [7] examined the phase transformation in barium titanate nanoparticles from metastable cubic to ferroelectric tetragonal phase using solvothermal treatment. The DSC result clearly presented an endothermic peak at 130°C after solvothermal treatment for 24 h at 170°C, using dimethyl formamide as an effective solvent. The solvothermal method is used to synthesize inorganic materials in organic media at elevated temperatures (200°C to 300°C) under autogenous pressure of the organics. The term "solvothermal" means reactions in liquid or supercritical media at temperatures higher than the boiling point of the medium [8]. Dimethyl formamide is a dipolar aprotic solvent with a boiling point at 153°C. It is largely basic and has high dielectric constants. Due to the high basicity of these solvents, cations are highly solvated, but anions are left unsolvated. Therefore, anions in these solvents have high reactivity [8]. Very few papers have dealt with the effect of these solvents in inorganic synthesis. Therefore, this study examined the phase transformation in lead zirconate nanofibers from the paraelectric to antiferroelectric phase by using solvothermal treatment. The optimum condition of chemical treatment for the phase transition in lead zirconate fibers was determined at different temperatures and times using dimethyl formamide as an effective solvent. The different temperatures and times were chosen according to the boiling point of the solvent. The influence of solvothermal treatment with dimethyl formamide solution on the fibers obtained is described and discussed.

2. Experimental Procedure

Lead zirconate nanofibers were synthesized by an electrospinning method, which utilized a solution that contained poly (ethylene oxide) (PEO, $M_w \sim 300,000$; Aldrich) and sol-gel precursor solution of lead zirconate [9]. After obtaining the lead zirconate fiber mats, chemical treatment was performed by mixing lead zirconate fiber (1 g) with 20 ml of dimethyl formamide solution. This mixture was then transferred to a Teflon reactor (autoclave), which was sealed and placed in an oven (Whirlpool XT-25ES/S, 900 W, 2.45 GHz). The reaction was performed under autogenous pressure developed by heating for 6 and 24 hours at two difference temperatures of 170°C and 200°C. After cooling to room temperature, the resulting powder was recovered by filtration and washed several times with a mixture of water/alcohol (50:50 by volume). Finally, the sample was dried for 24 h at 80°C. X-ray diffraction (XRD; Bruker-D8 Advance) using CuK_α radiation was used to determine the phases formed. The fourier-transform infrared spectroscopy (FT-IR) spectrum (range 4,000–370 cm^{-1}) was recorded at room temperature by a Perkin Elmer Spectrum GX FT-IR/FT-Raman spectrometer, with 8 scans and a resolution of 4 cm^{-1} using KBr pellets. A scanning electron microscope (SEM, JEOL JSM5910LV) was used to observe the microstructures of the PZ nanofibers before and after chemical treatment. Differential scanning calorimetry (DSC) was performed on a Perkin-Elmer Pyris DSC at a heating rate of 10°C/min under a nitrogen gas flow from 50°C to 400°C in order to investigate phase transition.

3. Results and Discussion

The morphology of lead zirconate fibers was revealed by scanning electron microscopy. Figure 1 shows SEM micrographs of comparison between lead zirconate fibers treated with dimethyl formamide as solvent and untreated lead zirconate fibers. This Fig. reveals that morphological fiber change is provided by chemically treated fibers. The samples before chemical treatment present non-woven fabrics, with a structure of packed particles or crystallites. The fibers present continuous structures without grain boundaries (Fig. 1(a)). After chemical treatment for 6 and 24 h at both 170°C and 200°C, the lead zirconate fibers still had continuous structures. However, the nature of the nanofibers was changed dramatically. The surface of the nanofibers had become rough, as seen in Fig. 1(b–e), because when the solvent molecules or additives were adsorbed preferentially on (or had specific interaction with) a certain surface of the products, surface growth was prohibited

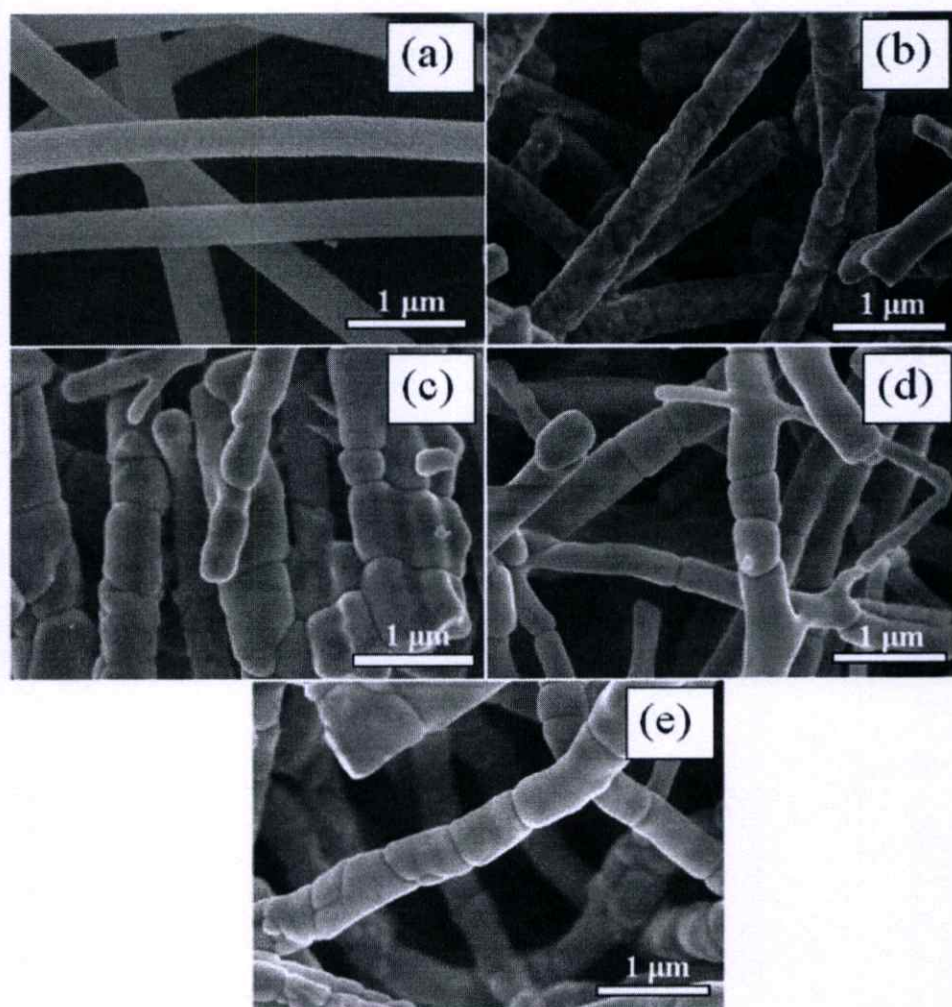


Figure 1. SEM micrographs of the PZ fibers (a) before and after chemical treatment for (b) 6 h at 170°C (c) 24 h at 170°C (d) 6 h at 200°C and (e) 24 h at 200°C, consecutively.

and, therefore, solvothermal reaction may form products with unique morphologies [8]. Fig. 1 revealed by heat treatment that grain boundaries were prominent, due to reduced internal stress. The average diameter of fibers before solvothermal treatment was 300 ± 64 nm and after solvothermal treatment at $170^\circ\text{C}/6$ h, $170^\circ\text{C}/24$ h, $200^\circ\text{C}/6$ h, $200^\circ\text{C}/24$ h were 274 ± 64 nm, 344 ± 99 nm, 369 ± 93 nm, 420 ± 81 nm, respectively. It was revealed that the diameter size of the fibers decreased slightly after the dimethyl formamide chemical treatment. This is consistent with the research of Badheka et al. [7], who reported that after chemical treatment, the particle size was reduced in order to alleviate the lattice strain. However, increasing the temperature and time caused the diameter to increase, due to grain growth.

Figure 2 shows comparison between X-ray diffraction patterns of lead zirconate nanofibers that were treated chemically with dimethyl formamide for 6 and 24 h at both 170°C and 200°C and those of untreated lead zirconate nanofibers. The JCPDS file no. 75-1607 shows that all patterns fit well with the peak positions of standard lead zirconate. All of the chemically treated lead zirconate nanofibers could be indexed readily as the orthorhombic phase. XRD patterns show that there is no change in the phase transition after chemical treatment by increasing the temperature above the boiling point of the solvent and giving more time. The above XRD results show that after chemical treatment for 24 h at

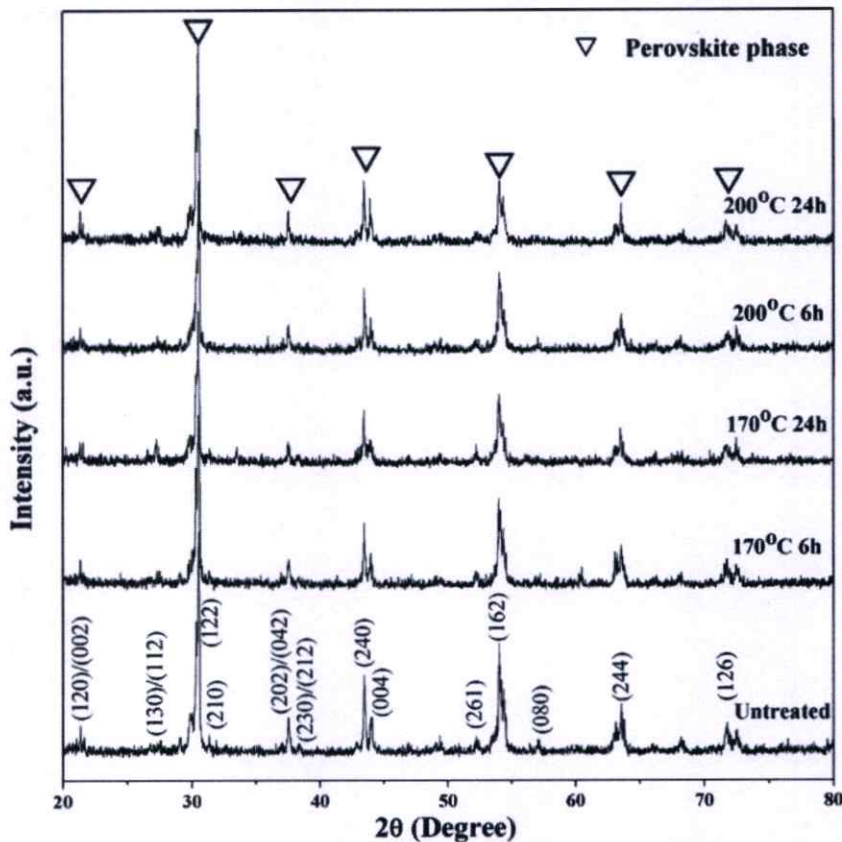


Figure 2. XRD patterns of the PZ particles compared with those of the PZ nanofibers before and after chemical treatment.

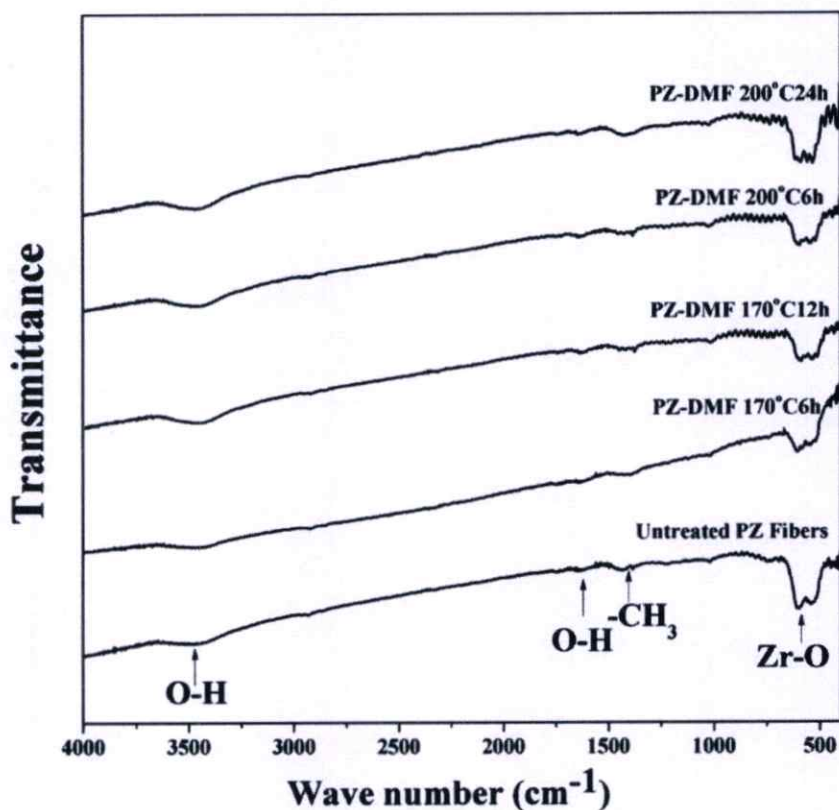


Figure 3. FT-IR spectra of the PZ particles compared with those of the PZ nanofibers before and after chemical treatment.

200°C, the lattice parameter with the refined cell parameters, $a = 5.7652 \text{ \AA}$, $b = 11.6855 \text{ \AA}$ and $c = 8.2760 \text{ \AA}$, are close to reported values [10].

Formation of the perovskite structure in the lead zirconate fibers before and after chemical treatment was supported further by FT-IR spectra, as shown in Figure 3. The spectrum shows an absorption peak at $\sim 548 \text{ cm}^{-1}$, which attributed to Zr-O stretching vibration [11]. This corresponds to the occurrence of polycrystalline lead zirconate fiber. It was found from the Fig. that the spectrum of lead zirconate fibers did not change after dimethyl formamide chemical treatment, which indicates that the crystallization of the lead zirconate fibers also remained, as suggested in the XRD results. In addition, the spectrum shows multiple absorption bands in the region 1,000 to 4,000 cm^{-1} , which corresponds to the stretching and bending vibrations of moisture and organic solvent. Of these vibrations, peaks of around 1,450 cm^{-1} correspond to the aliphatic CH group vibrations of the CH_2 mode [12]. The wave number at $\sim 1,600 \text{ cm}^{-1}$ and broad peak at around 3,400 cm^{-1} are assigned for O-H bending and O-H stretching vibration [13], respectively.

Figure 4 shows results from the solid state method of DSC for the lead zirconate particles, and compares with the electrospinning and solvothermal method of that for the lead zirconate nanofibers and lead zirconate nanofibers treated with dimethyl formamide, respectively. The DSC result of the lead zirconate particles shows two distinct endothermic peaks that are closer together at around 230°C. The lower temperature corresponds to the

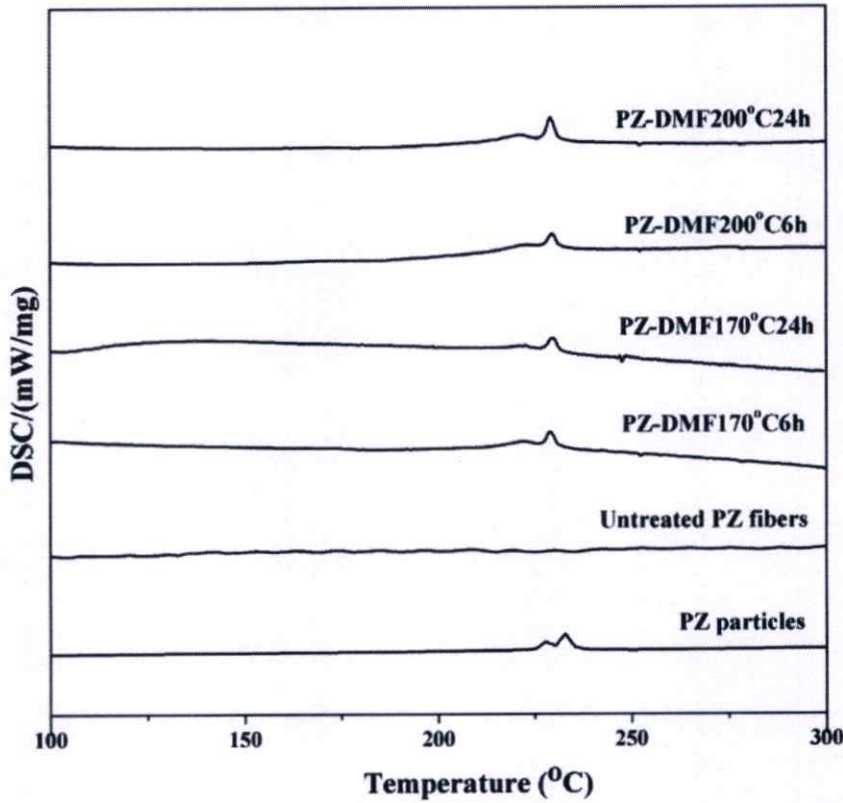


Figure 4. DSC results for the PZ particles compared with those for PZ nanofibers before and after chemical treatment.

transition temperature of the antiferroelectric (AFE) \rightarrow ferroelectric (FE) phase transition, while the higher temperature corresponds to the ferroelectric (FE) \rightarrow paraelectric (PE) phase transition. It was found from the Figure that when lead zirconate is fabricated in nanosize by the electrospinning method, there is no phase transition or endothermic peak at around 230°C. This result is very similar to those in other researches. Lu et al. [5] reported that if barium titanate particles are synthesized hydrothermally in nanosize, there is no phase transition or endothermic peak at around 130°C. This is because the nanocrystals are so small that structural defects in the particles prevent the completion of structural transition, leading to high strains within the crystals. Frey et al. [14] suggested that strains in the crystallites are related to defects in the lattice. Lin et al. [15] reported that coarse-grained ceramics have internal stress caused by phase transition, which can be relieved by formation of 90° domains. With grain size decreasing further, the single domain becomes favorable energetically. Consequently, in fine-grained ceramics, the contribution of stress should be taken into account, due to the absence of 90° domains [15], whereas, after chemical treatment with dimethyl formamide, the lead zirconate nanofibers clearly show an endothermic transition on heating at 230°C, as seen in Figure 4. This corresponds to the orthorhombic to cubic phase transition at the Currie point of lead zirconate. This may be due to the effect of grain boundaries, because the SEM micrograph of lead zirconate fibers treated with dimethyl formamide shows the structure with grain boundaries, as mentioned

earlier. Areas around impure ions within grains have a strong field of elastic strain, while those around impure ions at grain boundaries have an open structure and a low strain field. Therefore, impure ions will diffuse from grains into grain boundaries to form segregation in order to reduce strain energy and eliminate or release stress [16]. According to the DSC curve, increased intensity of endothermic peak with increasing temperature and time in the solvothermal process is seen clearly. Additionally, enthalpy (ΔH) values calculated from the DSC curve also increased. Increased temperature leads to greater thermal vibration of the atoms in a material, and on to increase the average distance separating adjacent atoms [17]. With increasing temperature, stress is relieved gradually in order that free energy of the antiferroelectric phase could decrease and allow enthalpy values to increase. The enthalpy (ΔH) values of lead zirconate fibers after chemical treatment at 170°C/6 h, 170°C/24 h, 200°C/6 h, 200°C/24 h were 1.9469 J/g, 2.0259 J/g, 2.5334 J/g and 2.6879 J/g, respectively.

4. Conclusions

The thermal properties of lead zirconate fibers, using dimethyl formamide solvent before and after solvothermal treatment were investigated by the DSC method. The results suggested that the antiferroelectric-paraelectric phase transition was found after chemical treatment at 170°C for 6 h. Furthermore, the enthalpy values for the orthorhombic-cubic transition increased with increasing temperature and time, due to reduction of internal stresses. Microstructures were observed by SEM, which revealed grain boundaries that were prominent through heat treatment. The diameter size of the fibers decreased slightly after dimethyl formamide chemical treatment and increased with increasing temperature and time.

Acknowledgments

This research was supported by the National Nanotechnology Center (NANOTEC) NSTDA, Ministry of Science and Technology, Thailand, through its "Center of Excellence Network" program, KMITL Research Fund and Thailand Research Fund (TRF) for supporting the grant through the Royal Golden Jubilee Ph.D. Program (Grant No. PHD/0090/2554).

References

1. K. Uchino, *Ferroelectric Devices*. (Dekker, New York, 2000).
2. E. E. Oren, E. Taspinar, and A. C. Tas, Preparation of lead zirconate by homogeneous precipitation and calcination. *J Am Ceram Soc.* **80** (10), 2714–16 (1997).
3. L. R. Xu, L. Li, C. M. Lukehart, and H. Kuai, Mechanical characterization of nanofiber-reinforced composite adhesives. *J Nanosci Nanotechnol.* **7**, 1–3 (2007).
4. A. Safari, Development of piezoelectric composites for transducers. *J Phys III Fiance.* **4**, 1129–1149 (1994).
5. S. W. Lu, B. I. Lee, Z. L. Wang, and W. D. Samuels, Hydrothermal synthesis and structural characterization of BaTiO₃ nanocrystals. *J Crystal Growth.* **219**, 269–276 (2000).
6. M. B. Smith, K. Page, T. Siegrist, et al., Crystal structure and the paraelectric-to-ferroelectric phase transition of nanoscale BaTiO₃. *J Am Chem Soc.* **130**, 6955–6963 (2008).
7. P. Badheka, L. Qi, and B. I. Lee, Phase transition in barium titanate nanocrystals by chemical treatment. *J Eur Ceram Soc.* **26**, 1393–1400 (2006).
8. M. Inoue, *Chemical Processing of Ceramics: Solvothermal Synthesis: Second Edition*. (2005), pp. 22–56.

9. C. Nawani, B. Boonchom, J. Prachayawarakorn, W. Vittayakorn, and N. Vittayakorn, Synthesis and phase evolution of electrospun antiferroelectric lead zirconate (PbZrO_3) nanofibers. *Mater Sci Eng B*. **177**, 1009–1016 (2012).
10. N. Vittayakorn, P. Charoonsuk, P. Kasiansin, S. Wirunchit, and B. Boonchom, Dielectric properties and phase transition behaviors in $(1-x)\text{PbZrO}_3-x\text{Pb}(\text{Mg}_{1/2}\text{W}_{1/2})\text{O}_3$ ceramics. *J App Phys*. **106**, 064104 (2009).
11. M. Mai, C. Lin, Z. Xiong, H. Xue, and L. Chen, Preparation and characterization of lead zirconate titanate ceramic fibers with alkoxide-based Sol–gel route. *J Phys; conference series*. **152**, 012077 (2009).
12. Z. Zhang, X. Li, C. Wang, L. Wei, Y. Liu, and C. Shao, ZnO hollow nanofibers: Fabrication from facile single capillary electrospinning and applications in gas sensors. *J Phys Chem*. **113**, 19397 (2009).
13. S. Maensiri, W. Nuansing, J. Klinkaewnarong, P. Laokul, and J. Khemprasit, Nanofibers of Barium Strontium Titanate (BST) by sol–gel processing and electrospinning. *J Colloid Interface Sci*. **297**, 578 (2009).
14. M. H. Frey, and D. A. Payne, Grain-size effect on structure and phase transformations for barium titanate. *Phys Rev B*. **54** (5), 3158–3167 (1996).
15. S. Lin, T. Lu, C. Jin, and X. Wang, Size effect on the dielectric properties of BaTiO_3 nanoceramics in a modified Ginsburg-Landau-Devonshire Thermodynamic Theory. *Phys Rev B*. **74**, 134115 (2006).
16. Q. Yin, B. Zhu, and H. Zeng, *Microstructure, Property and Processing of Functional Ceramics*. (Metallurgical Industry Press, Beijing and Springer-Verlag GmbH Berlin Heidelberg, 2009), pp. 1–168.
17. C. J. Xiao, Z. X. Li, and X. R. Deng, Grain-size effects on thermal properties of BaTiO_3 ceramics. *Bull Mater Sci*. **34** (4), 963–966 (2011).

Preparation and Dielectric Properties of 3-3 Lead Zirconate/Polyvinylidene Fluoride Nanocomposite

CHANISA NAWANIL,^{1,2} WANWILAI VITTAYAKORN,^{1,2}
JUTARAT PRACHAYAWARAKORN,^{2,3}
AND NARATIP VITTAYAKORN^{1,2,3,*}

¹Electroceramic Research Laboratory, College of Nanotechnology, King Mongkut's Institute of Technology Ladkrabang, Bangkok 10520, Thailand

²Advanced Material Research Unit, Faculty of Science, King Mongkut's Institute of Technology Ladkrabang, Bangkok, 10520, Thailand

³Department of Chemistry, Faculty of Science, King Mongkut's Institute of Technology Ladkrabang, Bangkok 10520, Thailand

Communicated by Professor Amar S. Bhalla
(Received in final form February 10, 2013)

Composites made of electroactive ceramics and a ferroelectric polymer are very attractive for applications since they exhibit good piezoelectric and pyroelectric properties, low densities and their properties can be tailored to various requirements. Here, we reported the preparation and dielectric properties of 3-3 PZ/PVDF nanocomposites by infusion of polyvinylidene fluoride (PVDF) into the PZ nanofiber mat followed by heating of the composite at 80°C. The 3-3 PZ/PVDF composites were characterized by X-ray diffraction, FT-IR, SEM and LCR meter. The dielectric constant of the PZ/PVDF nanocomposite are relatively stable in the range of 21.98–18.21 within the measurement frequencies from 100 Hz to 2 MHz. This value is higher than the dielectric constant of the polyvinylidene fluoride. Moreover, the dielectric loss of the composite is below 0.09 at low frequencies.

Keywords PZ; PVDF; composite; dielectric

1. Introduction

Piezoelectric ceramic-polymer composites were intensively studied within the last decades because of their considerable potential for applications such as pyroelectric sensors, ultrasonic transducers, and hydrophones [1]. Piezoelectric ceramics have high piezoelectric strain coefficient and high electromechanical coupling coefficient [2]. However, the relatively high density, high acoustic impedance and mechanical stiffness limit their applications. On the other hand, piezoelectric polymers have acoustic impedance well matched to water and biological issues, but their piezoelectric strain coefficient and electromechanical coupling coefficient, are lower than those of piezoelectric ceramics [3]. Thus, in many applications, one might optimize conflicting requirements by combining the most useful properties of two or more phases that do not ordinarily appear together in nature. Therefore,

*Corresponding author. E-mail: naratipcmu@yahoo.com

different kinds of composites such as porous ceramics and ceramic-polymer composites are typically developed.

Antiferroelectric materials have attracted much research interest due to their potential applications in microactuators and energy conversion devices [4]. Lead zirconate, PbZrO_3 (PZ), is a well known antiferroelectric materials. This material can be processed into various forms such as bulk ceramics, thin films, and fibers, depending on the application area. The hysteresis characteristics of Antiferroelectric PbZrO_3 regions are well suited for either power-storage or actuator applications. Moreover, the extremely large charge which is released from the FE state to the AFE state may be useful as alternate capacitor materials in DRAMs [5]. In recent years, researchers have focused on synthesizing nanosized PZ fibers to improve desired properties. Fibrous PZ have potential for utilization in high performance electric-mechanical application such as actuators, sensors, high energy storage capacitors and microelectromechanical systems (MEMS). Due to the high surface-to-volume ratio and their novel properties that are significantly different from their bulk, such as mechanical [6] and electrical property [7]. Nanoscale PZ fibers incorporated into a piezoelectric polymer are expected to obtain smart piezocomposite structures and to find wide applications, particularly in nanoelectronics, photonics, sensors, and actuators. Both kinds of materials show different piezoelectric properties, such as resonance frequencies and electromechanical coupling coefficients because of differences in their microscopic structures, their elastic properties and their typical transducer geometries [8]. Due to such special qualities, piezoelectric polymers have been increasingly used in a rapidly expanding range of applications such as electromechanical transducers, position sensors and vibration control actuators [9]. Often piezo- and pyroelectric polymers such as nylon [10], polyvinyl chloride (PVC) [3] and polyvinylidene fluoride (PVDF) [11] were used as matrix. Based on our knowledge, there has been no previous report on the fabrication of PZ fibers/PVDF composite.

Polyvinylidene fluoride (PVDF) is a piezoelectric polymer that has been used in many applications including microphones, transducers, sensors and actuators, due to its high piezo-, pyro- and ferroelectric properties [12]. The PVDF has low permittivity, low thermal conductivity and is flexible and relatively low in cost [13]. In addition, it is exceptionally sensitive, for example, sensors based on PVDF film have been applied even in erosive media to detect pressure, in biological environments to aid minimally invasive surgery, test and characterize fabrics, and monitor human health [12].

Therefore this study fabricated 3-3 PZ/PVDF nanocomposite using PZ fibers embedded in PVDF matrix. The crystal structure and morphology were investigated. Moreover, the dielectric properties of the resultant 3-3 PZ/PVDF nanocomposite was characterized.

2. Experimental Procedure

PZ nanofibers were synthesized by an electrospinning method utilizing a solution which contained poly(ethylene oxide) (PEO, $M_w \sim 300,000$; Aldrich), and sol-gel precursor solution of PZ [14]. After obtaining the PZ fiber mats, PZ/PVDF nanocomposite samples were prepared. Firstly, Polyvinylidene fluoride (PVDF; $M_w \sim 534,000$; Aldrich) powder was dissolved in DMF solvent to obtain the polymer matrix of the composite. This solution was poured on to the calcined PZ fiber mat and this sample was kept under vacuum for 10 min to eliminate trapped air. Then, the sample was dried 24 h at 80°C . X-ray diffraction (XRD; Bruker-D8 Advance) using $\text{CuK}\alpha$ radiation was used to determine the phases formed. The room-temperature FTIR spectrum ranging $4,000\text{--}370\text{ cm}^{-1}$ was recorded by a Perkin Elmer Spectrum GX FTIR/FT-Raman spectrometer, with 8 scans and a resolution of

4 cm^{-1} using KBr pellets. A scanning electron microscope (SEM, JEOL JSM5910LV) was used to observe the microstructures of the PZ/PVDF nanocomposite. Finally, dielectric properties of the PZ/PVDF nanocomposites were measured from 100 Hz to 2 MHz using a precision LCR meter HP-4284A (Hewlett-Packard, Palo Alto, CA). The samples were prepared into thin, rectangular, parallel plates, and the dielectric measurements were taken by placing the samples between two parallel metal plates of the sample holder.

3. Results and Discussion

PZ/PVDF nanocomposite achieved from embedded PZ nanofibers in PVDF polymer has a smooth surface, with no buckling or folding over, thus indicating that the solvent evaporated uniformly. The morphology of the PZ/PVDF composite was revealed by scanning electron microscopy (SEM). Figure 1 shows SEM photographs of the composite. From Figure 1(a), it is shown that the polymer matrix phase was infiltrated thoroughly into the fiber network, and an intimate mixture of two phases was obtained. Figure 1(b) shows the backscattering electrons SEM image of the composite section, in which the PZ phase is visible with a bright-white contrast, and the PVDF phase is identifiable as the darker-gray region. The microgeometry of the inclusion and the interface between the filler and the matrix could be important. The mixing rules of a given property are controlled by the connectivity of the individual phases [13]. From the Figure, it reveals that the composite has 3-3 connectivity by using Newnham's convention on connectivity of piezocomposites, in which the active PZ and polymer matrix phases are both connected in three dimensions in the micrometer scale [7].

The crystalline phases of 3-3 PZ/PVDF composite were revealed by X-ray diffraction spectra. Figure 2 shows the XRD patterns of the 3-3 PZ/PVDF composite compared with PZ fibers and PVDF powder. From the Figure, it is revealed that crystalline PZ/PVDF composite were obtained. According to JCPDS card no.75-1607, the diffraction peaks can be indexed as an orthorhombic perovskite structure of lead zirconate. Moreover, peaks of polyvinylidene fluoride (PVDF) could be observed in the XRD patterns of the composite, because PVDF is a semi-crystalline polymer with typical crystallinity of 50%. The spectra of the PVDF polymer are also seen to have well defined peaks at $2\theta = 20.3^\circ$, referent to the sum of the diffractions in plane (110) and (200) characteristic of the β phase. Peak at $2\theta = 26.64^\circ$ referent to the diffractions in planes (021), which characteristic of α phase [15].

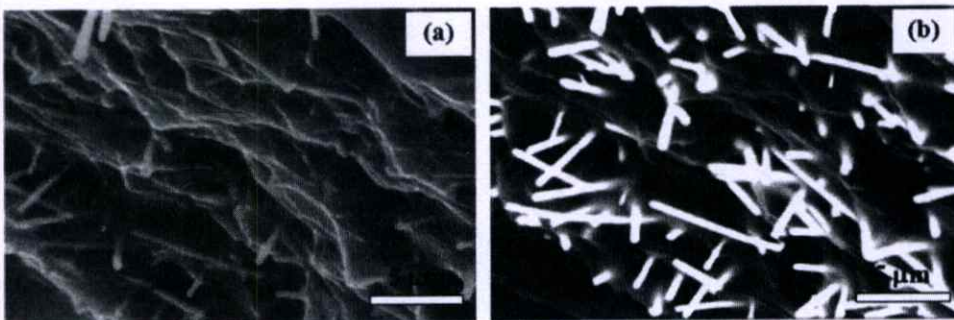


Figure 1. SEM micrograph of the composite structure of 3-3 PZ/PVDF nanocomposite.

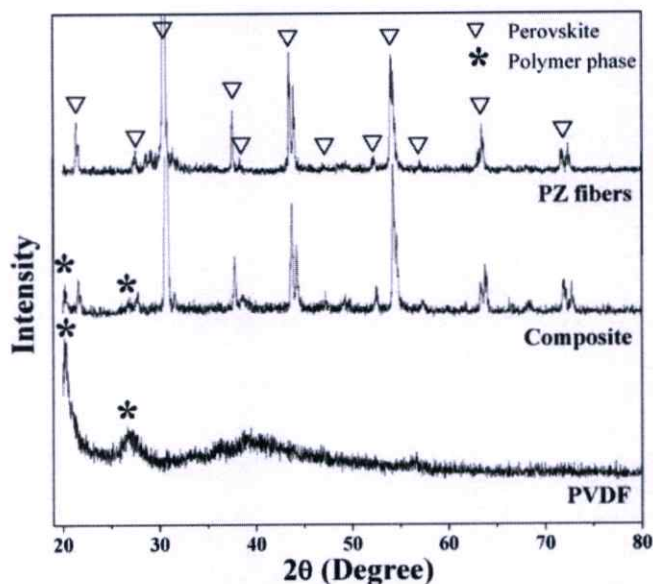


Figure 2. XRD patterns of 3-3 PZ/PVDF nanocomposite compared with PZ fibers and PVDF powder.

Formation of the 3-3 PZ/PVDF composite was confirmed further by the FTIR spectra, as shown in Figure 3. The spectrum of the 3-3 PZ/PVDF composite shows multiple absorption bands in the region of 400 to 4,000 cm^{-1} , which corresponds to the stretching and bending vibrations of ceramic, polymers and moisture. Peaks of around 1,450 cm^{-1} correspond to the aliphatic CH group vibrations of the CH_2 mode of PVDF polymer [9]. The wave number at $\sim 1,600 \text{ cm}^{-1}$ and broad peak at around 3,400 cm^{-1} both correspond

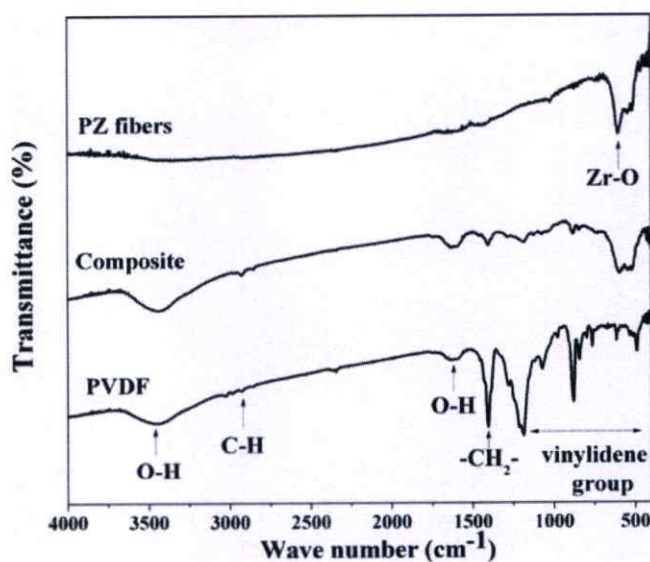


Figure 3. FT-IR spectra of 3-3 PZ/PVDF nanocomposite.

to the O—H stretching vibration of moisture [10]. The symmetric and asymmetric CH stretching vibration of PVDF is observed at 2900 cm^{-1} [16]. The absorption band at 480, 530, 612, 764, 797, 855, 976 and 1410 cm^{-1} correspond to large amount of α crystal phase, whereas peak at 1226 cm^{-1} indicates β phase of vinylidene group of polymer [15, 17]. In addition, the absorption peak at $\sim 548\text{ cm}^{-1}$ is attributed to Zr—O stretching vibration [11], which corresponds to the polycrystalline PZ fiber. This study can guarantee that its sample consists of two phases, including ceramic and polymer phases.

Dielectric properties of the resultant 3-3 PZ/PVDF nanocomposite was characterized by LCR meter. The dielectric constant of the 3-3 composite was found to be relatively stable in the range of 21.98–18.21 within the measurement frequencies from 100 Hz to 2 MHz (Figure 4). This value is higher than the dielectric constant of the polyvinylidene fluoride, which was measured as 13.14 (at 2 MHz) in this study. This is due to the increasing contribution of PZ to the dielectric properties of the composites, because PZ has a substantially higher dielectric constant ($\epsilon_r = 116$ at room temperature [18]) than the polymer. This result demonstrated that, a particular response of a composite to an external field may depend either on the corresponding response of individual phases or may result in a property not existent in the phases composing the material. In addition, a particular property of the composite may depend on several properties of the individual phase [19]. The polymer phase in the composite was burnt out at 600°C , and the weight of the sample was recorded. From the theoretical density of PZ (8.085 g/cm^3) and PVDF (0.6 g/cm^3), the volume fraction of the PZ fibers in this composite structure was determined to be about 10%. Using the rule of mixtures according to equation (1) and dielectric constants of the constituent phases, polyvinylidene fluoride and PZ, the calculated dielectric constant of the composite was 23.43. [20]

$$\epsilon'_{\text{composite}} = \epsilon'_{\text{polymer}} V_{\text{polymer}} + \epsilon'_{\text{ceramic}} V_{\text{ceramic}} \quad (1)$$

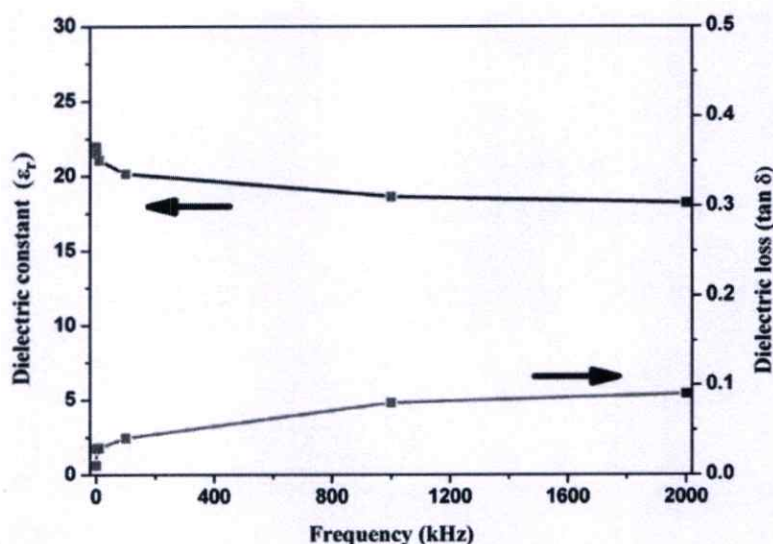


Figure 4. Dielectric properties of 3-3 PZ/PVDF nanocomposite within the measurement frequencies from 100 Hz to 2 MHz.

The calculated value is higher than the measured value, this may be due to the porosity and its contribution to the dielectric constant of the composite. The dielectric loss of the composite is below 0.09 at low frequencies.

4. Conclusions

In summary, this study prepared 3-3 PZ/PVDF nanocomposite successfully by infiltrating a polyvinylidene fluoride (PVDF) polymer into the PZ nanofiber mat. The composite has relatively smooth surface. The PZ/PVDF composite consists of two phases, including ceramic phase with orthorhombic perovskite structure and polymer phases. The dielectric constant of the composite measured at room temperature is higher than the polymer matrix and reasonably agrees with the prediction from the rule of mixtures.

Acknowledgments

This research has supported by The Royal Golden Jubilee Ph.D. Program (RGJ) under The Thailand Research Fund (TRF), the KMITL research fund and The Thailand Research Fund (TRF).

References

1. A. Petchsuk, W. Supmak, and A. Thanaboonsombut, *Journal of Applied Polymer Science*. **114**, 1048 (2009).
2. M. Wu, H. Huang, W. Chu, L. Guo, L. Qiao, and J. Xu, T.-Y. Zhang, *J. Phys. Chem. C*. **114**, 9955 (2010).
3. L. Xiaofang, X. Chuanxi, S. Huajun, D. Lijie, L. Rui, and L. Yang, *Journal of Wuhan University of Technology-Mater. Sci. Ed.* **20**, 4 (2005), 60.
4. X. J. Lou, and J. Wang, *Applied Physics Letters*. **96**, 102906. (2010).
5. I. Kim, S. Bae, K. Kim, H. Kim, J. S. Lee, J. Jeong, and K. Yamakawa, *Journal of the Korean Physical Society*. **33**, 2, 180 (1998).
6. L. R. Xu, L. Li, C. M. Lukehart, and H. Kuai, *Journal of Nanoscience and Nanotechnology*. **7**, 1 (2007).
7. A. Safari, *Journal of Physics III France*. **4**, 1129 (1994).
8. K. Arlt and M. Wegener, *IEEE*. **1178** (2010).
9. A. M. Vinogradov, V. H. Schmidt, G. F. Tuthill, and G. W. Bohannon, *Mechanics of Materials*. **36**, 1007 (2004).
10. A. Petchsuk, and W. Supmak, A. Thanaboonsombut, *Journal of Applied Polymer Science*. **114**, 1048 (2009).
11. H. L. W. Chan, W. K. Chan, Y. Zhang, and C. L. Choy, *IEEE Transactions on Dielectrics and Electrical Insulation*. **5**, 4 (1998).
12. Y. R. Wang, J. M. Zheng, G. Y. Ren, P. H. Zhang, and C. Xu, *Smart Materials Structure*. **20**, 7 (2011).
13. S. Hajesaeh, and S. Muensit, *Journal of Science and Technology*. **29** (2007).
14. C. Nawani, B. Boomchom, J. Prachayawarakorn, W. C. Vittayakorn, and N. Vittayakorn, *Materials Science and Engineering B*. **177**, 1009 (2012).
15. V. Ostasevicius, I. Milasauskaite, R. Dauksevicius, V. Baltrusaitis, and V. Grigaliunas, I. Prosycevas, ISSN 1392-1207, **6**(86) (2010).
16. K. Kitaoka, H. Kozuka, and T. Yoko, *Journal of American Ceramics Society*. **81**, [5] 1189 (1998).
17. A. Kumar, and M. Deka, ISBN 978-953-7619-86-2, **438** (2010).

18. N. Vittayakorn, P. Charoonsuk, P. Kasiansin, S. Wirunchit, and B. Boonchom, *Journal of Applied Physics*. **106**, 064104 (2009).
19. B. Hilczer, J. Kućek, E. Markiewicz, M. Kosec, and B. Mali, *Journal of Non-Crystalline Solids*. **305**, 167 (2002).
20. E. M. Alkoy, C. Dagdeviren, and M. Papila, *Journal of American Ceramics Society*. **92** [11], 2566 (2009).

Characterization and Dielectric Properties of Nanocomposite Made of Lead Zirconate Nanofibers and Polyvinylidene Fluoride Improved with Carbon Nanotubes

CHANISA NAWANIL,¹ APINAI RERKRATN,² PANPAILIN SEEHARAJ,³ AND NARATIP VITTAYAKORN^{1,3,*}

¹College of KMITL Nanotechnology, King Mongkut's Institute of Technology Ladkrabang, Bangkok 10520, Thailand

²Department of Instrumentation and Control Engineering, Faculty of Engineering, King Mongkut's Institute of Technology Ladkrabang, Bangkok 10520, Thailand

³Materials Science Research Unit, Department of Chemistry, Faculty of Science, King Mongkut's Institute of Technology Ladkrabang, Bangkok 10520, Thailand

A three-phase PZ/CNT/PVDF nanocomposite comprising lead zirconate (PZ) nanofibers, polyvinylidene fluoride (PVDF) and a small volume fraction of carbon nanotubes (CNT) was prepared by the solvent casting technique followed by composite heating at 80°C. The PZ/CNT/PVDF composites were characterized by X-ray diffraction, FT-IR and scanning electron microscopy (SEM). The dielectric properties of the composite were studied as a function of the frequency by an LCR meter. The dielectric constant of the PZ/CNT/PVDF nanocomposite was found to be in the range of 18–61 within the measurement frequencies from 100 Hz to 2 MHz. This value is higher than the dielectric constant of the PZ/PVDF nanocomposite. The measured dielectric properties demonstrate that the addition of CNT can improve the dielectric property appearance of the composite.

Keywords Lead zirconate (PZ); polyvinylidene fluoride (PVDF); carbon nanotubes (CNT); nanocomposite

1. Introduction

Composites made of electroactive ceramics and a ferroelectric polymer are very attractive for applications, since they exhibit low densities and good piezoelectric and pyroelectric properties that can be tailored to various requirements. Piezoelectric ceramics have been used extensively, due to their large dielectric constant, high piezoelectric strain and high electromechanical coupling coefficient [1]. However, the high leakage current, low dielectric strength and mechanical stiffness limit their applications [2], whereas, polymeric materials exhibit very high dielectric strength and low leakage current, but polymers generally show small dielectric constants ($\epsilon_r = 2 \sim 12$) [2]. Polymer based

Received December 9, 2012; in final form August 25, 2013.

*Corresponding author. E-mail: naratipcmu@yahoo.com

composite is considered as a solution to the problem by providing good opportunity for the development of a high dielectric constant, low leakage and high breakdown strength materials.

Antiferroelectric materials have attracted much research interest due to their potential applications in microactuators and energy conversion devices. Lead zirconate [PbZrO₃ (PZ)] is a well known antiferroelectric material that can be processed into various forms such as bulk ceramics, thin films, and fibers. The hysteresis characteristics of antiferroelectric PbZrO₃ regions are well suited for either power-storage or actuator applications. Furthermore, the extremely large charge released from the FE to AFE state may be useful as alternate capacitor materials in DRAMs. In recent years, researchers have focused on synthesizing nanosized PZ fibers by the electrospinning technique and incorporated that into a piezoelectric polymer to obtain smart piezocomposite structures, using polyvinylidene fluoride (PVDF) as a matrix. This is because PVDF has superior piezoelectric properties when compared with other types of polymeric materials, due to its polar crystalline structure. This research reports the preparation and dielectric properties of PZ/PVDF nanocomposite, with modification of the carbon nanotube (CNT). PZ/PVDF nanocomposite was chosen as an excellent candidate for acquiring high dielectric constant polymer matrix composites, according to the percolation theory, which is formation of long-range connectivity in random systems. Carbon nanotubes (CNTs) have remarkable electrical and mechanical properties such as extremely high conductance and Young's modulus [3]. They are found to be attractive on account of their potential for applications in nanoscale devices [4]. The PZ-CNT/PVDF composites were characterized using different techniques. Morphological studies were carried out using scanning electron microscopy (SEM), with the crystal structures determined by X-ray diffraction (XRD). The functional groups and dielectric properties of the composite were confirmed using FT-IR and an LCR meter, respectively.

2. Experimental Procedure

PZ nanofibers were synthesized by an electrospinning method, which utilized a solution that contained poly (ethylene oxide) (PEO, $M_w \sim 300,000$; Aldrich), and sol-gel precursor solution of PZ [5]. After obtaining the PZ fiber mats, three-phase PZ/CNT/PVDF nanocomposite samples were prepared. Firstly, polyvinylidene fluoride (PVDF; $M_w \sim 534,000$; Aldrich) powder was dissolved in dimethyl formamide (DMF) solvent to obtain the polymer matrix of the composite, before mixing in carbon nanotubes in specific proportions (compositions of 1 wt% CNTs). After stirring for 1 hr, the mixture was poured onto the calcined PZ fiber mat for the final polymer nanocomposite product, and this sample was kept under vacuum for 10 min to eliminate trapped air. Then, the sample was dried for 24 h at 80°C. X-ray diffraction (XRD; Bruker-D8 Advance) using CuK α radiation was used to determine the phases formed. The room-temperature FT-IR spectrum ranging 4,000–370 cm⁻¹ was recorded by a Perkin Elmer Spectrum GX FT-IR/FT-Raman spectrometer, with 8 scans and a resolution of 4 cm⁻¹ using KBr pellets. A scanning electron microscope (SEM, JEOL JSM5910LV) was used to observe the microstructures of the PZ/PVDF nanocomposite. Finally, dielectric properties of the PZ/PVDF nanocomposite were measured from 100 Hz to 2 MHz using an HP 4194A Impedance Analyzer (Santa Clara, CA). Samples of thin, rectangular, parallel plates were prepared and placed between two parallel metal plates of the sample holder for dielectric measurements.

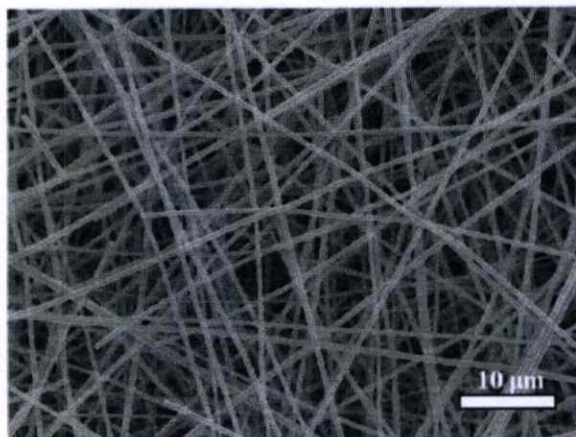


Figure 1. SEM micrograph of the PZ fibers.

3. Results and Discussion

Morphology of the PZ fiber and the three-phase PZ/CNT/PVDF nanocomposite were revealed by scanning electron microscopy (SEM). Figure 1 reveals that the continuous PZ nanofibers with average diameter of 300 ± 64 nm. Figure 2 shows SEM micrographs of the secondary electron (Fig. 2(a)) and backscattering electrons (Fig. 2(b)) images of the PZ/CNT/PVDF nanocomposite. In Fig. 2(b), the backscattering electrons image of the composite cross section shows that the polymer matrix phase thoroughly infiltrates the fiber network. The intimate mixture of three phases was obtained, in which the PZ phase and CNTs were visible in bright-white contrast, and the PVDF phase was identifiable as a darker-gray region. The figure revealed that the composite has 3–3 connectivity by using Newnham's convention [6] on connectivity of piezocomposites, in which the active PZ, CNT and polymer matrix phases are connected in three dimensions in the nanometer scale. The crystalline phases of PZ/CNT/PVDF nanocomposite were revealed by X-ray diffraction (XRD) spectra. Figure 3 shows the XRD patterns of the PZ/CNT/PVDF nanocomposite compared with those of PZ fibers. The figure revealed that crystalline PZ/CNT/PVDF nanocomposite was obtained. The strong diffraction peaks at 2θ values of 21.47° , 30.66° ,

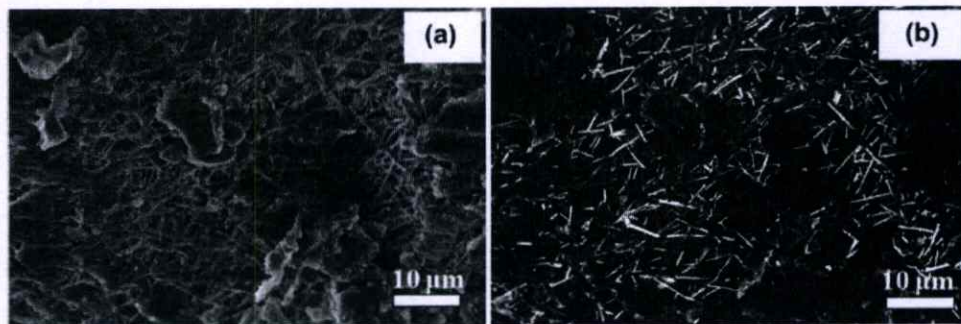


Figure 2. SEM micrographs of the (a) secondary electron and (b) backscattering electrons images of the PZ/CNT/PVDF nanocomposite.

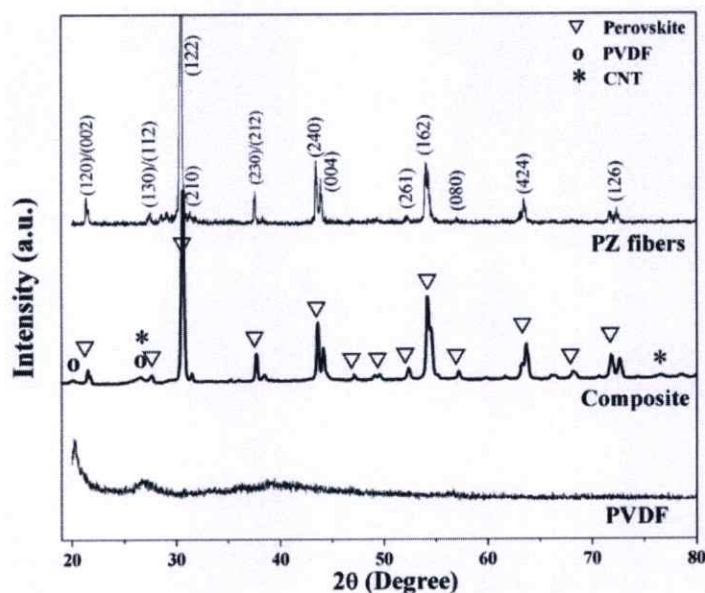


Figure 3. XRD patterns of PZ/CNT/PVDF nanocomposite compared with those of PZ fibers.

37.81°, 43.58°, 54.02°, 63.69° and 71.95° corresponding to (120), (122), (202), (240), (162), (424) and (126) crystal planes, respectively, indicating the formation of lead zirconate. According to JCPDS card no.75-1607, the diffraction peaks can be indexed as an orthorhombic perovskite structure. In addition, peaks of polyvinylidene fluoride (PVDF) could be observed in the XRD patterns of the composite, because PVDF is a semi-crystalline polymer with typical crystallinity of 50% [7]. Spectra of the PVDF polymer are seen at $2\theta = 26^\circ$ when referring to the diffractions in planes (021), which are characteristic of the α -phase [7]. The α -phase is the dominant crystalline phase most common upon crystallization from the melt [8], while the peak at $2\theta = 20^\circ$ refers to the sum of diffractions in plane (110) and (200), which are characteristic of the β -phase [7]. The β -phase exhibits the most piezoelectric, pyroelectric and ferroelectric activities. The latter form endues PVDF with great potential for various device applications [8]. The spectra also show that the (002) peak at 26° and (110) peak at 77° correspond to a crystal structure of graphite [9]. This study guarantees that the sample consists of three phases, including lead zirconate, carbon nanotubes and polymer phases. FT-IR is used to characterize the functional group of the PZ/CNT/PVDF nanocomposite. Figure 4 shows the FT-IR spectra in the range of 400–4,000 cm^{-1} . At $\sim 548 \text{ cm}^{-1}$, the absorption peak is attributed to Zr–O stretching vibration [10], which corresponds to the polycrystalline PZ fiber. The broad peak at around $3,400 \text{ cm}^{-1}$ corresponds to the O–H stretching vibration of moisture [10]. Peaks of around $1,450 \text{ cm}^{-1}$ correspond to the aliphatic CH group vibrations of the CH_2 mode of PVDF polymer [11]. The symmetric and asymmetric CH stretching vibration of PVDF is observed at $2,900 \text{ cm}^{-1}$ [11]. The absorption band at 760, 800, 860, 980 and $1,400 \text{ cm}^{-1}$ corresponds to a large amount of α crystal phase, whereas a peak at $\sim 1,220 \text{ cm}^{-1}$ indicates β phase of the vinylidene group of polymer [12]. A small peak at around 1650 cm^{-1} is associated with the C=C stretching of CNT [4]. A dielectric property of the PZ/CNT/PVDF nanocomposite was characterized by an LCR meter. Figure 5 presents frequency dependence of the dielectric constant (ϵ_r) of the PZ/CNT/PVDF nanocomposite at room temperature, and

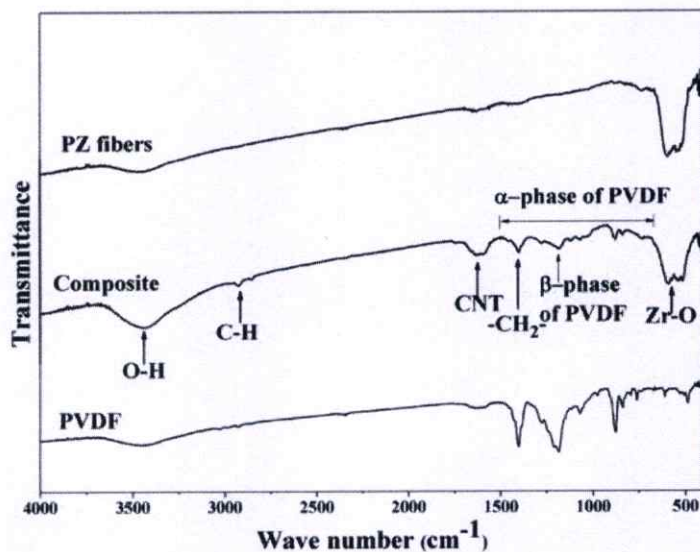


Figure 4. FT-IR spectra of PZ/CNT/PVDF nanocomposite compared with those of PZ fibers.

comparing with that of PZ/PVDF nanocomposite. It was found that the dielectric constant of the PZ/CNT/PVDF nanocomposite was in the range of 97–49, within the measurement frequencies from 100 Hz to 2 MHz. This value is higher than the dielectric constant of the PZ/PVDF nanocomposite measured as 18.21 (at 2 MHz), which may be due to the PZ fibers being well distributed by forming a complex mixture with CNT networks. This is in accordance with the percolation theory [13], which is the formation of long-range connectivity in random systems. This phenomenon is depicted in the schematic illustrations

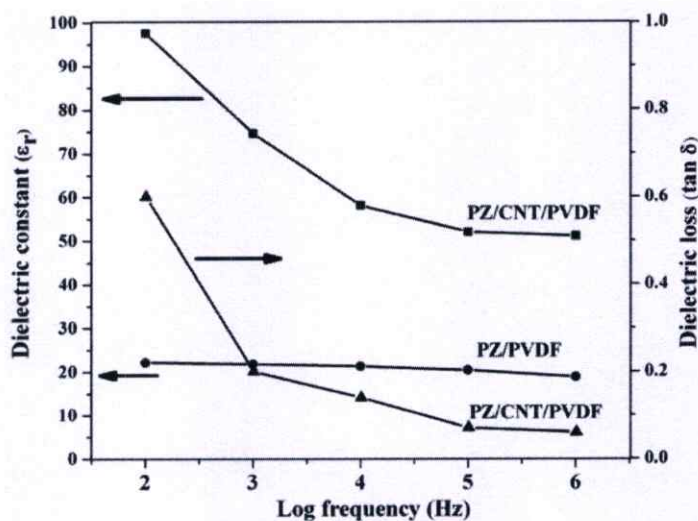


Figure 5. Dielectric constant and dielectric loss of PZ/CNT/PVDF nanocomposite compared with that of PZ/PVDF nanocomposite as a function of log frequencies.

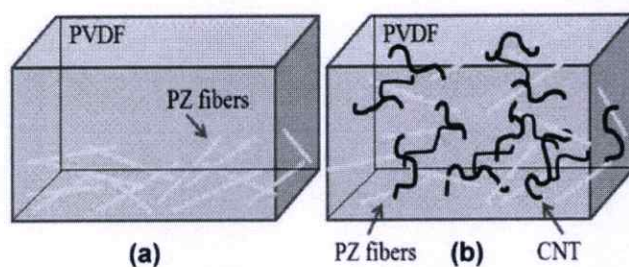


Figure 6. Schematics of the cross-sectional structure of PZ/PVDF nanocomposite (a) with CNT and (b) without CNT. (Color figure available online.)

of Figure 6, which demonstrates the sample with [Fig. 6(a)] and without [Fig. 6(b)] CNT. Since the CNT in Fig. 5(b) is mixed well and entangled with PZ fibers in the PVDF matrix, the task of dispersing PZ fibers uniformly inside the composite for a high-performance material is challenging. As a result, a high dielectric constant is generated. Furthermore, the conduction paths formed by the CNT networks can reduce the internal resistance of nanocomposite material [14]. Dang *et al.* [13] reported that CNTs reinforced by composites possess a much lower percolation threshold than those of composites containing conventional spherical fillers, such as metallic particles or carbon black. This is due to high-aspect ratio conductive fillers easily producing percolation (a conducting network) at a lower volume fraction. Thus, the CNT can act as dispersant and conduct functional material in nanocomposite. Additionally, it is noticeable that a low dielectric loss was obtained together with a high dielectric constant, as shown in Fig. 4. The minimum value of loss is 0.02 and the maximum value is still less than 0.6, which is attractive for practical applications.

4. Conclusion

In summary, three-phase PZ/CNT/PVDF nanocomposite in carbon nanotubes filled with PZ/PVDF mixture was prepared via a simple casting technique using PZ fibers from the electrospinning process. The effects of CNT on the dielectric properties of PZ/PVDF nanocomposite were examined. The dielectric constant of the PZ/CNT/PVDF nanocomposite measured at room temperature was found to be in the range of 97–49, within the measurement frequencies from 100 Hz to 2 MHz, and higher than the PZ/PVDF nanocomposite without CNT. This result agrees reasonably well with the percolation theory of CNT. Thus, adjustable dielectric properties were discovered by employing the three-phase system.

Acknowledgments

This work has been fully supported by research fund from National Nanotechnology Center (NANOTEC) NSTDA, through its “Center of Excellence Network”.

References

1. M. Wu, H. Huang, and W. Chu, *et al.*, Tuning the ferroelectric and piezoelectric properties of $0.91\text{Pb}(\text{Zn}_{1/3}\text{Nb}_{2/3})\text{O}_3\text{-}0.09\text{PbTiO}_3$ single crystals and lead zirconate titanate ceramics by doping hydrogen. *J. Phys. Chem. C.* **114**, 9955–9960 (2010).

2. N. J. Joshi, Studies of nano-sized high dielectric constant materials. The Maharaja Sayajirao University of Baroda Vadodara, Gujarat India 2012
3. X. Zeng, X. Xu, P. M. Shenai, E. Kovalev, C. Baudot, N. Mathews, and Y. Zhao, Characteristics of the electrical percolation in carbon nanotubes/polymer nanocomposites. *J. Phys. Chem. C.* **115**(44), 21685–21690 (2011).
4. B. P. Ramesh, W. J. Blau, P. K. Tyagi, D. S. Misra, N. Ali, J. Gracio, G. Cabral, and E. Titus, Thermogravimetric analysis of cobalt-filled carbon nanotubes deposited by chemical vapour deposition. *Thin Solid Films.* **494**, 128–132 (2006).
5. C. Nawani, B. Boonchom, J. Prachayawarakorn, W. Vittayakorn, and N. Vittayakorn, Synthesis and phase evolution of electrospun antiferroelectric lead zirconate (PbZrO_3) nanofibers. *Mater Sci. Eng B.* **177**, 1009–1016 (2012).
6. A. Safari, Development of piezoelectric composites for transducers. *J. Phys. III. France.* **4**, 1129–1149 (1994).
7. V. Ostasevicius, I. Milasauskaite, R. Dauksevičius, V. Baltrusaitis, V. Grigaliunas, and I. Prosycevas, Experimental characterization of material structure of piezoelectric PVDF polymer. *Mechanika.* **6**(86), 1392–1207 (2010).
8. G. Mago, F. T. Fisher, and D. M. Kalyon, Deformation-induced crystallization and associated morphology development of carbon nanotube-PVDF nanocomposites. *J. Nanosci. Nanotechnol.* **9**, 3330–3340 (2009).
9. A. Cao, C. Xu, J. Liang, D. Wu, and B. Wei, X-ray diffraction characterization on the alignment degree of carbon nanotubes. *Chem. Phys. Lett.* **344**, 13–17 (2001).
10. Y. Wang, and J. J. Santiago-Aviles, Synthesis of lead zirconate titanate nanofibres and the Fourier-transform infrared characterization of their metallo-organic decomposition process. *Nanotechnology.* **15**, 32–36 (2004).
11. A. M. Vinogradov, V. H. Schmidt, G. F. Tuthill, and G. W. Bohannon, Damping and electromechanical energy losses in the piezoelectric polymer PVDF. *Mech. Mater.* **36**, 1007–1016 (2004).
12. V. Ostasevicius, I. Milasauskaite, R. Dauksevičius, V. Baltrusaitis, V. Grigaliunas, and I. Prosycevas, Experimental characterization of material structure of piezoelectric PVDF polymer. *Mechanika.* **6**(86), 1392–1207 (2010).
13. Z. M. Dang, S. H. Yao, J. K. Yuan, and J. Bai, Tailored Dielectric Properties based on Microstructure change in BaTiO_3 -carbon nanotube/polyvinylidene fluoride three-phase nanocomposites. *J. Phys. Chem. C.* **114**, 13204–13209 (2010).
14. K. I. Park, M. Lee, Y. Liu, et al., Flexible Nanocomposite generator made of BaTiO_3 nanoparticles and graphitic carbons. *Adv. Mater.* 1–6 (2012).

CURRICULUM VITAE

1. Name: Chanisa Nawani
2. Nationality: Thai
3. Date of birth: May 23, 1986
4. Sex: Female
5. E-mail Address : g_aob_d@hotmail.com
6. Tel. : 0846694115
7. Education:

2005 – 2009

BSc. Industrial Chemistry, Faculty of Science, Department of Chemistry, King Mongkut's Institute of Technology Ladkrabang, Bangkok, Thailand

- Subjects studied:

Major studies: General Chemistry, Physics, Physical Chemistry, Analytical Chemistry, Organic Chemistry, Inorganic Chemistry, Petrochemical Industry, Rubber Technology, Polymer Chemistry, Polymer Physics, Mathematic for Physics and Chemist, Calculus, Principle and Calculations in Chemical Engineering, Scientific Programming, Chemical Engineering Thermodynamics and Kinetics, Elementary Statistics, Chemical Industrial Processes, Unit Operation for Chemical Industry, General Production Quality Control, Process Dynamics and Control, Polymer Technology, Production Organization and Industrial Management, Special Topics in Industry.

Minor studies: Industrial Chemicals, Polymer Measurement, Usage and Transformation of Polymers, Applied Chemical Instrumental Analysis, Spectroscopy, Industrial Management, Instrumental Analysis, Engineering Workshop, Engineering Drawing, Introduction to Physical Education, English

Selective studies: Money and Banking, Library Usage, Business Administration, Art of Living.

- Has been awarded the SCG Talent Scholarship-2nd Place of 2008 and participated in the SCG Smart and Ethical Camp.
- Attended the Organization and Industrial Management Course (Business Management, TQM, GMP and HACCP, ISO9001, ISO140001, OHSAS180001, ISO22000, ISO17025, Six Sigma, Water and Energy Management, Job analysis, Leadership)
- **Project:** Synthesis Lead Free Piezoelectric in $[(\text{Bi}_{1/2}\text{K}_{1/2})_{1-x/2}\text{Li}_x]_{0.99}\text{Ba}_{0.01}\text{TiO}_3$ System
- **Graduated** with 3.52 GPA (First class honors).

2010 – 2015

PhD. Nanoscience and Nanotechnology. College of Nanotechnology, King Mongkut's Institute of Technology Ladkrabang, Bangkok, Thailand

- **Subjects studied:** Quantum Mechanics for Nanotechnology, Materials Characterization, Polymer Nanocomposites, Testing of Materials Properties, Nanostructure Optical Materials and Their Applications, Electroceramic Materials and Applications
- **Project:** Preparation and Dielectric Properties of Piezoelectric/Polymer Nanocomposite Materials.
- Attended a research project titled "Electrocaloric effect in ceramic/polymer composites" at Department of Materials, Imperial College London for 6 months (July 4, 2014 – December 24, 2014).

8. Review articles

- [1] Chanisa Nawani and Naratip Vittayakorn. "Ceramic Nanofibers". Journal of Science Ladkrabang, Vol.20 No.2 July-December 2011 p. 13-28.

9. Presentations

- [1] Chanisa Nawani and Naratip Vittayakorn. "Synthesis of Blended Lead Zirconate (PbZrO_3) / Poly(Ethylene Oxide) Nanofibers via Electrospinning". The 27th Annual

Conference of the Microscopy Society of Thailand, Samui, Thailand, January 20-22, 2010 (Poster presentation)

- [2] Chanisa Nawani and Naratip Vittayakorn. "Synthesis of Lead Zirconate (PbZrO_3) Nanofibers via Electrospinning". The 7th Asian Meeting on Ferroelectricity and The 7th Asian Meeting on Electroceramics, Ramada Plaza Jeju Hotel, Jeju, Korea, June 28 – July 1, 2010 (Poster presentation).
- [3] Chanisa Nawani, Wanwilai Vittayakorn, Banjong Boonchom, Jutarat Prachayawarakorn and Naratip Vittayakorn. "The Effect of Thai Glutinous Rice Starch on the Synthesis of Antiferroelectric Lead Zirconate (PbZrO_3) Nanofibers via the Electrospinning Method". International Conference on Advanced Electromaterials 2011, ICAE2011, Ramada Plaza Jeju Hotel, Jeju, Korea, November 7 – 10, 2011 (Oral presentation).
- [4] Chanisa Nawani and Naratip Vittayakorn. "Synthesis of Blended Lead Zirconate (PbZrO_3) / Poly(ethylene oxide) / Glutinous Rice Starch Nanofibers via Electrospinning Combined with the Sol-Gel Process". The 7th Annual Conference of the Thai Physics Society, SPC2012 Phra nakhon Si Ayuttaya, Thailand, May 9-12, 2012 (Oral presentation).
- [5] Chanisa Nawani, Apinai Rerkratn, Panpailin Seeharaj and Naratip Vittayakorn. "Characterization and Dielectric Properties of Nanocomposite Made of Lead Zirconate Nanofibers and Polyvinylidene Fluoride Improved with Carbon Nanotubes". Special International Workshop and Symposium on Emerging Frontiers in Multiferroics and Electronic Metamaterials (INAMM), Amari Orchid Hotel, Pattaya, Thailand, November 9-10, 2012 (Poster presentation).
- [6] Chanisa Nawani, Apinai Rerkratn, Panpailin Seeharaj and Naratip Vittayakorn. "Effect of Chemical Treatment on Phase Transition of Lead Zirconate Nanofibers". The 8th Asian Meeting on Ferroelectrics (AMF-8), Amari Orchid Hotel, Pattaya, Thailand, November 9-14, 2012 (Oral presentation).

10. Publications

- [1] Chanisa Nawani, Banjong Boonchom, Jutarat Prachayawarakorn, Wanwilai C. Vittayakorn and Naratip Vittayakorn. "Synthesis and phase evolution of

electrospun antiferroelectric lead zirconate (PbZrO_3) nanofibers". *Materials Science and Engineering B* 17 (1012) 1009-1016.

- [2] Chanisa Nawani, Wanwilai Vittayakorn, Rangson Muanghua, Surasak Niemcharoen, Jutarat Prachayawarakorn and Naratip Vittayakorn. "The Effect of Thai Glutinous Rice Starch on the Synthesis of Lead Zirconate (PbZrO_3) Nanofibers via the Electrospinning Method". *Journal of Nanoscience and Nanotechnology* 13 (2013) 3700-3704.
- [3] Chanisa Nawani, Wanwilai Vittayakorn, Jutarat Prachayawarakorn and Naratip Vittayakorn. "Preparation and Dielectric Properties of 3-3 Lead Zirconate/Polyvinylidene Fluoride Nanocomposite". *Ferroelectrics Letters Section* 40 (2013) 94-100.
- [4] Chanisa Nawani, Apinai Rerkratn, Panpailin Seeharaj and Naratip Vittayakorn, "Effect of Chemical Treatment on Phase Transition of Lead Zirconate Nanofibers". *Ferroelectrics*, 450 (2013) 49-56.
- [5] Chanisa Nawani, Apinai Rerkratn, Panpailin Seeharaj and Naratip Vittayakorn, "Characterization and Dielectric Properties of Nanocomposite Made of Lead Zirconate Nanofibers and Polyvinylidene Fluoride Improved with Carbon Nanotubes". *Integrated Ferroelectrics*, 149 (2013) 18-24.